Università degli Studi di Torino
Scuola di Scienze della Natura

Master of Science Thesis

Near-Surface Turbulence in Complex Terrain

Example of the Mountain-top Site Arbeser Kogel

Alessio Golzio

Supervisors
Prof. Dr. Mathias W. Rotach
Institute of Atmospheric and Cryospheric Sciences
University of Innsbruck, Austria

Dr. Silvia Ferrarese
Department of Physics
University of Turin, Italy

Academic Year 2015-2016

July 14, 2016

To my future
and present family;
Mum, Dad and
Francesca.

Contents

Abstract

Little is known concerning the boundary layer structure and turbulence characteristics over complex mountainous terrain. Much effort and dedicated studies have been started in the last decades, and the i-Box project is one of the long-term and most comprehensive project on surface layer turbulence over complex terrain. This MSc Thesis work is the first insight on a particular station of this project: Arbeser Kogel.

This station is located at a mountain-top (2015 m a.s.l.), almost at the upper border of a conventional valley boundary layer. It is also set in a harsh environment where the data-collection is quite difficult.

Here an accurate analysis with different methods and thresholds compared to other stations is done. In this first part of the study the attention is focused on particular patterns of wind, radiation, humidity and temperature, that are analysed starting from standard meteorological measurements. From this data-pool a classification of most significant days was done, the attention was particularly focused on thermally driven days, which are selected by a Clear Day Algorithm. A comparison within thermally driven flow theories in mountainous terrain and wind behaviour at Arbeser was done. The results partially agree with the theories and in some days the valley wind circulation arrives up to Arbeser, but a prevalent wind direction is found and not fully understood in this frame.

In the second part the turbulence data of those thermally driven days is studied. In particular the theories for the surface layer over horizontal homogeneous and flat terrain are compared with the measurements at Arbeser. The results partially agree with other experiments settled in complex terrain, but on the other side, some discrepancies with respect to flat terrain are found.

Introduction

The Atmospheric Boundary Layer over horizontally homogeneous and flat terrain has been thoroughly studied since 1950s, but this is a simplification of the reality, or better, this simplification works well only over flat terrain. However in complex terrain, like mountainous terrain or a truly complex Alpine valley in the case of study of this Master Thesis, most of these simplifications and reductions fail or they are too much inaccurate. Comprehensive studies on boundary layer turbulence structure and exchange processes in complex terrain have not developed yet. Only starting from 1990s the interest of some scientists began to focus on this topic.

Since these years first on field campaign were organised, at the beginning with one-site studies, with measurements on multiple levels on high masts, then new campaign starts to study valley's cross sections, but mostly for a shorter time period.

This Master of Science Thesis deals with the study of the near-surface turbulence within the i-Box Project (where the "i" means Innsbruck) lead by Professor Dr. Mathias Rotach. The i-Box project is a long therm project that, differently from previous studies, involved three dimensional volume in a truly complex terrain: the Inn Valley.

This experiment counts on six turbulence measurements site, five of those are settled inside the Inn Valley with different expositions and slope angles, one, the topic of this thesis, is settled at a nearby mountain-top site: Arbeser Kogel.

The Arbeser station is placed in a quite unique and particular position, it is near the summit cross of Arbeser Kogel at the altitude of 2015 m, nowadays anyone has published papers about similar sites yet.

The aim of this thesis is to explore the data collected at this particular site, analyse them and try to understand better the near-surface turbulence behaviour. The approach to this study will follow three research questions. The first one is about the valley wind system and how it interacts with a mountain-top site. The second question is about the turbulence behaviour and its scaling expectations,

the approach used consists in the application of the nowadays known theories for Homogeneous and Horizontally Flat terrain as a reference, but their applicability at such complex site will be investigated. The third research question examines the surface energy balance, does a mountain-top station respect the scientist knowledge on the energy balance closure?

This is not a simple task, it requires long preliminaries, first of all because anyone has analysed this data before, and secondly because this site is out-of-scheme for nowadays surface layer studies.

For these and other reasons this report is divided in two parts, the first one concerns the Boundary Layer Meteorology and studies: a long introduction to what is known and a review of the literature about boundary layer and surface layer in complex terrain. In this part it is also included an overview on the i-Box Project as its concern, aims and results. The second part is strictly about Arbeser Kogel station, with an introduction on the station itself and then all the analysis done on standard meteorological data (temperature, humidity, wind speed and direction, and radiation) and turbulence data (acquired by the ultrasonic anemometer and the Krypton hygrometer).

In the conclusions chapters are summarised the main results of this work and also some suggestions on what can be done in the future. For the difficulties encountered, especially the scarcity of data due to the harsh environment, the results are only preliminary, and they have to be developed.

Introduzione

Lo strato limite atmosferico su terreno pianeggiante e omogeneo è studiato a partire dagli anni '50, ma questo rappresenta una semplificazione della realtà, o per meglio dire, funziona bene solamente ove è stato idealizzato, ovvero su terreno pianeggiante. Queste assunzioni, che funzionano egregiamente sul terreno piano ed omogeneo, se applicate in terreno complesso, come può essere l'interno di una valle alpina o in generale una zona montuosa, falliscono o sono troppo inaccurate per garantire un risultato soddisfaciente. Studi esaurienti sulla turbolenza nello strato limite e relativi scambi energetici in terreno complesso non sono ancora stati compiuti. Solamente a partire dagli anni '90 alcuni scienziati dell'atmosfera si sono rivolti con interesse allo studio di queste tematiche.

Dunque a partire da questi anni sono state organizzate le prime campagne sperimentali, dove inizialmente si compivano studi puntuali della turbolenza, seppur con lo studio di diversi livelli sovrapposti. Da qui la comunità scientifica si è orientata sullo studio di sezioni trasversali di valli, ma comunque per periodi di tempo limitati.

Questa Tesi Magistrale tratta, appunto, la turbolenza atmosferica nello strato più superficiale. L'ambito di studio è il progetto i-Box (dove la "i" rappresenta Innsbruck) guidato ed ideato dal Prof. Dr. Mathias Rotach. Il progetto i-Box è un esperimento a lungo termine, quindi con misure che proseguono pressoché ininterrotte da qualche anno - a differenza degli studi precedenti - e che ha i siti di misura disposti in modo da rappresentare un volume tridimensionale all'interno della valle dell'Inn.

Fanno parte di questo esperimento sei stazioni di misura equipaggiate per misurare le variabili della turbolenza. Cinque di esse sono nella valle dell'Inn, disposte su versanti con diverse esposizioni ed inclinazioni, una, l'oggetto di questa Tesi, invece è disposta presso la vetta di una vicina montagna: Arbeser Kogel.

La stazione Arbeser è installata in una posizione unica; poco sotto la croce di vetta alla quota di 2015 m s.l.m., e oggigiorno nessuno ha ancora pubblicato studi che coinvolgano un sito analogo.

Lo scopo di questa Tesi è di esplorare per la prima volta i dati raccolti in quasi due anni di misure in questo sito particolare, analizzarli e cercare di capire meglio il comportamento della turbolenza presso la vetta di una montagna. Lo studio di questa Tesi si sviluppa attorno a tre domande fondamentali, alle quali si cercherà di rispondere con grafici, dati e analisi. La prima riguarda l'interazione tra la circolazione dei venti all'interno della valle e il sito posto in cima alla montagna: risentirà la stazione della circolazione valliva? La seconda domanda riguarda la turbolenza, come si comporta in un sito di alta montagna e come "scalano" le variabili turbolente; segue le aspettative che si hanno da precedenti studi? L'approccio utilizzato, infatti, consiste nell'applicazione delle teorie ad oggi note, che sono state sviluppate su terreno piatto e orizzontalmente omogeneo, quindi bisogna verificare che queste relazioni siano accettabili, oppure quali modifiche possano subire per essere valide anche in terreno complesso. La terza ed ultima questione invece esamina il bilancio energetico alla superficie. Nel sito oggetto di studio, esso rispetta ciò che già si conosce sulla chiusura del bilancio energetico? Questo è tutt'altro che semplice, ha richiesto infatti un lungo trattamento preliminare dei dati, questo perché ancora nessuno li aveva trattati e poi perché è un sito particolarmente fuori dagli schemi.

Per questo ed altri motivi questa Tesi è stata suddivisa in due parti, la prima riguarda in generale la meteorologia dello strato limite e tutti i precedenti studi fattivi. Il primo capitolo è un riassunto e introduzione a ciò che si conosce (e ciò che tornerà utile sapere per il seguito), con un'attenta raccolta dei principali articoli nella letteratura scientifica riguardanti lo strato limite in terreno complesso. Il secondo capitolo invece tratta in modo generale il progetto i-Box con un breve riassunto dello scopo e dei principali risultati fin'ora ottenuti. La seconda parte, invece, è relativa unicamente alla stazione Arbeser Kogel. Nel capitolo terzo quindi si potrà trovare una descrizione fin nei minimi dettagli della stazione. Il capitolo quarto invece introduce all'analisi e ai preparativi ad essa delle variabili sia meteorologiche standard (temperatura, umidità, direzione e velocità del vento e radiazione) che turbolente (acquisite con l'anemometro ultrasonico e con l'igrometro al Kripto).

Nel capitolo quinto si farà un'attenta analisi dei risultati ottenuti e cosa ancora vi è da fare per gettare maggior luce sui dati acquisiti. A causa delle difficoltà incontrate, dovute essenzialmente alla scarsità di dati e all'ambiente poco favorevole alle misure, questi risultati sono una prima luce nel buio, e molto altro ancora è possibile fare.

Part I

Boundary Layer Meteorology and the i-Box

Chapter 1

The Atmospheric Boundary Layer

The Earth's atmosphere can be divided into several parts, and in order to do that it is possible to choose from a lot of different ways. The easiest subdivision of Earth's atmosphere is by using the air temperature variation. Using this method it is possible to identify four layers. Bottom-up the *troposphere, stratosphere, mesosphere and thermosphere*. The boundaries between the layers are called *tropopause, stratopause and mesopause*.

This is not the only way to separate the atmosphere. Different layers description of the atmosphere are possible, and every description is useful in one particular field of studies. For example it is possible to classify the layers using the chemical composition; in this another classification could be found with the *omosphere* and the *eterosphere*; otherwise using the ion amount, and consequently focusing on electromagnetic properties of the atmosphere it is possible to find the *ionosphere*.

The topic of this MSc Thesis is the *Boundary Layer*, that comes from another classification of the atmosphere. In this instance there is the lower part of the atmosphere, the Atmospheric Boundary Layer (in short ABL), that is directly affected by the ground, especially from the friction drag, and in which there are momentum and heat transfers. Instead the upper part is called the *free atmosphere*.

The first classification cited is also useful for our understanding of this topic. Indeed the lowest layer, the troposphere, supports life on the planet and it is the layer in which "weather" occurs. This layer is very important for us - we live in it - and it also contains more than 98% of the water vapour. This is the reason why the weather phenomena occurs only (or almost) there; further the ABL is

entirely contained in the troposphere, and we are interested in the physics of this lower and thin layer.

Then let's examine in depth the atmospheric boundary layer.

1.1 A Boundary Layer Definition

As I said in the introduction of this chapter, the boundary layer is totally in the troposphere; usually the troposphere extends up to between 6, over poles, to 17 km over the equator, and boundary layer is only high 1 to 3 km. The most clear and simple definition of the Boundary Layer (BL) comes from Roland Stull:

> The boundary layer is that part of the troposphere that is directly influenced by the presence of the Earth's surface, and responds to surface forcing with a timescale of about an hour or less.
> (Stull, 1988 [45])

The surface forcing cited by Stull includes first of all frictional drag, then all the interaction with the biosphere, thus evapotranspiration, heat transfer, anthropic air pollutant emissions and the terrain complexities that modifies the flow (this point will be fundamental in the following sections). Sometimes the *turbulence*, the major responsible for all transport processes, is used to define the boundary layer.

Another aspect of the boundary layer is cloudiness. In this part of the atmosphere only two different types of clouds could be found: the first one is the *fair-weather cumulus cloud* (see Figure 1.1), and the second one is the *stratocumulus cloud*, that sometimes in particular condition may have the lower part of the cloud in contact with the ground, and in this case we talk of *fog* (see Figure 1.2).

1.2 Boundary Layer Structure

The depth and the structure of the boundary layer changes due to local and synoptic perturbation (especially over oceans). If firstly a stable, high pressure and over flat terrain situation is considered, it is possible to well define the structure of the boundary layer. In this situation a day-night cycle occurs (see Fig. 1.3), with a diurnal Convective Mixed Layer (ML), a nocturnal formation of a Stable Boundary Layer (SBL) from the ground, and upon it a Residual Layer (RL). Within these three major part it is also possible to define a thin part attached to

Figure 1.1: Fair-weather cumulus cloud above Pino Torinese.

the ground, the Surface Layer (SL), where the variation of turbulence fluxes is less than 10% of their magnitude. The SL represents about the 10% of the boundary layer height, convective either stable boundary layer. Above the mixed layer there is the *entrainment zone* where the air from the free atmosphere is brought into the mixed layer. For this reason in this part - the highest part - sometimes, a *cloud layer*, due to the entrainment could be found. The cloud layer is showed during high pressure days by fair-weather cumulus clouds, the Figure 1.1 is a clear example.

1.2.1 Convective Mixed Layer

After the sunrise, the heating of the ground leads air in the lowest layer to rise due to the solar radiation. In this moment, since the first thermal starts, the convective layer starts to grow rapidly until the mid-afternoon, when it reaches the heights of 1 to 2 km. This height mostly depends on the type of the ground, the season and the turbulence. The top of the mixed layer is capped by the entrainment zone, that sometimes is characterised by a thermal inversion also called *inversion layer*, that it is an heritage of the night strong inversion (that is further explained in the Section 1.2.3). The entrainment zone separates the boundary layer from the upper free atmosphere, and in this zone there are incursions of warm and less turbulent air that forms the inversion. In the mixed layer during free convection, buoyant thermals rise and gains momentum. When they reach the capping inversion the buoyant force changes into a negative one, but this packet overshoots in the free

Figure 1.2: Fog in a tree-lined avenue in Torino.

atmosphere, due to inertia. The overshooting is called *penetrative convection*. In the free atmosphere there is little turbulence, then this packet remains all together and the negative buoyancy sinks it back in the mixed layer mostly intact. There there is limited exchange of matter between mixed layer and free atmosphere, then pollutants can not escape. The results of this process is the entrainment of less-turbulent air from the free atmosphere into the mixed layer.

In the convective mixing layer it is usual to find thermals, as aforementioned, that starts from the ground and reaches the highest part of the layer. Their horizontal dimensions are about $1.5z_{ML}$, where z_{ML} is the height of the mixing layer. That means the vertical velocity can reach 5 m/s and, obviously, there are updraft zones and downdraft zones.

Usually the wind in the ML is subgeostrophic and has a nearly logarithmic profile in the surface layer. The mixing ratio, due to the evapotranspiration and the entrainment, decreases with height, indeed in the lower part a higher moisture is measured, instead in the upper part there is the entrainment of cold and usually dry air. A negative result of a stable boundary layer, with strong high pressure, consists of an air pollutant trapping into the mixed layer. This situation, especially in flat zone (for example northern Italy, in particular Po Valley), frequently happens during winter time, with several problems in urban area.

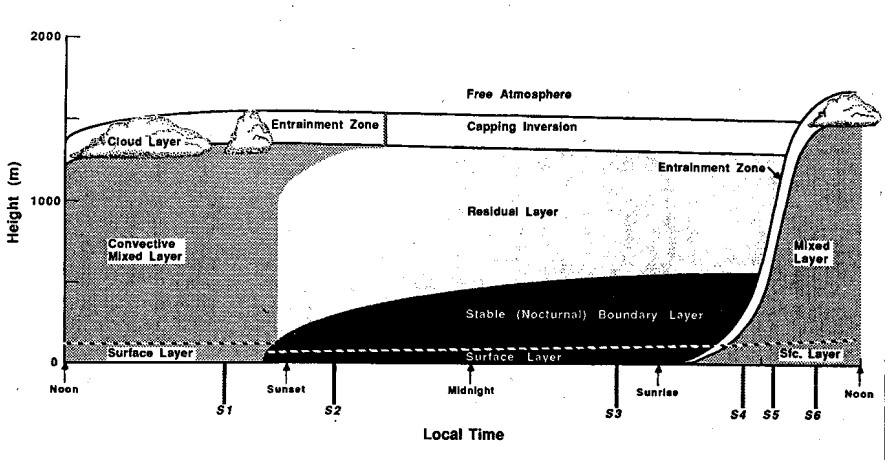

Figure 1.3: The boundary layer in high pressure regions over land consists of three major parts: a very turbulent mixed layer; a less-turbulent residual layer containing former mixed-layer air; and a nocturnal stable boundary layer of sporadic turbulence. The mixed layer can be subdivided into a cloud layer and a subcloud layer. From Stull, 1988 [45]

1.2.2 Residual Layer

After the sunset the energy necessary to maintain thermal convection is over, then in half an hour the turbulence decreases and the resulting layer is the *residual layer*. This layer has a constant virtual potential temperature (θ_v), then a neutral profile. This results in a isotropic turbulence; in this condition it is simple to observe the *coning* effect on smoke plumes.

1.2.3 Stable Boundary Layer

During the night, under the residual layer the *stable boundary layer* grows, a stable layer with a positive bottom-up potential temperature gradient. The stable boundary layer grows from the ground for the different heat capacity of the soil related to the air; in fact the ground cools down fastest than the upper air, and for conduction cool the air above it. This bottom-up cooling creates the inversion. When this happens during the night the *Nocturnal Boundary Layer* is formed, instead the stable boundary layer can also be formed by advection of warm-air over a cold surface. In the stable boundary layer there is a strong wind shear, small eddies and occasionally wave activity. It is often possible to observe a wind

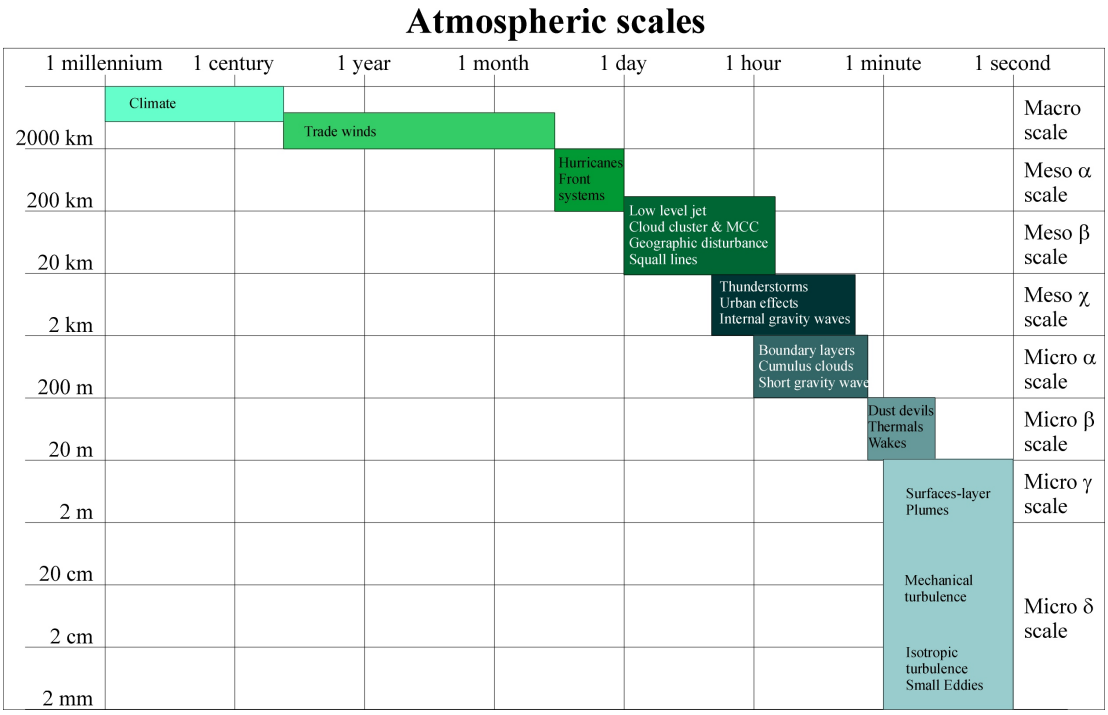

Figure 1.4: Typical atmospheric time and space order of magnitude, from macro to microscales, with the associated main phenomena.

maximum above the stable layer, at the top of the inversion. The wind direction is strongly affected by topography, and sometimes in valley it is possible to have calm winds. Furthermore, along slopes it is possible to find *katabatic winds* or *slope flows* (see Section 1.8 page 33), winds created by sliding cold and dense air.

1.3 Boundary Layer Studies

The issue now is how to approach the study of the boundary layer. The branch of atmospheric sciences that studies this part of the atmosphere is the *boundary layer meteorology*, and specifically to the surface layer is the *micrometeorology*.

The micrometeorology studies the microscale phenomena, phenomena with a time-scale approximately of 1 hour (always less than 1 day according to Foken 2008 [12]), and spatial-scale less than 1-2 km. In Figure 1.4 there are shown all the atmospheric scales, how they are distributed, and which is the field of micrometeorology.

Micrometeorology deals with the exchanges of heat, mass and momentum oc-

curring continuously in the lowest layer of the atmosphere between the Earth's surface and the ABL. Micrometeorologists study the vertical distributions of variables such as temperature, humidity and wind, as well as turbulent fluxes in the surface layer using fast response instruments. The aim is to understand the energy balance and other processes so close to the surface with a better understanding of these processes in the surface layer that will let them to clarify a lot of local phenomena. This part of meteorology usually deals with short time scale, and the exchanges of energy (e.g.) are studied on average period between 30 minutes and 1 hour. It is important not to confuse micrometeorology and microclimatology; in microclimatology it is usually considered longer time intervals (much bigger than 1 hour) and climatological averages.

1.3.1 Praise to the Turbulence

The turbulence is the most important characteristic of the boundary layer. Thanks to turbulence there is an efficient mixing in the lower part of the atmosphere (especially in daytime) and the exchanges of mass, heat and momentum are performed; if turbulence does not exist the timescale for these phenomena will be highly bigger. With all the exchanges in the ABL the life is possible, without turbulent remix of heat during the day near the ground temperature will raise to reach unlivable conditions.

Another important role of turbulence in the Earth system is the exchange of water vapour. It brings vapour from the surface of lakes, rivers, oceans and starts the hydrological cycle. As well as regarding the carbon dioxide; nowadays with high anthropogenic emissions by factories, house-heating, means of transport, the turbulent remixing in the boundary layer prevents our poisoning by air pollutants. With very stable boundary layer is also a problem because all these pollutant remains in the lowest 1 to 2 km, and the air quality terribly decreases.

Turbulence is also useful for pollen dispersion, and then for plant reproduction and spreading, nearby examples are pioneer plant in de-glaciated areas in the Alps.

Turbulence picks up dust, salt particles and generates in this way the cloud condensation nuclei, essential for the start-up of condensation in the troposphere.

Turbulent transfer of momentum is very important and act through the friction of the ground on the lower layer of the atmosphere. This friction drag deviates the wind from a geostrophic motion to a non-geostrophic one and permits the existence of convergence and divergence areas.

As we see the turbulence is very important; we cannot live without it and this is the reason why micrometeorology studies turbulence and the atmospheric boundary layer.

1.4 Radiation and Energy Balance

The electromagnetic radiation is the most important way to transfer energy through the atmosphere, and between the earth and the atmosphere. The electromagnetic spectrum is from very high energy waves of Gamma rays (γ), to the low energy and very long wave length of radio waves. The frequency spans between 300 EHz (exahertz, 10^{18} Hz) and 3 Hz, and the wave length, that it is defined by the formula

$$\lambda = \frac{c}{f} \tag{1.1}$$

where c is the light speed, ranges from $1 \cdot 10^{-12}$ m to $1 \cdot 10^{8}$ m.

1.4.1 Basic Laws of Radiation

Blackbody Radiation

The first equation is the Planck's law, most common for nowadays physicist but not for early 20th century scientist, that have found the so called *ultraviolet catastrophe*, the wrong prediction of the classical physics about the blackbody irradiance for small wave length.

Classical physics laws do not work well with the electromagnetic waves. Only after the understanding of Planck and Einstein, they started to describe the electromagnetic waves as waves and at the same time fluxes of photons, so the problem of blackbody radiation was solved.

The Planck's law states

$$B_\lambda(T) = \frac{2\pi hc^2}{\lambda^5(e^{\frac{hc}{\lambda k_B T}} - 1)} \tag{1.2}$$

where $h = 6.626 \cdot 10^{-34}\mathrm{J\,s^{-1}}$ is the Planck's constant, $c \approx 3 \cdot 10^8\mathrm{m/s}$ is the light speed, λ is the wave length, $k_B = 1.28 \cdot 10^{-23}\mathrm{J/K}$ is the Boltzmann's constant and T is surface temperature of the blackbody. Every blackbody emits energy in a spectrum described by the Planck's law (1.2).

The second basic equation is the Stefan-Boltzmann law, that is the total radiant density of a blackbody. This law is the integral of Planck's law over all wavelengths.

$$B(T) = \int_0^\infty B_\lambda \,\mathrm{d}\,\lambda = \int_0^\infty \frac{2\pi hc^2\lambda^{-5}\,\mathrm{d}\,\lambda}{(e^{\frac{hc}{\lambda k_B T}} - 1)} \tag{1.3}$$

introducing $x = hc/k_B\lambda T$ it is possible to obtain

$$B(T) = \frac{2k_B^4 T^4}{h^3 c^2} \int_0^\infty \frac{x^3 \,\mathrm{d}\, x}{e^x - 1} = \frac{2\pi^4 k_B^4}{15c^2 h^3} T^4 \tag{1.4}$$

Considering the emission from an hemisphere over a plane surface, and also the isotropic emission, the flux is

$$F = \pi B(T) = \sigma_{SB} T^4 \tag{1.5}$$

where σ_{SB} is the Stefan-Boltzmann constant

$$\sigma_{SB} = \frac{2\pi^5 k_B^4}{15c^2 h^3} \simeq 5.67 \cdot 10^{-8} \frac{W}{m^2 K^4}. \tag{1.6}$$

The third basic law is the Wien's displacement law, that is the derivative of (1.2); this equation chooses the absolute maximum of the $B_\lambda(T)$ and gets the λ_{max}

$$\frac{\partial B_\lambda(T)}{\partial \lambda} = 0 \tag{1.7}$$

that is

$$\lambda_{max} = \frac{a}{T} \tag{1.8}$$

where $a \simeq 2898 \mu m\, K$.

Solar Radiation: Short Wave

The Figure 1.5 shows the incoming radiation from the Sun. It is possible to see that is very similar to what is predicted by the Planck's law, but only outside of the atmosphere (yellow shading), at the Earth's surface only the red shaded part still arrive. The top of atmosphere (TOA) mean irradiance on a plane surface is the *Solar Constant*, nowadays this constant is

$$S_0 = (1367 \pm 2) \frac{W}{m^2} \tag{1.9}$$

the peculiarity of this constant is that it is *not* constant! The Sun is not always in the same regime, it has low and high energy production phases, correlated to sun's activity, and then to the TOA irradiance, are the solar sunspots. Studies have proved that a period with a a lot of sunspots the irradiance is higher. This because photosphere with many sunspots is disturbed by many outbursts. The burst of radiation and energetic particles from the sun increases the irradiance at

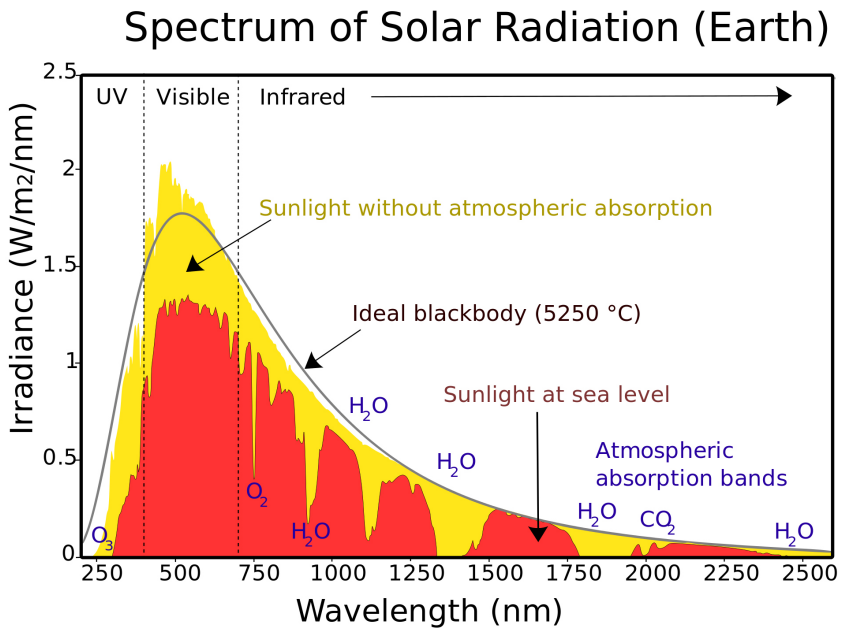

Figure 1.5: The solar irradiance. The grey curve is the Planck blackbody curve for a temperature of 5250 °C. The red parts represent the irradiance at Earth's surface, instead the yellow area represents the irradiance at the top of atmosphere. From WikiCommons http://commons.wikimedia.org/wiki/File:Solar_ spectrum_ ita.svg

the TOA and sometimes electromagnetic storms may produce interferences with the Earth's magnetic field and disturb radio communications.

Sunspots have a cycle of 11 years (if we look at the polarity of the sunspot we have to wait 22 years), and this changes the intensity of solar irradiance at TOA.

The instantaneous solar radiation at the TOA changes also for astronomic factors, indeed the Earth orbits around the Sun, and also rotates on its own axis. The principals astronomic parameters that influences the solar radiation in a specific place on the earth are:

eccentricity , e, of the Earth's orbit around the sun, it changes with a period of 100,000 years (according to Milankovitch theory) between 0.000055, nearly circular, and 0.0679 most elliptical. It changes the differences between perihelion and aphelion, and than the incoming energy. Now it is approximately $0.0166980 \pm 9 \cdot 10^{-7}$.

obliquity , ε, of the ecliptic, or axial tilt, is the inclination between the Earth's rotation axis and the normal at the ecliptic plane. This angle change from 22.1 to 24.5 degrees with a 41,000 years cycle. Now it is approximately $23.4378 \pm 3 \cdot 10^{-4}$ degrees.

axial precession , or equinox precession, is the continuous change in the orientation of the Earth's rotation axis, and the seasons, correlated with the position of the Earth around the Sun change their "place" in the Earth orbit. The precession of equinox has a cycle of about 26,000 years.

declination δ is directly connected with the obliquity and the seasons, in fact it is the angle between the sun's rays and the equatorial plane. At equinoxes $\delta = 0°$, instead at solstices $\delta = 23.4°$ or the same values of obliquity, it changes continuously during the year.

solar distance from Earth is connected with the *eccentricity* of the orbit, the mean distance is $1.4960 \cdot 10^{11} m$.

latitude ϕ of the place where we would like to calculate the solar irradiance,

With some trigonometric formulas it is possible to calculate the instantaneous solar irradiance at the TOA, and by knowing the radiation properties of the atmosphere it is possible to obtain the solar irradiance at the altitude and latitude needed. Referring to the Figure 1.5 the red shaded area is the irradiance on the earth surface, it is possible to understand that the atmosphere has adsorbed a relatively huge part of the TOA total radiation. Effectively in the atmosphere there are many gases absorbing in specific *windows* of the solar spectrum. Principals absorber are water vapor (H_2O_v), carbon dioxide (CO_2), oxygen (O_2) and ozone (O_3).

First of all it is useful to calculate the total insolation at TOA, then, with the use of an approximation of atmosphere transmissivity coefficient the theoretical energy that reaches the ground could be evaluated.

The solar constant S_0 is the mean energy reaching a perpendicular surface to the sun rays at the main distance Earth-Sun. However the earth is approximately spherical, most of planet's surface is inclined at an oblique angle to the solar beam, so this energy by square meter is redistributed on a bigger surface. It is possible to define the *solar zenith angle*, θ_s, to include all these different correction on the solar incidence angle. This is the angle between the normal to the Earth's surface and the sun ray. The flux per unit area at TOA is then

$$Q = S_0 \left(\frac{\bar{d}}{d} \right)^2 \cos \theta_s. \tag{1.10}$$

As above-mentioned *latitude* (ϕ) and *declination angle* (δ) are included in the θ_s, and they are related in this way

$$\cos\theta_s = \sin\phi\sin\delta + \cos\phi\cos\delta\cos h \tag{1.11}$$

if the cosine of solar zenith angle is negative, the Sun is below the horizon, otherwise the Sun is above and the surface is lighted up. The h angle is the *hour angle*, when the solar zenith angle is 90° it is possible to find the h of sunrise and sunset, that is

$$\cos h_0 = -\tan\phi\tan\delta \tag{1.12}$$

The next step is to describe the solar distance, and declination for each day of the year. First has to be introduced the *day angle*, θ_d, that is the representation of the year as a circle, where each day can be related to an angle

$$\theta_d = \frac{(2\pi(d_n - 81))}{365} \tag{1.13}$$

where the 1st of January is the day $d_n = 1$ and the 31st of December is $d_n = 365$[1]. Secondly an approximated formulas is applied to describe the declination and the sun distance using the θ_d angle

$$\left(\frac{\bar{d}}{d}\right)^2 = \left(1 + e\cdot\cos\left(\theta_d - \left(\frac{\varpi\pi}{180}\right)\right)\right)^2 \tag{1.14}$$

where $\varpi = (283.152 \pm 0.018) degrees$ is the longitude of perihelion starting from the vernal equinox[2]. Instead the declination is

$$\delta = \arcsin\left(\sin\varepsilon\cdot\sin\left(\theta_d - \left(\frac{\varpi\pi}{180}\right)\right)\right) \tag{1.15}$$

with these variables and integrating form sunrise to sunset it is possible to find the daily insolation on a level surface at the top of atmosphere

$$\bar{Q}_{TOA}^{day} = \frac{S_0}{\pi}\left(\frac{\bar{d}}{d}\right)^2 [h_0\sin\phi\sin\delta + \cos\phi\cos\delta\sin h_0] \tag{1.16}$$

[1]Leap year are not considered, but if you use a year of 366 days the result does not differ much. The important it is to clarify the subtraction of 81 in the Equation 1.13; this is necessary to start the θ_d on the vernal equinox, in this way all the following formulas are physically well-defined.

[2]This is the average of the ϖ in the years 2014, 2015, 2016. Data from the website of NASA *http://data.giss.nasa.gov/ar5/srorbpar.html*

The Equation 1.16 will be used for evaluate the mean maximum daily insolation above (TOA) for the chosen location (later this will be used for Arbeser station).

Our interest is to find the maximum insolation at a fixed altitude, it can be done applying the following equation to the previous (1.16)

$$t = (0.79 + 2.4 \cdot 10^{-5} \cdot altitude)\left(1 - 0.08\frac{2\theta_s}{\pi}\right) \tag{1.17}$$

this is the *transmissivity* of the atmosphere until the altitude desired (Oerlemans, 2001 [32]). If the atmosphere will not scatter any sun's ray the $t = 1$, indeed the atmosphere is composed by a lot of scattering particles and gases then $t < 1$. The transmissivity maximum is reached when the sun is most perpendicular then with a low θ_s.

Terrestrial Radiation: Long Wave

The terrestrial radiation is in the longwave-part of the spectrum, almost entirely in the Infrared part of the electromagnetic spectrum. Usually pyrgeometer[3] measure in the range 3 µm to 50 µm. The Earth emit long wave radiation following the Stefan-Boltzamann law (Eq 1.5). The peak of emission is at the temperature of $T = 288$K (around 15 °C) and this temperature is given by the natural greenhouse effect. The long wave outgoing is absorbed (about 98% according to Hartmann is absorbed in the Troposphere[4]) by greenhouse gases in the atmosphere (contributing to the heating of the atmosphere itself) and radiates downward (89%) as long wave.

The atmospheric long wave ($LW\downarrow$) is highly variable with the cloudiness; for this reason is widely used for calculating a *Clear-Sky Index* (Marty and Philipona, 2000 [27]). In the analysis phase of this MSc Thesis I used the Clear-Sky Index (CSI) defined by Marty and Philipona for separate clear days from the other. The CSI is define in Section 4.3.4.

1.4.2 Energy Balance at Earth's Surface

The net radiative flux is a result of the radiation balance at the Earth's surface. It is usually dominated by the solar radiation during daytime (directed downward to

[3] In the second part I talk about the Arbeser instrumentation, there is installed a Kipp&Zonen Net Radiometer with a pyrgeometer with a range of measure $(4.2 \div 42)$µm.

[4] Refer to Figure 2.4 page 28 of Hartmann, 1994 [16]

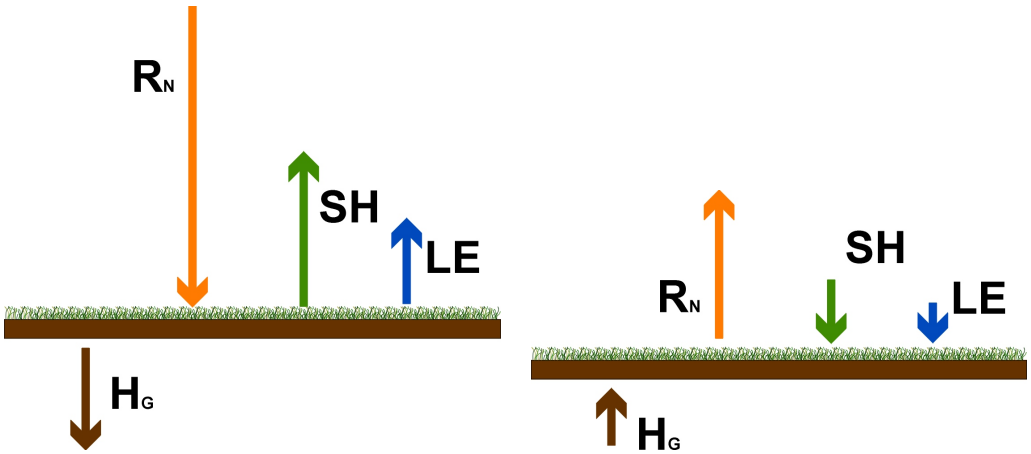

(a) Daytime. (b) Nighttime.

Figure 1.6: Surface energy balance for a typical clear day. The R_N represents the net radiation at the surface, while SH is the sensible latent heat, relative to the heating of the surface, LE is the latent heat of evaporation, due to e.g. plants evapotranspiration and H_G is the ground heat flux. From Arya, 2001 [2], redraw by the author.

the surface), while in the night is weaker and directed upward, outside the surface, then the balance is dominated by outgoing long wave radiation. This is for clear-sky condition; when the sky is cloudy it may be totally different (this is also at the base of CSI's working principle). In Figure 1.6 I schematise (following Arya, 2001 [2]) the Earth surface balance. The most simple energy balance equation is

$$R_N = SH + LE + H_G \tag{1.18}$$

where the inhomogeneities of the surface is not considered, in fact the surface could be complex, with grassland, trees, cornfields that needs a *storage term*. Introducing this term we obtain

$$R_N = SH + LE + H_G + \Delta H_S \tag{1.19}$$

where R_N is the net radiative balance, SH is the turbulent flux of *sensible heat*, LE is the turbulent flux of *latent heat*, H_G is the flux of *soil heat* and ΔH_S is the change in the heat (energy) storage per unit time, per unit horizontal area and over the whole depth of the surface layer. The rate of energy stored in the layer can be expressed as

$$H_S = \int \frac{\partial}{\partial t}(\rho c T) dz \tag{1.20}$$

in (1.20) ρ is the mass density, T is the absolute temperature at level z, and the integration is over the height of the layer. The $\Delta H_S > 0$ when the layer warm up and the incoming energy (e.g. SW and LW incoming radiation is higher than outgoing), indeed when the outgoing energy is higher the layer cools down and $\Delta H_S < 0$.

The net radiative balance can be expressed in terms of long and short wave radiation balance. In particular

$$R_N = SW\uparrow + SW\downarrow + LW\uparrow + LW\downarrow \tag{1.21}$$

here I have schematised using arrows, up arrow means outgoing from the Earth's (or layer) surface, instead down arrow means incoming radiation toward the Earth's surface. The (1.18) (or the more specific (1.19)) and (1.21) give us the same thing: the first one uses turbulent fluxes, the second one uses radiation measurements. Using the short wave radiation it is also possible to define the whiteness of a surface or *albedo* (from the Latin "albus", white), it is the rate of reflected short wave.

$$a = -\frac{SW\uparrow}{SW\downarrow} \tag{1.22}$$

In (1.22) the minus sign is due to the convention where upward radiation is negative because it is leaving the surface, instead the downward radiation is positive because it is entering into the surface. The albedo is a positive number between 0 and 1, where 1 is a perfect reflecting surface, and 0 a perfect absorber surface.

In Table 1.1 are reported the most common natural and anthropic surfaces, in the last column there is the emissivity; this is the long wave emissivity of a surface, that is the ability of a surface to re-emit the incoming radiation. This emission is related to the Stefan-Boltzmann equation (1.5) and the emissivity ε

$$LW\uparrow_{surface} = \varepsilon_{IR}\sigma_{SB}T^4 \tag{1.23}$$

In order to measure radiation it is necessary a net radiometer or a couple of pyrgeometer and pyrradiometer. Since turbulent fluxes are more complicated to measure, fast response instrumentation is needed, specific parametrisations and theories (eg. Eddy Coviariance).

Turbulent Fluxes and Heat Transport

Turbulent fluxes - introduced in the previous subsection using the net energy balance - basically are the *sensible heat flux* and the *lantent heat flux* while the *ground heat flux* is a molecular heat transfer. Heat exchange in the air using

Surface type	Other specifications	Albedo(a)	Emissivity(ε)
Water	Small zenith angle	$0.03 - 0.10$	$0.92 - 0.97$
	Large zenith angle	$0.10 - 1.00$	$0.92 - 0.97$
Snow	Old	$0.40 - 0.70$	$0.82 - 0.89$
	Fresh	$0.45 - 0.95$	$0.90 - 0.99$
Ice	Sea	$0.30 - 0.45$	$0.92 - 0.97$
	Glacier	$0.20 - 0.40$	
Bare sand	Dry	$0.35 - 0.45$	$0.84 - 0.90$
	Wet	$0.20 - 0.30$	$0.91 - 0.95$
Bare soil	Dry clay	$0.20 - 0.40$	0.95
	Moist clay	$0.10 - 0.20$	0.97
	Wet fallow field	$0.05 - 0.07$	
Paved	Concrete	$0.17 - 0.27$	$0.71 - 0.88$
	Block gravel road	$0.05 - 0.10$	$0.88 - 0.95$
Grass	Long (1 m)	0.16	0.90
	Short (0.02 m)	0.26	0.95
Agricultural	Wheat, rice, etc.	$0.18 - 0.25$	$0.90 - 0.99$
	Orchards	$0.15 - 0.20$	$0.90 - 0.95$
Forest	Deciduous	$0.10 - 0.20$	$0.97 - 0.98$
	Coniferous	$0.05 - 0.15$	$0.97 - 0.99$

Table 1.1: Radiative properties of some natural surfaces. From Arya, 2001 [2].

turbulence is much more effective and rapid than molecular heat transfer. This is due to turbulence acting from very small scales (millimeters) to large scales (kilometers). Turbulent elements can be thought of as air parcels with largely uniform thermodynamics characteristics. The transport of energy goes from the larger turbulent elements, that receive energy from the mean motion, to the smallest elements by a cascade of energy. Important studies dealt with the turbulence, first among all is the *K41 Theory* published by Kolmogorov in 1941. This theory states the existence of a low limit status, the *Kolmogorov's microscale*, and the decrease of the turbulence-spectra with the increase of frequency by a factor $k^{-\frac{5}{3}}$, where $k = 2\pi/r$ is the wavenumber corresponding to the scale r.

The calculation of turbulent fluxes caused by turbulent elements can be carried out using the Reynolds decomposition (see equation (1.34) and following explanation) on the conservation equations, it is possible to obtain, from the advection term, additional terms including the covariances, these correspond to the

turbulent fluxes

$$SH = \rho c_p \overline{w'\theta'} \tag{1.24}$$

$$LE = \rho L \overline{w'q'} \tag{1.25}$$

these equation can be simplified or parametrised in particular condition, and the turbulent fluxes can be described using the vertical gradients of potential temperature (θ) and specific humidity (q)

$$SH = -\rho c_p K_H \frac{\partial \theta}{\partial z} \tag{1.26}$$

$$LE = -\rho L K_E \frac{\partial q}{\partial z} \tag{1.27}$$

.

The equations (1.26) and (1.27) derive from the previous two; in micrometeorology it is most common to use a single sonic anemometer and fast response hygrometer instead of more levels. The Equations (1.26) and (1.27) describe a simplification that permit to measure turbulent flux in a simple way, only with meteorological instrumentation (temperature and humidity instruments). The shape of all these fluxes during a typical daily cycle on a cornfield is sketched in Figure 1.7. In this figure G is the ground heat flux, and R_s is previously called R_N. This is not the simplest case, in fact the LE has a little depression at noon, this might be due to the orientation of corn rows.

Energy Balance Closure Problem

It was found that the available energy, given by the sum of net radiation R_N and the ground heat flux H_G, in most cases is larger than the sum of turbulent fluxes of latent and sensible heat. Nowadays the problem is not completely solved, indeed several studies were conducted on this topic but nobody has solved the closure problem yet (Foken 2008 [13]).

In the past some possible explanations were stated. First of all it was discussed about measuring errors, and secondly about the possible different footprint of measurements. In fact the measuring height of the net radiation is usually lower than 2 meters (then the area for outgoing radiation is about one square meter), the ground heat flux is measured in the top 50 cm of soil, instead turbulent fluxes are measure between 2 and 5 meters (for example at Arbeser station is 4.67 m)

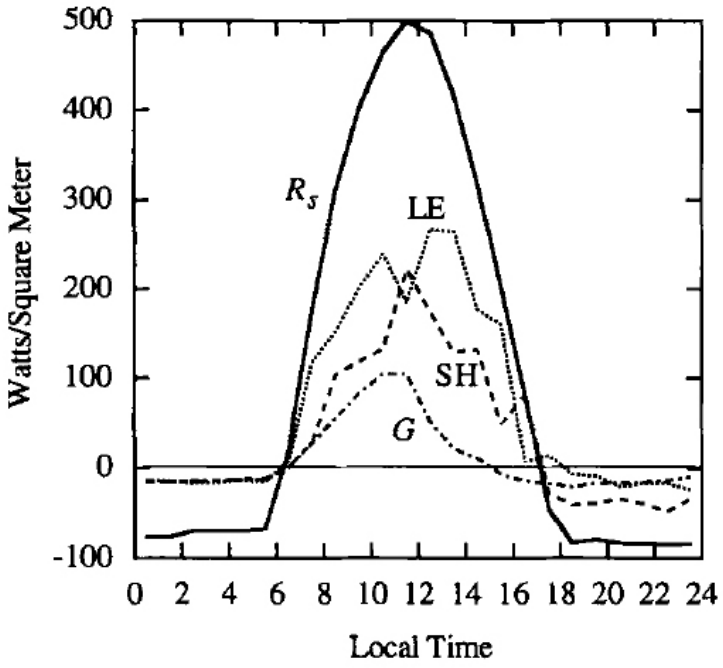

Figure 1.7: Heat budget for a field of mature corn in Madison, Wisconsin, on September 4, 1952. From Hartmann, 1994 [16]

and this means a different footprint, the turbulent parcel arrive from a different place, even far than 100 metres from the mast[5].

It is possible to assess the problem using a *residual term*

$$Res = R_N - H_G - LE - SH \tag{1.28}$$

it was found that the residual term of energy balance closure in daytime is about $50 - 300\text{W/m}^2$.

Measuring errors can derive from an underestimation of fluxes with the eddy covariance method (see Section 1.10) or from an occasional overestimation of the net radiation, but in the last years the data accuracy and quality has increased significantly, so it feasible to exclude this issue from the energy balance closure problem, while the ground heat flux and storage could be measured more accurately. The fundamental issue risen from studies is that for a better closure it

[5]According to footprint models the ratio between the measuring site and the turbulence source can be 1:100, in other words if the sonic anemometer is settled at 2 m above the ground the source could be 200 m far (Foken, 2008 [12])

is necessary to extend the averaging period, which means an inclusion of bigger turbulent structures, that are now excluded with a 30 minutes or 1 hour average. Some attempts to include this larger eddy have been carried by many authors using Large Eddy Simulation (LES) models and in-situ measurements. The result is that it is possible to reach the closure for simplest terrain (deserts, bush land) and to mostly close the balance on more complex surfaces (Foken, 2008 [13]).

1.5 Basic Motion Equations

The first classification of fluid flows is in inviscid and viscid flows. The inviscid ones are ideal, with a null viscosity, instead viscid flow has a viscosity different from zero, that gives a lot of peculiarities to the flow. It is responsible for the frictional resistance between adjacent layers. With higher velocity this shearing stress modifies the flow from laminar to turbulent and thus heat, momentum and mass transfers are possible. The transition from one to another flow regime can be estimated using the dimensionless *Reynolds Number*

$$Re = \frac{L_z U}{\nu} \tag{1.29}$$

that is the ratio between inertial forces and the molecular frictional forces. L_z is a characteristic vertical length scale for the flow considered. Usually in the boundary layer the flow lies into a turbulent regime. There are other important dimensionless quantities, such as the *Rossby Number*

$$Ro = \frac{U}{f L_h} \tag{1.30}$$

that is the ratio between inertial forces and Coriolis' force, the *Gradient Richardson Number*

$$Ri = \frac{\frac{g}{\overline{\theta_v}} \frac{\partial \overline{\theta_v}}{\partial z}}{\left[\left(\frac{\partial \bar{U}}{\partial z} \right)^2 + \left(\frac{\partial \bar{V}}{\partial z} \right)^2 \right]} \tag{1.31}$$

that comes from the *Flux Richardson Number* R_f the ratio of buoyant production/consumption term and mechanical production/loss term of the Turbulent Kinetic Energy (TKE) Equation (1.47). Using the Ri it is possible to separate laminar and turbulent flows and the transition more accurately, with two thresholds: the critic Richardson number and R_T. Usually $R_c = 0.21 \div 0.25$ and $R_T = 1.0$. In order to move from turbulent to laminar flow it must be $Ri > R_T$,

instead to move from laminar to turbulent flow it must be $Ri < R_c$; an hysteresis cycle could immediately be found.

1.5.1 Navier-Stokes Equations

The mathematical treatments of fluid flows - including atmospheric flows - is based on the Navier-Stokes equations for the conservation of momentum. In a Cartesian coordinate system it is possible to write

$$\underset{\mathbf{I}}{\frac{\partial U_i}{\partial t}} + \underset{\mathbf{II}}{U_j \frac{\partial U_i}{\partial x_j}} = \underset{\mathbf{III}}{-\delta_{i3} g} + \underset{\mathbf{IV}}{f_c \varepsilon_{ij3} U_j} - \underset{\mathbf{V}}{\frac{1}{\rho} \frac{\partial p}{\partial x_i}} + \underset{\mathbf{VI}}{\nu \frac{\partial^2 U_i}{\partial x_j^2}} \tag{1.32}$$

where $i = 1, 2, 3$ and $j = 1, 2, 3$ and represent the three coordinates x, y and z, when two different indices are present (e.g. term II) a sum on j running index is done, δ is the Kroneker delta, is 1 only if $i = 3$ (the gravitation force act only along z), ε is the alternating unit tensor (Ricci's tensor), is 1 for cyclic permutation, -1 for displacement of two indexes and 0 for all the other combinations. In Equation (1.32) the meanings of terms is:

I storage of momentum (inertia)

II advection

III gravitational force (act only vertically)

IV Coriolis force (negligible in the boundary layer)

V pressure gradient force

VI viscous stress

Another way to write Navier-Stokes equations is to use the divergence of the gradient instead of Einstein's summation notation:

$$\frac{\partial \vec{U}}{\partial t} + (\vec{U}\nabla)\vec{U} = -2\vec{\Omega} \wedge \vec{U} + \rho \cdot \vec{\nabla} p + \vec{g^*} + \vec{f_r} \tag{1.33}$$

1.5.2 Mean Variables Equations in a Turbulent Flow

The first step to study boundary layers turbulent flow is to write somehow a series of turbulent equations. In order to write them we have to separate measured quantities in a main part (trend) and a perturbation part. The turbulence lies in the fluctuating part, in variances and covariances; this is the base of the *Eddy Covariance Method*, and to split main from fluctuations it is usually used the *Reynolds decomposition* and *Reynolds averaging rules*.

Reynolds Decomposition

Usually in boundary layer studies of turbulence a mean over a time period of 30 minutes or one hour is calculated. This mean could be subtract to the original 30 minutes (or 1 hour) data and obtain the fluctuations, that is the turbulent part. Regarding the U wind velocity it is possible to write:

$$U = \bar{U} + u' \tag{1.34}$$

but also for all the other variables it is the same.

Concerning averages we have to be more accurate, in fact there are many different methods to calculate an average. It is possible to average in *time* coordinates, it is possible to average in *space* coordinates, or on an *ensemble* of experiments. Without going further it is obvious that all these means are different, only if the turbulence can be defined *homogeneous* and *stationary* all these mean means the same thing

$$^{e}\overline{(\quad)} = \ ^{t}\overline{(\quad)} = \ ^{s}\overline{(\quad)} \tag{1.35}$$

The time average represents the most used instrument. I used mostly this way of averaging, because the station is usually in a precise location and thus you can observe the flow going through your position, so you will compute a time average.

It is important to introduce now Reynolds Averaging, that concerns means of splitted variables. For example if we have the variable U of the x wind speed component we can average it in this way:

$$\overline{(U)} = \overline{(\bar{U} + u')} = \overline{(\bar{U})} + \overline{u'} = \bar{U} + \overline{u'} \tag{1.36}$$

but since the only way to fulfil the equality between right and left hand side is to set

$$\overline{u'} = 0 \tag{1.37}$$

this is not a surprisingly result, in fact we know that the sum of all the positive fluctuation from the mean are the same of the sum of all the negative fluctuations from the same mean.

Another possible matter of studies is the product of two variables

$$\begin{aligned}\overline{(U \cdot V)} &= \overline{(\bar{U} + u')\,(\bar{V} + v')} \\ &= \overline{(\bar{U}\,\bar{V} + u'\,\bar{V} + \bar{U}\,v' + u'\,v')} \\ &= \overline{(\bar{U}\,\bar{V})} + \overline{(u'\,\bar{V})} + \overline{(\bar{U}\,v')} + \overline{(u'\,v')} \\ &= \bar{U}\,\bar{V} + 0 + 0 + \overline{u'\,v'}\end{aligned} \tag{1.38}$$

the nonlinear product $\overline{u'\,v'}$ is not necessarily zero, and this is true also for moment of higher order, such as $\overline{u'^2\,v'^2}$.

Conservation of Momentum

In this subsection the equation for the conservation of momentum (see Eq. (1.32)) is written, using Reynold's averaging rules and the Boussinesq approximation[6] on this equation

$$\frac{\partial U_i}{\partial t} + U_j \frac{\partial U_i}{\partial x_j} = -\delta_{i3}\left[g - \frac{\theta'_v}{\bar{\theta}_v} g\right] + f_c \varepsilon_{ij3} U_j - \frac{1}{\bar{\rho}} \frac{\partial P}{\partial x_i} + \nu \frac{\partial^2 U_i}{\partial x_j^2} \tag{1.40}$$

many turbulent terms can be simplified and eventually we get[7]

$$\frac{\partial \bar{U}_i}{\partial t} + \bar{U}_j \frac{\partial \bar{U}_i}{\partial x_j} = -\delta_{i3} g + f_c \varepsilon_{ij3} \bar{U}_j - \frac{1}{\bar{\rho}} \frac{\partial \bar{P}}{\partial x_i} + \nu \frac{\partial^2 \bar{U}_i}{\partial x_j^2} - \frac{\partial(\overline{u'_i u'_j})}{\partial x_j} \tag{1.41}$$

A new term completely due to the turbulent part is appeared, that is to say a *covariance* which force us to consider turbulence even if we would like to forecast a mean quantity.

[6] The Boussinesq Approximation is applied to the vertical component of Navier-Stokes Equations ($i = 3$ in (1.32)). When we multiply the equation by ρ, using Reynold's decomposition on density, vertical speed and pressure, and suddenly dividing by $\bar{\rho}$ we obtain:

$$\left(1 + \frac{\rho'}{\bar{\rho}}\right) \frac{d(\bar{W} + w')}{dt} = -\frac{\rho'}{\bar{\rho}} g - \frac{1}{\bar{\rho}} \frac{\partial p'}{\partial z} + \nu \frac{\partial^2 (\bar{W} + w')}{\partial x_j^2} - \frac{1}{\bar{\rho}} \left[\frac{\partial \bar{P}}{\partial z} + \bar{\rho} g\right]$$

the Boussinesq Approximation suggests that we neglect the density variations $\rho'/\bar{\rho}$ in the inertia (storage) term, but keep it in the buoyancy term. With some calculation - starting from the perfect-gas equation - we can write the fluctuation of density as fluctuation of potential virtual temperature:

$$\frac{\rho'}{\bar{\rho}} = -\frac{\theta'_v}{\bar{\theta}_v} \tag{1.39}$$

[7] The complete derivation is in Chapter 3 of Stull 1988

Conservation of Heat

The equation for conservation of heat is directly tied to turbulent fluxes, in fact writing the equation of heat for mean quantities (as previously done for the momentum equation) a new term will uniquely bound to the turbulent part.

The heat conservation equation is

$$\frac{\partial \bar{\theta}}{\partial t} + \bar{U}_j \frac{\partial \bar{\theta}}{\partial x_j} = \nu_\theta \frac{\partial^2 \bar{\theta}}{\partial x_j^2} - \frac{1}{\bar{\rho} c_p} \frac{\partial \overline{Q_j^*}}{\partial x_j} - \frac{L_v E}{\bar{\rho} c_p} - \frac{\partial (\overline{u_j' \theta'})}{\partial x_j} \tag{1.42}$$

In the previous equation the first and second term have the same meanings of (1.41): mean storage of heat and advection of heat due to mean wind. The first right hand side term is the mean conduction of heat where ν_θ is the thermal diffusivity. The next term is the loss of heat by net sensible heat flux (Q_j^*) divergence in the j^{th} direction; the following term is the source of heat due to latent heat (L_v is the latent heat and E is the mass of water vapour involved). The last term is a divergence of a *covariance* that represent heat turbulent transport.

1.5.3 Turbulent Fluxes Equations

In the same way, as done for mean values, it is possible to write prognostic equations for variances, such as $\overline{u_i'^2}$, $\overline{\theta'^2}$, $\overline{q'^2}$, and covariances in other word turbulent fluxes, such as $\overline{u_i' \theta'}$, $\overline{u_j' q'}$. These equations, especially those about heat flux, are useful to understand the behaviour of the boundary layer. Beforehand I have introduced latent heat flux and sensible heat flux (Equations (1.25) and (1.24)), the following equation allow us to calculate these fluxes. The derivation of these equations passes through the calculus of prognostic equation for turbulent departures; then it is necessary to multiply by the second term of covariance this equation and then sum it to the other prognostic (of the second variable) multiplied by the first one.

Momentum Flux

The equation for momentum flux after some scaling arguments is

$$\begin{aligned}
&\frac{\partial\left(\overline{u_i' u_k'}\right)}{\partial t} + \bar{U}_j \frac{\partial\left(\overline{u_i' u_k'}\right)}{\partial x_j} = -\left(\overline{u_i' u_j'}\right)\frac{\partial \bar{U}_k}{\partial x_j} - \left(\overline{u_k' u_j'}\right)\frac{\partial \bar{U}_i}{\partial x_j} - \frac{\partial\left(\overline{u_i' u_j' u_k'}\right)}{\partial x_j} + \\
&\quad \mathbf{I} \qquad\quad \mathbf{II} \qquad\quad \mathbf{III} \qquad\quad \mathbf{III} \qquad\quad \mathbf{IV} \\
&+ \left(\frac{g}{\bar{\theta}_v}\right)\left[\delta_{k3}\overline{u_i'\theta_v'} + \delta_{i3}\overline{u_k'\theta_v'}\right] + \overline{\frac{p'}{\bar{\rho}}\left(\frac{\partial u_i'}{\partial x_k} + \frac{\partial u_k'}{\partial x_i}\right)} - 2\varepsilon_{u_i u_k} \\
&\quad \mathbf{V} \qquad\quad \mathbf{V} \qquad\quad \mathbf{VIII} \qquad\quad \mathbf{X}
\end{aligned} \tag{1.43}$$

in this equation I have used the same numeration and notation of Stull 1988. The most important thing is the appearance of term IV a triple correlation (or third moment). The new term involves a most complicated turbulence variable and to solve this equation we need it. This is the *turbulence closure problem*, it will be discussed in the section 1.6.

Heat Flux and Moisture Flux

Identically as momentum flux, the equation for heat flux is

$$\begin{aligned}
&\frac{\partial\left(\overline{\theta' u_i'}\right)}{\partial t} + \bar{U}_j \frac{\partial\left(\overline{\theta' u_i'}\right)}{\partial x_j} = -\left(\overline{\theta' u_j'}\right)\frac{\partial \bar{U}_i}{\partial x_j} - \left(\overline{u_i' u_j'}\right)\frac{\partial \bar{\theta}}{\partial x_j} - \frac{\partial\left(\overline{\theta' u_j' u_i'}\right)}{\partial x_j} + \\
&\quad \mathbf{I} \qquad\quad \mathbf{II} \qquad\quad \mathbf{III} \qquad\quad \mathbf{XI} \qquad\quad \mathbf{IV} \\
&+ \delta_{i3}\left(\frac{\overline{\theta'\theta_v'}}{\bar{\theta}_v}\right)g - \left(\frac{1}{\bar{\rho}}\right)\left[\overline{\frac{p'\partial\theta'}{\partial x_i}}\right] - 2\varepsilon_{u_i q} \\
&\quad \mathbf{V} \qquad\quad \mathbf{VIII} \qquad\quad \mathbf{X}
\end{aligned} \tag{1.44}$$

With this is possible to know the sensible heat flux SH, instead for the latent heat flux, LE, the moisture flux is needed.

$$\begin{aligned}
&\frac{\partial\left(\overline{q' u_i'}\right)}{\partial t} + \bar{U}_j \frac{\partial\left(\overline{q' u_i'}\right)}{\partial x_j} = -\left(\overline{q' u_j'}\right)\frac{\partial \bar{U}_i}{\partial x_j} - \left(\overline{u_i' u_j'}\right)\frac{\partial \bar{q}}{\partial x_j} - \frac{\partial\left(\overline{q' u_j' u_i'}\right)}{\partial x_j} + \\
&\quad \mathbf{I} \qquad\quad \mathbf{II} \qquad\quad \mathbf{III} \qquad\quad \mathbf{XI} \qquad\quad \mathbf{IV} \\
&+ \delta_{i3}\left(\frac{\overline{q'\theta_v'}}{\bar{\theta}_v}\right)g + \left(\frac{1}{\bar{\rho}}\right)\left[\overline{\frac{p'\partial q'}{\partial x_i}}\right] - 2\varepsilon_{u_i q} \\
&\quad \mathbf{V} \qquad\quad \mathbf{VIII} \qquad\quad \mathbf{X}
\end{aligned} \tag{1.45}$$

1.5.4 Turbulence Kinetic Energy

The Turbulence Kinetic Energy (TKE) is a very important variable in the atmospheric boundary layer. It is a measure of the turbulence intensity. It is directly related to momentum, heat and moisture transport through the boundary layer. The TKE equation, that will be soon analysed, is composed by all the terms that describe physical processes which generates the turbulence.

The definition of TKE per unit of mass is

$$\bar{e} = \frac{1}{2}\left(\overline{u'^2} + \overline{v'^2} + \overline{w'^2}\right) \tag{1.46}$$

we can obtain the budget TKE equation starting from the prognostic equations for velocities variances[8] dividing by two and summing on the three components

$$\underbrace{\frac{\partial \bar{e}}{\partial t}}_{\mathbf{I}} + \underbrace{\overline{U_j}\frac{\partial \bar{e}}{\partial x_j}}_{\mathbf{II}} = \underbrace{+\delta_{i3}\frac{g\left(\overline{u_i'\theta_v'}\right)}{\overline{\theta_v}}}_{\mathbf{III}} \underbrace{-\overline{u_i'u_j'}\frac{\partial \overline{U_i}}{\partial x_j}}_{\mathbf{IV}} \underbrace{-\frac{\partial\left(\overline{u_j'e}\right)}{\partial x_j}}_{\mathbf{V}} \underbrace{-\frac{1}{\bar{\rho}}\frac{\partial\left(\overline{u_i'p'}\right)}{\partial x_i}}_{\mathbf{VI}} \underbrace{-\varepsilon}_{\mathbf{VII}} \tag{1.48}$$

Similarly to all the previous equations the terms are:

Term I represents the local storage of TKE. This term grows during the daytime when there is a huge storage of TKE in the air. It starts growing during the morning and reaches the maximum around late afternoon (during a clear day), a spin down that dissipates the turbulence occur during the night. This is in course of action with the section that describes the diurnal evolution of the boundary layer (see Section 1.2).

Term II the advection of TKE by the mean wind. This term is relevant only on small scales; averaging on a greater area, up to 10 km^2, this term is negligible (Stull 1988 [45]).

Term III is buoyant production or consumption term. This term is only present in the vertical equation (due to the Kronecker delta), where the flux of virtual potential temperature $\overline{w'\theta_v'}$ is. This flux is directly connected with the sensible heat flux (it is only necessary to multiply that by ρc_p, see

[8] The prognostic equation for variances is

$$\frac{\partial \overline{u_i'^2}}{\partial t} + \overline{U_j}\frac{\partial \overline{u_i'^2}}{\partial x_j} = +2\delta_{i3}\frac{g\left(\overline{u_i'\theta_v'}\right)}{\overline{\theta_v}} - 2\overline{u_i'u_j'}\frac{\partial \overline{U_i}}{\partial x_j} - \frac{\partial\left(\overline{u_j'u_i'^2}\right)}{\partial x_j} - \frac{2}{\bar{\rho}}\frac{\partial\left(\overline{u_i'p'}\right)}{\partial x_i} - 2\varepsilon \tag{1.47}$$

the meaning of each term is similar to prognostic equation for covariances.

(1.26)), thus this flux is usually positive near the surface during the daytime, then term III is large and positive and represents the effect of *thermals* in the mixing layer. Nevertheless during nighttime or with *stable profile* the buoyant term is negative, indicating a loss or a consumption of TKE.

Term IV is the mechanical or shear production/loss term, due to the wind shear. In presence of wind shear (mainly variation of wind intensity with the altitude $\partial \bar{u}_i / \partial z$) combined with turbulent momentum flux $\overline{u_i' u_j'}$, the interaction tends to generate more turbulence. This term is larger, obviously, during windy days, and during nighttime when the boundary layer becomes stratified with cold air in contact with the ground. It can be the only term that produces turbulence. Joining the term III with the term IV it is possible to classify the nature of convection into *free convection* and *foced convection*; the free convection is verified when term III is greater than IV, then buoyancy is dominant, by contrast when term IV is greater than III we have forced convection, and the mechanical production of TKE is more relevant.

Term V the turbulent transport of TKE by u_j'. This term only moves the turbulence without creating or destroying it.

Term VI redistribution of TKE by pressure perturbations.

Term VII represents the viscous dissipation of TKE, its transformation into heat.

1.6 Turbulence Closure Problems

In the previous section some of the most important equations for the boundary layer have been treated. Proceeding from equation for mean values to covariances at every passage, a new higher order term compares, and to evaluate it a new prognostic equation is needed, but this new equation will contain another even higher term that is a new unknown. Thus, for any finite set of those equations, the description of turbulence is not closed. This is the *turbulence closure problem*.

It is possible to reach a closure solution making some assumptions and approximations on the last order moment involved in the equation. For example if we consider the heat flux equation (1.44) we need to approximate the fourth term.

There are two different methods to resolve the closure problem: the *local* and *nonlocal* closure method. As regards the local closure method the unknown is

Order	Local	Nonlocal	Other (Bulk or Similarity)
Zero			×
Half	×	×	×
First	×	×	
One-and-a-half	×		
Second	×		
Third	×		

Table 1.2: Classification of closure techniques.

parameterised by values of known quantities in the *same* point, while for nonlocal closure the parameterisation is done using *many points* in space.

The closure order is determined by the high order moment equation evaluated, the next higher moment is approximated, for example a second-order closure keep covariances equations and parameterised triple correlations. The *half-order* closures use only a restricted set or a combination of equation, for example the *one-and-a-half order closure* use equations for TKE, temperature and moisture variances along with first order moment equations.

There are different closure orders listed in Table 1.2.

1.7 Similarity Theory

In Table 1.2 there is another way to resolve the turbulence closure problem (column "Other"), and it uses totally different assumptions. In fact the *similarity* approach is not focused on parameterisation of high order moment, but to find out whether there are means to predict the "characteristics of the result" (Rotach, 2015 [35]). The aim of similarity theory is to find similarities between variables measured in different places and time using particular scaling operations. For that purpose variables are organised into *dimensionless groups*. This dimensional analysis is done using a procedure named *Buckingham* π *Theorem* that aids us to form the appropriate groups of variables.

The approach can be summarised in four steps:

1. The first step is to choose which *key* variables are necessary to describe as best as possible the process that we want to investigate. We do not know a priori if our choice is the best; only after step 4 we will know that.

2. Secondly we have to find the maximum number of independent dimension-

less groups using the Buckingham's π-Theorem; any other mean variables can be expressed as a linear combination of those π-groups with the function f_a, where a is the variable that we would like to scale.

3. Perform an experiment in order to determine the values of dimensionless groups.

4. Fit an empirical curve or regress an equation on the experimental data in order to obtain the f_a function.

Therefore it is necessary to briefly introduce the π-Theorem. The procedure described by the π-Theorem is a physical dimension analysis, where our problem has n variables, then we write them using the **fundamental dimensions**:

L = length;

M = mass;

T = time;

K = temperature;

A = electric current;

I = luminous intensity.

we will find a smaller number of fundamental dimensions r. With these two numbers we can state the number of possible $\pi - groups$ to $N = n - r$.

The next step is to choose from our n variables at *least* r *key-variables* in which all the fundamental dimensions are represented *and* and where it is not possible to create dimensionless groups from any combination of those. Now it is possible to form dimensionless equations of the remaining variables in term of key variables. For example if our *key-variables*, related to the problem that we wish to solve, are ρ, density, D, the diameter of a pipe, and U, the fluid velocity inside the pipe, the other variables (shear stress τ, pipe roughness length z_0 and dynamic viscosity μ) can be written as

$$\begin{aligned} \tau &= (\rho)^a (D)^b (U)^c \\ z_0 &= (\rho)^d (D)^e (U)^f \\ \mu &= (\rho)^g (D)^h (U)^i \end{aligned} \tag{1.49}$$

Class	Variable	Description
Length	z	height above the surface
	h or z_i	depth of the boundary layer
	L	$= -[\overline{u'w'}_s^2 + \overline{v'w'}_s^2]^{3/4}/[\kappa \cdot (g/\bar{\theta}_v) \cdot (\overline{w'\theta'_v})]$ Obukhov length
	h_e	$= u_*/f_c$ Ekman layer depth
	z_0	aerodynamic roughness length
Velocity	u_*	$= [\overline{u'w'}_s^2 + \overline{v'w'}_s^2]^{1/4}$ friction velocity
	$(TKE)^{1/2}$	square root of turbulent kinetic energy
Temperature	θ_*^{ML}	$= \overline{w'\theta'_{vs}}/w_*$ convective ML temperature scale

Table 1.3: Summary of some boundary layer scales.

and we solve them using physical dimensions and we find the exponents. Then we build the dimensionless groups dividing the left-hand side of (1.49) by the right-hand side.

The choice of key-variables is fundamental, the best is to pick them from variables that represent forcings on the boundary layer for example surface fluxes.

Several key-variables frequently appear in common classes of similarity problems, and hence are known as *scaling variables*.

Scaling variables can be mainly grouped in: length, velocity, temperature, time and moisture scale variables. In Table 1.3 I have listed some of the mostly used in boundary layer meteorology.

It is possible to distinguish in different similarity classes; each one is relative to a particular case of interest. The most used in the surface layer is the *Monin-Obukhov Similarity (MOST)*, this class is usually applied to the surface boundary layer. In the surface layer fluxes vary by less than 10% of their value, then it is possible to define the surface layer as a constant flux layer, and use fluxes as key-variables for the lower part of the atmosphere.

Other similarity classes are:

1. the *Mixed Layer Similarity*, used in mixed layer that are in a state of free convection;

2. the *Local Similarity* used for statically stable boundary layers, this class recognises that turbulence in the upper part of SBL may not be in equilibrium with the surface fluxes, than instead of using surface fluxes as done by MOST, this class uses *local* fluxes, shears and stability;

3. the *Local Free Convection Similarity*, used in statically unstable surfaces layers, where buoyancy is the driving. This approach is useful when mean winds are calm, and consequently the MOST does not work;

4. the *Rossby-number Similarity* useful in large-scale modeling.

1.7.1 Monin-Obukhov Similarity Theory

In the approach of Monin and Obukhov (1954 [29]) they define some characteristic variables before applying the π-Theorem. In particular they choose the *friction velocity*[9] as representative of friction

$$u_* = \sqrt[4]{\overline{u'w'}^2 + \overline{v'w'}^2} \tag{1.52}$$

then they define a characteristic temperature scale that takes into account the heat flux

$$\Theta_* = -\frac{\overline{w'\theta'}}{u_*} \tag{1.53}$$

and as length scale they introduce

$$L = -\frac{1}{\kappa}\frac{u_*^3}{\overline{w'\theta'_0}\left(\frac{g}{\theta_0}\right)} \tag{1.54}$$

that is also called *Obukhov length*. The $\kappa \approx 0.4$ and it is the von Kàrmàn constant, and where g/θ_0 is the buoyancy parameter. This length has a pole in 0, when neutral condition is approached, then sensible heat flux tends towards zero. In order to resolve this singularity Obukhov constructed the dimensionless group z/L.

The dimensionless group that they form, as previously mentioned, is z/L. In convective condition (unstable profile) it is $z/L < 0$ because the sensible heat flux is positive, otherwise for stable condition the opposite is verified $z/L > 0$.

[9] The friction velocity comes from the Reynolds stress tensor τ, in particular it is the magnitude of the stress tensor, concerning only the vertical flux of momentum. The friction velocity can be expressed as following

$$|\tau_{Reynolds}| = [\tau_{xz}^2 + \tau_{yz}^2]^{1/2} \tag{1.50}$$

where $\tau_{xz} = -\bar{\rho}\overline{u'w'}$ and $\tau_{xz} = -\bar{\rho}\overline{v'w'}$, from those it is possible to write the friction velocity of eq. (1.52) as:

$$u_*^2 = |\tau_{Reynolds}|/\bar{\rho} \tag{1.51}$$

According to Monin and Obukhov in the surface layer, and according to the Backingham's Theory too, it is possible to express every dimensionless variable as a function of z/L.

1.8 Mountain Meteorology

Moving from the ideally flat and homogeneous terrain to a more complex terrain, such as a mountainous terrain, the approach has to be changed, both in boundary layer and mesoscale meteorology. Now the most interesting mountain meteorology mesoscale phenomena for our purpose are presented.

The mountain terrain is composed by valley of different deepness and orientation, thus the interaction with the large-scale winds completely modifies the flow especially in the lower part of valleys, where the wind can be channeled into the valley.

Winds associated to mountainous terrain can be grouped into two big categories:

1. *Terrain-forced flows*, generated by the interaction of synoptic (or meso-α) scale motions, and

2. *Diurnal mountain winds*, generated by temperature contrast between the valley bottom and slopes; henceforward I will refer to this category as *thermally driven circulations*.

Let's briefly analyse this two groups.

1.8.1 Dynamic Interaction at Meso-α Scale

In this case we have to start from the synoptic or mesoscale meteorology, the meteorology that deals with large scale phenomena, such as frontal system and all the phenomenology directly connected with them. Then in this case we have to explore what happens when a front (cold or warm) or simply an air mass reaches a mountain barrier and starts to interact with a complex terrain. We focused our attention on large scale first, starting from this planetary scale.

The large-scale effects of mountain barrier on an airflow can be explained as a consequence of the relationship between divergence and vorticity, then using the equation of conservation of *potential vorticity*

$$\frac{D_h}{Dt}\left[\frac{\zeta + f}{h}\right] = 0 \tag{1.55}$$

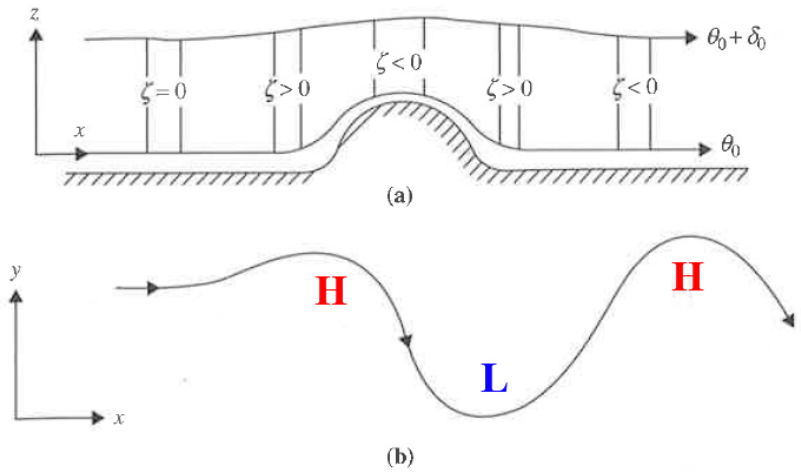

Figure 1.8: Schematic view of westerly flow over a mountain: (a) the depth of a fluid column as a function of x and (b) the trajectory of a parcel in the (x,y) plane. From Holton, 2013 [18] modified.

in the (1.55) a simplification of the equation of potential vorticity with the shallow water equation is presented (see Ch. 4 Holton an Hakim, 2013 [18]), where ζ is the relative vorticity, f is the Coriolis parameter and h is the height of the column in pressure coordinates. In this case the assumption made is an incompressible atmosphere and consequently the flow can be considered isentropic.

In this situation, for the equation (1.55) stated before, if a westerly flow is forced to flow over a mountain ridge a $\zeta > 0$ in the windward side is obtained, then a relative high pressure, on the top of the mountain chain a $\zeta < 0$ will occur that is a low pressure on the leeward and at the end, on the leeward side again a $\zeta > 0$. In Figure 1.8 there is a simple scheme of this situation.

In this case the flow will be reinforced to pass the mountain barrier because the pressure gradient force (PGF) will grow.

Moving to the synoptic scale we have three major effects on air flow:

1. flow blocking;
2. frontal modifications;
3. enhancing of cyclogenesis on the lee side.

The *flow blocking* strongly depends on speed and stability of the air. If the velocity is low the mountain barrier will surely block the motion, and also if the

air is very stable it will not lift, but it will flow around the barrier.

When the mountain chains block an air flow there are other effects; first, it is possible to find pressure gradients (of the order of 10hPa at the surface) between lee and windward side slopes. Other times the air flow is not blocked and a different pressure field is visible, so we have (very typical on the Alps, but also in other countries and mountains) the Föhn nose, and relative wind.

Frontal modifications occur when a front line (cold or warm front) reaches a mountain chain and hit it not perpendicularly. The effect is totally similarly to sea waves near the beach, that change direction of propagation caused by the different depth. In other cases the *masking* is possible, that is the hiding of a front due to pre-existent air masses (cold pool), or the effect of lee winds such as Föhn.

In closing the *lee cyclogenesis enhancing* it is possible especially when the barrier modifies the flow through another path. A familiar case is represented by the Alps arch. With cold north-westerly winds the Alps are like a wall, a part of such flow will raise and pass the Alps (and maybe generating north Föhn), another part will deviate south and create then a cyclone in Liguria bay (see Figure 1.10).

Going further in smaller scale we can find local modification of airflow: *wave phenomena*. I have previously mentioned them, and people from Piedmont and from Innsbruck are very used to these phenomena. When stably stratified air flows over a mountain range, *gravity waves* or *mountain waves* can be generated either over the mountain and in the lee side. In other words the mountain moves the air from its equilibrium position and after that the air parcel tries to return to this equilibrium position oscillating around it. The behaviour of airflow over an obstacle depends principally on:

1. the vertical wind profile;
2. the stability structure;
3. the shape of the obstacle;

and analysing these factors Förchgott (1949) distinguished three basic types of flows: (1) *laminar streaming*, with weak winds and a constant vertical profile, (2) *standing eddy*, with a stronger wind and a almost logarithmic profile, and (3) with stronger winds and vertical gradients the *lee waves*, followed by lenticular clouds (Figure 1.9) and on the ridge crest cloud.

Directly connected phenomena with lee waves is Föhn wind. It is usually a warm, dry downslope wind. The warming and drying are caused by adiabatic

Figure 1.9: Altocumulus lenticularis, above Serre Chevalier France.

compression as air descends the slopes on the leeward side of a mountain range. Innsbruck is the capital city of Föhn, both for the long series of study done and for the yearly occurrence of this wind. The particular position of Innsbruck in the middle of the Alps allows two different directions of Föhn: the north and the south. In the other side Turin is only affected from the north Föhn.

In North America the downslope warm wind equal to Föhn is called Chinook. Another downslope wind is Bora but in this case this is a cold wind. It usually brings very cold air to the Adriatic Sea, and it generates in central Asia with very low temperature, so low that after the adiabatic heating is still cold (Whiteman, 2000 [52]).

1.8.2 Thermally Induced Wind

In this section a smaller scale is explored, that regards valley and plain system as the biggest scale. These wind systems are more interesting for the purpose of this Thesis because with this work (and in the frame of i-Box Project) I investigate the boundary layer (or more precisely the surface layer) in truly complex terrain like an alpine valley and a top mountain station.

I start to classify possible wind configurations in a valley following Whiteman (2000) scheme:

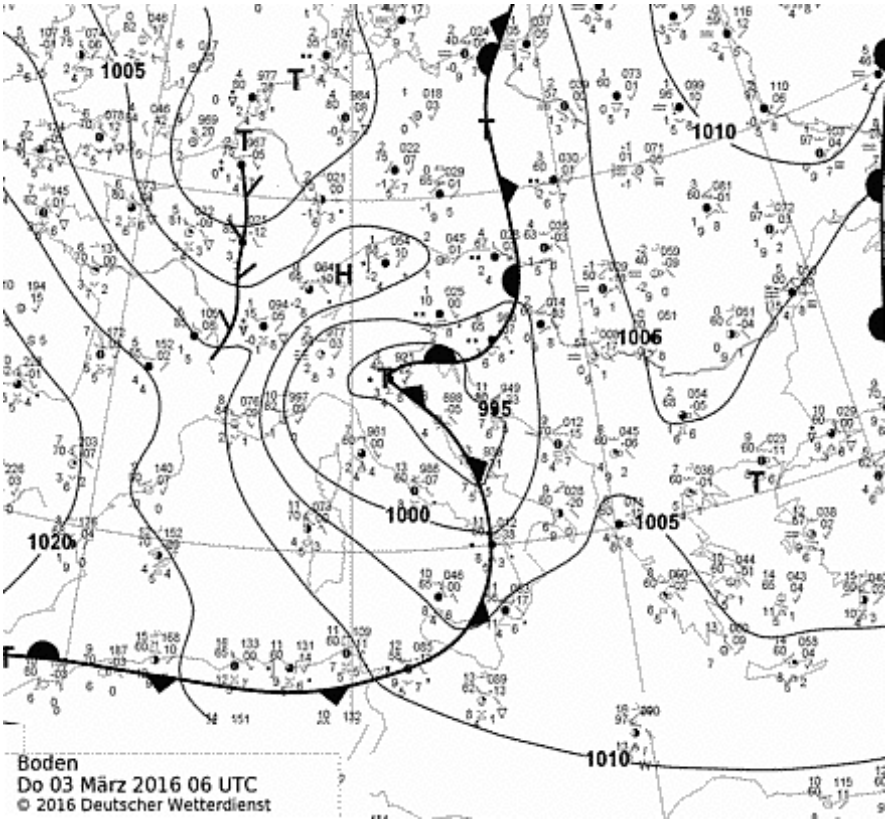

Figure 1.10: Surface pressure chart analysis of 2016.03.02 at 06:00 UTC. In this surface map it is possible to see the formation of a leeward cyclone and the Föhn nose rounding the western Alps.

- The **slope wind system** (*upslope* and *downslope winds*) is driven by horizontal temperature gradients between the valley center and the slopes.
- The **along-valley wind system** (*up-valley* and *down-valley winds*) is driven by horizontal temperature gradients along the valley axis.
- The **cross-valley wind system** driven by temperature gradients between the two side of the valley, this system generates a cross wind, perpendicular to the valley axis.
- The **mountain-plain wind system** results from temperature gradients between mountainous terrain and the nearby plain. This produces a mountain-plain circulation where the upper level return flow is not confined by the topography. It is the biggest system of the above-mentioned.

Figure 1.11: The effects of mountain barriers are visible in a lot of different clouds; here it is a waterfall cloud shot over Les Arnauds a hamlet of Bardonecchia.

Complex terrain wind systems are usually a mixture of the above-listed systems, and all of them - if dynamical wind system forcing is excluded for the moment - are temperature driven. Thus for those it is crucial the day evolution of the boundary layer. Previously we have seen how the stability and stratification of the boundary layer change during the day and the nighttime (see Figure 1.3 and Section 1.2). The pure thermally developed winds are complicated by the influence, as I mentioned, of other wind systems that develop on different scales, on regional pressure gradients, on mechanical effects due to topography or on overlying wind systems.

Several studies have been done, some of which took place in the Inn Valley and are very useful for understanding the surrounding condition of Arbeser station. Before going further (see Chapter 3) it is necessary to introduce the basis theory of valley and slope winds.

Slope winds blow parallel to the inclination of the sidewalls, they can have an up or down slope direction depending on the buoyancy conditions. Up-slope winds are also called *anabatic winds*, while down-slope winds are also called *katabatic winds*. Thus those winds are driven by buoyancy forces due to temperature difference between the air near to the slope and the air in the valley at the same

level. It is also possible to write the momentum equation in a slope-normal coordinate system

$$\frac{\partial u}{\partial t} + u\frac{\partial u}{\partial s} + w\frac{\partial u}{\partial n} = -\frac{1}{\rho}\frac{\partial p'}{\partial s} + B\sin\alpha - \frac{\partial \overline{u'w'}}{\partial n} \tag{1.56}$$

$$\frac{\partial w}{\partial t} + u\frac{\partial w}{\partial s} + w\frac{\partial w}{\partial n} = -\frac{1}{\rho}\frac{\partial p'}{\partial s} + B\sin\alpha \approx 0 \tag{1.57}$$

In the Equations (1.56) and (1.57), n is the slope normal coordinate, s is the up-slope coordinate (following the increasing gradient), u is the wind velocity in the plane parallel to the mountain slope, w the wind velocity normal to the slope and α is the slope angle. It is possible to think the last one approximately equals to zero, there are no slope normal motion. The driving force is the buoyancy B due to the heating or cooling of the slope. Slope winds react instantaneously to insolation; they start when the slope is hit by sunlight. They can be intermittent in space and time and they are a succession of thermal bubbles from favourable, rocky, dry spots on the slope (Vergeiner and Dreiseitl, 1987 [49]).

Valley winds blow horizontally on the valley floor and parallel to the valley axis. They are produced by pressure gradients between different places into the valley, or between the valley and the adjacent plain. These pressure gradients are the result of a greater diurnal temperature range in a vertical column within the valley, than in a similar column with its base at the same elevation outside the valley (Whiteman, 1990) see Figure 1.12.

The differences in the diurnal temperature cycle can be explained using the first law of thermodynamics, which is, in case of $\mathrm{d}\,p/\,\mathrm{d}\,t = 0$,

$$Q = \rho c_p V \frac{\mathrm{d}\,T}{\mathrm{d}\,t} \tag{1.58}$$

where Q is the heating rate in Joule per Kelvin. Then the same solar radiation heats more the internal valley air, because there is the same exposure surface to sun rays but less air. The amplification of temperature cycle is also quantified by a *topografic amplification factor* (Steinacker, 1984 [42]), that compare valley and plain areas.

Valley winds start later than slope winds; the onset time is between 9:00 and 12:00 UTC, earlier in spring and summer and later in autumn; whereas the end time in usually within 16:00 and 19:00 UTC. Valley winds are slower to onset and for this reason they mainly exist with fair-weather condition, thus the outflow dominates winter season, whereas the up-valley phase last longer during summer.

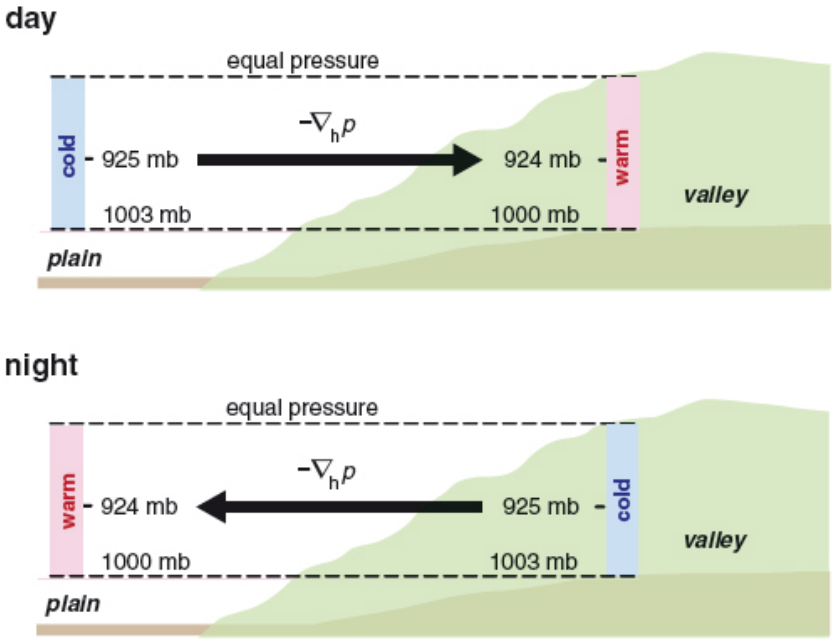

Figure 1.12: Illustration of the thermal forcing of valley-plain pressure gradients leading to the development of an along-valley wind system. From Markowski and Richardson 2010 [25], adapted from Whiteman 1990 [53].

Valley winds intensities are usually around 4 m/s for up-valley in mid-afternoon, and 7 m/s for down-valley during nighttime.

Valley and slope winds are connected in a big valley circulation that evolves during the day following the previously cited boundary layer day-night cycle. Essentially there are six stages. Starting from the early morning, when the first sun rays start to warm the south facing slope (or western if the valley is north-south oriented), and they interrupt the down-slope winds reversing the surface energy budget. The heat is transferred from the ground to the air above the slope and start the anabatic wind. This anabatic flow brings cold air from the valley floor and slowly removes the nighttime stable boundary layer. The down valley wind is wiped out and it remains only in a stable core at mid altitude over the valley floor; it is surrounded by up-valley wind that starts to blow at the end of the morning.

At noon and in the afternoon the up-valley and up-slope winds are completely developed. In the evening, when the sun is laying down to the horizon and one

side of the valley begins to be darkened by higher peaks, the energy balance starts to reverse again. On the shadowy side of the valley down-slope winds start, and gradually the katabatic winds win on the up-valley wind. A stable layer starts to grow from the slope ground and during the night a thermal inversion divides the valley (with down-valley winds) from the upper part of the boundary layer: the residual layer. For a better comprehension of the valley-slope winds daily cycle it is useful to see Figure 1.13 that well describes the evolution of the boundary layer over complex terrain, and Figure 1.14 that describes the transition between up to down valley winds.

1.9 Flat compared to Complex Terrain

In all the previous sections, excluding the last one about Mountain Meteorology (Sec. 1.8), I have talked about boundary layer on homogeneous and flat terrain. Unfortunately the homogeneous and flat terrain is too much a restrictive hypothesis, in fact only over an uninhabited plain region or a desert it is possible to fulfil the requirement of this description. Even worse it is on mountainous terrain, where the description given by this theory is mostly incomplete, thus the aim is to explore to what degree one of those aspects can be adopted or possibly modified to fit in complex terrain.

From the previous section it is possible to see that there are complex behaviours of winds and circulation in a mountainous terrain, and more if we move to micrometeorology, turbulence and to study heat fluxes, we will understand that a simplistic description completely fails.

Several studies have been done on this point, both to understand the boundary layer physics, the similarity relationship and the numerical modelling. Numerical Weather Prediction (NWP) models are nowadays very important for weather forecast and public safety, especially when extreme events affect a complex and crowded area. The main problem in NWP is the resolution scale, that cannot be too small for computational problems, but also it cannot be too wide because a valley, or a complex terrain, changes rapidly the border conditions.

First works on boundary layer and turbulence have been cited before, such as Monin-Obukhov similarity theory (1954) [29], Kolmogorov (1941), Kaimal *et al.* (1972). In all of these studies the authors focused on flow over flat and homogeneous terrain, and the main experiments were conducted over large plains of Kansas (USA) or Wangara (Australia).

We can see that assumptions were done to simplify the complexity of boundary layer studies, but they cannot be translated completely to a inhomogeneous

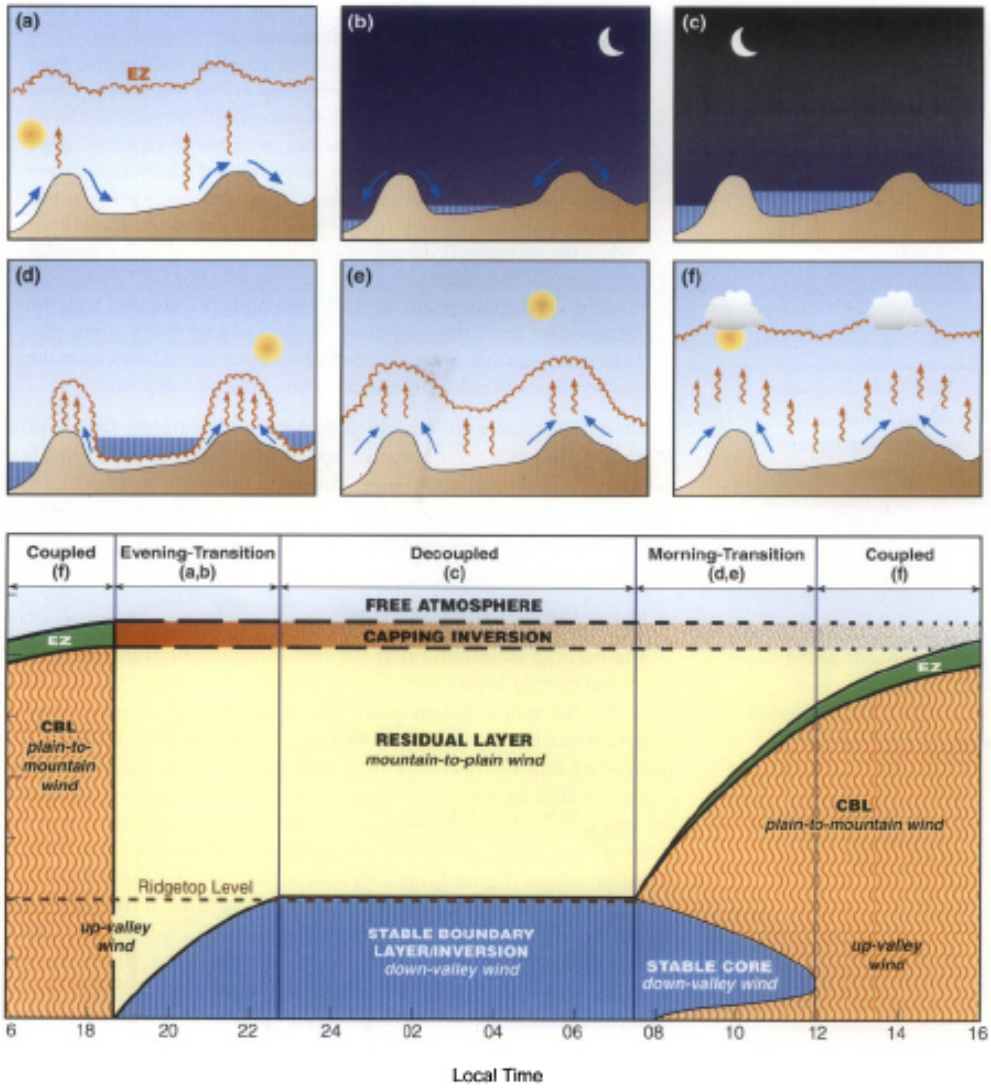

Figure 1.13: In this figure we start from the late afternoon-evening, when the transition from well formed up-valley wind is weakened by the progressive onset of down-slope winds in the dark side of the valley. Then there is in (c) the growing of the nighttime temperature inversion and the night stable boundary layer. We pass through the sunrise in (d), when the first up-slope winds start, and the erosion of the stable boundary layer starts too. In picture (e) we have a growing ML and in (f) we have a well formed convective boundary layer with up-valley and up-slope winds. From Whiteman, 2000 [52].

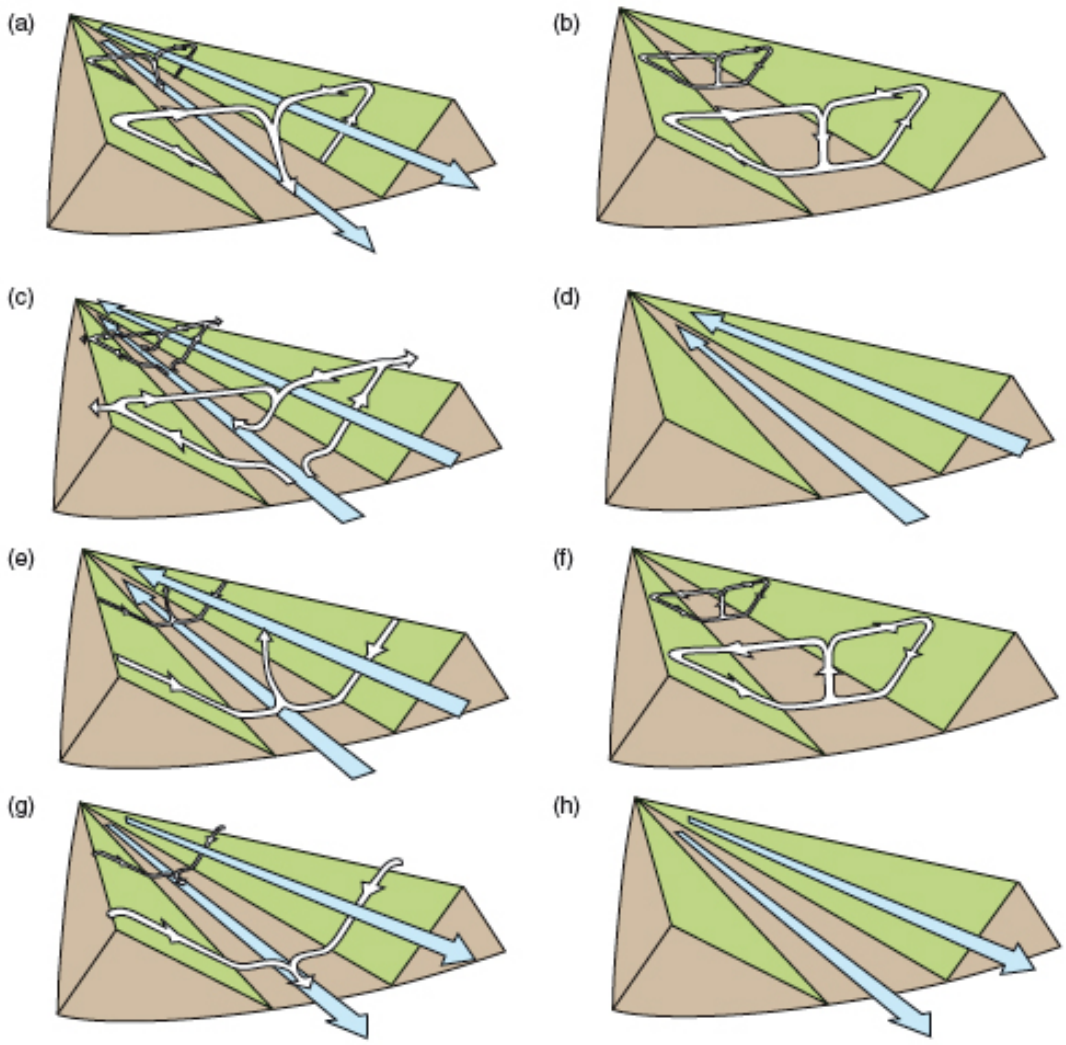

Figure 1.14: This figure depicts the daily evolution of slope-valley winds. In Fig. 1.13the evolution of BL over mountainous terrain is shown, and here it is possible to see the wind system directly connected. The only difference is that picture (a) is the early morning onset of up-slope winds, then corresponds to picture (d) of Fig. 1.13. In picture (d) there is a well formed up-valley wind during the afternoon, that is progressively destroyed by down-slope winds during the evening transition in (e) and (f). During the night down-valley winds occur as depicted in picture (h). From Markowski and Richardson, 2010 [25].

terrain. First attempts with more complicated terrain concern only gentle slopes, or a change in surface roughness. Studies in complex mountain terrain were done mainly on thermal and wind structures (see Witheman 2000 [52] and the section 1.8), but as noted by Rotach and Zardi (2007) [36] whenever it is necessary to include turbulence aspects in complex terrain suddenly the *flat and horizontally homogeneous* hypothesis had to be invoked. This approach may work (and it works quite well) when the NWP used have not a too fine resolution and the topography is very simple and smoothed. However, as soon as higher spatial resolutions were reached, and nowadays LAM with a very fine grid is already present, adequate parametrizations are necessary. The Mesoscale Alpine Programme had as main purpose to fill in some of these gaps.

The MAP was settled in the Alpine region. It started in Zurich in 1994 and last to about five years ago with the last D-PHASE of this project. The main aim of MAP was to improve the understanding of orographically influenced precipitations - especially correlated with floods - improve the NWP models and improve the knowledge of Föhn and gravity waves. The D-PHASE (it stands for Demonstration of Probabilistic Hydrological and Atmospheric Simulation of flood Events in the Alpine region, June-November 2007) is the last part of this project, that involved many scientist from all over Europe, but especially from Alpine countries. It aimed to demonstrate some of the many achievements of the Mesoscale Alpine Programme (MAP), in particular the ability of forecasting heavy precipitation and related flooding events in the Alpine region. In this phase an "end-to-end" flood warning system was set up (Rotach et al, 2009 [34]), where "end-to-end" means that this system includes from the atmospheric forecast model to the end user.

In the frame of MAP there were some projects about the boundary layer:*Riviera project* (settled in Riviera Valley, southern Switzerland), *FORM project* (Föhn in the Rhine Valley during MAP), *GAP flow project* (settled in Wipp Valley, between Innsbruck and Brenner pass) and *Toce catchment*.

1.10 The Eddy Covariance Method

The Eddy Covariance method for measuring exchanges of heat, mass and momentum was first proposed by Montgomery in 1948 [30] and other authors like Swinbank and Obukhov. This first formulation was obviously for flat and horizontally homogeneous surfaces. Under these conditions, the density flux is simply the covariance between the fluctuation of variable of interest and the vertical wind (e.g. $\overline{w'\theta'}$).

When these first theses were proposed there were not the necessary instrumentation to measure the turbulent fluctuations. Only with the advent of sonic anemometer (see Sec. 3.3.2) and fast response instrumentation it is possible to full apply the Eddy Covariance method.

Basically this method has been introduced in previous sections about heat fluxes, Reynolds approximation and turbulence. But it is necessary to go further in details; in fact in order to obtain the Eddy Covariance method the conservation equation (see Sec. 1.5) has to be integrated on a control volume, with an area of interest $A(2L \times 2L)$, where L is the control volume half side measured from the measurements mast, and vertically from the soil to the measurement height h_m.

The first step done by Foken *et al.* [3] is the integration of the *mass continuity equation*[10] that is the dry air budget equation

$$\int_0^{h_m} \overline{\frac{\partial \rho_d}{\partial t}} \, \mathrm{d}\, z + \bar{w}\overline{\rho_d}|_{h_m} + \overline{w'\rho_d'}|_{h_m} = 0 \tag{1.60}$$

the assumption of zero flux of dry air is made, this is quite true because the imbalance of carbon dioxide and oxygen due to photosynthesis or respiration is very small.

Integrating on the same control volume the conservation equation for the mean

[10] The mass continuity equation with NSE describes the dynamics of the atmosphere. The mass continuity states the conservation of mass in a volume of air, so there are neither source nor sinks of dry air in the atmosphere. It states

$$\frac{\partial \rho_d}{\partial t} + \nabla(\vec{u}\rho_d) = 0 \tag{1.59}$$

value of a scalar (that is very similar to Eq. (1.41))[11] we get

$$\begin{aligned}&\frac{1}{4L^2}\iint_{-L}^{+L}\int_0^{h_m}\left[\frac{\partial\bar{C}}{\partial t}+\frac{\overline{U_j}\partial\bar{C}}{\partial x_j}-\frac{\nu_C\partial^2\bar{C}}{\partial x_j^2}+\frac{\partial(\overline{u_j'c'})}{\partial x_j}\right]\mathrm{d}\,x_j\\ =&\frac{1}{4L^2}\iint_{-L}^{+L}\int_0^{h_m}S_C\,\mathrm{d}\,x_j\end{aligned}\tag{1.63}$$

Equation (1.63) is the equation for the *Generalised Eddy Covariance Method* where C can be any component. With the hypotheses of horizontally homogeneous equilibrium layer all gradients on that plane are negligible, and from three integral only one remains.

The Eddy Covariance method works well over homogeneous and flat terrain, with some correction or very small errors can be applied also to inhomogeneous terrain, but the application of this method in highly complex terrain, and especially for long term measurements, has to be proved. There are some studies in complex terrain, for example Hammerle *et al.* (2007) [15] by applying this method on a meadow slope in the Stubai Valley in Austria, finds that his site compared to a site in the valley floor has quite the same energy balance, than if a good quality control is done the EC method can be applied.

[11] The conservation equation for a scalar quantity is

$$\frac{\partial C}{\partial t}+U_j\frac{\partial C}{\partial x_j}=\nu_C\frac{\partial^2 C}{\partial x_j^2}+S_C\tag{1.61}$$

where S_C is the body source term for the rest of processes not included in the equation, ν_C is the molecular diffusivity of the scalar C.

The equation for the mean value is obtained following the same rules of averaging for all previous equation (see Sec. 1.5.2) and it is

$$\frac{\partial\bar{C}}{\partial t}+\frac{\overline{U_j}\partial\bar{C}}{\partial x_j}=\frac{\nu_C\partial^2\bar{C}}{\partial x_j^2}+S_C-\frac{\partial(\overline{u_j'c'})}{\partial x_j}\tag{1.62}$$

this equation is the same as Aubinet *et al.* [3] scalar equation's (pg. 8) but with a different notation and without explicit air density.

Chapter 2

The Innsbruck Box Project

2.1 Introduction

The atmospheric boundary layer (ABL), as previously described in Chapter 1, is well known and studied over flat and homogeneous terrain. A few studies and even less investigations in the fieldwork have been carried out in complex terrain. Nevertheless the ABL in complex terrain remains one of the major challenges of today's boundary layer research (Stiperski *et al.*, 2012 [44]). The necessity to have more knowledge on boundary layer in complex terrain is directly related to weather forecast. In fact, in complex terrain it is difficult to generate a trustworthy forecast, even if nowadays numerical prediction models are always more detailed and with finest grids. In order to strengthen these local area numerical weather prediction models has to be reached a better comprehension of processes and turbulence in the lowest part of the atmosphere, and over a complex topography.

Nowadays there is no other long term project that investigates the boundary layer in truly complex mountainous terrain, then in August 2011 the Dynamic Meteorology Group of the Institute for Atmospheric and Cryospheric Sciences (ACINN, former IMGI Institute for Meteorology and Geophysics), University of Innsbruck set up the Innsbruck Project (henceforth i-Box).

The i-Box is such a "reference box" with the aim to fill in the gap found in the ABL's knowledge. The meaning of "box" is that they would like to have measurements and modelling in a three dimensional volume. In this project the high-resolution long-term turbulence observations in the Inn Valley have been combined with high-resolution numerical modelling.

The i-Box sites are chosen to be representative of specific topographic features. There are six sites:

Station	Longitude (N)	Latitude (E)
Kolsass	47.305341	11.622190
Terfens	47.325538	11.652470
Eggen	47.316500	11.616200
Weerberg	47.299754	11.672969
Hochhäuser	47.287550	11.631220
Arbeser Kogel	47.320654	11.746592

Table 2.1: Coordinates table of core site stations.

- Kolsass, valley floor station (id CS-VF0, see 2.3.1) active since July 2013;
- Terfens, south facing slope (id CS-SF8, see 2.3.2) active since Semptember 2012;
- Eggen, south facing flat slope (id CS-SF1, see 2.3.3) active since April 2013;
- Hochhäuser, north facing steep slope (id CS-NF27, see 2.3.4) active since August 2013;
- Weerberg, north facing gentle slope (id CS-NF10, see 2.3.5) active since September 2012;
- Arbeser Kogel, mountain top (2015 m a.s.l.) (id CS-MT21, see Chapter 3) active since September 2014.

The geographical coordinates of these stations are reported in Table 2.1.

The mountain top station is the topic of this Thesis and I will speak extensively about Arbeser Kogel in the next Chapter.

Other "additional sites" are considered in the i-Box. The main additional site is on the University roof, identified by the code AS-VF0. It is an urban site fully equipped. The standard meteorological Ellbögen (AS-SV14, 1069m), Sattelberg (AS-SV19, 2111m) and Obergurgl (AS-YF19, 1938m) are also involved in the project.

An important component of the i-Box approach is numerical modelling at very high resolution (VHR)[1]. As said before, the aim of the i-Box is to improve local area numerical model, but in this case the gain is doubled: on one side i-Box data

[1]For example the COSMO-1 has a grid horizontal dimension of about 1.1km with 80 vertical levels with the lowest at 10m above the ground, and the higher around 500hPa.

improve models results, on the other the simulations (run with an ideal-terrain characteristics) are invaluable for both experimental planning and data analysis (Rotach *at al.* re-submitted after revision [37]), because the model output can integrate temporal and spatial data absence or scarcity. Numerical models contain only a parameterisation of the BL structure, and especially in mountainous terrain they have a too wide grid to resolve the complexity of an Alpine valley, even more peaks are always cut away. But there is also a computational power problem: in fact by reducing the grid and, at the same time, run the model on a wide area needs many processors and fast computers.

Local studies have been developed on this topic, but the idealisation from numerical model cannot fully fill in the gap between ideal to real-terrain; this is the reason of the necessity of a long term experiment.

2.2 The Alpine Region of the i-Box

The experimental field of the i-Box is the Alpine Inn Valley. It is located in the western Alps, and the Inn Valley divides the central-western sector (where it is located Arbeser) from north-western Alps. More in detail, the stations are settled in the Tux Alps a subgroup of the Tyrol Schistose Alps (see Fig. 2.1). The Inn Valley is approximately SW to NE oriented and has many side valleys. At the valley floor it is 2 to 3 km wide, and ridge-to-ridge is about 20 km wide (Rotach *et al.* [37]). The depth is around 1700-2100 m, ranging from approximately 600 m at the valley floor to 2300 m of the north ridge and 2700 m of the south ridge.

The valley is characterised by mixed agricultural lands and quite a lot of medium and small villages. The biggest city is Innsbruck and it is 20 km away from the stations in up-valley direction (south-west). The slopes of the valley are characterised by grassland spaced out by fir and others conifers. The treeline is at the altitude of 1900 m, thus Arbeser is totally outside of the wood.

Lateral valleys, inhomogeneities of the valley floor (different soil use), mountain passes and the direction of the main valley help to complicate the air flow. This is a typical example of truly complex terrain, and this is the test-bed of the i-Box project.

2.3 Stations

The stations are disposed quite symmetrically compared with the valley axis. In the Figure 2.2 you can see where they are settled.

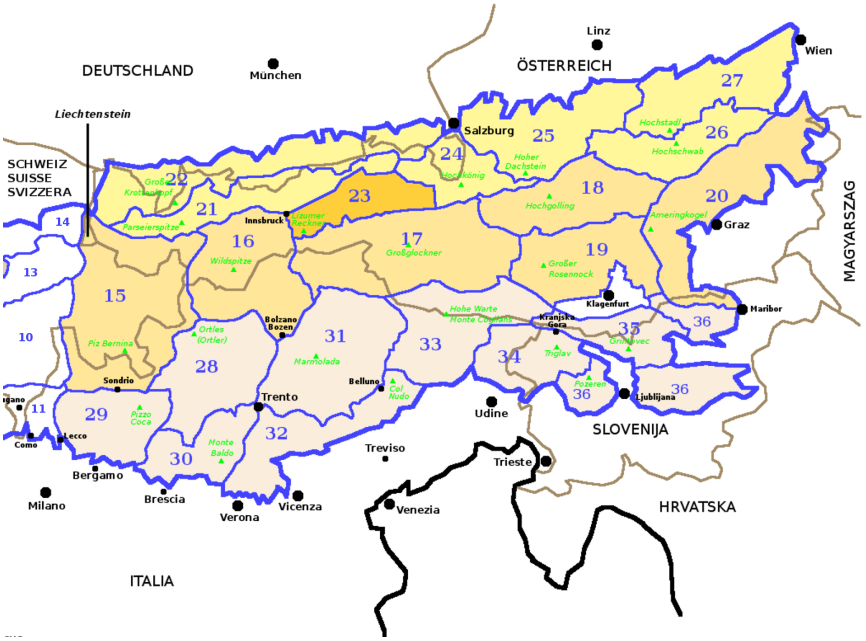

Figure 2.1: The Western Alps following SOIUSA classification, with highlighted the sector 23 of Tyrol Schistose Alps where i-Box project's stations are settled.
From Wikipedia by Luca Bergamasco - Own work, CC BY 3.0, https://commons.wikimedia.org/w/index.php?curid=5184003

Every single station will be briefly described in the following sections.

2.3.1 Kolsass

This is the main site, the valley floor station (545m a.s.l.). Its tower is the highest with 17 metres high lattice mast (see Fig. 2.3 on the left). This station is equipped with three levels of sonic anemometer Campbell CSAT3, one level of fast response hygrometer and a gas analyser Campbell Scientific EC150. At the base of the mast (approximately 2 metres high) are mounted a net pyrgeometer and a net pyranometer. The surroundings of the mast are characterised by flat fields and grassland; in direction West there is a cylindrical water tank used for field irrigation. The real inclination of the valley floor is estimated in less than 0.5°.

Figure 2.2: In this Google Earth's image all the six core-site i-Box stations are shown, five of them are quite symmetrically disposed with respect to the valley axis, instead Arbeser is out-of-scheme.

2.3.2 Terfens

The first south facing station is Terfens (575 m a.s.l.). It is located next to an helicopter landing field. The local slope inclination is 8° but on the back of the mast there is an embankment which its slope is 28°. The total height of the tube mast is 12m, and on the top is located a sodium vapour lamp (see Fig. 2.3 on the right).

This station is equipped with two levels of sonic anemometer Campbell CSAT3, and on the highest level there are a Krypton hygrometer and a HC2-S3 thermo-hygrometer.

The surrounding terrain has changed since the measurements started, in fact in east direction there is a 20 m tall artificial hill, that probably has changed the flow behaviour.

2.3.3 Eggen

The second south facing slope station is Eggen (829 m a.s.l.). It is settled in the middle of an alpine meadow, on an almost flat slope ($\approx 1°$) near the village of Eggen. The equipment is one sonic anemometer and one Krypton hygrometer at the top of the mast, at approximately 6.6 m.

Figure 2.3: Kolsass (on the left) and Terfens (on the right) stations.

2.3.4 Hochhäuser

The first north facing station is Hochhäuser, in Figure 2.4 on the left (1009 m a.s.l.). It is settled near a road that cross a steep meadow (27°) bordered by fir and approximately 100 metres wide. On the mountain side (upstream) the treeline is about 400 metres far.

Hochhäuser is equipped with one sonic anemometer CSAT3 at the top of the mast (6 m high) and a KH20 Krypton hygrometer. There are also three levels of cup anemometer and a wind vane in the lowest level. The net radiometer is a CNR4 disposed in the upslope side and parallel to the slope.

2.3.5 Weerberg

Weerberg is the second north facing station, it is located on a gentle slope with an inclination of 10° at an altitude of 930 m (see Fig. 2.4 on the right). The surroundings are characterised by alpine meadow and some trees that separate the fields. On the six metre tall mast there is mounted one sonic CSAT3 and one KH20, next to them there is a slow response thermo-hygrometer HC2-S3. The net radiometer is mounted in South direction.

2.4 First Results

The first results are presented in the paper not yet published by Rotach *et al.* [37] and the explanation of quality assessment is given in Stiperski and Rotach (2016) [43].

First studies on i-Box data are related to scaling the most important variables usually considered in the surface layer. These scaling properties are studied in the Monin-Obukhov Similarity Theory (MOST) over horizontally and homogeneous flat terrain, and it is not sure that this scaling is applicable to Truly Complex Mountainous Terrain (TCMT) situations. Thus the first approach is to study the departure from MOST in different sites, and if it is possible to identify additional processes for a possible extension of MOST. Preliminary studies tell us that a local scaling is possible, but these similarity relations are not conform to the MOST.

A second point is the evolution of temperature structure in a broad valley. The potential temperature vertical profile ($\mathrm{d}\,\bar{\theta}/\,\mathrm{d}\,z$) is very important to study the stability of a layer, and then the exchange processes between the valley BL and the free atmosphere. This is fundamental when, for example, the pollutants dispersion is treated. In fact in presence, especially in nighttime, of ground based inversion, the pollutants are trapped in the lower layer of the BL, so the air

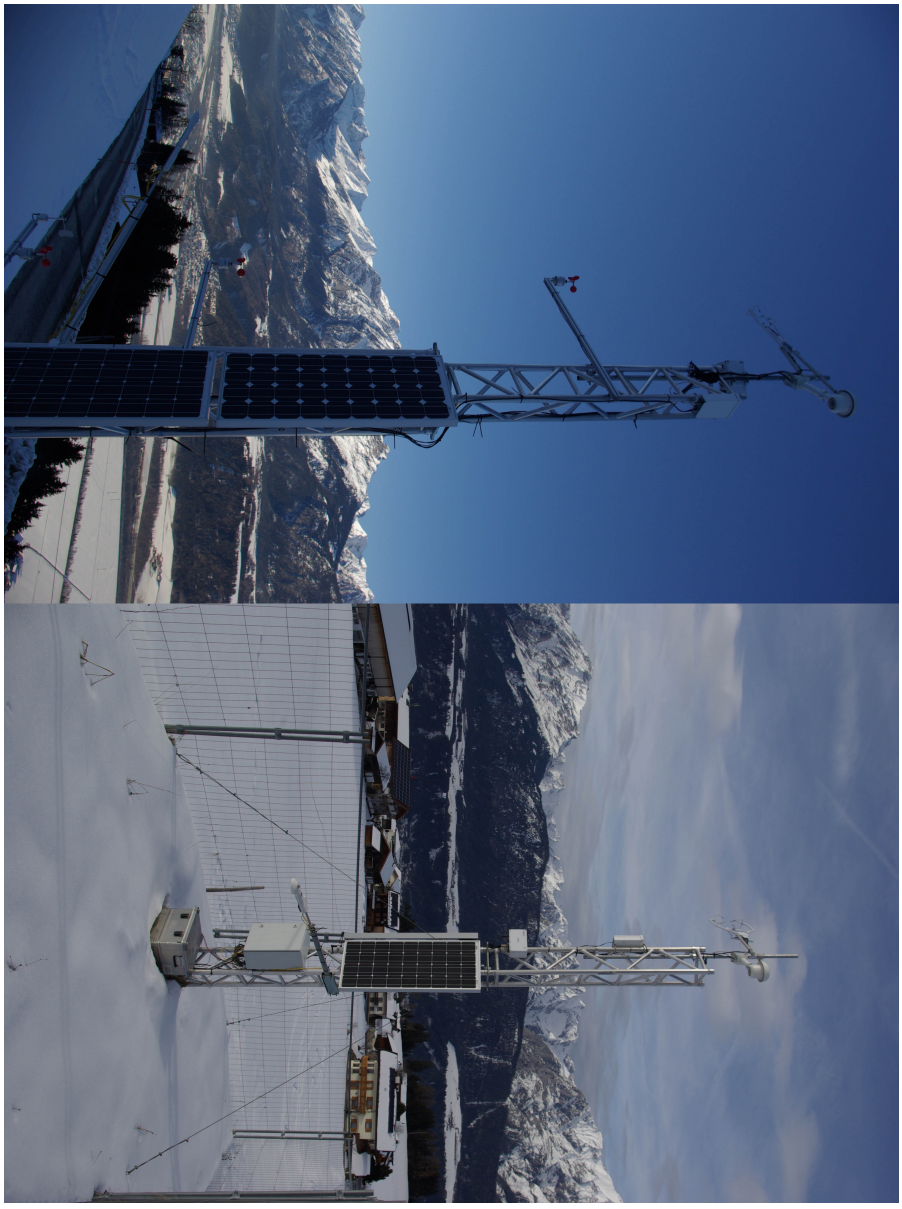

Figure 2.4: Hochhäuser (on the left) and Weerberg (on the right) stations.

pollution raises near the urban areas. The study of vertical profile of θ is possible with soundings or with the RPG-HATPRO microwave radiometer (Massaro *et al.*, 2015 [28]). In this case a new calibration algorithm was proposed and a substantial improvement reached in particular in detection of static stability information in the valley BL. This is crucial when profiler data are used to control the model output and its accordance with observed data.

Moreover an intercomparison study between the heat flux measurements by scintillometers and by Kolsass station has been done. It has to be recall that the horizontal inhomogeneity is a peculiar characteristic of BL structure in complex terrain. The application of scintillometer is possible also in TCMT, but only if the height of the path is correctly specified and it remains in the SL. In the experiment conduced the scintillometer path, in most cases, was clearly outside of the SL and this frustrates the MOST-based assumption for the operating condition of this instrument. Nevertheless in two sample days, when the heat flux seems to be constant, the scintillometer provides an according result to Kolsass station. An open question remains on not constant fluxes.

Another study was conducted on TKE forecast by high resolution NWP COSMO-1. This model was run with 1.1km horizontal grid spacing and 80 vertical levels, and the lowest vertical grid spacing was 20 m. This study compared the nearest grid point (or an average of the nearest) output to station observation in Kolsass (CS-VF0) and Hochhäuser (CS-NF27). The magnitude of the TKE is quite well represented, but the day-cycle not.

The last result and application of the i-Box data is about air quality and dispersion modelling. The Austrian Weather Service provides air quality assessment report for various costumer. In complex terrain it is difficult to go through with this task, in fact the orography deeply modifies the behaviour of winds. Different numerical models (INCA, WRF, GRAMM and LASAT) are compared in four situations: two low-wind periods and two with stronger winds (föhn and a frontal passage). The model results have been compared with i-Box stations. For the last two models Kolsass station data is also used as input. The frame depicts is that generally with low wind the uncertainties are bigger, especially in the wind direction, instead in case of föhn and front (stronger wind situations) there is not a winner model, each one has some good and bad skills.

The overall scheme of the interactions of different i-Box project parts, is depicted in Figure 2.5.

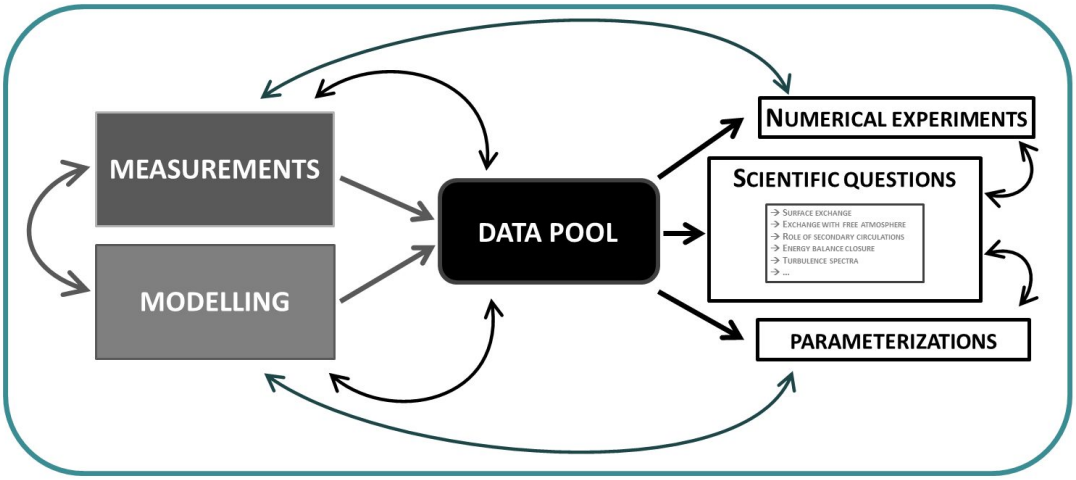

Figure 2.5: This scheme summarises the interaction and aims of the i-Box project. A strength point of i-Box project that results from this scheme is the double side arrow that connects measurements and modelling, in fact the interaction between numerical modelling and the measurements permit an improvement in models quality and a correct understanding of turbulence measurements, as well as a spatial integration of direct measurements.

Part II

Arbeser Kogel

Chapter 3

The Arbeser Kogel Station

3.1 Introduction

In this chapter the Arbeser Kogel station is presented. The station is devoted to the measurements of mean and turbulent quantities. The collected data will be analysed in the following chapters.

Arbeser is a particular site, quite unique[1], because the boundary layer turbulence is usually studied over plains, or when campaign in complex terrain starts the choice fall on gentle or also steep slope. A mountain top station has many technical complications. First the power supply is a problem; in Arbeser there is not a direct electricity supply from the power network. Other problems are the maintenance and the harsh condition, for instance.

3.2 Site Characteristics

Arbeser station is settled on a ridge 5 metres under the Arbeser Kogel[2] top, at an altitude of 2020 m above the sea level. The nearest big city is Schawz, and the road access is from Pill (Tirol, Austria).

The ridge where the station is settled is 20 metres wide and has a west to east orientation, where the summit cross is on the east side of the Station. At the north and south border of this wide west shelving ridge (local slope 21°) there

[1] I have only found a cloud microphysics and turbulence study by Siebert *et al.*, 2015 [40] settled near Innsbruck too, in Schneefernerhaus. Another study published at the beginning of 2016 was settled on a 1926 metre high mountain in Himalayas (Solanki *et al.*, 2016 [41]). In this second study the station involved is much similar to Arbeser.

[2] Kogel in Austrian means conical peak, it is referred to a mountain top.

are two steeper slopes, with an inclination greater of 33° the north one and 31° the south one. About 500 straight metres down valley there is a top ski-station restaurant that works mainly during the winter season from November to Easter holidays, and again in the summer season; then the access to the station is possible during the winter by the chair lift through the restaurant, while during spring and autumn the access is with the car up to Naunzalm-Hochleger (1830 m) and then with approximately one hour hiking.

The geographical coordinates of the station are:

- 47.320654 N and 11.746 592° E;
- UTM 5244456.79 N, 707552.34 E reference system 32T.

The site is a perfect terrace on the Inn Valley and, as you can see from the 360° panorama in Figure 3.1, the sight is open in all directions from NE (north-east) to SE (south-east), instead in east direction there is Arbeser Kogel top, and more far Kellerjoch (2344 m).

The station then is shadowed only for some hours during the morning especially in winter.

The power supply for the instrumentation is given by a couple of solar panels and a fuel cell. The fuel cell works with methanol and raise the batteries voltage when it falls under 12.5 Volts. The station is supplied by ten 12V car long-life batteries.

The structure of the Station is a triangle lattice mast in aluminium 4 metres high and 36 cm of side. All the instrumentation is mounted on this mast and all the specifications are summarised in Tables 3.1 and 3.2. The ground in the surrounding of the mast is not flat, then the height are not the same for all instruments even if they are at the same level; this because heights are measured on the vertical of the instrument. For example it is possible to see that cup anemometers are higher than thermometers, in fact cup anemometers are mounted on the descending side of the ridge (see Figures 3.2 and 3.3).

3.3 Weather Station's Instrumentation

In Tables 3.1 and 3.2 the low frequency instrumentation installed at Arbeser station is shown. There are three levels of temperature and humidity sensors, while there are three level of cup anemometer and a wind fan vane, approximately mounted between first and second cup level. At the top of the mast there is the sonic anemometer, and when it works, nearby the Krypton hygrometer is installed.

Figure 3.1: This 360° panorama was shoot on the 5th November 2015, on a sunny and very clear day, from the top of Arbeser Kogel, near the summit cross. In the valley behind the station there is Innsbruck.

Thermometer - Hygrometer			
	Level 1	Level 2	Level 3
Distance from mast (cm)	45 ± 1	45 ± 1	45 ± 1
Height (cm)	54 ± 2	191 ± 2	388 ± 2
Cup anemometer			
	Level 1	Level 2	Level 3
Distance from mast (cm)	91 ± 1	91 ± 1	91 ± 1
Height (cm)	77 ± 2	212 ± 2	427 ± 2

Table 3.1: Thermometer, hygrometer and cup anemometers position relatively to the mast and the ground under the instrument.

Net Radiometer		
	pyranometer	pyrgeometer
Distance from mast (cm)	230 ± 1	217 ± 1
	incoming	outgoing
Height (cm)	95 ± 1	92 ± 1
Snow sensor		
	From mast	From ground
Distance (cm)	179 ± 1	85 ± 1
Young Vane		
	From mast	From ground
Distance (cm)	78 ± 1	217 ± 2

Table 3.2: Radiometer and snow sensor position relatively to the mast and the ground under the instrument.

After a lightning strike on the sonic a lightning rod was mounted in direction NE to the sonic.

The data logger is a Campbell Scientific CR3000, the Krypton hygrometer output is directly measured by the ultrasonic anemometer electronic device and then the signal is collected by the CR3000. The data are locally stored and periodically send to the institute via an EDGE communication system.

3.3.1 Low Frequency Instrumentation

The low frequency instrumentation is composed of:

1. three levels of ventilated thermometer and hygrometer;
2. three levels of cup anemometer;
3. one wind fan vane;
4. one infrared snow-height sensor;
5. one net radiometer (pyrgeometer and pyranometer);
6. three levels of ground temperature and heat flux measurements;
7. one pressure gauge settled in the logger box[3] (see Fig. 3.4).

Temperature and Humidity

The station is equipped with three temperature and humidity sensors disposed at three levels on the east part of the mast. These sensors are Rotronic HygroClip 2, and the third level is an HC2-S3. Each sensor is into an actively ventilated shield RS12T (12VDC power supply). The hygrometer is an Hygromer IN-1 capacitive sensor with an accuracy of $\pm 0.8\%$. The temperature sensor is a Pt100 resistance thermistor with an accuracy of 0.1K in the range $10 \div 30°C$, while the temperature range is $-50 \div 100°C$.

The sensor typical time constant is 10s for humidity measurements, and 3s for temperature measurements.

Since 29th of October 2014 the station has three levels of ground temperature measurements, instead in the first part of October there was not the third level

[3]There is no further description of this instrument then I resume here its characteristics. It is a Setra model 278 serial 5320479, with range from 600 to 1060 hPa, the accuracy is ± 0.5hPa at 20°C and the resolution is 0.01hPa.

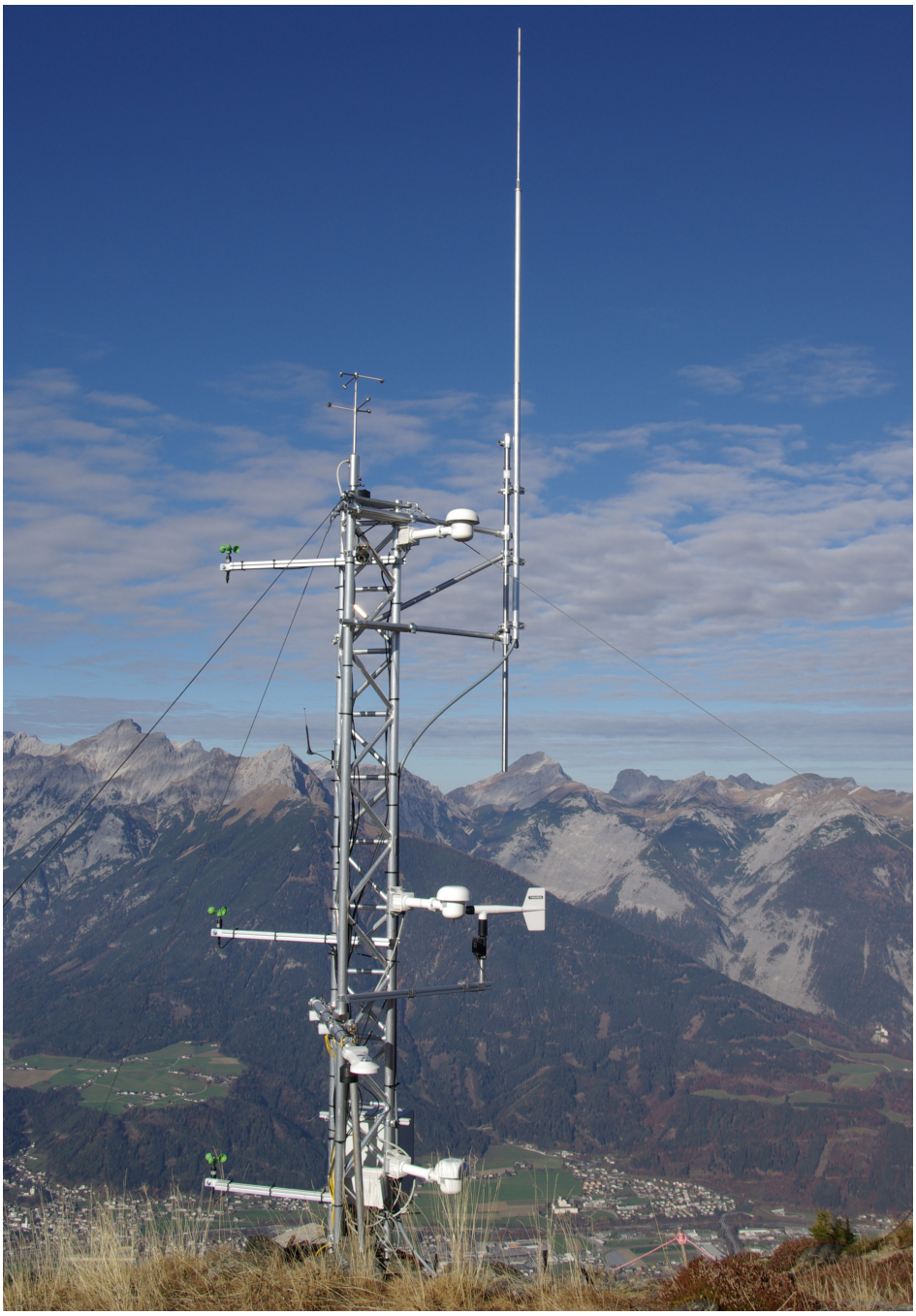

Figure 3.2: The Arbeser station mast, and we can clearly distinguish the three levels of cup anemometers and temperature/humidity measurements.

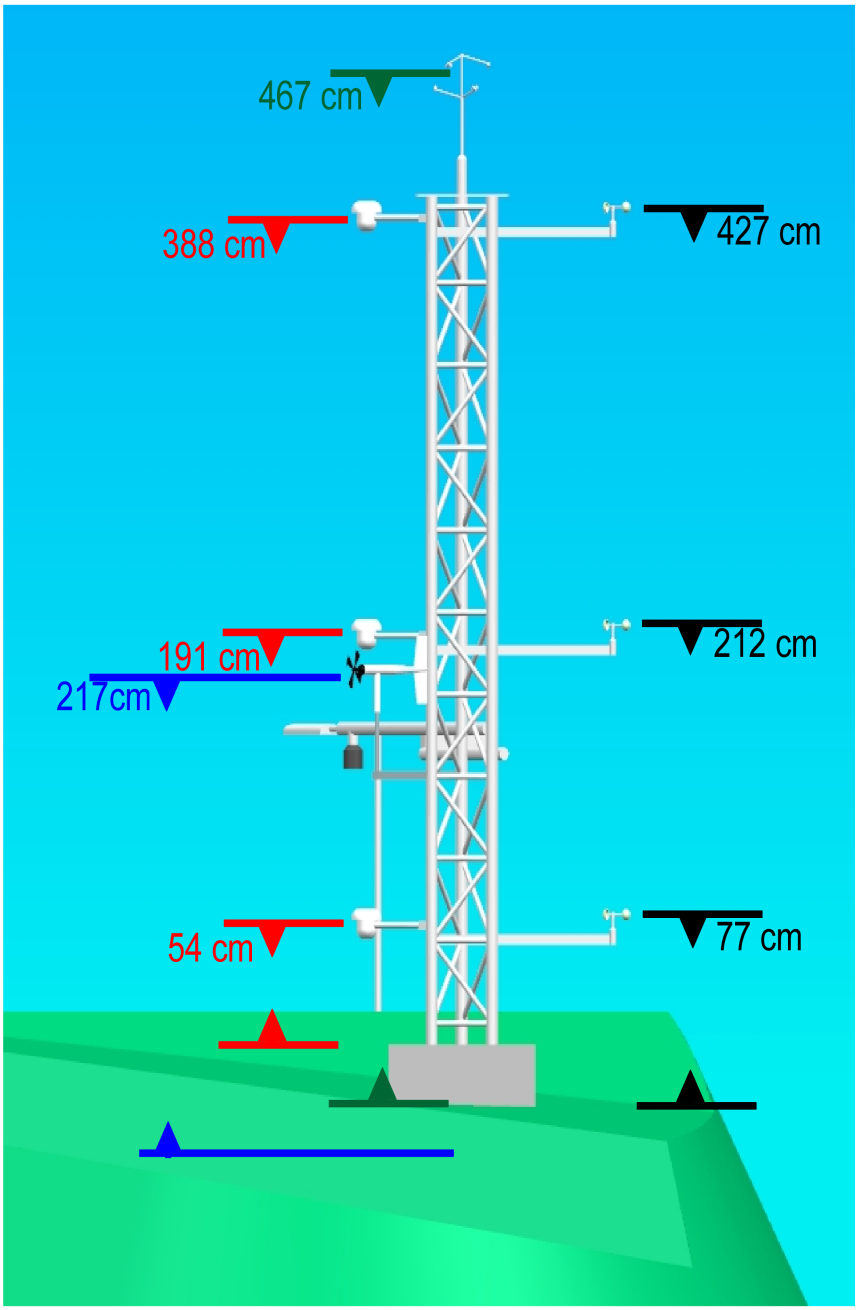

Figure 3.3: The Arbeser station mast draw with CAD and with superimposed heights of instruments, with this picture is simple to understand the real heights of each instrument. Black heights: cup anemometers; red heights: thermo-hygrometers; blue height: Young wind vane and green height: sonic anemometer. View from north. Draw by Luciano Golzio

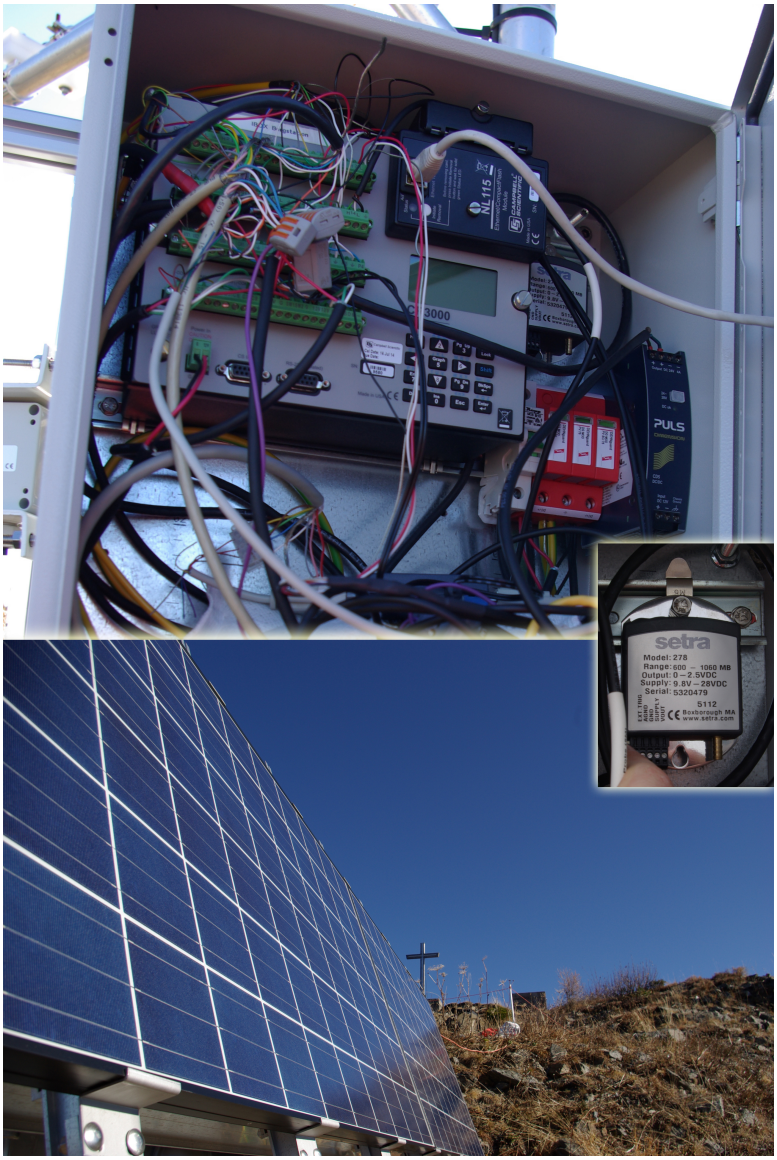

Figure 3.4: The logger box with the CR3000 data logger (at the image top), the Setra pressure gauge (enlarged in the middle), the solar panel settled in the South side of the station (at the bottom).

Figure 3.5: Rotronic temperature and humidity sensor inside the RS12T ventilated shield, it was unmounted on 1st April 2016 for routine maintenance of the station.

of ground temperature. The position of these sensors is approximately under the radiometer in direction SE from the mast. Unfortunately I was not able to find the file or paper where the installers wrote the depth of each sensor[4]. Thus these data are quite useless.

There is also a soil heat flux measurement with the HFP01–7565 sensor (Hukseflux manufacturer), that is a thermopile measuring the temperature difference across the ceramics-plastic composite body. The output is a potential difference in mV that is converted in heat flux using the calibration constant.

Wind Sensors

The station is equipped with three cup anemometers (mounted at different absolute height of temperature and humidity sensors) disposed on three levels in the west side of the mast, where the terrain descends along the ridge. Thus the lowest level, that is less high than the first temperature level with respect to the mast, results higher. These cup anemometers are not high precision instruments, but

[4]Observing the data I was able to identify the order of depth. According to Table 4.3 the level 3 is the closest to the ground level, level 2 is in the middle and level 1 is the deepest.

Figure 3.6: The Yuong wind monitor and the second temperature-humidity level (on the left) installed on the north side of Arbeser station; in the back ground the Inn Valley with Vomp village.

can be used to get an approximative wind profile.

The high precision instrument is the wind monitor. It is a wind vane and fan anemometer (see Fig. 3.6), it is mounted in the north side of the mast. This sensor is conceived for harsh climate, then also with light ice condition it continues to work. It is a R.M. Young model 05103, its accuracy is ± 0.3 m/s and its starting threshold is 1.0 m/s. The measuring range for wind speed is $0 \div 100$ m/s. In wind direction the accuracy is $\pm 3°$, with a starting threshold of 1.1 m/s.

Radiation Sensors

The radiation is measured by a net radiometer Kipp&Zonen, model CNR4 (serial number 121149). This is a compact instrument, that measures four radiation parameters with two pyrgeometers and two pyranometers: incoming Long wave ($LW \downarrow$), outgoing long wave ($LW \uparrow$), incoming short wave ($SW \downarrow$) and outgoing short wave ($SW \uparrow$). Thus a couple of pyrgeometer (measuring long wave radiation) and pyranometer (short wave radiation) is disposed on the upper part of the instrument (incoming radiation denoted by $\downarrow$) and another couple is disposed on the lower part (outgoing radiation from the Earth $\uparrow$).

This sensor is ventilated and a Pt100 thermistor measures the instrument body temperature.

Each sensor needs a specific calibration and the transformation of the signal from mV to $\mathrm{W\,m^{-2}}$. This is simply done using the Stefan Boltzmann Equation

CNR 4 calibration serial 121149

Sensor	Incoming	Outgoing	Uncertainty	Impedance [Ω]
Pyrgeometer	8.37	9.40	±7.0%	60
Pyranometer	14.12	14.92	±3.5%	60

Table 3.3: Calibration sheet for CNR 4 net radiometer mounted at Arbeser. Calibration constants (columns "Incoming" and "Outgoing") in µV/(W/m^2). Date of calibration 30th October 2012.

(1.3) and especially (1.5), and the calibration constants measured by Kipp&Zonen (Table 3.3) for the pyrgeometer the irradiance is

$$E = \frac{V}{C \cdot 1000} + \sigma_B T^4 \tag{3.1}$$

where V is the output in mV of the pyrgeometer and C is the calibration constant, multiplied by 1000 because it is in µV. The temperature T is the instrument temperature, given by the Pt100 thermistor settled inside the radiometer. For the pyranometer it is only necessary to calibrate the voltage

$$E = \frac{V}{C \cdot 1000} \tag{3.2}$$

The characteristics of this instrument are resumed in the following Table 3.4.

Sensor	Accuracy	Spectral range	Irradiance	Field of view
Pyranometer	$10 \div 20$	$300 \div 2800$ nm	$0 \div 2000$	up:180° dw:150°
Pyrgeometer	$5 \div 15$	$4.5 \div 42$ µm	$-250 \div 250$	up:180° dw:150°

Table 3.4: Characteristics of CNR 4 net radiometer. Accurancy in µV/(W/m^2), and Irradiance in W/m^2.

3.3.2 Sonic Anemometer and Krypton Hygrometer

The high frequency instrumentation at Arbeser is a Metek®ultrasonic anemometer and a Campbell Scientific®KH20 Kripton hygrometer.

The specifications are:

Figure 3.7: Arbeser station's CNR 4 Radiometer. It is possible to see the upper and lower plexiglass pyranometer domes, on the left there is the infrared snow sensor.

Figure 3.8: Arbeser's third level cup anemometer, view in direction of Innsbruck along the ridge.

1. one ultrasonic anemometer Metek, first a USA-1 Scientific model (with turbulence extension, serial 0101061582 operating since 2014.09 to 2015.02.21) and after a lightning strike a uSonic3 Scientific SC (standard configuration, former USA-1, serial 0105123843 operating since 2015.02.21), on the top of the mast.

2. one Krypton Hygrometer KH20 Campbell Scientific (serial number 1735, dismissed on 2015.05.13), next to the sonic in direction N.

The Metek sonic at the beginning was a USA-1 model and now it is installed a uSonic3 Scientific installed. The main difference between the two of them is the coordinate system reference frame, in USA-1 the output vector $x - y - z$ is in a left-hand Cartesian coordinate system, instead in the uSonic3 it is a right-hand coordinate system. This is an important issue for all the following analysis carried out with EdiRe software.

The Krypton hygrometer KH20 worked only for a short period, then there was a problem with water, ice and snow and since the 13th of May 2015 it was unmounted (in the next chapter I report the exact days of successful operation). In these few days of work it is possible to obtain something useful for the analysis.

Principle of the Sonic Anemometer

The sonic anemometer mounted at Arbeser station has three sonic path not orthogonally placed, but with an angle of 45° from the main pole, with a non-crossing path (see Figure 3.9).

The sonic anemometer measures wind components from the transit times of the acoustic signals travelling between the transducers in both directions, the theory of measuring wind components by sound mean dates back to Schotland (1955) [39], where he theorised the possibility of measuring wind velocity by sound wave propagation perturbation. The first use of sonics dates back to middle XX century, Kaimal and Businger (1963) [21] described an experimental instrument composed by one vertical sound path of about 1 metre. This was one of the first experiments with those new equipments. The importance and the applications of sonic anemometer developed especially in 1980s and 1990s, and nowadays it is a key instrument not only for micrometeorological applications.

In our case the instrument measures 3 non-orthogonal component, and then with a rotation matrix it creates the three Cartesian wind components according to the reference system chosen by the constructor.

The measurement is in two steps: in the first one the signal travels from transducer "A" to "B" (Fig. 3.10), where A is the emitter and B is the receiver;

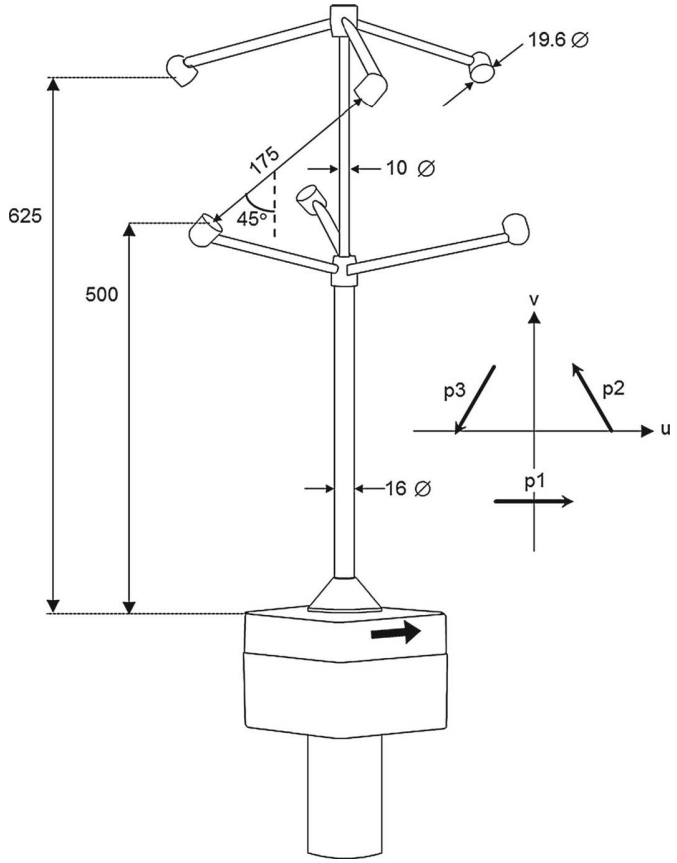

Figure 3.9: Metek uSonic3 Scientific ultrasonic anemometer specifications. From Horst *et al.*, 2015 [19]

in the second step emitter and receiver are exchanged and the ultrasonic impulse travels in the opposite direction. In Figure 3.10 it is possible to see how the wind velocity affects and deviates the sound wave path, and knowing the distance between the two transducers is possible to calculate the velocity V_d along the transducers path.

The two time equation of the sonic anemometer (one component) are:

$$d = t_1(c_d + V_d) \tag{3.3}$$

$$d = t_2(c_d - V_d) \tag{3.4}$$

where d is the distance between the transducers and (3.3) is for the first impulse and (3.4) is for the second impulse (see Fig.3.10), clearly the assumption that the wind vector $\vec{V}$ is constant in the time step $t_1 + t_2$, has to be made. The velocity

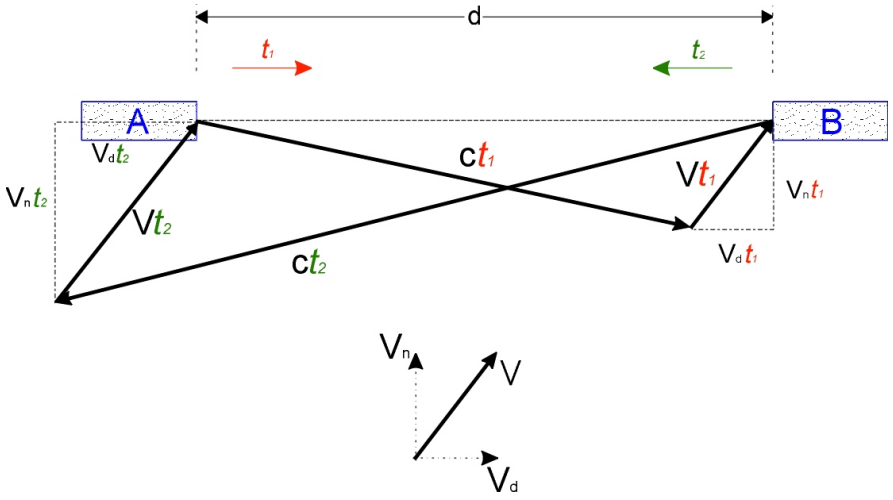

Figure 3.10: Schematic of one couple of transducers of a generic sonic anemometer. The wind vector $\vec{V}$ modifies the path of sound waves, and so the fly-time change. Redrawn by the author, from Kaimal and Finnigan, 1994 [22]

of sound has to be found for measuring the sonic temperature, I will do it later, but from these equations it is simple to find the velocity of the wind, because the distance is known and the travelling time is directly measured. Then

$$V_d = \frac{d}{2}\left(\frac{1}{t_1} - \frac{1}{t_2}\right) \tag{3.5}$$

The crosswind component V_n is affected by the knowledge of the sound speed, and the sound is a pressure wave, propagating in the air-mean. Since the sound speed $\vec{c}$ is directly connected with the air pressure, density (temperature) and the air moisture, it is possible to calculate (Schotanus, 1983 [38]) the sonic temperature. Similarly to Equation (3.5) it is possible to write

$$c_d = \frac{d}{2}\left(\frac{1}{t_1} + \frac{1}{t_2}\right) \tag{3.6}$$

the sound wave is a perturbation in the air-mean, and it propagates at sound speed $\vec{c}$, that depends on the properties of the fluid. In this case density and pressure are related in this way

$$\mathrm{d}\, p = -\rho \vec{c}\, \mathrm{d}\, \vec{c}, \tag{3.7}$$

with the continuity equation is obtained

$$\frac{\mathrm{d}\,\rho}{\rho} = -\frac{\mathrm{d}\,\vec{c}}{\vec{c}} \tag{3.8}$$

combining with the Equation (3.7) of the sound propagation

$$\frac{\mathrm{d}\,p}{\mathrm{d}\,\rho} = c^2 \tag{3.9}$$

now using the state equation for a perfect gas, and coefficients for dry and moist air it is possible to write[5]

$$c^2 = \gamma RT(1 + 0.51q) \tag{3.10}$$

where $\gamma R = 403\ \mathrm{m^2\,s^{-2}\,K^{-1}}$ and q is the specific humidity.

From Eq. (3.10) it is possible to see the relation between sound speed and temperature, then using the (3.6) and the time lag is possible to find the *sonic temperature*[6]

$$T_s = \frac{d^2}{4\gamma R}\left(\frac{1}{t_1} + \frac{1}{t_2}\right)^2, \tag{3.11}$$

that is the sonic temperature on-field calculated by the instrument[7].

Sonic Temperature Corrections

The sonic temperature, as it is possible to see from previous equations and figures (Fig.3.10), is affected by the cross wind V_n that deviates the sound wave from the transducers joining line and consequently increases the transit time. Another factor that influences the sound wave is the air density that affects the sound velocity. These effects has to be taken into account, and correct the instrument sonic temperature calculates via (3.11).

At the beginning of 1980s it is possible to find an important publication by Schotanus *et al.* (1983, [38]), where they analyse the temperature measurement with a sonic anemometer. In fact a corrected and calibrated temperature is needed because heat fluxes have to be evaluated as accurately as possible, and to use the

[5]The state equation for perfect gas states $p = \rho R^* T$, then the propagation of the sound wave is an adiabatic process $p = k\rho^\gamma$ where $\gamma = c_p/c_v$ with $c_{p,v}$ specific heat at constant pressure or volume. Substituting ρ after derivation in (3.9), the result is $c^2 = \frac{\mathrm{d}\,p}{\mathrm{d}\,\rho} = \gamma k\rho^{\gamma-1} = \gamma\frac{p}{\rho} = \gamma R^* T$.

[6]I have to recall that the *sonic temperature* $T_s = c^2/\gamma R$ is different form the real air temperature, later we will see that, in order to obtain the air temperature, the sonic one has to be corrected for humidity and crosswind components.

[7]It is possible to refer to Metek calculation report for further details, see Appendix A

eddy covariance method temperature measurements at the same frequency of velocity measurements are needed[8].

Then the sonic temperature has to be corrected in order to obtain the real or virtual air temperature. From Schotanus (1983), Kaimal and Gaynor (1991) [23], Hignett (1992) [17], and Liu *et al.* (2001) [24], the relation between sonic temperature and real temperature is

$$T_{si} = T_i(1 + 0.51q) - \frac{V_{ni}^2}{\gamma_d R_d} \tag{3.12}$$

in this equation the index i indicates the i^{th} set of transducers, T_i is the air temperature, q is the specific humidity and the last term is the crosswind correction, V_{ni} is the wind component normal to the i^{th} sonic path.

Applying to (3.12) Reynolds average rules, separating mean and fluctuating parts, the equation for T_s' is obtained (Eq. 3.13), this expression is similar to Schotanus, but with the coefficients A and B different depending on the sonic used.

$$T_s' = T' + 0.51q'\bar{T} - \frac{2\bar{T}}{c^2}(u'\bar{u}A + v'\bar{v}B) \tag{3.13}$$

In our case the coefficients for Metek USA-1 and uSonic3 are $A = B = 3/4$. By reversing this formula it is possible to correct the sonic temperature fluctuations, only if the fluctuations of humidity are known, thus a fast response hygrometer is needed, and the mean value of temperature along the averaging period used for the evaluation of variances.

In a similar way it is possible to correct the sonic temperature variance $\sigma_{T_s}^2$

[8]The Eddy Covariance (EC) method is not the only one for evaluating heat and moisture fluxes, but it is the direct one that brings fluctuations from a high frequency set of variables (u, v, w, T_s), other methods, such as the aerodynamic method, do not use high frequency data but only evaluate a gradient between the ground and a standard temperature level (e.g. 2m). Then with the Bulk formula it is possible to obtain the heat flux and all the characteristic scale variables for the SBL. (Stull, 1988 [45] Ch. 12)

$$\begin{aligned}\sigma^2_{T_c} =&\sigma^2_{T_s} - 1.02\bar{T}\overline{q'T'_s} - 0.51^2\overline{q'^2}\bar{T}^2 - \\ &- \frac{4\bar{T}^2}{(\bar{T}_s\gamma R)^2}(\overline{u'^2}\bar{u}^2A^2 + \overline{v'^2}\bar{v}^2B^2 + 2\overline{u'v'}\bar{u}\bar{v}AB) + \\ &+ \frac{4\bar{T}}{\bar{T}_s\gamma R}(\overline{u'T'_s}\bar{u}A + \overline{v'T'_s}\bar{v}B) + \\ &+ \frac{2.04\bar{T}^2}{\bar{T}_s\gamma R}(\overline{u'q'}\bar{u}A + \overline{v'q'}\bar{v}B)\end{aligned} \tag{3.14}$$

applying this correction after a double rotation (as I did in the sonic data analysis) the mean speed $\bar{v}$ results equal to zero then many terms are zero.

In the study of Liu *et al.* they compared all these terms of (3.14) with a platinum wire thermometer variance σ^2_p, and the result is that terms IV and VI are negligible, instead the second right-hand-side term contributes for about a 20% in unstable conditions (only 10% in stable conditions) whereas terms III and V contribute for 2% (1% in stable conditions) and 5% respectively.

The sensible heat flux can also be corrected following the same procedure. Liu *et al.* (2001) [24] give us the following equation

$$\overline{w'T'_c} = \overline{w'T'_s} - 0.51\overline{w'q'}\bar{T} + \frac{2\bar{T}}{\bar{T}_s\gamma R}(\overline{w'u'}\bar{u}A + \overline{w'v'}\bar{v}'B) \tag{3.15}$$

in this case term II contribute as 20% (5% in stable conditions) and term III as 5% in both stable and unstable cases.

Sonic Angle Correction

The sonic anemometer is mounted at the top of the mast and has in direction north a place where is possible to screw a stick and align the sonic north to the geographical North. This operation was done by who set up the uSonic3 (the latter sonic), I have controlled if the alignment was done correctly.

Unfortunately near the mast a magnetic compass does not work, because the mast generates itself a perturbation to the Earth magnetic field. I have tried with the compass of a GPS device, that use the satellite but it did not work properly. The last chance is to use an "old" method. I climbed the mast and I shot four photos aligning the camera to the sonic's cardinal points. Thus in the perfect middle of the photo there is the sight from this particular cardinal point of the sonic.

Using a photo editing software I drew a line in the middle of the photo (see Figure 3.11) and I searched on Google Earth the matching position. I did this procedure for each direction, and I have obtained four displacement angles between the true cardinal points.

The average of the correction is 6.04° and the associated uncertainty is about 2°. The meaning of this angle is that the sonic looks 6.04° on the right of the true geographical North. I inserted this correction into EdiRe processing calculations (see Chapter 4).

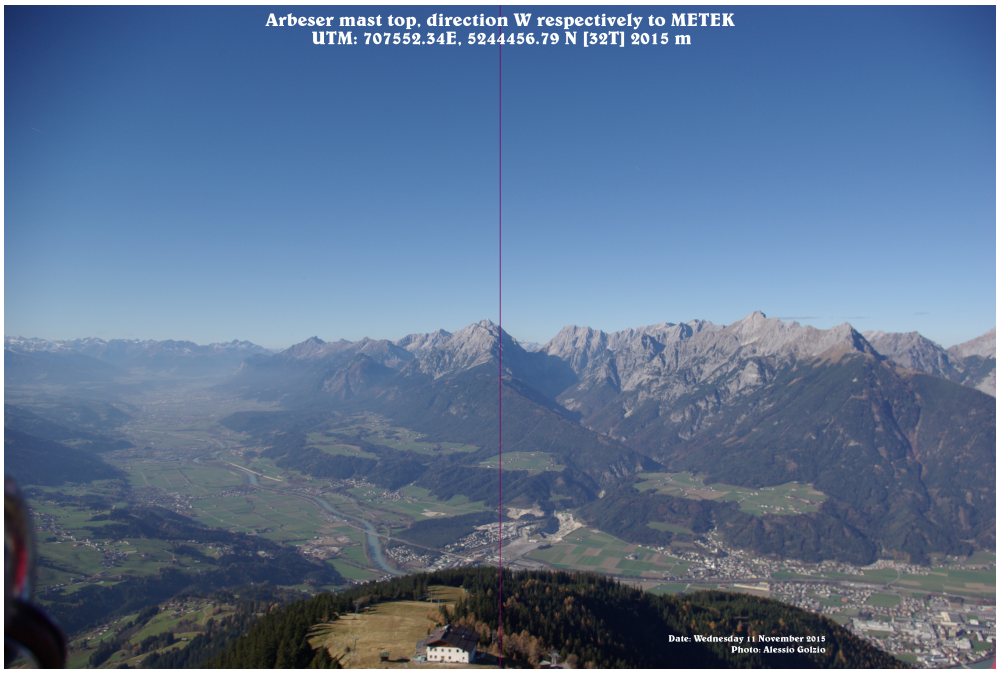

Figure 3.11: The view from the mast top in direction west. The purple line indicates the west direction relative to the sonic, using this point of reference and also other three directions (north, south and east) relative to the anemometer I calculated the true north orientation of the uSonic3 instrument.

Principle of the Krypton Hygrometer

The fast response hygrometer used in Arbeser station is a KH20, the name comes from $K - H_2O$. It uses a Krypton lamp that emits two absorption lines: major line at 123.58 nm and minor line at 116.49 nm (see Figure 3.12). Both of them are absorbed by water vapour and the minor line partly by oxygen.

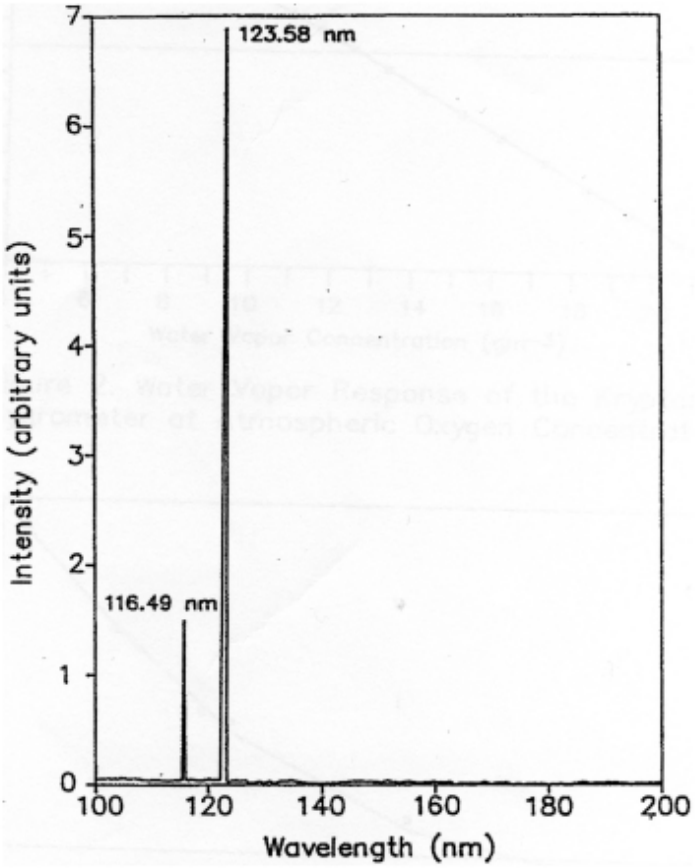

Figure 3.12: Krypton lamp spectrum. From Campbell and Tanner, 1985, Courtesy Scientific Services, Rocky Hill, (NJ)

The Lambert-Beer's law governs the operating principle of this type of hygrometers (Campbell and Tanner, 1985 [6])

$$I = I_0 \exp(-qkx) \tag{3.16}$$

with the light intensity at the receiver I and of the lamp I_0, the absolute humidity q, the absorption coefficient k and the path length between lamp and receiver x.

As I said the KH20 has two emission wavelength, thus the Equation (3.16) become (Foken and Falke, 2012 [10])

$$I = I_{01} \exp[-x(k_{w1}q_1 + k_{o1}\rho_{o1})] + I_{02} \exp[-x(k_{w2}q_2 + k_{o2}\rho_{o2})] \tag{3.17}$$

where the indices 1 and 2 indicate the two different absorption lines, "w" stays for water vapour and "o" for oxygen.

According to Tillman (1965) [47] the absorption coefficient in the short wavelength is half of that in the longer wavelength. Because of this, and because only the signal of these two wavelengths is measured, it is possible to combine both water vapour absorptions. For the oxygen absorption the fraction of band 1 is f and of band 2 is $(1 - f)$. It is possible to simplify Eq. (3.17) in

$$I = I_0 \exp(-xk_w q)\left[f \exp(-xk_{o1}\rho_{o1}) + (1 - f)\exp(-xk_{o2}\rho_{o2})\right] \tag{3.18}$$

For direct application, as also suggested by Campbell Scientific in the user manual of KH20, it is possible to further simplify this equation taking the logarithm and considering the ddp (V) measured by the instrument, that is proportional to the intensity of the light I

$$\ln V_q = \ln V_0 - xk_w q - xk_o\rho_o \tag{3.19}$$

It is possible to re-write Eq. (3.19) expressing the absolute humidity

$$q = -\frac{\ln V_q - \ln V_0}{xk_w} - \rho_o \frac{k_o}{k_w} \tag{3.20}$$

and neglecting the oxygen correction we get

$$q_m = -\frac{\ln V_q - \ln V_0}{xk_w} \tag{3.21}$$

The parameters included in Eq. (3.21) are obtained from the calibration of the instrument (Table 3.5).

From Eq. (3.21) we get the absolute humidity in g/m^3. In this equation the contribution of oxygen was neglected; for a correct measurement is necessary to adjust the value of q_m. Campbell Scientific assumes that the concentration of oxygen is constant with a value $C_o = 21\%$, and the density varies according to the perfect gas law

$$\rho_o = \frac{C_o M_o P}{RT} \tag{3.22}$$

Combining Equations (3.21) and (3.22) it is possible to write:

$$q = q_m - \frac{k_o C_o M_o P}{k_w RT} \tag{3.23}$$

where $k_o = -0.00714$ m^3/(g cm), and M_o is the molar mass of oxygen 32 g/mol. In Table 3.5 there are all the calibration constants for the KH20.

Scaled windows $x = 1.254$cm				
Vapour range	xk_w ln(mV)m^3/g	Constant V_0 ln(mV)	k_w ln(mV)m^3/(g cm)	Intercept mV
Full	-0.189	8.281	-0.151	3946
Dry	-0.204	8.354	-0.163	4247
Wet	-0.185	8.219	-0.147	3711
Clean windows				
Full	-0.189	8.608	-0.150	5475
Dry	-0.205	8.694	-0.163	5969
Wet	-0.181	8.504	-0.145	4934

Table 3.5: Calibration constants for KH20 serial number 1735. Vapour ranges for scaled windows: Full $1.79 \div 19.25$g/m^3, Dry $1.79 \div 9.31$g/m^3, Wet $8.08 \div 19.25$g/m^3. Vapour ranges for clean windows: Full $1.75 \div 19.28$g/m^3, Dry $1.75 \div 9.34$g/m^3, Wet $8.15 \div 19.28$g/m^3. Calibration date 11-09-2013.

Chapter 4

Data Analysis

4.1 Introduction

The first part of this work consists in an overview of all available data, that could be classified into two main groups, the data collected by high frequency sensors (sonic anemometer and Krypton hygrometer) and by low frequency sensors.

The completeness and data quality assessment will be discussed in this chapter, they are the basis for a reliable analysis and comment, that follow in Chapter 5. The data quality assessment is conducted following the same procedure of the others i-Box stations, even if Arbeser station has many difficulties due to the harsh environment.

4.2 Data Overview

4.2.1 Data Completeness

As I mention in the introduction of this chapter the first part consists in to ensuring data completeness. Firstly, the data availability has been checked (if the instrument was working or if it was stopped) than in a further analysis, the data quality has been evaluated.

In first instance we can say that the low frequency instruments work regularly, they are more stable and require less maintenance in comparison with the fast sensors that are more sophisticated and require higher power supply. As we see in the previous Chapter 3, the power supply for this station is entirely "green", with a fuel cell and a solar panel. The problem with a so energy-consuming instrumentation, due to ventilated devices and heating, is that sometimes blackout

occurs, and the data collection stops for some periods. Other times the technical staff decide to shut down some instruments, especially the energy-eater sonic anemometer, or only the heating or ventilation. In these cases the data collection proceeds, but the quality undoubtedly falls down. Surely the low frequency instrumentation, both for easiness and low power consumption, works better than the high frequency one.

The beginning of the work was to compare data stored in the raw storage and first-elaborated data. With first-elaborated data I refer to time-organised data, that for example cover half-hour or a whole day. Instead with raw data, directly sent from Arbeser by the data logger, I refer to random-time ending (or starting) files. The data logger tries to send data every half-hour, but sometimes the connection fails and then it tries later to resend the data. In this phase I have found some mistakes into data re-organisation (some periods were not generated in the time-organised files). Henceforth I will use only organised-data storage.

The first control on the completeness of high frequency data consists in a file-name control.

A typical raw high frequency file has the name:
`106_arbeser_hf_2016_01_18_1330.dat`, from this name is simple to retrieve year, month, day and also sending time. In this way I can have an approximative idea of how many periods were sent from the station to the institute. I repeat that this is only a qualitative procedure, but is useful to find discrepancies inside the storage.

In this way I learnt that from the 4th October 2014 to 20th April 2016 we have 18 days missing in raw data respect to calendar days. The analysis of the *iBoxfilecreator*[1] shows that the number of 30-minutes file is 21271 instead of 27072 as expected if the sensors worked without interruptions. Each day theoretically contains 48 half-hour files so complete days (48 files) are 417 (20016 files), days 70% complete (more than 33 files) are 24, days 50% complete (more than 24 files) are 4, days 25% complete (more than 12 files) are 4 and bad days (less than 12 files) are 16[2].

These statistics do not tell us if these files contain good data (or complete data), then the next step is to assess a first glance data completeness and quality control. This job can be done using some daily plots produced with a Phyton script. In Figure 4.1 you can see two days plot's. The first one is with the USA-1 sonic anemometer, the second one is with the uSonic3 sonic anemometer, and it

[1]The iBoxfilecreator is a software that creates time-organised files, for example thirty minutes or daily file. Every file created start on a full hour (e.g. 00.00 UTC or 21.30 UTC) or on a full day (e.g. midnight).

[2]This statistic values are updated to the 20th of April 2016.

Start Date	End Date	Number of days
2014.10.12	2014.10.21	10
2014.10.24	2014.12.26	3
2015.02.27	2015.03.02	4
2015.03.06	2015.03.29	24
2015.03.31	2015.03.31	1
2015.04.03	2015.05.14	42
2015.07.09	2015.08.28	51
2015.09.16	2015.09.23	8
2015.09.28	2015.11.26	59
2015.11.28	2015.11.30	3
2016.01.27	2016.02.03	8
2016.02.12	2016.02.23	12
2016.04.01	2016.05.03	33
2016.05.05	2016.05.10	6
2016.05.21	2016.05.21	1
	Total days	265

Table 4.1: Metek sonic anemometer days of available data. Update on 31st May 2016.

is possible to see that in this case there is a new channel called CQT, this is an on-line quality control value[3]. Looking at these plots it is easy to separate good data from bad data. In Table 4.1 there are all the sonic anemometer working days, whereas in Table 4.2 there are all KH20 hygrometer working days.

Tables 4.2 and 4.1 will be useful in the second part of the analysis where I talk about high frequency data. In the first part, instead, is interesting to see how good and how much low frequency data, or standard meteorological data, is present. For this purpose in the averaging program I built for each low frequency variable a quality control variable, that essentially is 1 when all data in the averaging period is present and falls linearly towards zero when one or more data is missing. Figure 4.2 shows us some of the quality variables for low frequency data. The station shut down only one time from 28th August 2015 to 9th September 2015.

In the following section I will talk about the quality assessment and treatment for low frequency and high frequency datasets.

[3]Later I will include the CQT in the "harsh flags".

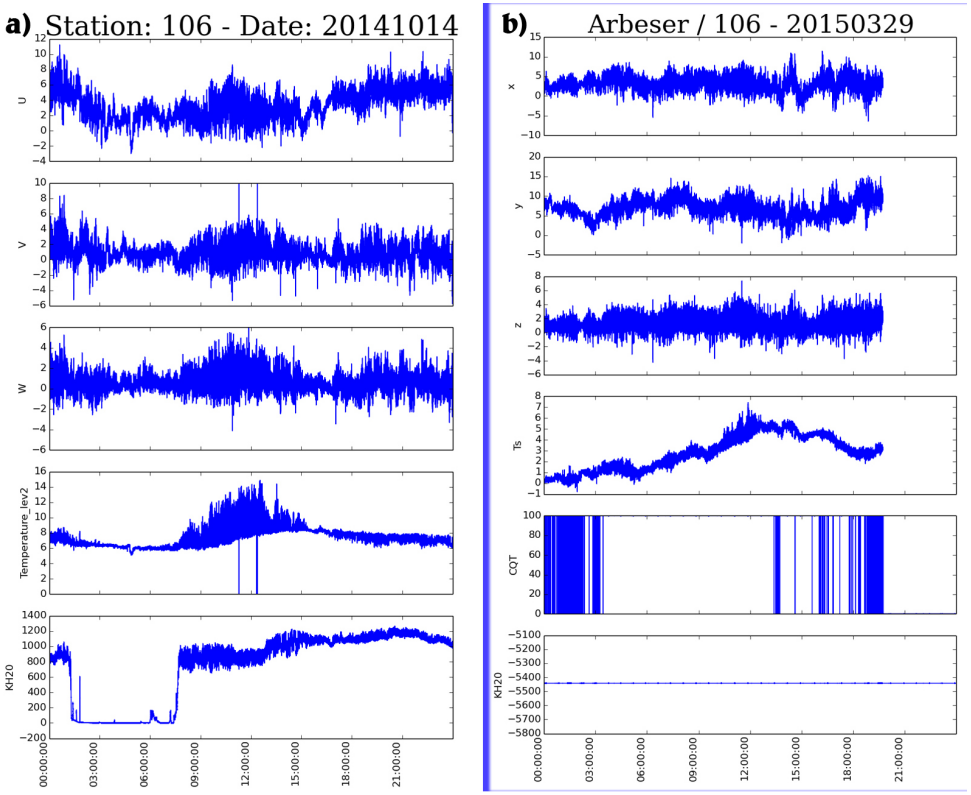

Figure 4.1: The daily before-analysis graphs in a) of 14th October 2014. In this case the sensors had been worked well both the sonic and Krypton hygrometer. In b) there is the 29th March 2015. In this case there is some problem at the end of the day, and also during the day with the quality flag frolicing up and down. The KH20 in this case does not working. In a) the plots are (bottom-down) u, v, w wind speeds, T_s sonic temperature and KH20 signal. In b) the plots are in the same order with after the T_s the CQT flag.

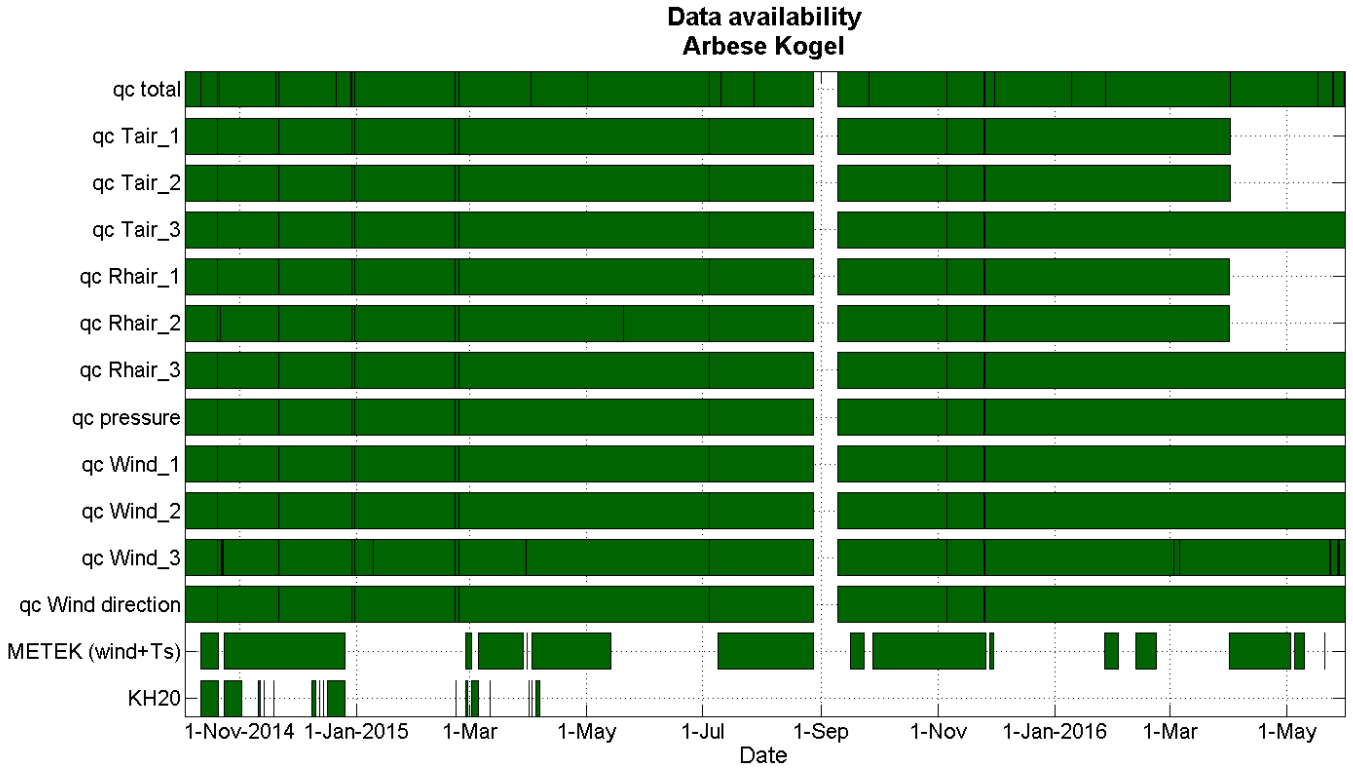

Figure 4.2: Time-line plot with some of the low frequency measured variables. The "qc_total" refers to all the variables measured not only these ones reported here. In the low part of this time-line plot we can see the Metek and KH20 available data. Data base from 2014.10.03 to 2016.05.31. When the day is complete of data the $qc = 1$, instead the qc falls linearly to 0. Green shading means that $qc = 1$, thus during this day the instrument had worked properly.

Start Date	End Date	Number of days
2014.10.12	2014.10.21	10
2014.10.24	2014.11.02	10
2014.11.11	2014.11.12	2
2014.11.14	2014.11.14	1
2014.11.19	2014.11.19	1
2014.12.09	2014.12.11	3
2014.12.13	2014.12.13	1
2014.12.15	2014.12.15	1
2014.12.17	2014.12.26	10
2015.02.22	2015.02.22	1
2015.02.27	2015.02.28	2
2015.03.02	2015.03.06	5
2015.03.12	2015.03.12	1
2015.04.01	2015.04.01	1
2015.04.03	2015.04.03	1
2015.04.05	2015.04.07	3
	Total days	53

Table 4.2: Krypton hygrometer KH20 days of available data. Update on 31st May 2016.

4.3 Low Frequency Data

4.3.1 Introduction

Standard meteorological data is stored in a TOA5 ASCII file format. This file format is typical of Campbell data logger; the first line is a header with the key word `TOA5` at the beginning, followed by some specifications of the station, second and third header lines contain variables names and units, the fourth line contains some specification such as `Avg` that means *average*.

This data are stored every one minute, instruments collect more data than one per minute, then the data logger evaluates a mean value and saves it in the low frequency table. In Table 4.3 all the variable stored by the data logger are summarised.

As we can see from Table 4.3, some variables are one minute averages ("Avg"), because the instrument sends more than one measurement by minute, then the data logger evaluates an average and writes it on the low frequency file. Some

Variable name	Units	Avg	Details
TIMESTAMP			Date and time written by CR3000
RECORD			Record number
TAact_1m_Avg	°C	yes	First level temperature
TAact_2m_Avg	°C	yes	Second level temperature
TAact_3m_Avg	°C	yes	Third level temperature
RHact_1m_Avg	%	yes	First level relative humidity
RHact_2m_Avg	%	yes	Second level relative humidity
RHact_3m_Avg	%	yes	Third level relative humidity
TPT100act_3m_Avg	°C	yes	PT100 temperature 3rd level
Pact	hPa	no	Air pressure
panel_temp_Avg	°C	yes	CR3000 temperature
batt_volt_Avg	V	yes	Battery voltage input at CR3000
SW_in_Avg	mV	yes	Short wave incoming radiation
SW_out_Avg	mV	yes	Short wave outgoing radiation
LW_in_Avg	mV	yes	Long wave incoming radiation
LW_out_Avg	mV	yes	Long wave outgoing radiation
cnr4_T_C_Avg	°C	yes	Radiometer temperature
WS_1_Avg	m/s	yes	First level cup anemometer
WS_2_Avg	m/s	yes	Second level cup anemometer
WS_3_Avg	m/s	yes	Third level cup anemometer
WS_Young_Avg	m/s	yes	Young wind speed
Wdir_Young_Avg	°	yes	Young wind direction
WS_Young_WVc(1)	m/s	no	Young raw wind speed
WS_Young_WVc(2)	°	no	Young raw wind direction
WS_Young_WVc(3)	*NA*	no	Correction factor to wind direction
Soil_107_1	°C	no	Ground temperature 1
Soil_107_2	°C	no	Ground temperature 2
Soil_107_3	°C	no	Ground temperature 3
Soil_HF_Avg	W/m^2	yes	Soil heat flux
Snow_Depth	m	no	Snow height
Raw_Dist	m	no	Distance snow sensor-ground
SignalQuality	value	no	Snow sensor signal quality

Table 4.3: Low frequency variables table from CR3000. The first column is the variable name, the second the physical unit, the third one state if the value comes from more measurements average during one minute (yes), or (no) whether the variable is measured only in the exact time of "TIMESTAMP".

Variable	Unit	Lower limit	Upper limit
Air temperature	°C	−40	+50
Air humidity	%	0	100
Wind direction	°	0	360
Wind speed	m/s	0	50
SW↑	W/m^2	0	2000
SW↓	W/m^2	0	2000
LW↑	W/m^2	0	*NA*
LW↓	W/m^2	0	*NA*
Net SW	W/m^2	0	*NA*
Net LW	W/m^2	−250	250

Table 4.4: Physical limits applied to meteorological data, most of those came from the instrument's range. Regards to humidity values grater than 100% but less than 110% are rewritten as 100%; values grater than 110% are considered wrong and substituted with NaN.

variables, such as soil temperatures, snow height and air pressure, are measured in the same moment when they are written on the output file. This happens for two reasons: the instrument is not fast enough to produce more than one data per minute; the measured quantity is not fast-changing (air pressure is the best example), then it is useless to evaluate a one-minute average.

I have written the function `read_toa5.m` that performs the reading (see B.2).

4.3.2 Preliminary Quality Control

The first treatment done on meteorological data is the quality control with "physical bound condition". Sometimes the instruments produce bad data for several reasons, first above all for a breakdown of the sensor, other times the reason might be a interference with radio waves, problems with the electronic part, problems with the data logger (that save wrong data), and so on.

In this preliminaries it is necessary to convert some output variables into physical quantities. This is the case of radiometer output, given in mV, that is possible to convert in W/m^2 with equation in Section 3.3.1 (at page 68).

In Table 4.4 it is possible to see the boundary condition imposed to each variable.

Conducting a deeper analysis on standard deviation distribution it is possible to refine this quality control. In particular imposing an upper limit for the stan-

dard deviation under which we can find the 99.5% of data, we can remove the remaining 0.5% composed by out-of-bounds averages. This operation is awkward, because I do not know what is the reason for such bigger standard deviations. In the most of the cases they derive from non-stable conditions during the half-hour averaging period, a clear example is the transit of a cloud during a partially cloudy day, in this case the shadow of the cloud causes a fast decrease in short wave incoming radiation, the air temperature falls down and it is also possible to appreciate a variation in relative humidity. If the cloud passage is within the half-hour period, I get an average associated with a relatively high standard deviation. In some cases this average is representative of the period (when the linear regression of data contained in the period is flat), in other cases the average could be less representative. This is a first glance correction, with more sophisticate statistical methods it is possible to improve the correction.

4.3.3 Averaging Data

The script that I used for the low frequency data analysis is "`lf_analyzer.m`", useful to evaluate the 30 minutes averages (according to the averaging time chosen for high frequency data). It has been also used for a first analysis and also for provide an input to EdiRe for its analysis.

The averaging system was developed from a basis file written by Stiperski for the other i-Box stations. The main improvement that I have inserted is the flexible averaging period. The previous program, when there is not a full start date (e.g. 13th October 2014, 14:00 UTC) while the following minute (e.g. 14:01 UTC) is available, it immediately jumps to the next averaging cluster (14:30), then it looses a huge quantity of data. In order to prevent that problem, this script moves forward the starting time, and also moves backward the ending time, until an available data is found. In this way it is possible to evaluate much more averages, but these are with less data. The problem is solved with a quality variable associated to each variable and to each averaging period.

In the meanwhile that the averages are computed I also convert temperature into potential temperature. The potential temperature is the temperature that the air parcel would acquire if adiabatically brought to a standard reference pressure level $P_0 = 1000$ hPa

$$\theta = T\left(\frac{P_0}{P}\right)^{R/c_p} \tag{4.1}$$

where the temperature T is expressed in Kelvin.

After the averages calculation the function "`profile_arb.m`" organises the data into multidimensional matrices which have the days on the rows, on the

columns the *periods* and on the third dimension any variable.

The *periods* are the half-hour time clusters used previously for averages, the associated time is relative to the midpoint of the period. As an example if I have evaluated the average of data spanning from 14.00 UTC to 14:30 UTC the time associated is 14:15 UTC. The purpose of this organisation is to easily plot and analyse daily profiles.

4.3.4 Data classification

The next step in the analysis of meteorological data is the separation in classes, following several methods. The main idea is to find some days where simple weather conditions occur.

I choose different ways to separate the data pool, the purpose remains the same: separate *thermally driven* days from *dynamically driven* days.

First of all I have to clarify what is a thermally driven or a dynamically driven day. In the first chapter about the atmospheric boundary layer it is explained that the circulation in a valley is mainly driven by radiation (energy) and by synoptic conditions. Usually it is not easy to distinguish between these two different driving forces, because they are intrinsically linked. In fact the radiation, the incoming energy from the sun, is the main forcing for atmospheric motion. We have to make a distinction on the scale of the phenomena (see Fig. 1.4), between the global circulation, with fronts, ridges and though, and the local circulation, with valley-plain winds, slope winds and so on.

A thermally driven flow is always possible if the sun is shining, because it is related to local buoyancy, it is the slope and valley circulation. The dynamically driven flow is instead related to the pressure field over a huge area, for example central Europe.

After this introductory explanation, I am able to list the basic requirements for a thermally driven day[4]:

[4]Before this definitive and more trustworthy classification, I tried another approach on which I spent plenty of time. This first classification was based on the detection of dry days, hence days without rain. Finding these days was quite complicate, because a rain gauge is not installed at Arbeser, I start selecting the relative humidity in three categories: "dry days" with $RH < 80\%$ on all three levels; "middle days" with $80\% < RH < 92\%$; "rainy days" with $RH > 92\%$. This classification was enhanced using an algorithm to find if the short wave incoming radiation had been a Gaussian-shape.

This method completely failed, in fact the solar radiation has not a Gaussian-shape, and also some days with a uniform cloudiness (high-medium not so thick clouds) have the same shape as a clear day, but with a lower irradiance. This was the main problem, but some good idea already implemented in this classification, such as the pressure subdivision, have been kept in

1. A synoptic situation with low pressure gradients, on long and short-range.
2. A clear day, with no or very scattered clouds, in this way we have a homogeneous distribution of energy on the ground and the only complication comes from the complex terrain, thus the valley and slope flows can grow-up.
3. A valley wind pattern. This is a more fine requirement; to check for this condition I will analyse the wind speed and direction at the core site CS-VF0 Kolsass.

Surface Pressure Gradients

In this classification the first aim is to distinguish between different synoptic and local situations. As previously said a thermally driven day needs a flat surface pressure field, then the best situation is an high pressure on the entire central Europe. In order to check this, four barometric stations were chosen: Torino Bric della Croce (709 m a.s.l. code 16061), Bolzano Airport (239 m a.s.l. code 16020), Innsbruck Airport (579 m a.s.l. code 11120) and München Airport (453 m a.s.l. code 10870). The data comes from the ECMWF initial condition tables at 00 UTC, thus one measurement per day is available. The gradients were always evaluated in this way

$$\Delta p = p_{North\ station} - p_{South\ station} \tag{4.2}$$

For each day four different gradients are considered:

1. München-Torino
2. München-Innsbruck
3. Innsbruck-Torino
4. Innsbruck-Bolzano

as you can see pressure at Bolzano was only compared with Innsbruck, this because from the experience of Innsbruck's meteorologists the south Föhn (coming from the Wipp Valley) is mostly verified with a pressure gap of 500 Pa, or greater, between the two cities.

Starting from this experience knowledge and from the theory of valley wind pressure gradients (Markowski and Richardson, 2010 [25]), the thresholds set are reported in Table 4.5.

the classification adopted.

Stations	Low [Pa]	High [Pa]
MU-TO	400	700
MU-IBK	300	500
IBK-TO	400	700
IBK-BZ	300	500

Table 4.5: The thresholds chosen for the pressure differences across the Alpine Arch. MU München, TO Torino, IBK Innsbruck, BZ Bolzano.

I have used the mentioned thresholds to identify four pressure classes, that I have called P1, P2, P3 and P4. These classes satisfy the following inequalities (with respect to the values given in Table 4.5):

P1 all pressure gradients are *lower than* the low threshold;

P2 all pressure gradients are *greater than* low threshold and *lower than* high threshold;

P3 all pressure gradients are *greater than* high threshold;

P4 everything not included in previous categories, then with mixed levels (span in different threshold gaps) or without the pressure data.

Clear Sky Days

The detection of clear sky days is the crucial point in this classification. I perform this part using different methods: the most important, previously mentioned in Chapter 1, is the Clear-Sky Index, flanked by a standard deviation method and the maximum irradiance method. Later I will describe all these methods.

I start to present the Clear-Sky Index. It was introduced by Marty and Philipona in their article "The Clear-Sky Index to separate Clear-Sky from Cloudy-Sky situations in climate research" (2000 [27]), and also Marty *et al.* (2002 [26]).

The CSI is calculated starting from long wave incoming radiation, and this is the main strength of the Clear-Sky index, because it is possible to calculate this index also during the night. The basis principle of this index consists in the different emissions of long wave radiation from the sky. In fact if the sky is overcast the long wave (IR) from the Earth is trapped by the water vapour contained in the clouds and then re-emitted downward. Instead if the sky is cloudless the long wave incoming radiation is rather small.

Thus, thinking the sky as a grey body, it is possible to write the *apparent emittance*

$$\varepsilon_A = \frac{LW\downarrow}{\sigma T_a^4} \tag{4.3}$$

this variable tends to unity the more the sky is overcast.

The next step is to introduce the *clear sky apparent emittance*, this can be accurately calculated when the temperature and the humidity profiles of the atmosphere above the station are known, but in my case (and in most others) I wish to use a simplification considering only one level of temperature and humidity (the second of Arbeser station, because is the closest to standard meteorological observations level).

The Brutsaert formula (1975 [5]) is judged by Marty and Philipona to the best one

$$\varepsilon_{AC} = k\left(\frac{e_a}{T_a}\right)^{1/7} \tag{4.4}$$

where k is a location dependent constant, for Arbeser I found $k = 0.433$ analysing some clear-sky days; e_a is water vapour pressure in Pa ("a" means air) and T_a is the air temperature[5].

This is not the final formula, in fact it does not consider all the major greenhouse gasses other than water vapour. Thus an altitude dependent clear-sky emittance of a completely dry atmosphere ε_{AD} has been introduced. Then the Eq. (4.4) revised is

$$\varepsilon_{AC} = \varepsilon_{AD} + k\left(\frac{e_a}{T_a}\right)^{1/8}. \tag{4.7}$$

It is immediately evident that the exponent of (4.7) has changed from 1/7 to 1/8, this because Marty and Philipona found that this exponent best corrects for mountain stations (ASRB project).

[5]The water vapour pressure was obtained starting from the relative humidity measured at the second level. The relative humidity is related with vapour pressure with this equation

$$e_a = \frac{RH}{100} e_{sat} \tag{4.5}$$

where e_{sat} is the saturation vapour pressure for the temperature T_a in Celsius

$$e_{sat} = \begin{cases} 6.1078 \exp\left(\frac{17.269388 T_a}{T_a + 237.29}\right) & \text{if } T_a \geq 0, \\ 6.1078 \exp\left(\frac{21.8745584 T_a}{T_a + 265.49}\right) & \text{if } T_a < 0. \end{cases} \tag{4.6}$$

the vapour pressure e_a and the saturation vapour pressure e_{sat} are in hPa.

At the end the Clear-Sky index can be written as

$$CSI = \frac{\varepsilon_A}{\varepsilon_{AC}} \tag{4.8}$$

if it is less or equal to 1 the sky is cloudless (clear-sky conditions).

Thanks to the ARAD database (Olefs *et al.*, 2016 [33]) I was able to include directly and high quality estimation of the Clear-Sky index measured in Innsbruck (University roof). This contributes as a high quality control on the CSI calculated at Arbeser station.

Together with the CSI, for a better estimation of clear days, I considered also the standard deviation of incoming short wave radiation. Two threshold levels were set after a brief analysis on some clear and cloudy days (see Table 4.6).

Quality	$\sigma_{SW\downarrow}$ Level
Best	$\leq 20 \mathrm{W/m^2}$
Good	$\leq 40 \mathrm{W/m^2}$
Bad	$> 40 \mathrm{W/m^2}$

Table 4.6: Threshold levels for standard deviation of SW incoming radiation in clear-sky assessment.

The third method involved in the clear-sky detection consists in a control of the average incoming short wave radiation for the analysed day. From Section 1.4.1 is known, that the incoming solar radiation can be evaluated at the top of atmosphere on the basis of astronomical parameters, and then corrected for the transmissivity of the atmosphere. This gives the maximum available radiation for the position and altitude of the station.

Combining these three methods: the evaluation of CSI, standard deviation and available radiation, I can identify all the clear-sky days. In my analysis a clear-sky day, is a day with 90% of the periods with clear-sky, and that give a good level of reliability (standard deviation of SW incoming radiation less than 40 $\mathrm{W/m^2}$ and the day mean SW incoming radiation matching the theoretically evaluated one with astronomical calculations).

Valley Wind Regime

The previous two sections describe firstly how to find the weak pressure gradient days (class P1), and secondly how to find the clear days. Intersecting these two groups it is possible to obtain the *thermally driven days*. Instead considering class

P3 (strong pressure gradients) in clear days, it is possible to obtain the *dynamically driven days*, that can be Föhn days (especially south Föhn) or immediately before a frontal passage.

I focusing my attention on clear and weak pressure gradient days (called in Chapter 5 "P1-CSD"), and I can add another parameter to refine the classification of *thermally driven days*: the valley wind.

As reported in Section 1.8, in a valley there is a "normal" wind regime. This regime has during the night a down-valley wind in the center of the valley, and an up-valley wind during the daytime. In my case the Inn Valley, where the experiment is settled, has an orientation NE-SW, thus a "normal" afternoon valley wind for a thermally driven day is from east-north-east at the valley floor station Kolsass.

The amplitude of the up-valley wind sector is $40° \div 130°$ and the time of up-valley wind regime is between 13:00 and 20:00 UTC. While the down-valley wind sector is $220° \div 310°$.

4.4 High Frequency Data

4.4.1 Introduction

In this section I will talk about the assimilation and analysis of high frequency data, thus from the sonic and from the Krypton hygrometer. The high frequency data analysis was done with two softwares: EdiRe as first step and Matlab for unify the analyses of high and low frequency dataset.

First I will introduce the data treatment with EdiRe, later I will move on to data quality assurance done with Matlab.

4.4.2 Eddy Covariance Analysis

Arbeser data are stored in binary files created by the Campbell Scientific data logger CR3000. It is not possible to directly analyse them, especially with a standard personal computer, and so it is not useful to take every data at the high frequency rate (20Hz that is one data point every 0.05s).

The approach is the Eddy Covariance Method (see Section 1.10), where I choose an averaging interval that covers approximately the whole turbulence spectrum, from the largest eddies to the Kolmogorov's scale. The time interval from which the software EdiRe (v.1.5.0.32 Clement and Moncreif, 2007 [8]) calculates

covariances, averages and fluxes was set to 30 minutes[6], and it assigns a time stamp in the middle of this interval. For example if the starting time is 18:00 UTC and the end time is 18:30 UTC the assigned time is 18:15 UTC. I did the same thing with the low frequency data averages.

In Appendix B.3 you can read the entire processing list, or in other words what I ask EdiRe to do.

The process and format list used are summarised in Table 4.7, with all the periods analysed.

In this section I explain better the high frequency binary file processing with this software.

There is a relevant difference between Arbeser analysis and other i-Box stations analysed up to now. At other i-Box sites a high-pass recursive filter (with length of 200 s) was applied on the time interval before averaging (Stiperski and Rotach, 2016 [43]). The aim is to de-trend the time interval and possibly to avoid the influence, e.g., of gravity waves that invalidate the arithmetic mean. In Arbeser I decided to make a different choice: I use the Block Averaging (normal arithmetic mean). That for a very complex site may be advantageous, but it should be tested in comparison with the filtered data.

Data Extraction, Spike Removal and First Controls

The extraction from binary files is done on the shape given by the "format list", this list can be found from EdiRe on a sample file. In my case I have three different format lists: two for the first sonic data (USA-1) and one for the latter sonic (uSonic3). The first two differ on one channel that was moved in a different position.

Since when the uSonic3 anemometer was installed a new variable is saved in high frequency tables: the CQT, a quality control variable of the sonic itself. The CQT value considerably help in the estimation of good and bad operating status of the sonic, in fact in some case only looking at the data may conducts to a misunderstanding and to think that it is well enough, but for example the sonic has some time delay, transducers covered by water (rain or snow, the case of snow produce totally nonsense data) and so on. In these cases the CQT is zero, otherwise it is 100.

The first operation on high frequency data done with EdiRe is the spike removal, or in other words the removal of occasionally bad (very high or low) data, that would invalidate the averages and all the following calculations. The *despike*

[6]This time interval is variable, but the i-Box default averaging time is 30 minutes.

Out file	Initial date	End date	Processing list	Format list
201410	2014.10.12	2014.10.31	Proc1	Format1
201411-1	2014.11.01	2014.11.18	Proc1	Format2
201411-2	2014.11.19	2014.11.30	Proc2	Format1
201412	2014.12.03	2014.12.26	Proc1	Format2
201503	2015.03.01	2015.03.31	Proc3	Format3
201504	2015.04.01	2015.04.30	Proc3	Format3
201505	2015.05.01	2015.05.31	Proc3	Format3
201506	2015.06.01	2015.06.30	Proc3	Format3
201507	2015.07.01	2015.07.31	Proc3	Format3
201508	2015.08.01	2015.08.28	Proc3	Format3
201509	2015.09.09	2015.09.30	Proc3	Format3
201510	2015.10.01	2015.10.31	Proc3	Format3
201511	2015.11.01	2015.11.30	Proc3	Format3
201602	2016.02.01	2016.02.29	Proc3	Format3
201604	2016.04.01	2016.04.30	Proc3	Format3

Table 4.7: The analysed output file by EdiRe, their name starts with the date (showed in the first column of the table), and concludes with `_Arbeser_106.csv`.
Files legend:
Proc1 = `Proc_106_arbeser_USA1-1_final.txt`;
Proc2 = `Proc_106_arbeser_USA1-2_final.txt`;
Proc3 = `Proc_106_arbeser_uSonic3_final.txt`;
Format1 = `Format_106_arbeser_USA1_1.txt`;
Format2 = `Format_106_arbeser_USA1_2.txt`;
Format3 = `Format_106_arbeser_uSonic3.txt`.

function (from row 94 in B.3) is applied directly on signal *u, v, w, T, q* and evaluate if the selected value is out of 10 standard deviations, the σ is evaluated on neighbour data points. If the spike is larger than 4 data points it is not detected. I have applied the *despike* also on CQT, because if only one point is bad the mean of CQT starts to decrease, and since I use this mean value to assess the goodness of average periods, I need that this CQT smoothly varies.

After the *despike* controls I set a series of statistical quality control variables that count per each half hour interval how many bad points are present. The threshold levels are the same as the high frequency data quality assurance (see later Section 4.4.3).

In this part the process list has a quality control on the KH20 output. In particular if the signal is under 5mV, the signal is bad, and the variable QC_Q is set to 1 at the end of the calculations.

Sonic Temperature Corrections

The sonic temperature, as stated before, needs a correction for the cross wind and for the pressure and humidity fluctuations. Some of those are already introduced in Section 3.3.2, and they are done following Clement (2004) [9] and Liu *et al.* (2001) [24]. Here I only summarise the corrections and I write the formulas used by the program, these equations are slightly different from the internal subroutine of EdiRe.

The correction for the *cross wind* on sonic temperature T_s is

$$T_{sc} = \left[(T_s + 273.15) + \frac{3}{4\gamma_d R_d}(u^2 + v^2) \right] - 273.15 \tag{4.9}$$

where $\gamma_d R_d = 403$ m^{2}s^{-2}K^{-1}, and u, v are the raw wind speed in the reference system of the sonic anemometer.

The second correction is on the standard deviation of sonic temperature, done using a simplification of Equation (3.14) by Liu *et al.* (2001). First there is the evaluation of moist air density (ρ_m) using the water vapour pressure e_a

$$\rho_m = \frac{(p - 0.38e_a)}{0.28704(T_{air} + 273.15)} \quad [\text{g/m}^3] \tag{4.10}$$

where $R_a = 0.28704$ Jg^{-1}K^{-1} is the gas constant for the air.

Using this, and some covariances of the specific humidity[7], I can calculate the

[7] If the Krypton lamp does not work, this correction works only partially, thus the specific humidity correction is not applied.

correction for the standard deviation of T_{sc}

$$\sigma_{T_{sc}} = \sqrt{\left|\sigma_{T_s}^2 - 1.02(T_{air} + 273.15)\frac{\overline{q'\theta'}}{\rho_m} - 0.51^2\frac{\overline{q'^2}(T_{air} + 273.15)^2}{\rho_m^2}\right|}. \quad (4.11)$$

Coordinate Rotation

The coordinate rotation applied is the *double rotation* (DR). The algorithm aims is to set the reference system in a streamline coordinate system, with $\overline{v} = \overline{w} = 0$ (Kaimal and Finnigan, 1994 [22], Wilczak *et al.*, 2001 [54], Cassardo *et al.*, 1995 [7]). The sonic acquires data in its reference system, in theory this reference system (SR) is according to Earth geographic coordinates, with the velocity parallel to the main cardinal directions and vertical speed normal to the geoid. The DR rotates the sonic SR into a new one parallel to the streamlines. Thus there are two rotation angles applied, the first is called α and it is

$$\alpha = \arctan\frac{\overline{v}}{\overline{u}} \quad (4.12)$$

where $\overline{u}$, $\overline{v}$ and $\overline{w}$ are mean wind speed in sonic SR.

The first rotation is in the plane XY, and with this one the $\overline{v_1} = 0$. The first rotation matrix is

$$C = \begin{pmatrix} \cos\alpha & \sin\alpha & 0 \\ -\sin\alpha & \cos\alpha & 0 \\ 0 & 0 & 1 \end{pmatrix} \quad (4.13)$$

After the first rotation the velocity still has two components, one in x and one in z. The second rotation, keeps the Y_1-axis fixed, and the angle in the plane X_1Z is

$$\beta = \arctan\frac{\overline{w}}{\sqrt{\overline{u}^2 + \overline{v}^2}} \quad (4.14)$$

and the second rotation matrix is

$$D = \begin{pmatrix} \cos\beta & 0 & \sin\beta \\ 0 & 1 & 0 \\ -\sin\beta & 0 & \cos\beta \end{pmatrix} \quad (4.15)$$

In Figure 4.3 a sketch of these two rotations are presented.

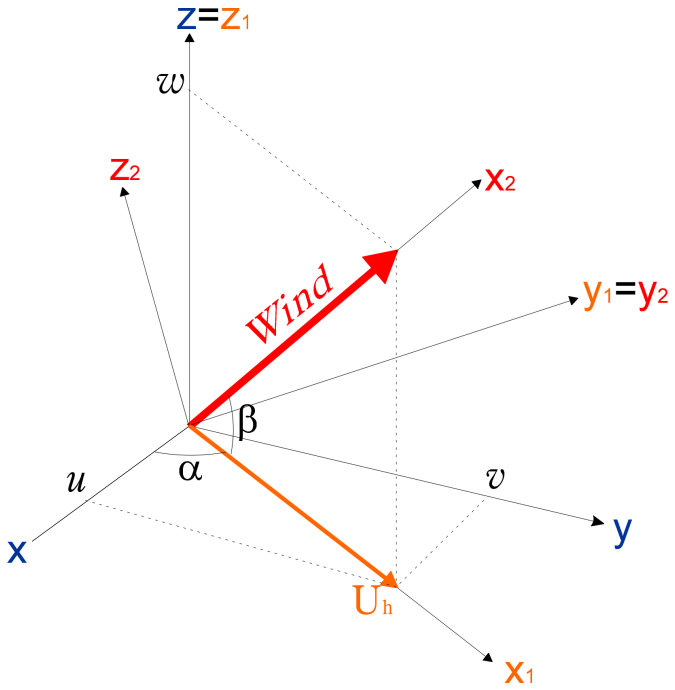

Figure 4.3: Double rotation angles. The red arrow is the wind direction for averaged period, and xyz is the sonic anemometer reference system. The first angle, α, rotates xyz into $x_1y_1z_1$ (written in orange), after this rotation the wind component on the y_1-axis is zero (thus $v_1 = 0$). The second angle, β, rotates $x_1y_1z_1$ into $x_2y_2z_2$ and also the w_2 is nullified. From Cassardo *et al.*, 1995 [7] redrawn by the author.

Moment Calculation and Covariances

After the double rotation and the first correction on temperature EdiRe evaluates block averages, standard deviations, skewness, kurtosis, variances and covariance.

The mean is, as previously said, the block average without filtering the data.

The standard deviation is

$$\sigma_x = \sqrt{\frac{\sum \left(x'(n)^2\right)}{n}} \tag{4.16}$$

where the x' is the fluctuation with respect to the mean (see Reynolds decomposition Eq. (1.34)).

The skewness is

$$\frac{m_3}{\sigma^3} = \frac{\frac{\sum\left(x'(n)^3\right)}{n}}{\sigma_x^3}. \tag{4.17}$$

The kurtosis is

$$\gamma_2 = \frac{m_4}{\sigma^4} - 3 = \frac{\frac{\sum\left(x'(n)^4\right)}{n}}{\sigma_x^4} - 3. \tag{4.18}$$

The covariance between two variables x and y is

$$\overline{x'y'} = \sqrt{\frac{\sum_{i=1}^{n} xy(n)}{n} - (\overline{x}\,\overline{y})} \tag{4.19}$$

where $\overline{x}$ and $\overline{y}$ are the variable's averages and $xy(n) = x(n) \cdot y(n)$ is the product point to point of the two variables (each one has n values).

Frequency Response Corrections

During measurements, a real instrument miss some part of the turbulence spectra, usually the sonic looses the high frequency part, or the smallest eddies. Instead the low frequency losses regards bigger eddies that are not registered because a fixed averaging period have been chosen. Sometimes this period is long enough, but sometimes not, and thus a part of the spectra is lost. For knowing the real amount of fluxes and variances a correction for this frequency loss is needed. EdiRe applies a model to evaluate the theoretical spectra of the input data, and then evaluates the combination between the model and the real data and finds the spectral part losses.

Heat Flux Correction

For the same reason of sonic temperature, the sensible heat flux has to be corrected for the cross wind (already included in the sonic temperature correction) and for the humidity, and also for the cross dependences of these values.

The correction applied to the sensible heat flux is (following Liu *et al.*, 2001 [24], Kaimal and Gaynor, 1991 [23] and Clement, 2004 [9])

$$\begin{aligned}(w'T_s')_{corr} =& (\overline{w'T_{sc}'}) - 0.32(\overline{w'q'})_{corr}(T_{air} + 273.15)\frac{8.314472T_{air}}{18.01p} + \\ & \frac{3}{2}\frac{(T_{air} + 273.15)(\overline{u'w'})_{fc}\overline{U}}{(T_{sc} + 273.15)\gamma_d R_d}\end{aligned} \tag{4.20}$$

where $\chi = \varepsilon\eta = 0.32$ with $\eta = 0.51$ and $\varepsilon = m_v/m_d = 0.622$, p is the air pressure in Pa, $m_v = 18.0$ g/mol is the molar mass of water, $(\overline{u'w'})_{fc}$ is the momentum flux corrected for the frequency loss.

For the latent heat flux, is needed a correction on the oxygen content of the air sample measured by the Krypton lamp

$$LE_{cor} = LE_{fc} - LH\frac{0.0045 \cdot 0.2095 \cdot 32p}{-0.151 \cdot 0.008314(T_{air} + 273.15)^2}(\overline{w'T'_s})_{corr} \tag{4.21}$$

where:

p is in kPa,

0.2095 is the relative presence of Oxygen in the atmosphere,

$k_O = 0.0045$ is the Oxygen absorption effect coefficient,

$k_w = -0.151\,\ln(\text{mV})\text{m}^3\text{g}^{-1}\text{cm}^{-1}$ is the correction coefficient for the water content (see Table 3.5),

LH is the latent heat of evaporation and it is the coefficient that multiplied for the flux $\overline{w'q'}$ gives the latent heat flux.

$$LH = 2500.25 - 2.365\left(\frac{240.97\ln\left(\frac{e_a}{6.1121}\right)}{17.52 - \ln\left(\frac{e_a}{6.1121}\right)}\right) \tag{4.22}$$

Webb Pearman and Leuning Correction

This is the correction on the latent heat flux due to flux of water vapour that influences the measure of the specific humidity. The main reference, as you can see from the title, is Webb *et al.* (1980)[51]. When the turbulent flux of any constituent, in my case the specific humidity, is measured by either the eddy covariance or the mean gradient technique, account may need to be taken of the simultaneous flux of any entity - in particular, heat or water vapour - which causes expansion of the air and thus affects the constituent's density [51].

Webb *et al.* focus their attention on vertical fluxes through the surface layer, and the frame of this master Thesis is the near-surface turbulence. The main problem is that when we consider a measurement that include the fluctuation of a minor constituent C, we need to correct the vertical heat flux by the density fluctuation due to C. The most important part that I must consider is the water

vapour fluctuation, that changes the density of the air and consequently the value of the heat flux.

Here I skip all the introduction part of [51] and I move immediately to flux relationships. Webb *et al.* write the sensible heat flux divided in two parts, one dry and one moist

$$SH = c_{pa}\overline{w\rho_a(T - T_b)} + c_{pv}\overline{w\rho_v(T - T_b)}, \tag{4.23}$$

where T_b is taken as constant and assumed as an initial "base" temperature from which each element of air is warmed (or cooled) during the vertical motion. The terms c_{pa} is the specific heat at constant pressure for dry air, meanwhile c_{pv} is the specific heat at constant pressure for water vapour.

In this equation it is possible to replace some terms, using the relationships between temperatures, densities and specific heat

$$\begin{aligned} SH =& (c_{pa}\bar{\rho}_a + c_{pv}\bar{\rho}_v)\overline{w'T'} + c_{pv}\overline{w\rho_v}(\bar{T} - T_b) - \\ & - c_{pa}\frac{\bar{\rho}_a}{\bar{T}}(1 + \mu\sigma)\overline{wT'^2} + (c_{pv} - \mu c_{pa})\overline{w\rho_v' T'}. \end{aligned} \tag{4.24}$$

The first term on the r.h.s. of Equation (4.24) is dominant, and introducing the specific heat for moist air given by $c_p\bar{\rho} = c_{pa}\bar{\rho}_a + c_{pv}\bar{\rho}_v$, we have

$$SH = c_p\bar{\rho}\overline{w'T'} \tag{4.25}$$

that is the SH as usual. But now considering the flux as usual and the correction that arise from the fluxes of both water vapour and heat, the corrected LE is obtained as following

$$LE = \lambda(1 + \mu\sigma)\left(1 + \frac{\lambda}{c_p}\frac{\bar{\rho}_v}{\bar{\rho}\bar{T}}B_{raw}\right)LE_{raw} \tag{4.26}$$

where $\mu = m_a/m_v = 29.002/18.01$ is the ratio of dry air molar mass and water vapour molar mass, $\sigma = \bar{\rho}_v/\bar{\rho}_a$, λ is the latent heat of evaporation, $B_{raw} = SH/(\lambda E_{raw})$ is he uncorrected Bowen ratio.

Stationarity

The stationarity is a requirement that assesses the steady state of a subset of the dataset. A set of data in a steady state has the same turbulence configuration, that means that I am looking to the same eddy structure during the thirty minute average, and so the average state (variances, covariances, averages, and so on) are

the right representation of the period. If this period is not in a steady state the values that I assign and that I retrieve from this period are not well representative of the inside turbulence.

The stationarity, or the *steady state test* is done as following. The major *run*, that is thirty minutes long, is divided in j segments of 5 minutes each. The sample frequency is 20Hz, thus in 5 minutes there is 6000 points. EdiRe evaluates the covariance between the two variables involved for each segments, and also for the entire run. The covariances of each segment are averaged. Thus it is possible to obtain the level of stationarity (Aubinet *et al.*, 2012 [3])

$$RN_{cov} = \left| \frac{\overline{(x'y')_{SI}} - \overline{(x'y')_{WI}}}{\overline{(x'y')_{WI}}} \right| < 30\% \tag{4.27}$$

The limit imposed on this value (Foken and Wichura, 1996 [11]) is too small for truly complex terrain. I tried to relax the condition on stationarity and set the threshold to 40%. Later in Section 4.4.3 I will show the results of stationarity requirement applied on Arbeser data.

Wyngaard Uncertainties

Every measurements has an uncertainty, in the particular case of covariances and fluxes this strongly depends on the integrating interval. Wyngaard (1973) [55], assesses that uncertainty, correlating it with the integrating interval. In order to reduce the error, he suggests to consider all the turbulent spectra, from the biggest eddy to the smallest. The turbulence is variable and evolves in time, then sometimes is enough to integrate over 15 minutes, other times is necessary to wait for hours.

Wyngaard's relationships are used to find the optimal averaging time, aimed at minimising the uncertainties on fluxes (covariances) and variances. From Lumley and Panofsky (1964) Wyngaard takes the expression of the averaging time as follow

$$I \approx \frac{2\tau_i \overline{f'^2}}{a^2 \overline{f}^2} \tag{4.28}$$

where I is the averaging time required to determine $\overline{f}$ to an accuracy a. Meanwhile τ_i is the integral scale of the time function f. In local free convection (when the turbulence is well developed) Wyngaard expects $\tau_i \approx z/U$, thus the Equation (4.28) become

$$I \approx \frac{z}{Ua^2} \frac{\overline{f'^2}}{\overline{f}^2}. \tag{4.29}$$

If the covariances uw and $w\theta$ are considered, this becomes

$$\begin{aligned} I_{\overline{uw}} &\approx \frac{z}{a^2 U}\left[\frac{\overline{(u'w')^2} - \overline{(u'w')}^2}{\overline{(u'w')}^2}\right] = \frac{z}{a^2 U}\left[\frac{\overline{(u'w')^2}}{u_*^4} - 1\right] \\ I_{\overline{w\theta}} &\approx \frac{z}{a^2 U}\left[\frac{\overline{(u'\theta')^2}}{u_*^2 \Theta_*^2} - 1\right] \end{aligned} \tag{4.30}$$

In this way it is possible to obtain the best integrating interval length, when a is fixed.

This is not comfortable in operational analysis, where it is difficult to deal with a non-constant averaging interval. Therefore Stiperski and Rotach (2016)[43] decided to invert this formula and answer to the question: how is the uncertainty if the integrating interval is $I = \tau_a = 1800$s?

Then the estimator of the relative uncertainty is a and the level usually requested for flat terrain is 20%. For the i-Box, a larger value, i.e. 50% was chosen (that corresponds to $a \leq 0.5$).

The new formulas for a are, for momentum fluxes:

$$\begin{aligned} a_{uw}^2 &= \frac{z}{\tau_a U}\left[\frac{\overline{(u'w')^2}}{u_*^4} - 1\right] \\ a_{vw}^2 &= \frac{z}{\tau_a U}\left[\frac{\overline{(v'w')^2}}{u_*^4} - 1\right] \end{aligned} \tag{4.31}$$

for sensible heat flux

$$a_{w\theta}^2 = \frac{z}{\tau_a U}\left[\frac{\overline{(w'\theta')^2}}{\overline{(w'\theta')}^2} - 1\right] \tag{4.32}$$

and for a scalar quantity, or variance:

$$a_{x^2}^2 = \frac{4z}{\tau_a U}\left[\frac{\overline{x'^4}}{\overline{(x')^2}^2} - 1\right] \tag{4.33}$$

These relations will be useful to set the High Quality filtering in the following section.

In the Results Chapter (Ch. 5) I obtain a new version of these relations to assign the uncertainties to fluxes (see Section 5.3.1).

4.4.3 Quality Assurance

In this Section I will introduce the quality assurance process adopted for sonic and Krypton data. In particular I decided to divide it in three parts, increasing for each step the level of goodness requested for the dataset. In this way I am able to distinguish between: *Low Quality Data* (LoQ) where I only control on the physical range of variables; *Medium Quality Data* (MeQ) where I introduce more restrictive parameters on the high order moment and *High Quality Data* (HiQ) that are the best of my dataset.

In this brief introduction it is necessary to answer immediately the question: how much data do we have in those three classes?

On each quality control step I loose more or less the 30-40% of the previous step, and also in the last, HiQ, I loose practically everything. Moving back to Tables 4.1 and 4.2, it is possible to see that for the Metek sonic 265 days are available to be analysed (thus from on-line plot I saw that the data seems to be good, in total the sonic has registered approximately 360 days). The EdiRe analysis was done on entire month and only if I see that a particular month is empty or with random data I decided to remove it from the analysis. This is the case of December 2015 and January 2016, when due to a low power supply the heating first and then the sonic was turned off. In other cases I have months with some bad days due to weather conditions or to the heating turned off. In fact the main problem, as stated before, is the heating of the sonic. It is possible to heat the sonic only when the fuel cell works correctly, only with batteries and solar panels there is not enough energy for all instruments.

To sum up the data available after each step is necessary to look at Table 4.8.

Quality level	Number of days	Percentage	Number of periods
None	386	100%	18540
Low Quality	230	59.6%	13926
Medium Quality	156	40.4%	12583
High Quality	0	0%	161

Table 4.8: Quality levels data availability. The first column state the quality level, "None" is with all the data measured by the sonic, "Low Quality" is after the harsh flagging with physical limits, "Medium Quality" is all data that has passed the first control and the kurtosis and skewness limits, and "High Quality" is data with all filters. Update on 31st May 2016.

As you can see there are only a few half hour periods in the HiQ dataset, for this reason the analysis that follows in Chapter 5, is done on Medium Quality data.

The first two columns of Table 4.8 report the number of days with more than 95% of half hour periods available (approximately 46 of 48 half hour periods) and the percentage relative to the first row, this is the reason why the number of periods reported in the last column does not match with those percentages. I have to underline the last row. There is no HiQ day, and Arbeser dataset has only 161 half hour periods distributed over 89 days. At the end of Chapter 5, I will show the HiQ data plots, but with these data it is not possible to conduct a deeper analysis.

Physical Range

The first control introduced on raw data is based on the physical range of sonic variables. The Metek ultrasonic anemometer outputs the three wind velocity components, in the sonic reference system, the sonic temperature and also collects the output of the KH20 hygrometer. The anemometer has a limit on wind intensity and sonic temperature. Those limits are for wind speed ± 50 m/s (USA-1) and ± 60 m/s (uSonic3), while for sonic temperature $-30 \div 50$ °C (USA-1) and $-35 \div 55$ °C (uSonic3).

With EdiRe I rotate first the reference system with a Double Rotation (see Sec. 4.4.2) and so I have only the mean streamline wind speed. Thus I control only the streamline velocity, its standard deviation distribution, the sonic temperature and its standard deviation.

The thresholds are shown in Table 4.9, and are chosen on the base of Arbeser climatology (see below, Section 5.2.1).

Variable	Lower limit	Upper limit
Wind speed	0 m/s	45 m/s
Sonic temperature	−30 °C	+40 m/s
Wind standard deviation		5 m/s
T sonic standard deviation		2 °C
CQT	100	

Table 4.9: First level of quality control: the physical range thresholds for Low Quality data assurance.

I have to spend some words on the *Standard Deviation* thresholds. These

are evaluated after a check of the standard deviation distribution of the entire dataset, then I set the threshold on the right tail of the χ-shaped distribution at approximately less than 0.3% of data in the tail. In particular with the choice done (see Tab. 4.9) I have 99.97% of $\sigma_{T_s} < 2$ °C and 99.84% of $\sigma_{\overline{u}} < 5$ m/s.

In the Figure 4.4 you can see the previously cited distribution of standard deviations.

The timeline plot of Figure 4.5 shows the data that survive to this *harsh flagging*.

The CQT is a flagging value produced by the uSonic3 only, then in the timeline it is always 100 when it does not exist, and when it is present it is actively used in harsh flagging. In fact if CQT is 0 the data acquired with the sonic are for sure bad.

In the analysis done with Matlab data that not fulfil the harsh flag requirements are removed from the data matrix, and never considered again.

Medium Quality Dataset

The second level of quality control is done using higher order moments like kurtosis and skewness (see Eq. (4.18) and (4.17)). Following Vickers and Mahrt (1997) [50] I use the thresholds in Table 4.10 for the variables u, v, w and T_s.

Parameter	Lower limit	Upper limit
Skewness	-2	$+2$
Kurtosis	$-\inf$	$+8$

Table 4.10: Thresholds for hard flagging, applied to u, v, w and T_s.

The Krypton hygrometer as previously highlighted, worked only for few days, but in any case has to be included into the analysis. I chose to include it in a separate way, I considered two levels of MeQ, and later HiQ, one with the KH20 quality control and one without.

The quality control in the Krypton is done only with the threshold on output voltage. If you scroll the processing list of EdiRe it is clear that many corrections involve the specific humidity, then is crucial to know if without this value all the correction implemented on heat flux and sonic temperature works in any case. I verify that with the statement of correction on KH20 signal it is introduced a displacement of 9999 that brings the value of q lower than zero. For more safety I substitute this negative value with 0 that means no humidity. Then the

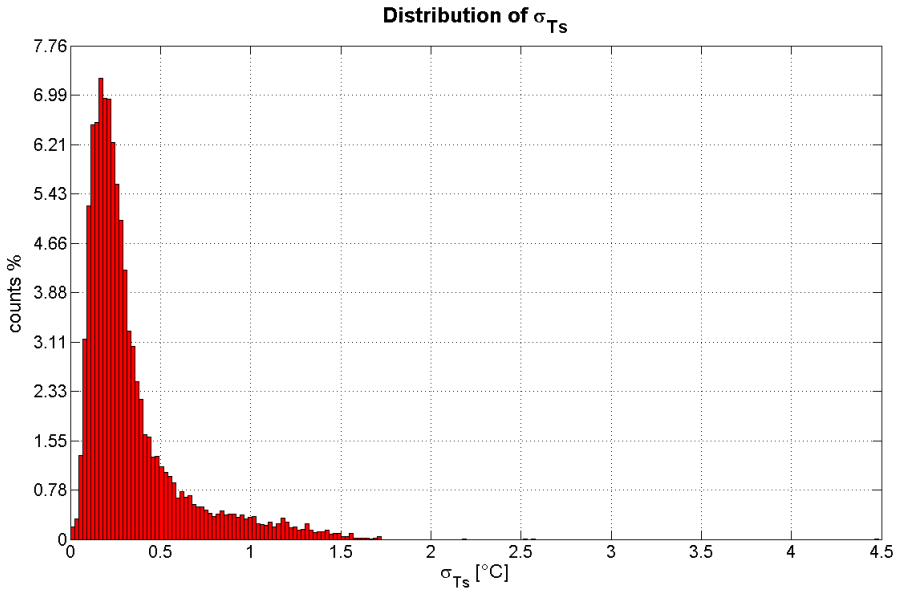

(a) Sonic Temperature.

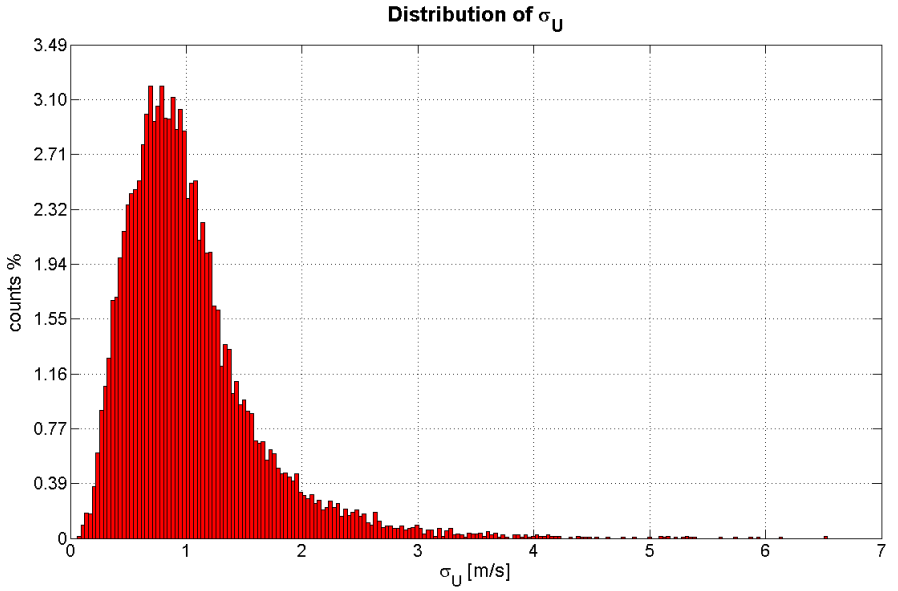

(b) Streamline wind speed.

Figure 4.4: Distribution of standard deviations for the streamline wind speed and sonic temperature of all periods measured. In this base I decided the thresholds in Tab. 4.9

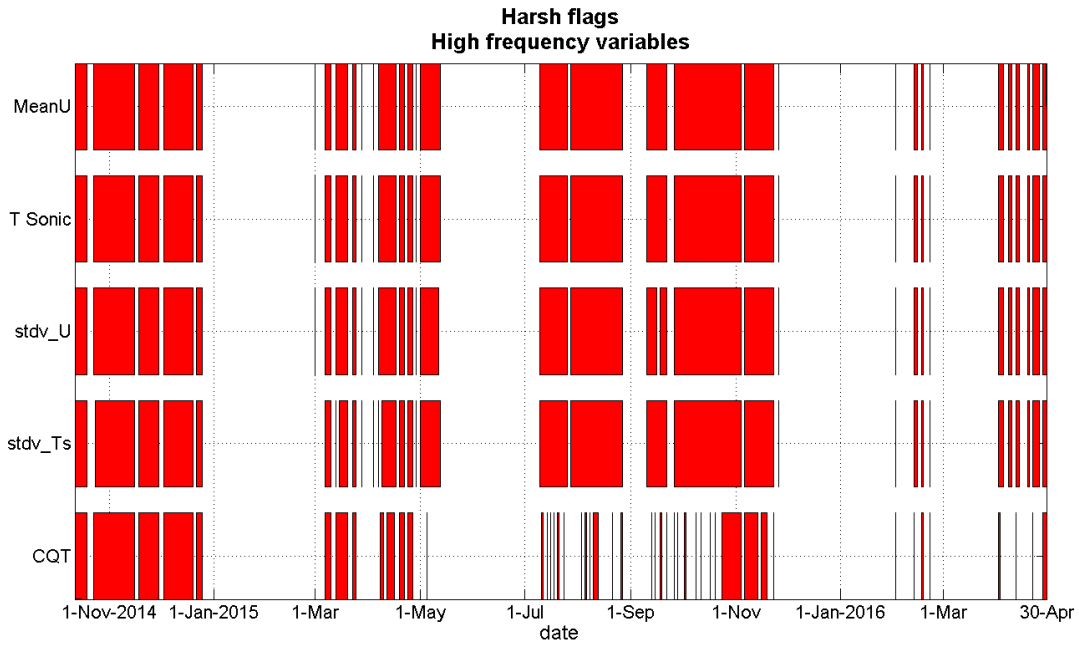

Figure 4.5: Timeline of "harsh" flags for sonic data, after the harsh flagging with thresholds in Tab. 4.9. Here the red zones are days that have passed the first quality control with at least the 95% of half hour periods.

assumption is a dry air when the Krypton does not work, and it means no further correction for humidity and no wrong LE flux.

A path that is possible to undertake is to use the low frequency humidity as an estimator for the mean specific humidity. Obviously it is not possible to use it to fulfil the fluctuations at 20Hz sampling frequency.

Combining all those controls I refine the first selection done with the *harsh flags*, and I obtain the Medium Quality data sub set. These control are the *hard flags*.

In Figure 4.6 there is the timeline of hard flags, red zone are data not flagged, then they are good data.

High Quality Dataset

The highest level of control is composed by Wyngaard uncertainties and stationarity (steady state test), previously introduced in Section 4.4.2.

The thresholds applied are summarised in the following Table 4.11.

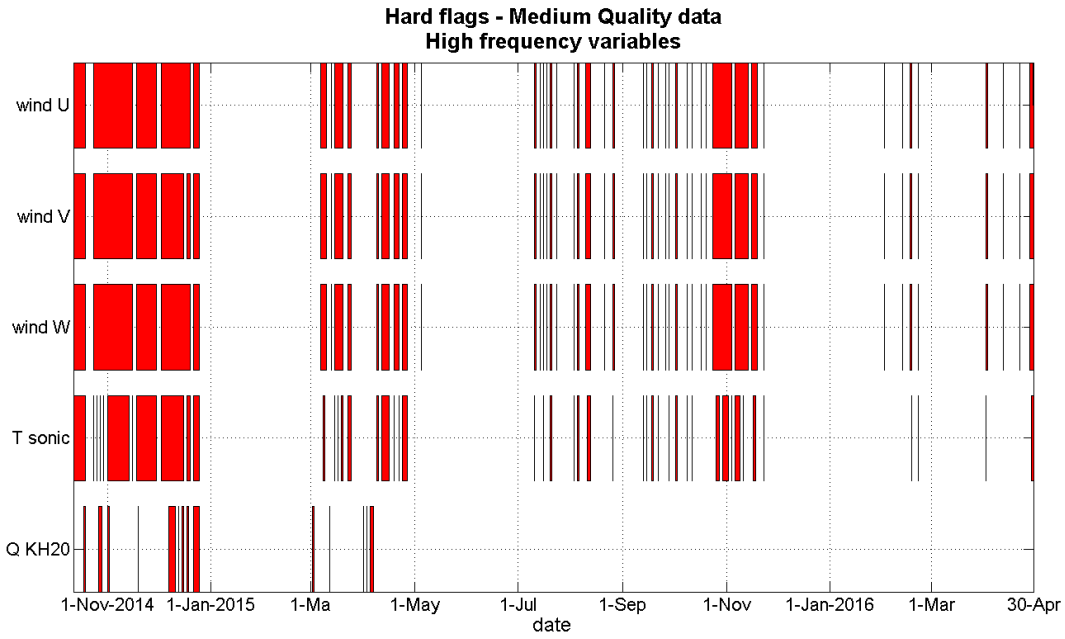

Figure 4.6: Timeline of "hard" flags for sonic and Krypton data. Here the red zones are days that have passed the first and second quality control with at least the 95% of half hour periods.

The *soft flag* filtering is applied after the "hard" and "harsh" flagging. I decided to split the soft flags into two groups, one only relative to momentum and one relative to heat fluxes, then involving the temperature fluctuation. I have also distinguished between stationarity and uncertainties, my aim is to understand if the stationarity condition is more restrictive (and then less achieved by the data) than the uncertainty condition.

At the end I also evaluate a general *soft flag* with both stationarity and uncertainties, and one more for including the Krypton hygrometer quality.

Figure 4.7 shows the timeline plot of data after the soft flagging (in orange the periods survived to this third step of flagging). In this timeline the threshold for drawing a line is 1 half hour period per day, instead in hard and harsh flag timelines for drawing one line is necessary that the 95% of the day is complete (up to 46 half hour periods). If I plot with the same requirement the soft flags I will obtain a blank timeline.

From this timeline it is possible to learn that for Arbeser data set:

1. Momentum ($\overline{u'w'}$, $\overline{v'w'}$, $\overline{u'^2}$, $\overline{v'^2}$ and $\overline{w}$) uncertainties and stationarity condi-

Variable	Lower limit	Upper limit
Stationarity	0%	40%
Uncertainties (a)	0.0	0.5

Table 4.11: Thresholds applied for soft flagging on previously selected data (MeQ).

tions is quite always fulfilled.

2. Heat flux ($\overline{w'T'_s}$ and $\overline{T'_s}$) uncertainties are quite well under the limit of 0.5, but the stationarity is hardly ever achieved.

3. The line "Total" in Fig. 4.7 shows the high dependence on heat flux stationarity. In fact looking at the following two lines ("Total uncertainty" and "Total stationarity") this dependence becomes clear. For the HiQ dataset I used the *Total soft flags*.

4. The last line is about the KH20 (specific humidity q) data quality and, as previously seen, there is almost nothing left.

Figure 4.7: Timeline of "soft" flags for momentum and heat flux, and separately for the Krypton. In this case the orange zones indicate each period that has passed the selection.

Chapter 5

Analysis Results

5.1 Introduction

In this chapter the data analysis results will be presented, both for standard meteorological data (or low frequency data) and turbulence data (or high frequency data).

I start from the beginning, then from standard meteorological data that came first in my work. From this dataset I retrieve some classes, following the classification explained in Section 4.3.4, and on those I study the turbulence data. This choice was done for start to analyse only the simplest conditions at a so complex site. I recall that this work is the first at this station and maybe one of the first at such a complex terrain site.

5.2 Standard Meteorological Data

5.2.1 Arbeser Climatology

The first part of the analysis consists in the organisation and to have a first look on low frequency data. First of all general daily cycles of the temperature and radiation as well as wind profiles (on the three levels) and the wind rose were plotted.

For summarising the general condition of wind direction and intensity, temperature, humidity, radiation and so on, it is possible to look at the "typical daily cycle". This day represents the average condition at the site over one and an half year of measurements; it shows the most frequent pattern on the condition of a symmetric distribution of these variables.

The title of this section is "Arbeser Climatology" but usually the definition of *climate* regards a longer periods, that for the WMO[1] has to be long at least thirty years. Arbeser station, thus, cannot gives such a climate information, but only a representation of 22 months of data.

Air Temperature

I verify that Arbeser temperature data has a distribution resembling a Normal distribution. In Table 5.1 I summarise some statistical parameters. From the statistics I know that a symmetric curve has a skewness (m_3/σ^3) that tends to zero, and for the kurtosis (m_4/σ^4) I expect, for the Normal distribution, the value 3. With a Normal distribution it is possible to use the mean as the representation of the most probable value. Observing the probability distribution plot of the temperature I can state that the mean represents approximately[2] the most frequent value.

Level	$\overline{T}$ [°C]	σ [°C]	m_3/σ^3	m_4/σ^4
1 (0.54 m)	1.71	7.43	0.30	2.81
2 (1.91 m)	1.76	7.30	0.21	2.70
3 (3.88 m)	1.82	7.11	0.19	2.71

Table 5.1: Statistical moments of all 30 minutes temperature averages data from 2014.10.03 to 2016.05.01.

In Figure 5.1 I plotted the *mean daily cycle* and from that you can see, as expected that the lower level cools down more than the others during the night, and on the other side warm up more during the day. This profile can represent a mid-autumn quite sunny day.

If the analysis of extreme values is done the result is that the highest temperature measured at Arbeser is (25.13 ± 0.01)°C[3], while the lowest temperature is (-17.00 ± 0.01)°C.

[1] World Meteorological Organisation

[2] I say approximately because the distribution of the temperature on each level has a peak near the mean value, around 1.5 °C, and two other peaks, one at 3°C and one at 5°C. But the mean is on the first peak because there are many data in the region $-11 \div 0$°C than in the opposite positive region.

[3] This value is taken from the second level, that is the only one that has a height according to the standard requirement of WMO.

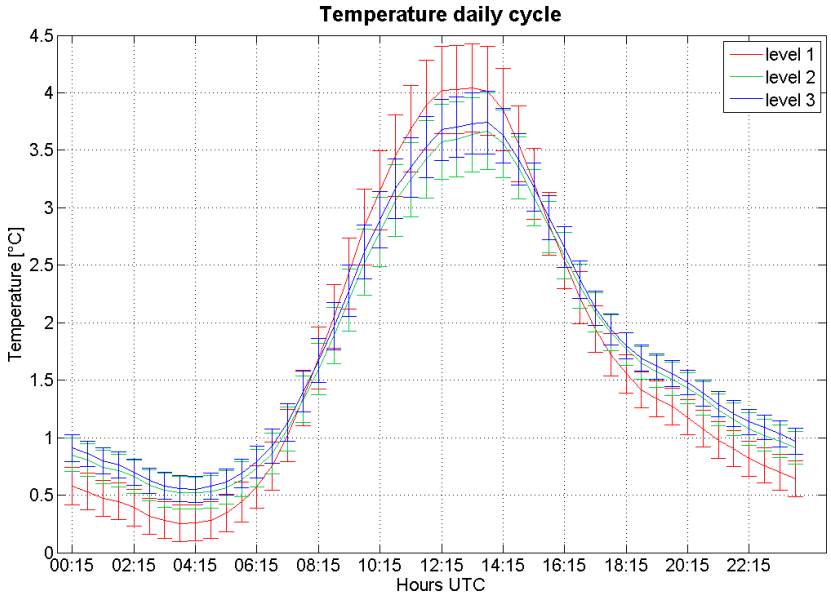

Figure 5.1: Mean daily cycle of temperature, evaluated from 30 minutes averages and using all data from 2014.10.03 to 2016.05.01. Level 1 with the red line is the lowest (0.54m), level 2 with the green line is the middle (1.91m) and level 3 with the blue line is the highest (3.88m).

Air Moisture

The air moisture is measured using capacitive hygrometer (see 3.3) and the data logger stores the relative humidity. On relative humidity, that is limited in the range $0 \div 100\%$, it is not possible to do the same consideration done on temperature, because the distribution is limited. However, it is possible to assess the frequency of different range of humidity.

As it is feasible see from Table 5.2 much data depict a saturation condition with relative humidity greater than 99%. Around 30% to 35% of the data is in a relatively wet situation, and only 5% is in a dry situation with an RH less than 30%.

I can try to explain the relatively high presence of high humidity values with the temperature distribution. Arbeser is a mountain-top site, where approximately half of temperature measurements are below zero, that means a lower value for the saturation vapour pressure, thus the relative humidity can frequently reach quite high values. At the end the air is saturated of water vapour but the

Level	$RH < 30\%$	$80\% < RH < 99\%$	$RH \geq 99\%$
1 (0.54 m)	4.13%	39.52%	14.05%
2 (1.91 m)	5.01%	36.80%	15.20%
3 (3.88 m)	6.79%	33.10%	11.99%

Table 5.2: Relative humidity distribution for the three levels of the station. Data base as in Fig.5.1.

total amount is not very high. This consideration can be done looking at the values of specific humidity q. I evaluate the specific humidity using the following equation (Iribarne and Godson, 1973 [20])

$$q = \frac{0.622 e_a}{p - (1 - 0.622) e_a} \tag{5.1}$$

and I use the equation in Footnote 5 on page 93 for calculating the saturation vapour pressure.

The distribution of the specific humidity is similar to a Beta function with parameters $B(2, 5)$, it has a maximum around $0.002 g_{vapour}/g_{air}$ for each level. In Figure 5.2 you can see the distribution for the second level.

Radiation

The radiation is measured in all its components, long and short wave, up-going and incoming. The radiation is used for the selection of clear days (see Section 4.3.4), especially in its long wave part, therefore only the radiation characteristics for those clear days are described here in detail.

The described earlier Clear Days Algorithm selects days with a mostly clear sky, in fact for obtaining a sizeable number of days, some of these days are not completely clear. In fact, some days have scattered clouds during the day, but for most of the time the sky is cloud-free. Another important feature is that the CSI (Clear-Sky Index, see Section 4.3.4) is evaluated on half hour averages, that considerably reduces the possibility to remove completely the clouds. Nevertheless the results of the Clear Days Algorithm are satisfying, and how I calibrate[4] it can work quite well at this station.

Deepening the analysis of these selected clear days, I find that in correspondence to approximately the same angle of incidence of the sun on the radiometer

[4]The calibration was done manually on some selected days during 2015 using different webcams in Arbeser neighbourhood.

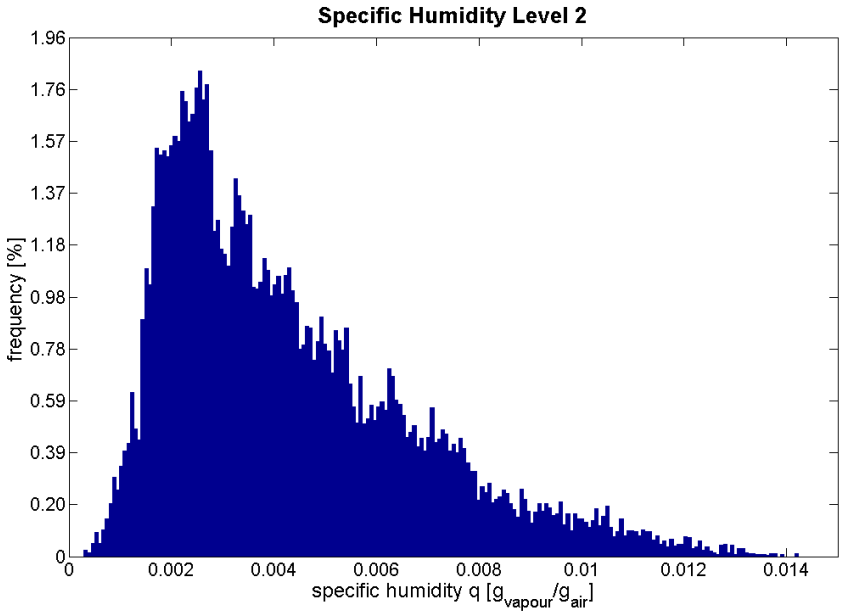

Figure 5.2: Distribution of specific humidity q evaluated at the second level. Data base as in Fig.5.1.

there were a darkness peak. Referring to Figure 5.3 it is possible to see that this peak has always the same amplitude, and it occurs approximately at the same hour. After a control on field during a clear day I verify that this dark peak is due to the shadowing of the south-east tie-rod on the radiometer dome. In fact the radiometer is not placed in the south side of the tower, due to practical constraints of this site.

The usual range of daily mean irradiance at Arbeser is between $\overline{Q}_{day} = 75\text{W/m}^2$ and $\overline{Q}_{day} = 405\text{W/m}^2$. As explained previously in 1.4.1 the evaluation of the total irradiance expected for a given location and altitude can be done with some equations. That was done for Arbeser, and I used it to calibrate the Clear Days Algorithm. In Figure 5.4 the two thick lines represent the theoretical curves of irradiance, the red one is referred to the top of atmosphere, and it is the result of Eq. (1.16), meanwhile the blue one is the daily mean irradiance at Arbeser altitude. The black oscillating line is the measured mean irradiance ($\bar{Q}_{day}$).

The most of days are under the blue curve. Some days, instead, have been registered a higher value of $\bar{Q}_{day}$ than the calculated daily irradiance at Arbeser. The most probable reason could be that I used an approximated formula (Eq, 1.17)

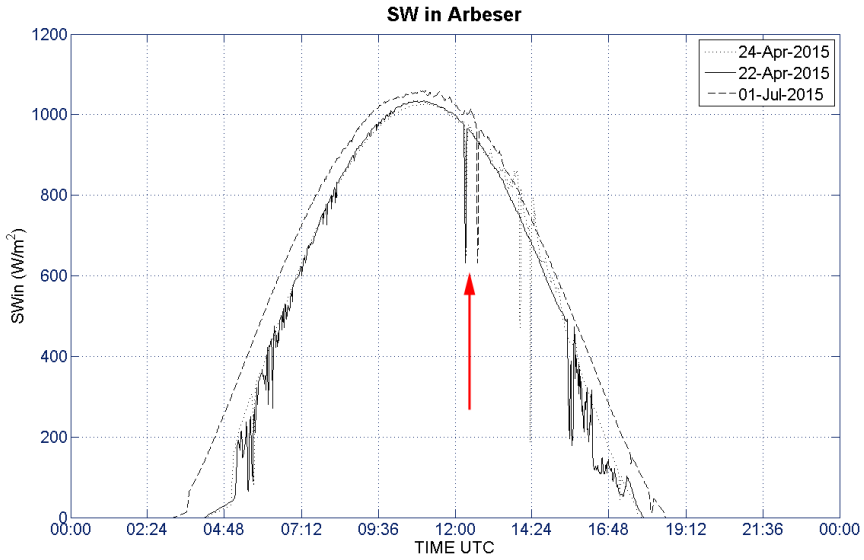

Figure 5.3: The incoming short wave radiation for three clear-sky days (see the legend). The red arrow indicates the same dark peak, this is probably due to the shadowing of the SE tie rod. The data plotted are measured every one minute.

for the transmissivity that is not the best one for Arbeser. Two strange periods appear at the end of October 2014 (between 26th and 29th) and again, but shorter, on 24th November 2015. There the $\bar{Q}_{day}$ is even bigger than the daily irradiance evaluated at the top of atmosphere. In both cases I cannot exclude a malfunctioning of the radiometer, in the first case I can dare do an hypothesis of high reflection from a low layer of clouds, combined with the snow (already present) that may raise somehow the amount of incoming short wave radiation. In the second case the day was completely clear, also in this case the ground was covered by snow, but the radiometer did not work in the second part of the day. Thus the mean short wave incoming radiation is higher, because the evening did not contribute to lower it. However in the first case this did not happen, the values are high for another reason, probably the scattered clouds had contributed.

After the detection of the clear days it is possible to state, according to the Arbeser dataset, that the probability of detection for a clear day is higher during autumn, late winter and spring. During summer the probability is lower because of the intense convection in that mountainous area.

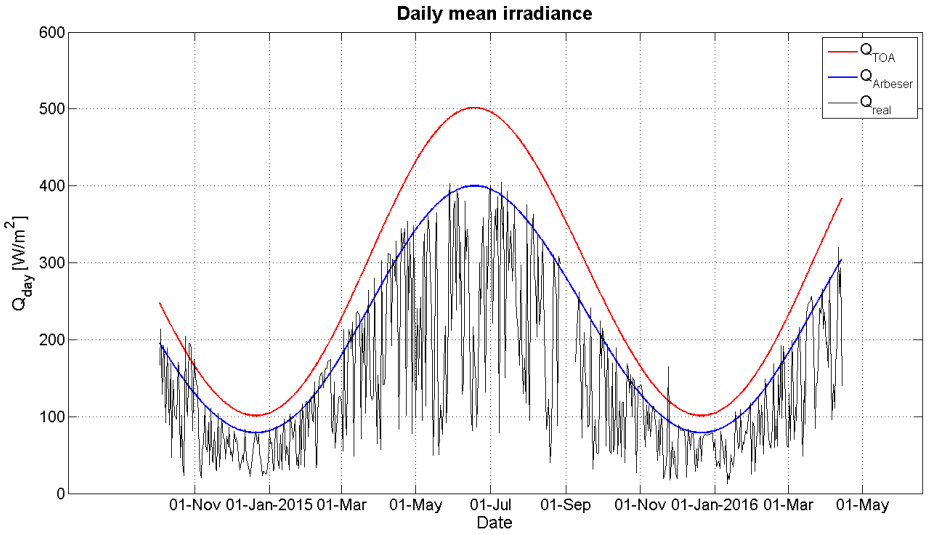

Figure 5.4: Daily mean irradiance over and at Arbeser. The red curve represents the daily mean irradiance at the top of atmosphere (TOA), the blue is the mean irradiance at TOA scaled with the transmissivity and the black curve is the mean short wave incoming radiation measured with the radiometer.

Wind

From a climatological point of view the wind direction and speed at Arbeser are quite well defined. In fact looking at the general wind rose plot (Figure 5.5) for the entire dataset it is possible to summarise that:

1. The prevalent wind direction is from west-southwest, precisely from direction 200°, where the wind came from for more than 18% of cases.
2. The second relevant sector, especially for intensities, is between north and east. This sector corresponds to the direction of up valley wind in the Inn Valley, and in some verified cases the high wind speeds are directly connected with the upvalley flow.
3. The southwest quarter by itself has more than 65% of wind directions.
4. The northeast quarter, instead, counts the 13, 60% of wind directions.
5. The higher intensities are registered in quarter southwest, but values around or greater than 8m/s can be reached also in quarter northeast.

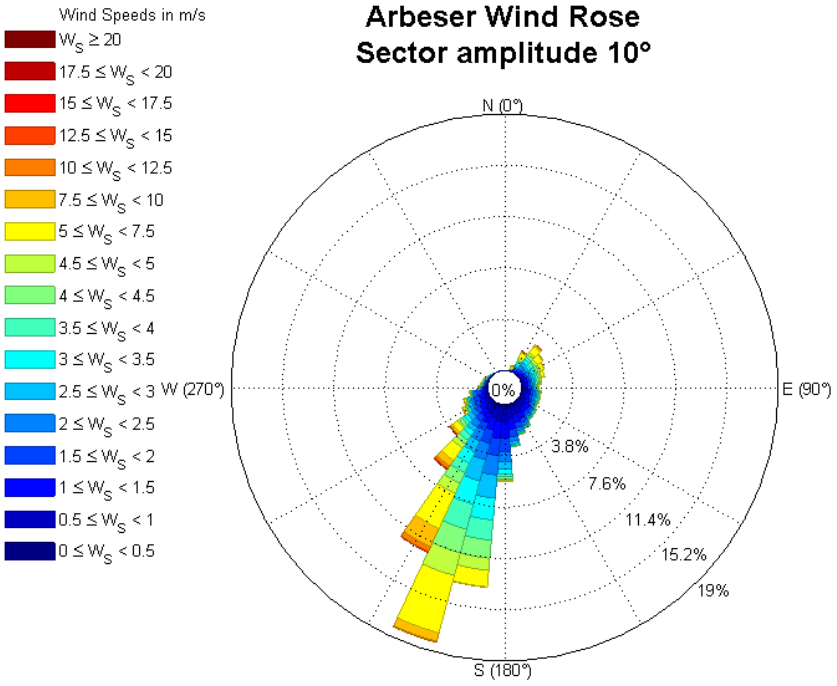

Figure 5.5: Wind rose for the entire dataset. The wind direction is drawn in meteorological way, thus pointing into the direction of wind origin. Each wedge is the sum of a 10° sector amplitude, and it points to the mean value.

5.2.2 Classification Results

In this section the core of the analysis concerning low frequency data has to be presented: the classification. As previously explained in Section 4.3.4 I have divided the meteorological data using two different approaches: the first is using pressure gradients and the second is using the Clear Sky Algorithm.

The pressure classification subdivides the data in the way showed by Table 5.3.

The class P3 is called *dynamically driven days*, because on these days the mean flow is governed by the synoptic flow motion (frontal passage, trough over middle Europe, ...).

The classification done by the Clear Days Algorithm results in 65 days selected and they are considered the "good" level of clear days.

Combining the two classifications it is feasible to obtain the *thermally driven days*, or rather the most interesting days for studying heat fluxes and the valley wind influence at a mountain-top site. I choose to concentrate my investigation

Class	P1	P2	P3	P4
Number of days	205	0	55	318

Table 5.3: The number of days collected by the pressure classification as explained in Section 4.3.4. I recall that class P4 contains all days with a "mixed" or a not available pressure gradient.

on this restricted selection of days because my knowledge (and partly that of scientific community) on mountain top site surface layer behaviour is very poor. Thus looking to those simple cases can help to reach some first results.

The thermally driven day comes up from the intersection of the P1 class and clear days. In particular I find 33 days. I have refined the classification adding a control on the valley wind regime at Kolsass station (centre valley floor); if during the afternoon between 13.00 and 20.00 UTC the wind comes from the down valley direction, in other words between 40° and 130°, and its velocity and turbulence are not very high, the situation is a normal valley wind regime (Vergeiner and Dreiseitl, 1987 [49]; Vergeiner, 1987 [48]).

Subclass	Number of days
P1 Clear Sky Days (CSD)	33
P1 CSD - East	17
P3 Clear Sky Days	2

Table 5.4: Number of days collected subclasses of P1 and P3. East indicates that the wind direction in Kolsass is up-valley.

From Table 5.4 is possible to appreciate this very restrictive selection output of only 33 clear days, and 17 of those are the most probable cases of thermally driven flow days. Instead the case of dynamically driven days, class P3, counts only 2 clear days. In class P3 usually there are not days characterized by stable meteorological conditions, quite the contrary there is a huge pressure gradient between the selected stations, thus means a contrast among an high and a low pressure field over middle Europe. Another interesting point, but not so far investigated, are the föhn cases. During south föhn conditions there is a high pressure difference through Innsbruck and Bolzano, larger than 500Pa. The sky conditions are not fixed, and it is possible to have a completely clear sky (but this happens usually far from mountain ridges), or scattered clouds. The distinctive condition is a low relative humidity on the mountain lee side.

Of this selection I plotted the daily cycle of temperature, wind direction and speed, the wind rose and some control plots on short wave incoming radiation to control the correctness of the Clear Days Algorithm.

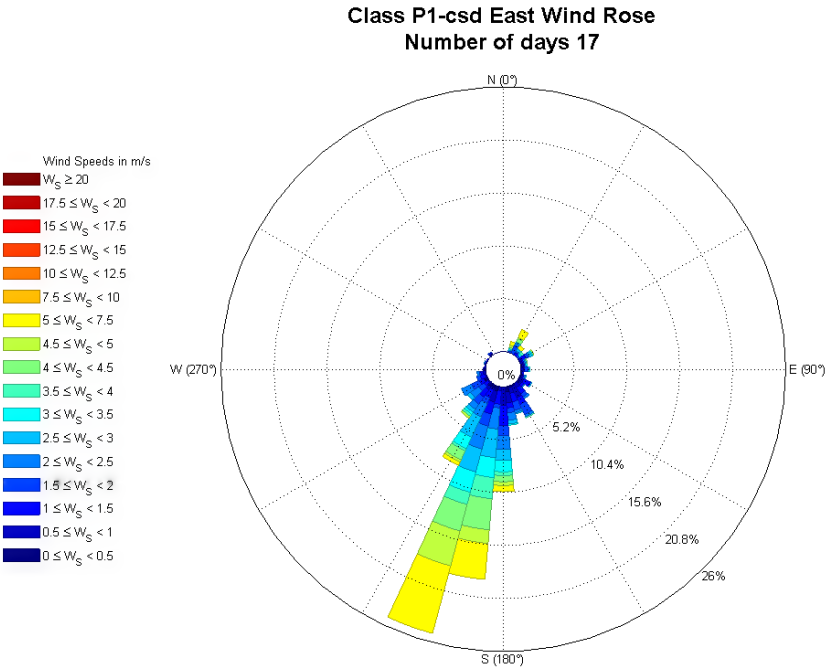

Figure 5.6: Wind rose for the clear and valley wind days (P1-CSD East).

From the wind rose (Figure 5.6, class P1-CSD East) all the halfway-cases have been removed, namely all the second and fourth quarter (SE and NW). It is still present the main sector, SW (southwest) and a few cases in the NE quarter, with a quite high speed (around 6m/s). In the quarter NE the main direction detected during clear and valley wind days, henceforth P1-csd East class, is 30° that corresponds to the direction of the Inn Valley nearby Arbeser station. I analyse these days in somewhat more depth, the purpose is to understand if the valley wind regime can influence the wind regime at the top mountain site, otherwise if this site is completely decoupled.

As I said before, the 30° wind direction can be related with the valley wind. From plots in Figures 5.7 and 5.8 it is possible to see the two days that contribute to this 30° peak shown in Figure 5.6. The first hypothesis is: the upvalley wind reaches Arbeser site, on the contrary this maybe a coincidence and this air parcel

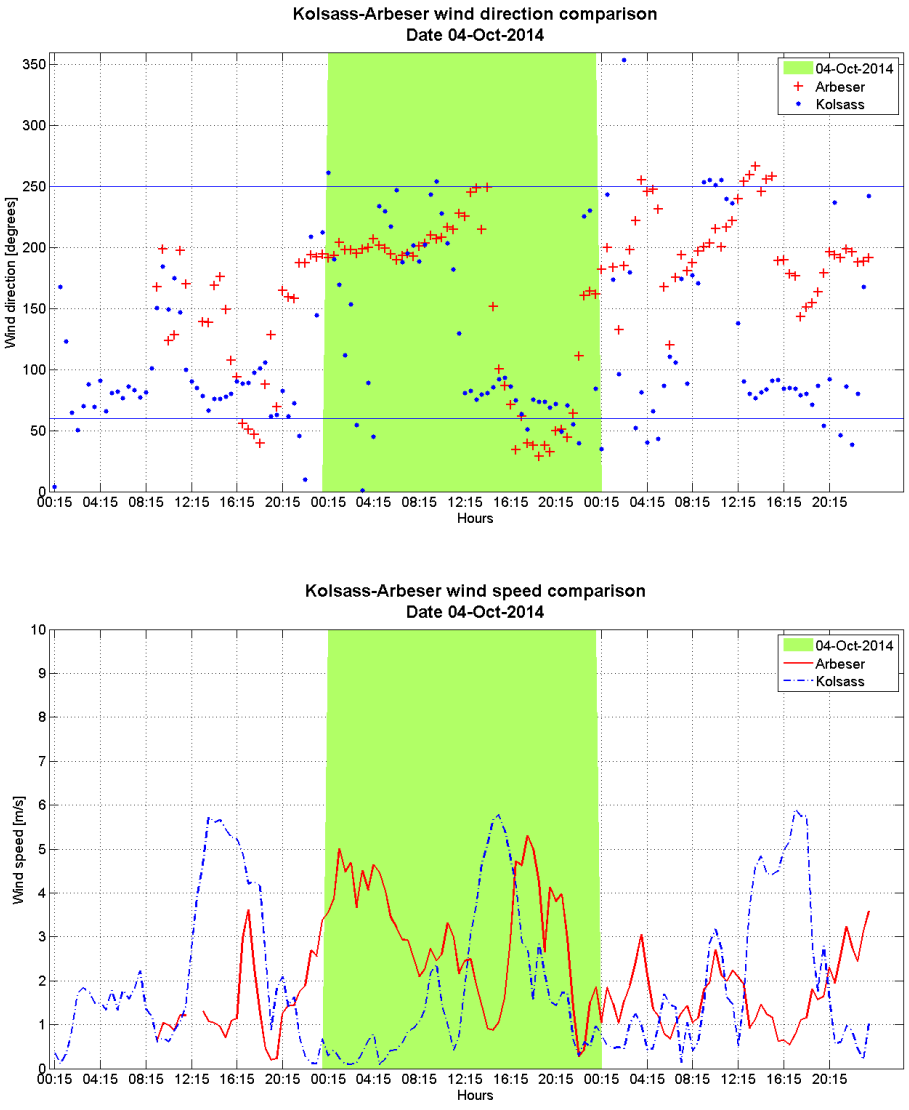

Figure 5.7: Wind direction (top panel) and speed (lower panel) on 4th October 2014 at site Arbeser Kogel with the red markers or continuous line, and at the site Kolsass (Inn Valley floor) with the blue markers or dashed line. In green shaded area there is the day of our interest (2014.10.04), on the side there are the previous and the following days.

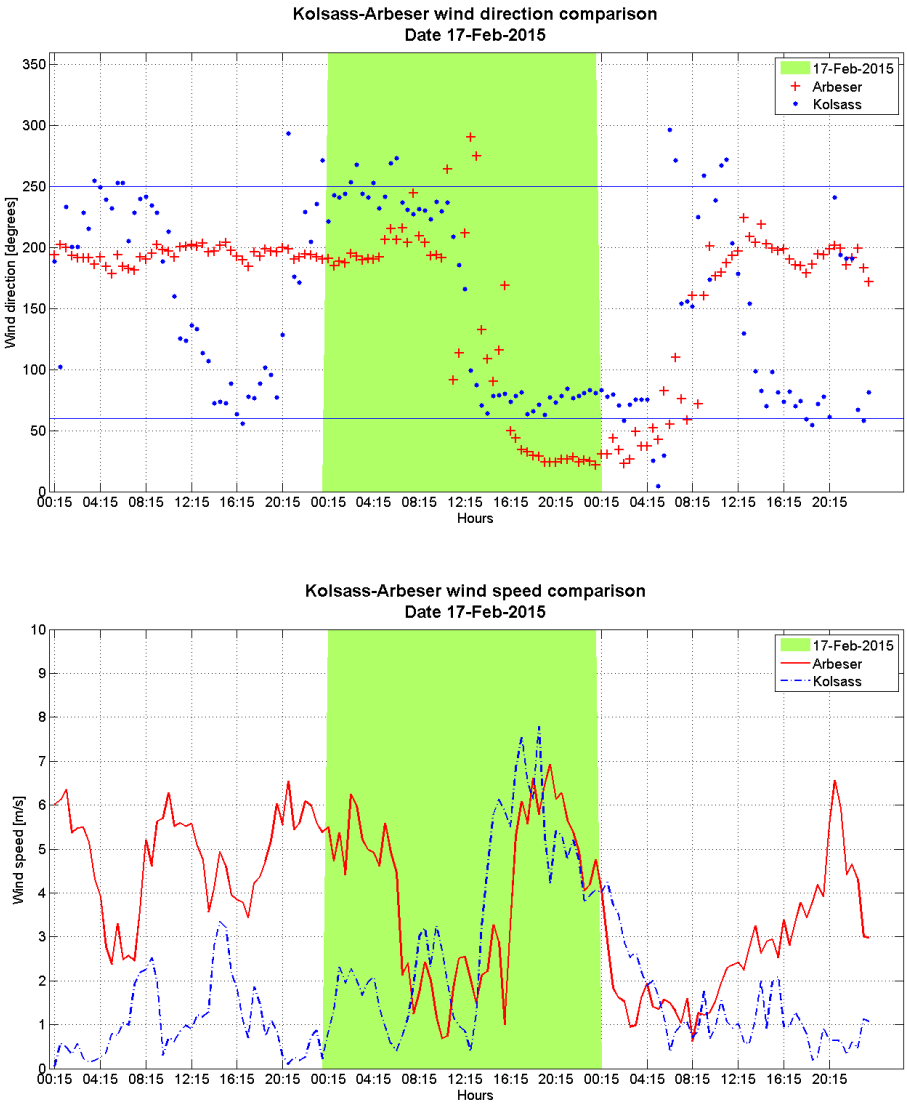

Figure 5.8: Wind direction (top panel) and speed (lower panel) on 17th February 2015 at the site Arbeser Kogel with the red markers or continuous line, and at the site Kolsass (Inn Valley floor) with blue markers or dashed line. In green shaded area there is the day of our interest (2015.02.17), on the side there are the previous and the following days.

from 30° comes from the free atmosphere.

It is possible to analyse more in-depth these two days, February 17th and October 4th, relating those to the wind direction at Kolsass. In Figure 5.7 it is possible to see the wind direction at Kolsass for the previous day does not follow the valley wind hypothesis, although for the selected day it is rather correct. At Arbeser the wind direction moves from 200°, the usual direction, to 50°-40°, that approximately corresponds to the Inn Valley direction. The following day is again totally out-of-scheme. The wind speed at Kolsass follows quite well the valley wind daily cycle.

I looked at surface pressure charts for these three days (3rd, 4th and 5th of October 2014). A weak high pressure field rested on middle Europe, in the following days a cold front started to move from England to Germany, thus an air advection on Austria was possible and the NE component observed can be explained with the synoptic meteorology.

The Figure 5.8 depicts the situation of February 17th. In this case the Kolsass wind follows the theories for valley winds, during the morning (night) there are downvalley winds instead during the day upvalley winds occur. The selected day (17th February 2015) shows a high upvalley wind speed. On this day the wind direction at Arbeser rotates from the usual 200° to 30°-40°. The analysis of surface pressure chart excludes the presence of frontal systems, and a relatively high pressure field rested on middle Europe. In this case it is possible to support the hypothesis of a well developed valley wind that reaches the valley ridge and in particular Arbeser site. Looking at wind speed it is possible to see that during the transition from the usual direction to the valley direction, the wind was weak. Moreover first the upvalley wind set in at Kolsass (the dashed blue line in Fig. 5.8 lower panel) and approximately one and a half hour later set in at Arbeser. Nothing can be asserted relatively to wind speed itself, the two stations are completely different and at two different altitudes, but in this case the upvalley wind core might have reached Arbeser crest.

The main wind direction is more difficult to explain, in fact this direction corresponds to halfway among the south slope and the ridge slope. First of all I decide to compare the data from the sonic to the Young vane, because first I thought that an angular displacement can affect the sonic direction. In Figure 5.9 I plot two randomly chosen days from the ten I selected to compare the wind speed and direction between the Young vane and the sonic anemometer (Metek). As you can see the direction is quite perfectly according, while the velocity is slightly different because the instruments are at different heights (the sonic is higher, thus it measures higher wind speed).

Some doubt still remains on this prevalent direction, as a control on this I

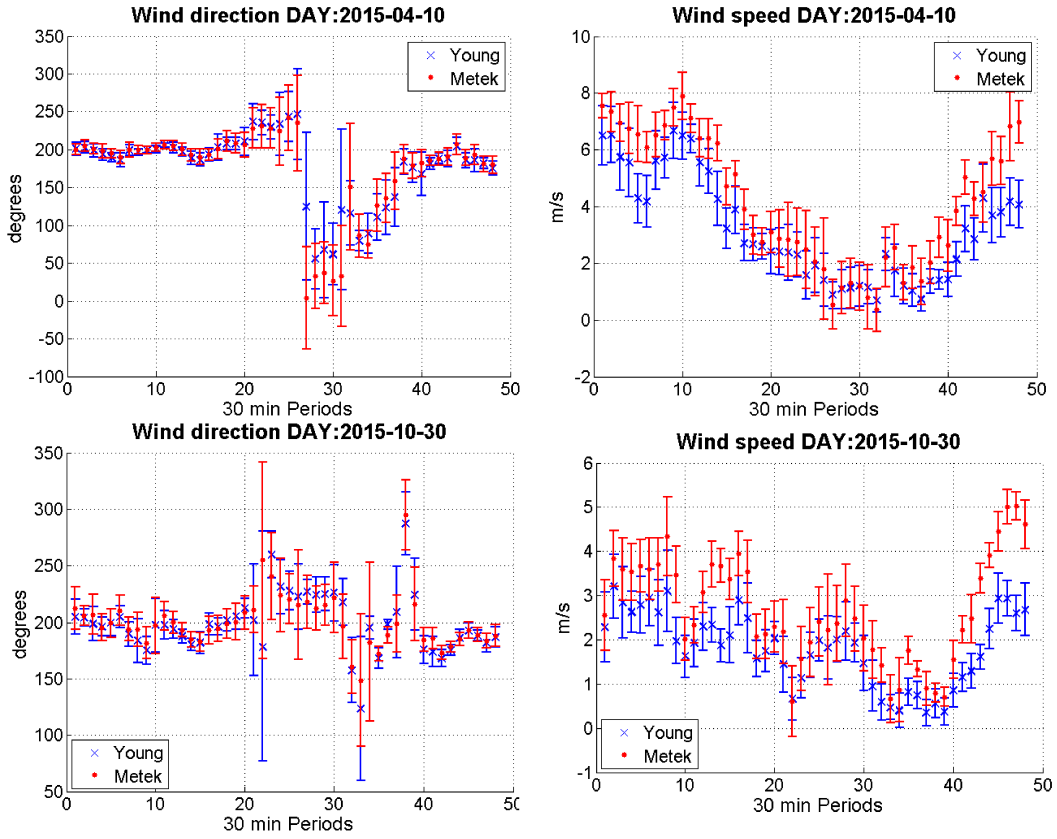

Figure 5.9: Comparison between sonic anemometer (Metek) and Young vane of wind speed and direction. The error bars represent the standard deviation computed on half hour periods.

choose another top mountain station from the Austrian national weather net: Patscherkofel. This mountain is located between Wipp Valley and Inn Valley, on the south-east side of Innsbruck (2251 m a.s.l., latitude 47.20889N, longitude 11.46222E). I took the wind direction and speed measurements from October 1st, 2014 to January 25th, 2016, and looking at the wind rose it is possible to see that the main wind direction is from south (170°, see Figure 5.10). Patscherkofel station is not very close to Arbeser, and also the Wipp Valley usually channels the south föhn, nevertheless the prevalent direction is from the same side, thus I can be quite sure about the correctness of Arbeser data.

The problem is to understand why at Arbeser there is this main wind direction also during thermally driven days. Moreover these south winds are stronger during nighttime and without south föhn conditions. In my opinion the most credible

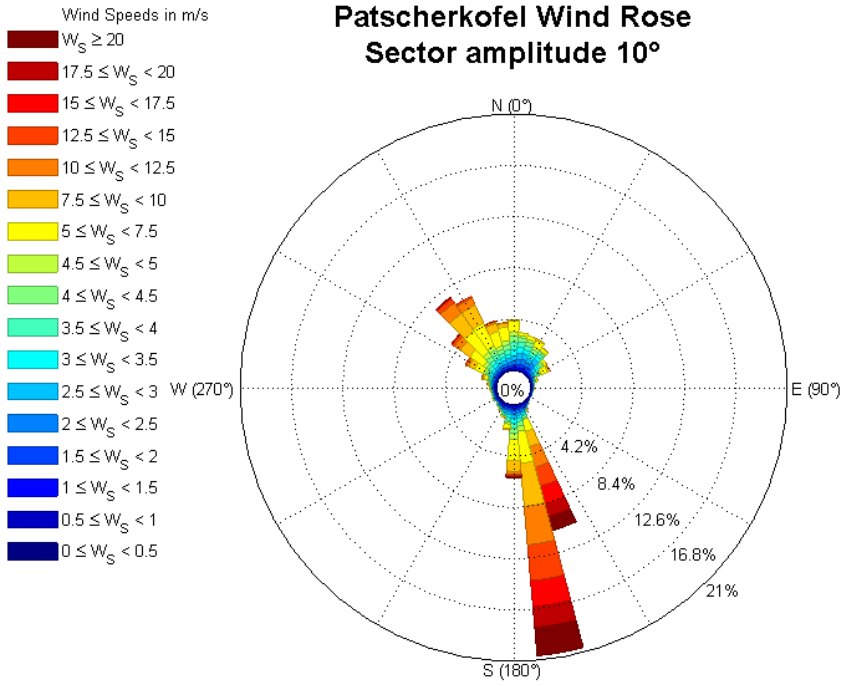

Figure 5.10: Wind rose of Patscherkofel station from 2014.10.01 to 2016.01.25.

explanation is that during the day the wind is driven by convection, then up-slope winds on both ridge and south slope, it seems that the south slope dominates and it is possible to explain that with the orientation and inclination of this slope relatively to sun rays; on the other side during the night is more difficult to explain. There might be a channeling of the down-valley wind of the Inn Valley into the side valley (of the river Pill, Pillbach), but this situation contrasts with the down flow inside the Pillbach Valley, and also the down valley flow is generally very weak.

I have also analysed the mean wind profile daily cycle. It is obtained after an average on all the 17 clear days, but keeping the daily cycle, at the end I obtained the clear days wind daily cycle profile. The plot in Figure 5.11 shows that the usual profile has a positive wind shear, and a shape that resembles the logarithmic profile state by the Monin-Obukhov similarity for the surface layer. The highest speed is reached in the middle of the night, this might be related with the stability of the nocturnal boundary layer that is more stable than the convective mixed layer; thus bring to a more organised motion that somehow leads to higher wind

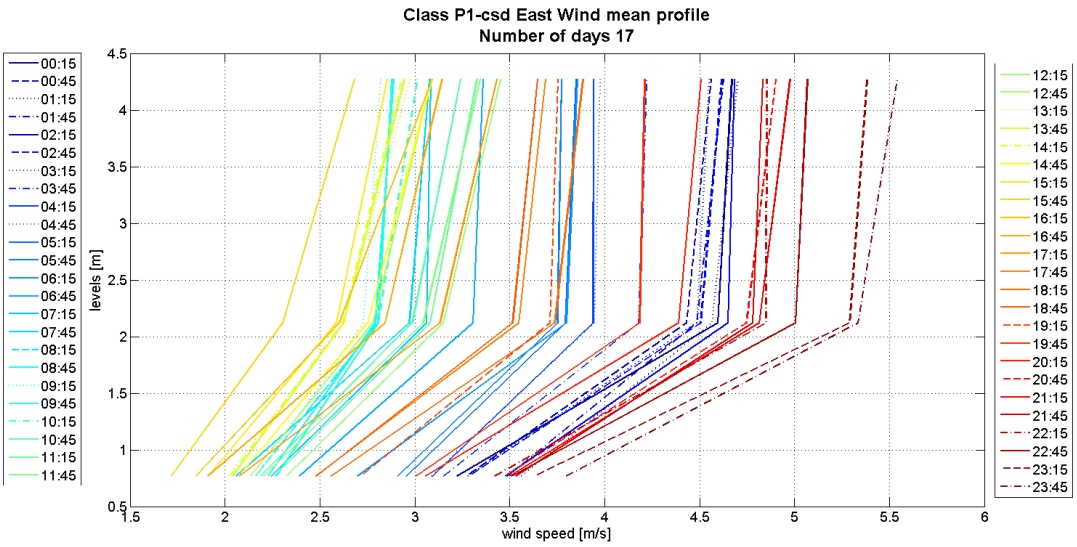

Figure 5.11: The mean wind profile of 17 clear days. Each line represent an half hour period, from the blue one (early morning) to the dark red one (late evening). On the x-axis there is the wind speed, instead on the y-axis there is the height of the cup anemometer.

speeds.

Preparatory to following section is the plot in Figure 5.12 of the potential temperature mean profile over the 17 thermally driven days found. The thicker lines represent time step of three hours (00:15, 3:15, 6:15 UTC etc.) and help us to catch the evolution of the profile of potential temperature for thermally driven days.

During the night the profile is typically stable, with a temperature increasing with the height. When the sun rises, progressively the entire profiled layer is warmed, thus there is a shift towards higher temperatures; around 9 UTC in the morning an inversion takes place and the middle level results colder than first and third. This inversion starts to disappear at 15 UTC in the afternoon, when the solar incoming radiation has decreased since 2 hours, and the stable profile is again established.

There is not, in this mean profile, a properly unstable profile, that is expected around noon. The first plausible reason is the height of the profile. Probably, at Arbeser, under 3.88m with a not calm wind conditions the unstable profile cannot develop. Another reason maybe found in the averaging itself, in fact a mixture of neutral, unstable and stable profiles may have changed toward a more stable

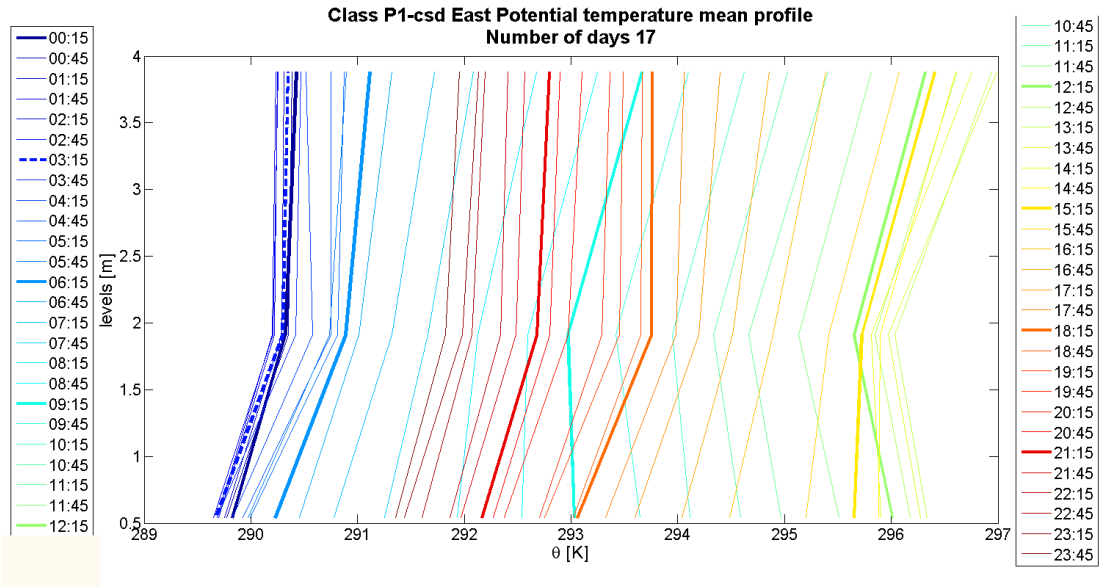

Figure 5.12: The mean potential temperature profile of 17 thermally driven days. Each line represents an half hour period, from the blue one (early morning) to the dark red one (late evening). On the x-axis there is the potential temperature in Kelvin, instead on the y-axis there is the height of the temperature measurements. Every three hours there is a thicker line to facilitate the comprehension.

situation. This fact, however, gives a hint: the *mean* θ profile of thermally driven days is mainly stable, or near neutral.

If the ground temperature estimation with the radiometer[5] is added, the profile results even more stable, and turns to unstable only between the ground and the second level around noon. The ground level temperature has to be treated very carefully, in fact in case of snow on the ground the influence is totally different because of the different albedo. A bare ground warms faster because it is darker than snow, in case of fresh snow the albedo is approximately 0.9 (see Tab. 1.1) and the calculated ground temperature is approximately constant during the day. Most of the selected thermally driven days are measured during winter season, or

[5]This parameter is calculated using the Stefan Boltzmann law and the upward long wave radiation:

$$T_{ground} = \sqrt[4]{\frac{LW\uparrow}{\sigma_{SB}}} \tag{5.2}$$

and the result is in Kelvin.

when the ground at Arbeser is covered by snow. To prove the snow coverage it is possible to analyse the *albedo* data, that is calculated with Eq. (1.22). It is not reliable to use the snow depth sensor measurements, because it was proved that it has a systematic error, but no further inspections were done in order to correct this error.

The albedo data of thermally driven days are presented in Table 5.5.

Date	Albedo	Snow on the ground
04-Oct-2014	0.15	No snow
27-Oct-2014	0.22	No snow
13-Feb-2015	0.64	Snow
16-Feb-2015	0.62	Snow
17-Feb-2015	0.62	Snow
20-Feb-2015	0.62	Snow
08-Mar-2015	0.67	Snow
20-Mar-2015	0.61	Snow
23-Mar-2015	0.65	Snow
09-Apr-2015	0.67	Snow
10-Apr-2015	0.61	Snow
19-Apr-2015	0.39	Scattered snow
01-Jul-2015	0.21	No snow
01-Oct-2015	0.19	No snow
27-Oct-2015	0.18	No snow
30-Oct-2015	0.20	No snow
12-Nov-2015	0.18	No snow

Table 5.5: The 16 clear-sky days detected with the Clear Days Algorithm on low frequency data. Here are shown the daily mean albedo values (second column) and the estimation of snow cover. The albedo varies a lot during the day, this is due to the sun declination and the hour of the day. In particular the albedo is approximately maximum (1) in late evening and early morning, when the snow is like a reflective surface. When the sun is at its zenith the albedo depends uniquely on the whiteness of the surface, and for old snow is around $0.4 \div 0.5$. When the daily average is around 0.6 probably the ground is covered by snow, instead with values of 0.2 I expect bare ground.

5.3 Turbulence Data

After the analysis of low frequency data just done, I move on to the high-frequency data collected with the ultrasonic anemometer and with the krypton hygrometer. In this section I apply, after all the quality control explained in Section 4.4.3, to the "medium quality" dataset the classification built on standard meteorological data (low frequency dataset).

5.3.1 Preliminaries on Application of Classification

The selected days with the P1-csd East classification are summarised in Table 5.6 and only 11 of 17 days can be analysed on the base of sonic anemometer data. Concerning the fast hygrometer data, there is only one complete day and three incomplete days.

Consequently the latent heat flux and all the covariances involving the fluctuations of humidity will be useless. Thus the main part of the work can be done only on momentum integral statistics (fluxes, variances, and other order moments) and sensible heat.

The Bowen Ratio Method

I try different methods to overcome this lack of data in absolute humidity. The most promising is the Bowen ratio method (Bowen, 1926 [4]). The Bowen ratio is defined as

$$B_0 = \frac{SH}{LE} = \frac{c_p \overline{w'\theta'}}{L_v \overline{w'q'}} \tag{5.3}$$

it can be used to obtain the latent heat flux starting from the sensible heat flux, this is useful because the measurements of SH are more accurate and for longer periods of time respect LE.

I calculate the Bowen ratio starting from the low frequency data using the following expression

$$B_0 = \gamma \frac{\Delta\theta}{\Delta q} = \gamma \frac{(\theta_{down} - \theta_{up})}{(q_{down} - q_{up})} \tag{5.4}$$

where *up* and *down* represent two different measuring levels of the mast. The specific humidity, q, is calculated starting from relative humidity by means of Equation 5.1. The γ is the psychrometric constant, that is

$$\gamma = c_p / L_v = 0.00041 (\mathrm{g_{water}}/\mathrm{g_{air}}) \mathrm{K}^{-1}. \tag{5.5}$$

The above Eq. (5.4) assumes that:

Date	Sonic availability	KH20 availability
04-Oct-2014	Not available	Not available
27-Oct-2014	Yes	Yes
13-Feb-2015	No data	No data
16-Feb-2015	No data	No data
17-Feb-2015	No data	No data
20-Feb-2015	No data	No data
08-Mar-2015	Yes	No data
20-Mar-2015	Yes	No data
23-Mar-2015	Yes	Incomplete data
09-Apr-2015	Yes	Incomplete data
10-Apr-2015	Yes	No data
19-Apr-2015	Yes	Incomplete data
01-Jul-2015	No data	Not available
01-Oct-2015	Yes	Not available
27-Oct-2015	Yes	Not available
30-Oct-2015	Yes	Not available
12-Nov-2015	Yes	Not available
Total	11 days of 17	4 days of 17

Table 5.6: Data availablity for turbulence (high-frequency) data at Arbeser for days (1st column) identified as P1-csd East from the low-frequency data. In the second column I write whether the sonic data is available (instrument installed) or not and if the instrument works or not (Yes/No data). The third column is about the Krypton hygrometer.

1. the turbulent fluxes can be approximated by a first order closure, for example for the sensible heat flux it is possible to write

$$\overline{w'\theta'} = -K_h \frac{\mathrm{d}\,\theta}{\mathrm{d}\,z} \tag{5.6}$$

and correspondingly for the latent heat flux

$$\overline{w'q'} = K_q \frac{\mathrm{d}\,q}{\mathrm{d}\,z}; \tag{5.7}$$

2. the gradients are approximated by differences

$$\frac{\mathrm{d}\,\theta}{\mathrm{d}\,z} \approx \frac{\Delta\theta}{\Delta z}; \tag{5.8}$$

3. K_h and K_q are assumed to be equal.

From the Chapter 3 is known that the station has three levels, thus I evaluated the Bowen ratio on the three possible combination of levels: first-second, first-third and second-third. In this calculation there is a background error due to possible temperature inversion within the three levels. In particular, the inversions are not rare within the first and the third level, but also within the other two, in these cases is quite impossible to find them. This is a problem because the temperature difference is damaged by the inversion, and the assumptions listed above for the Bowen ratio are not true in case of inversion, and moreover the heat flux that I want to calculate is definitely wrong.

However it is possible to evaluate the Bowen ratio introducing some controls. The first control is to prevent inversions within the three levels, more in details if θ_2 is at the same time bigger (smaller) than θ_1 and θ_3 an inversion occurs. The second control regards the temperature difference ($\Delta\theta$), if it is smaller than the standard deviation associated to θ the point is discarded. The third control is on specific humidity, in this case if the Δq is smaller than the smallest value $q = 0.0005 \mathrm{g}_{\mathrm{vapour}}/\mathrm{g}_{\mathrm{air}}$ the point is discarded.

Applying these three levels of control I am able to produce some reliable values for the Bowen ratio. To assess the reliability I decided to evaluate the Bowen ratio in those cases where the krypton hygrometer worked, using Eq. 5.3. Thus I plotted these values with a scatter plot against the same values evaluated with the low frequency data. The results are shown in Figure 5.13.

From the literature the range of Bowen ratio goes from 5 to 10 over semi-arid region, 0.5 over grasslands, 0.2 over irrigated orchards or grass, 0.1 over sea, to some negative values over oases (Stull, 1988 [45]).

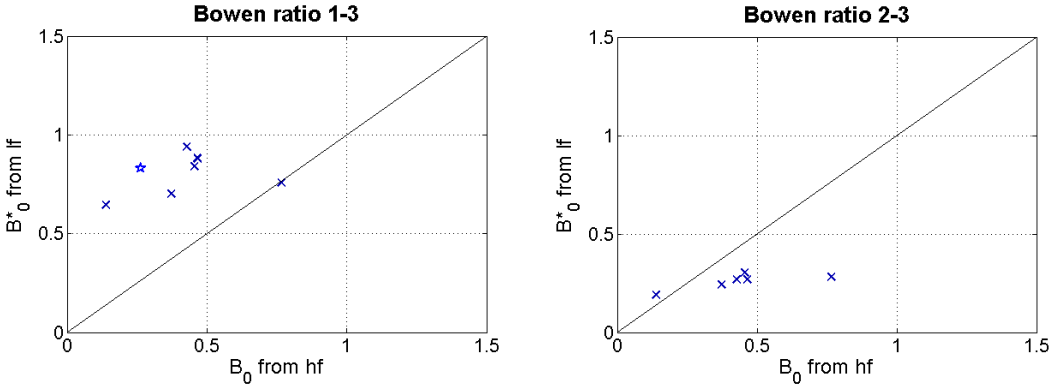

(a) Bowen ratio from levels 1 and 3.

(b) Bowen ratio from levels 2 and 3.

Figure 5.13: Bowen ratio comparison, the data base is the HiQ dataset, thus 89 days where only few periods are available, moreover due to the restrictions on Bowen ratio calculation only few data is comparable. In panel (a) the B_0^* is calculated using gradients between the first and the third levels. In this case the B_0^* is bigger respect to B_0 from high frequency data. In panel (b) the B_0^* is calculated using gradients between the second and the third levels. In this case the B_0^* is lower respect to B_0.

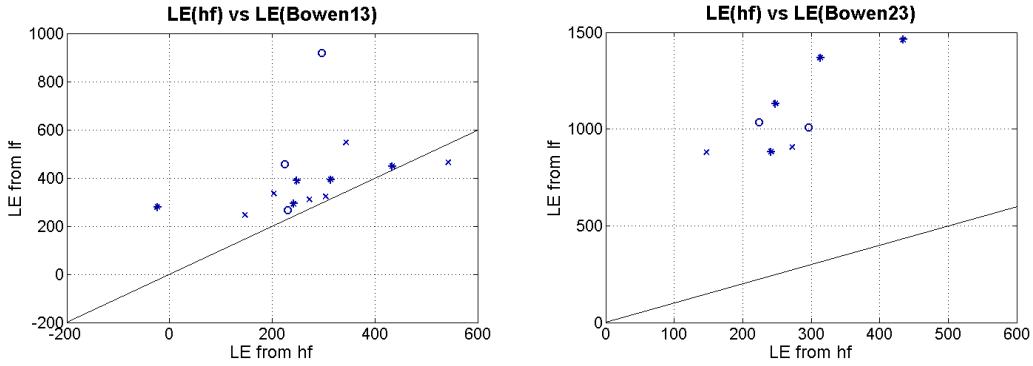

(a) (b)

Figure 5.14: The comparison between LE from high frequency data and low frequency data for two different Bowen ratio. In (a) the levels involved in the calculation of B_0 are the first and the third, in (b) are the second and the third. The black line represent equal values for LE from high frequency and low frequency data. In (a) LE values from low frequency (with the Bowen ratio evaluated with levels 1 and 3) are slightly greater, but near this line. Instead, in (b) the values of LE from Bowen ratio are much bigger, between 2 and 3 times. The data base is the HiQ dataset.

I also estimated the uncertainty for the Bowen ratio. The procedure applied is not conform to the theory of error analysis (it can be called error estimation), in fact I summarise all the error propagation on specific humidity with the estimation of its relative error. This relative error on q is around 0.6%, then from this I calculate properly the uncertainty on the Bowen ratio as follows:

$$\begin{aligned} \sigma^2_{B_0} &= \gamma^2 \left[\left(\frac{1}{\Delta q} \right)^2 \sigma^2_{\Delta\theta} + \left(\frac{\Delta\theta}{(\Delta q)^2} \right)^2 \sigma^2_{\Delta q} \right] \\ \sigma_{\Delta\theta} &= \sigma_{\theta_i} + \sigma_{\theta_j} \\ \sigma_{\Delta q} &= q_i \cdot 0.6\% + q_j \cdot 0.6\% \end{aligned} \tag{5.9}$$

In (5.9) the indexes i,j refer to the two levels considered in the evaluation of differences. In Table 5.7 are shown the Bowen ratio calculated from low frequency data with its uncertainties. As you can see the uncertainties are very big, this is due to both the method used to assess the uncertainties and the method used to calculate the Bowen ratio.

${}^{13}B_0^*$	${}^{13}\sigma_{B_0^*}$	${}^{23}B_0^*$	${}^{23}\sigma_{B_0^*}$	${}^{hf}B_0$
0.65	2.94	0.19	1.08	0.14
0.70	2.96	0.24	1.37	0.37
0.76	3.50	0.28	1.69	0.77
0.84	4.46	0.30	2.03	0.46
0.83	8.31	NaN	NaN	0.27
0.94	5.64	0.27	1.88	0.43
0.88	5.53	0.27	1.86	0.47

Table 5.7: Values and uncertainties of the Bowen ratio evaluated with low frequency data. In the last column there are the values of Bowen ration calculated with high frequency data. These values are used to plot Figure 5.13.

Starting from these results I tried to evaluate the latent heat with the Bowen ratio method, I used the reversed formula of (5.3) where the B_0 is evaluated starting from low frequency data with (5.4). In Figure 5.14 are shown the LE results corresponding to data in Fig. 5.13. I used the three different levels combinations for the B_0, and the mean results for the entire dataset are showed in Figure 5.15. In Figures 5.13 and 5.14 the levels combination 1-2 is not showed, because there are not points of B_0^* matching the B_0 from the high frequency data. From this

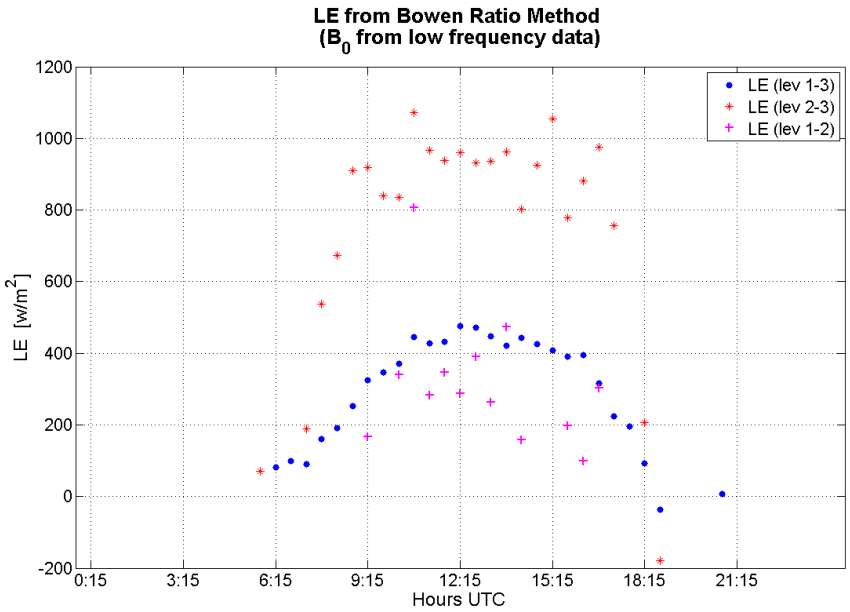

Figure 5.15: The LE is evaluated using the reversed formula of (5.3), where the Bowen ratio is calculated using (5.4) starting from low frequency data with different combinations of three available levels. The represented data is the averaged daily cycle of all available data.

figure is possible to distinguish two similar behaviour for the LE evaluated from levels 1-3 and 1-2, and a generally higher LE from levels 2-3.

To find the best combination of levels is necessary to compare, as done for the Bowen ratio itself, the LE from low frequency data with the LE from the high frequency data. The results are shown in Figure 5.14

Therefore it is possible to use the Bowen ratio calculated from first and third level to integrate the lack of specific humidity measurements with the high frequency hygrometer. I will use it later within the energy balance.

Scaling approach

The analysis continues with testing the surface layer similarity and is involved in the understanding on what happens in a such complex site. First of all it is necessary to remember that at a peak location the shape and behaviour of the boundary layer are not already well known and neither of the surface layer. Even if it is not possible to expect surface layer characteristics to prevail, because the

requested conditions are violated, they are used as a reference since at least the height range of the sonic anemometer measurements (4.67 ± 0.02m) corresponds to that of a surface layer.

The scaling approach used aimed to follow the nowadays knowledge on surface layer scaling, thus the Monin-Obukhov similarity theory (MOST) for stable surface layer with constant fluxes. The MOST is concerned for homogeneous and horizontally flat terrain, so in principle is not certain its validity in complex terrain. The first approach is to use Monin-Obukhov scaling variables, and test them with Arbeser data, and control whether these variables scale properly. The second approach is to use others scaling relationships founded by experiments in complex terrain. The main reference is Nadeau *et al.* (2013)[31], in their case the MOST as it is cannot be applied. In fact, they do not have constant fluxes (within the 10% of variation) in the vertical profile of the surface layer (up to 6 m), but probably, as they say, the surface layer was, sometimes, too thin to be detected, or the presence of advective fluxes had modified the expected results. At Arbeser there is only one sonic installed, thus it is not possible to assess the variation of fluxes on a vertical profile. A priori I do not know if the Monin-Obukhov requirement on fluxes is fulfilled, but depending on the results it will be possible to understand if the MOST is appropriate.

First of all I analysed the daily cycles for several variables, then I try to average them and create a mean daily cycle for the thermally driven days.

The variables considered are:

- Mean wind speed rotated on the flow direction with a double rotation, $\overline{U}$. It is useful to immediately normalise it with the friction velocity u_*, thus the expectation from the logarithmic profile predicted by MOST for neutral conditions is

$$\frac{\overline{U}}{u_*} = \frac{1}{\kappa} \ln\left(\frac{z}{z_0}\right) \tag{5.10}$$

  where z is the vertical coordinate, z_0 is the roughness length and κ is the von Kármán constant. In this case, assuming $\kappa = 0.4$ and the roughness length of $z_0 = 10$cm, the expectation is $\overline{U}/u_* \simeq 9.6$. In order to verify that expectation I evaluate the uncertainties for each variable.

- The Monin-Obukhov stability parameter z/L (elsewhere also called ζ, that has not to be confused with relative vorticity of Eq. (1.55)). The Obukhov length is given in Equation (1.54), and z is the height of the anemometer from the ground. This variable has positive values when the surface layer is *stable*, and negative values when it is *unstable*. Between stability and

instability situation there is a range in between crowded by near-neutral cases. The limits that I choose, and that are usually chosen, for the near-neutral cases are $|\zeta| < 0.05$.

- The Sensible Heat flux (SH) evaluated by EdiRe with the formula in Equation (1.24).
- The Turbulent Kinetic Energy, governed by the formula (1.46). I evaluate it using another equivalent formula

$$\overline{e} = \frac{1}{2}(\sigma_u^2 + \sigma_v^2 + \sigma_w^2) \tag{5.11}$$

that is the same as (1.46) applying Reynolds averaging rules.

- The standard deviation of velocity components scaled with the friction velocity

$$\frac{\sigma_u}{u_*}, \quad \frac{\sigma_v}{u_*}, \quad \frac{\sigma_w}{u_*} \tag{5.12}$$

and their comparison with surface layer scaling functions.

- The dimensionless standard deviation of sonic temperature

$$\frac{\sigma_\theta}{|\Theta_*|} \tag{5.13}$$

and its comparison with surface scaling function.

Uncertainties Estimation

Before introducing and commenting the plots of the aforementioned variables, it is essential to estimate for each variable its uncertainty in order to avoid plotting random points.

For eddy covariance variables it is not a simple matter, but based on the Wyngaard uncertainty estimation method, previously used for quality assessment (Section 4.4.3) in its inverted mode by Stiperski and Rotach (2016) [43].

In particular I have combined this way to estimate the error (starting from the a variables calculated by EdiRe, see Equations (4.32), (4.33) and (4.31)) with a standard error propagation.

As stated before when a turbulence parameter is measured some part of its spectrum is always kept out from the averaging period. Thus the obtained values of variance, covariance and all the related variables are not completely correct.

The real issue is that it is not possible to include everything in our averaging, and also the structure itself of the turbulence may vary extremely rapidly. Sometimes with an averaging period of 15 minutes everything is considered, from the bigger eddy to the small one, but other times hours are needed. To prevent the use of wrong data, or simply incomplete data, is fundamental to couple the measure with its uncertainty. On the other side a not constant averaging period is uncomfortable in a standard programming way.

Another issue that I have to mention is that I cannot use the High Quality (HiQ) dataset that itself contains data with low uncertainties and stationarity requirements (see Section 4.4.2). I use the Medium Quality (MeQ) dataset because it contains more data, and it permits me to create more than half-day plot. With the MeQ data I am not sure about their reliability, so that I produce plots with errorbars.

From Wyngaard (1973) [55] I can express the variance of a short-term averaged property whose true average is $\overline{f}$ as

$$\sigma^2 = a^2\overline{f}^2 = \overline{\left[\tau_a^{-1}\int_0^{\tau_a} f(t+t')\,\mathrm{d}\,t' - \overline{f}\right]^2} \tag{5.14}$$

I am interested in the first part of this equation, where I know both a (see Equations (4.31), (4.32) and (4.33)) and $\overline{f}$.

In the following equation I summarise all the uncertainties; I will express always the variance.

Sensible heat flux, SH is the mean sensible heat flux for the averaging interval considered

$$\sigma_{SH}^2 = a_{\overline{w'\theta'}}^2 \cdot SH^2 \tag{5.15}$$

Friction velocity, in this case for clarity I prefer to repeat the definition of friction velocity

$$u_* = \left(\overline{u'w'}^2 + \overline{v'w'}^2\right)^{1/4} \tag{5.16}$$

$$\sigma_{u_*}^2 = \frac{1}{4}\left[\left(\frac{\overline{u'w'}}{u_*^3}\right)^2 a_{uw}^2(\overline{u'w'})^2 + \left(\frac{\overline{v'w'}}{u_*^3}\right)^2 a_{vw}^2(\overline{v'w'})^2\right] \tag{5.17}$$

Turbulent Kinetic Energy

$$\sigma_{TKE}^2 = \frac{1}{2}\left(a_u^2\sigma_u^2 + a_v^2\sigma_v^2 + a_w^2\sigma_w^2\right) \tag{5.18}$$

Stability of Monin-Obukhov, first I evaluate the uncertainty on the Obukhov Length (see Equation (1.54))

$$\sigma_L^2 = \left(\frac{1}{\kappa g}\right)^2 \left[\left(3u_*^2 \frac{\overline{\theta}}{(\overline{w'\theta'})}\right)^2 \sigma_{u_*}^2 + \left(\frac{u_*^3}{(\overline{w'\theta'})}\right)^2 \sigma_\theta^2 + \left(\frac{u_*^3 \overline{\theta}}{(\overline{w'\theta'})^2}\right)^2 a_{w\theta}^2 \overline{w'\theta'}^2 \right] \tag{5.19}$$

where σ_θ is the corrected standard deviation of sonic temperature, that you can find from (3.14); $\kappa = 0.4$ is the von Káramán constant, and $g = 9.81\text{m/s}^2$ is the gravity acceleration. This σ_L can be used to evaluate the uncertainty on ζ, that is

$$\begin{aligned} \sigma_\zeta &= \left(\frac{\sigma_z}{z} + \frac{\sigma_L}{L}\right)\frac{z}{L} \\ &= \frac{1}{z}\left(\sigma_z \zeta + \sigma_L \zeta^2\right) \end{aligned} \tag{5.20}$$

and z is the height of the sonic, its uncertainty is $\sigma_z = 0.02\text{m}$.

Turbulent Kinetic Energy scaled with friction velocity

$$\sigma_{\overline{e}/u_*}^2 = \left(\frac{1}{u_*^2}\right)^2 \sigma_{\overline{e}}^2 + \left(\frac{2\overline{e}}{u_*^3}\right)^2 \sigma_{u_*}^2 \tag{5.21}$$

where $\overline{e}$ is the TKE.

Mean flow wind velocity scaled with friction velocity

$$\sigma_{U/u_*} = \left(\frac{1}{u_*}\right)^2 a_{U^2}^2 \overline{U}^2 + \left(\frac{U}{u_*^2}\right)^2 \sigma_{u_*}^2 \tag{5.22}$$

Monin Obukhov scaling temperature, this temperature is obtained with the formula (1.53), thus its error depends on the sensible heat flux and on friction velocity:

$$\sigma_{\Theta_*}^2 = \left(\frac{1}{u_*}\right)^2 a_{w\theta}^2 (\overline{w'\theta'})^2 + \left(\frac{(\overline{w'\theta'})}{u_*^2}\right)^2 \sigma_{u_*}^2 \tag{5.23}$$

Wind components standard deviations scaled with friction velocity

$$\sigma_{\tilde{\sigma}_i/u_*}^2 = \left(\frac{\tilde{\sigma}_i}{u_*^2}\right)^2 \sigma_{u_*}^2 \tag{5.24}$$

where the i index indicates the three components u,v,w.

Sonic temperature standard deviation scaled with MO scale temperature

$$\sigma_{\tilde{\sigma}_\theta/u_*}^2 = \left(\frac{\tilde{\sigma}_\theta}{\Theta_*^2}\right)^2 \sigma_{\Theta_*}^2 \tag{5.25}$$

where $\tilde{\sigma_\theta}$ is the corrected standard deviation of sonic temperature (3.14).

Weighted Averages on Daily Cycles

As I mentioned before, I evaluated for thermally driven days a mean daily cycle for the most relevant variables. I decided to evaluate a weighted mean where as weights I use the uncertainties just calculated.

In particular, a weighted mean and its uncertainty is expressed by these equations:

$$\overline{x} = \frac{\sum_{i=1}^{n} x_i w_i}{\sum_{i=1}^{n} w_i} \tag{5.26}$$

where the weights are

$$w_i = \frac{1}{\sigma_i^2}. \tag{5.27}$$

The uncertainty is

$$\sigma_{\overline{x}} = \frac{1}{\sqrt{\sum w_i}} \tag{5.28}$$

In some cases I notice that the uncertainty on the averaged mean calculated using the formula (5.28) is very small. I try then to calculate the maximum error, that is slightly greater:

$$\delta_{\overline{x}} = \frac{\overline{\sigma_{x_i}}}{\sqrt{n}} \tag{5.29}$$

Normal Averages on Daily Cycles

In some cases is not possible to use the weighted average. In fact, if the interested lay on the overall variability of the averaged variable, and this variable has, for example, values with small uncertainties around a specific value, the weighted mean will be invalidated. The simple approach is to use a normal average, that is expressed by the equation

$$\bar{x} = \frac{\sum_{i=1}^{n} x_i}{n} \tag{5.30}$$

and the uncertainty associated with this mean is (following Taylor 1997 [46])

$$\sigma_{\bar{x}} = \frac{\frac{1}{n}\sum_{i=1}^{n} \sigma_{x_i}}{\sqrt{n}}, \tag{5.31}$$

that is the maximum error of Eq. (5.29).

5.3.2 Results of the Application of Classification

Now I move on the results and on the comments of plots. I will subdivide this section in subsections specifically dedicated to one variable or scaling; at the end I will try to sum up the main results.

Local Stability

The local stability parameter, as previously introduced in Chapter 1, is $z/L \equiv \zeta$. For negative values the layer is unstable, instead for positive value it is stable. I consider near neutral values in the range $-0.05 < \zeta < 0.05$.

Summing up all the available periods (30 minutes averages) for thermally driven days I have 768 data points. They are subdivided in Table 5.8 according to stability.

Stability	Number of periods	Percentage
Stable $\zeta > 0.05$	58	7.55%
Near neutral	611	79.56%
Unstable $\zeta < -0.05$	99	12.89%

Table 5.8: Subdivision of thermally driven days data according to Monin Obukhov stability parameter. The data base is the Medium Quality.

From that it is possible to see that the majority of periods are near neutral, and thus if I try to calculate the average daily cycle I obtain a near neutral tendency (see Figure 5.16(b)). In Fig. 5.16(a) I plot all thermally driven periods, on zero line there are all the values less than 10^{-2}, and on the y-axis the scale is logarithmic. At first sight it is possible to state a major instability during daytime and a neutral-stability during nighttime.

Moving to Fig. 5.16(b) is much clear, in particular the negative values during daytime and a near neutral situation during the nighttime can be appreciated. In this case I have not applied a weighted mean because the near neutral points have a smaller uncertainty and will flatten all the data in the near neutral zone. If I remove the near-neutral period (more than 79%) I can plot the Figure 5.17. In this case (Fig. 5.17(a)) the central area of the plot, near the zero line, is empty. But if you look more carefully it is clear that in Fig. 5.17(b) some values, especially in nighttime hours, fall in the near neutral area. The reason in this case is to be ascribed to the different stability of each day in the average during the night.

Apart from this in the middle of the daily cycle it is possible to assess a unstable area. This is a normal behaviour for the surface layer, apparently even if in complex terrain. Also without the near neutral cases I obtain on average quite frequently unstable stratification during the night. I ascertain that the net radiation is negative (the ground is cooling), the ground heat flux is practically zero. To get a negative z/L I need a positive heat flux, but without radiation forcing the only reason my be assess in the advection, a warm advection.

I tried to relate the stability parameter of Monin-Obukhov z/L to the potential temperature profile, evaluated from low frequency data, for the analysed days. The results of the stability from θ profile agree quite well with the z/L, and some cases where a dubious stability value is measured the θ profile can support this value and gives a better comprehension of the situation. In these days the expectation is approximately an unstable layer near surface around midday. As you can see from Figure 5.16(a), a lot of points are near neutral or also stable in these hours. Looking at potential temperature profiles I realise that most of those days have a near neutral profile, or a stable profile. Thus confirm the high frequency measurements' behaviour. The motivations of these behaviours are not clear, first I thought that the snow coverage of the ground might influence the buoyancy and the air convection at small scales. Certainly the snow modifies the flow, it keeps the ground temperature more constant and has another value for the albedo, thus it might affects also the sensible heat flux[6].

[6]I try to verify that but no correlation was present, and the snow depth values are not reliable, due to a not well known systematic error.

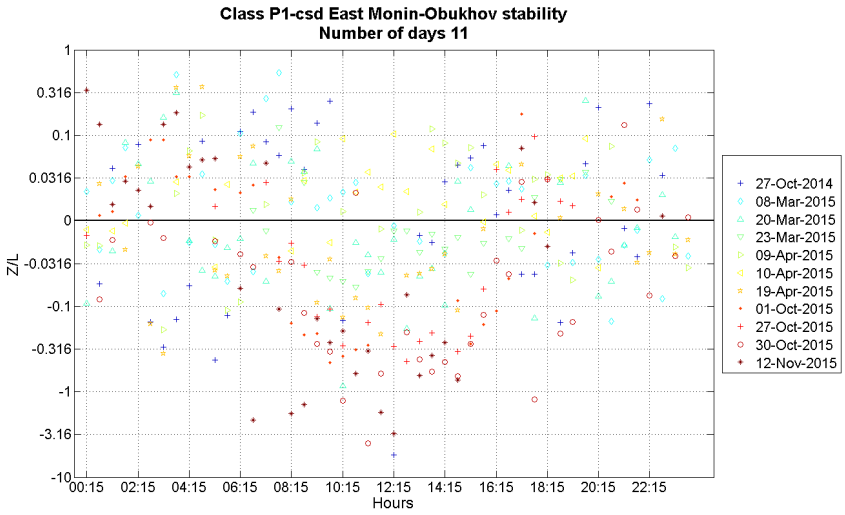

(a) All thermally driven days stability parameter. Here is not simple to see the clear day z/L daily cycle: negative values during daytime and positive or near neutral during nighttime. Thus instability during the day, due to bouyancy and wind shear, and stability during the night.

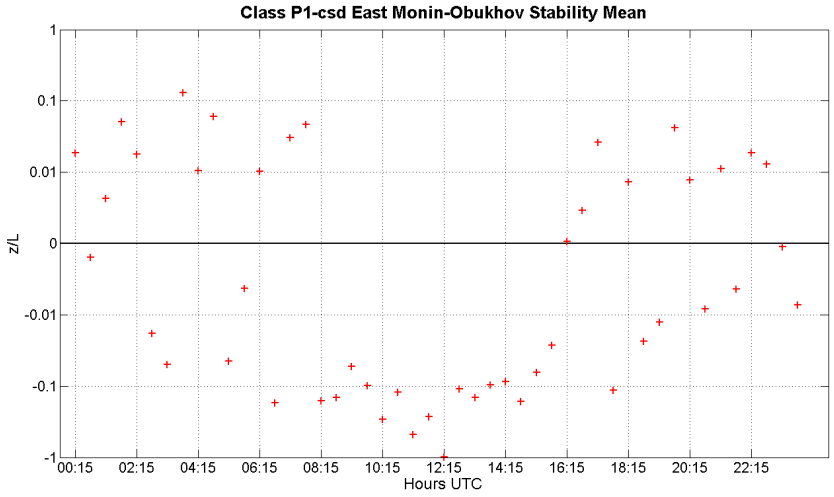

(b) Average of stability parameter over all data. Here is simple to catch the daily cycle, with a preponderance of negative values during the day and near neutral values during the night.

Figure 5.16: Surface layer stability parameter according to MOST.

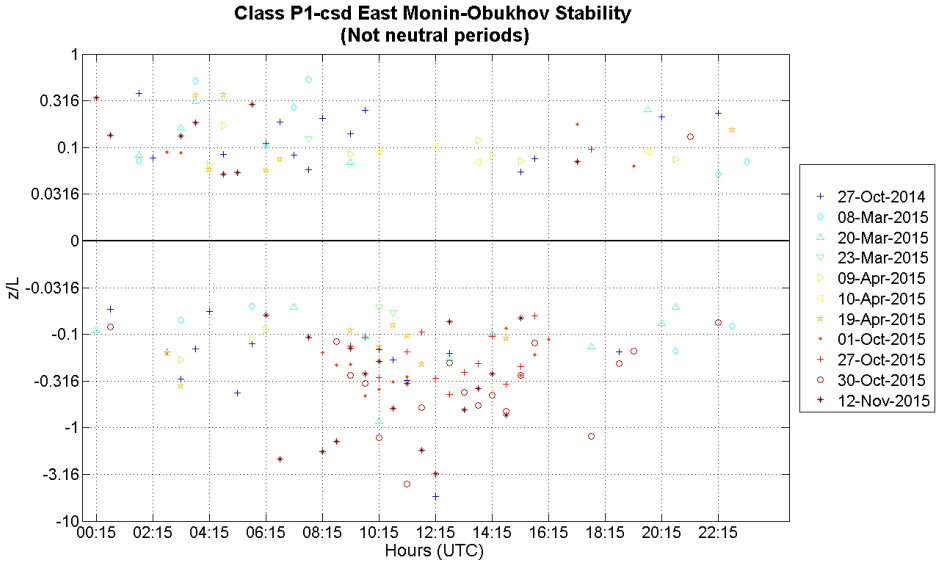

(a) All thermally driven days periods not near neutral.

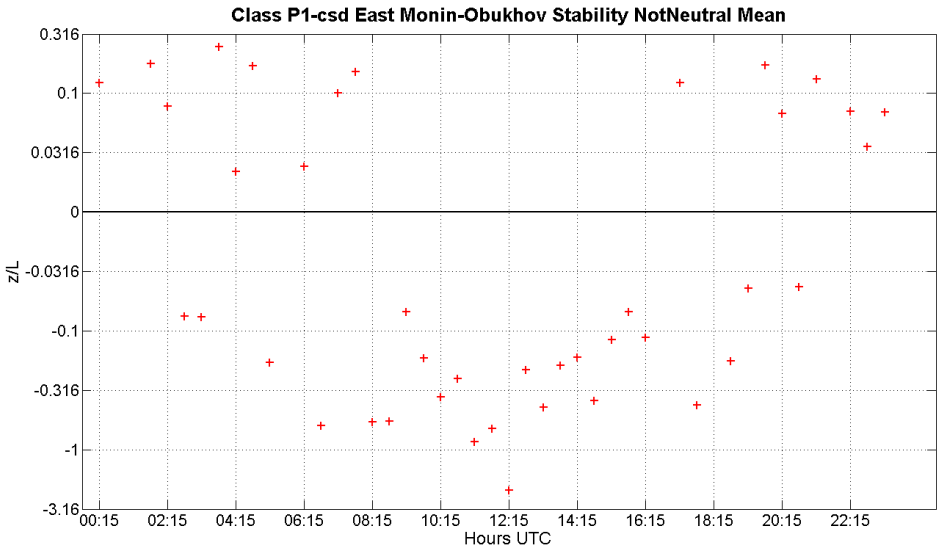

(b) Average of not near neutral cases. Some points during the night fall into the near neutral zone, this can be explained with a different contribution of each single day to the mean.

Figure 5.17: Surface layer stability parameter, the same plot of Fig. 5.16 but after the removing of near neutral points.

Mean Flow Velocity

The mean flow velocity is calculated by EdiRe applying a Double Rotation (DR) to the coordinate matrix. Thus this is the wind speed on the streamline, the other two components are nullified by the DR.

In this selection of days, represented in Figure 5.18, the wind speed does not exceed 9m/s and also the main direction is quite always from SSW. In this figure it is possible to see that the higher speeds are usually during night, when the measured layer has a stronger stability conditions.

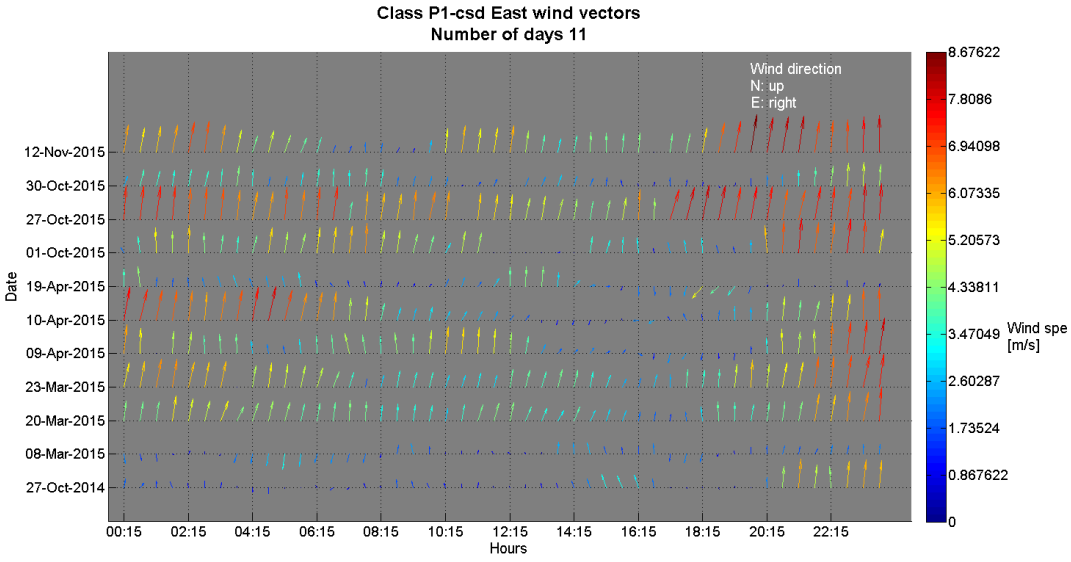

Figure 5.18: The eleven *thermally driven* days selected with all the previously explained choices. On x-axis there are the hours of the day, on y-axis the days; the vector are oriented in the same wind direction.

Rarely the wind direction changes and moves to the other side completely, that happens only four times in the second part of the day, and in particular on April 9th, 10th and 19th, 2015. On March 8th, 2015 the wind speed is very weak and the direction is oscillating from north to south several times.

The two days identified previously when analysing the low frequency data - February 17th, 2015 and October 4th, 2014, where a northeast wind component was discovered and related to the valley wind - are not available in the sonic dataset, because the instrument did not work during these days. This is a misfortune because is not feasible to check the turbulence of these flows.

Using the local stability parameter ζ I create two wind roses one for stable periods, where $\zeta > 0$, and one for unstable periods, with $\zeta < 0$. In this case I include the near neutral cases, namely with $-0.05 < \zeta < 0.05$. The two wind roses are depicted in Figure 5.19.

From these two wind roses it is clear that in the Arbeser's wind main direction is not possible to distinguish a prevalent stability pattern, in fact there are both stable and unstable cases. However, it is possible to notice that in the north-east quarter the little peak previously found is mainly stable. The reasons of this NE flow mainly stable are not completely understood, in fact, usually the upvalley wind brings unstable or neutral stratification due to the formation of the convective mixed layer in the valley. Probably the stable part of the NE flow detected is due to others reasons, for example, it could be a stable flow inside the capping inversion above the mixed layer.

Now it is interesting to take a look at the wind speed scaled with the friction velocity. I investigate at what degree the $\bar{U}/u_*$ for near neutral cases deviates from the ideal site expectation, that is approximately around 9.6. Thus I selected the near neutral cases using the aforesaid stability parameter ζ. The expectation is calculated using Eq.(5.10), and assuming a roughness length $z_0 = 0.1$ m (the vegetation is composed by alpine meadow, some small bushes downvalley on the ridge and stones), and $z = 4.67$m is the height of the sonic.

In Figure 5.20(a) the mean wind speed, in the flow direction after the double rotation, for near neutral half hour periods is shown. From this figure it is possible to see that the near neutral periods are equally distributed all over the daily cycle, some days (e.g. 8th and 23rd of March 2015) are showing many half hour periods in near neutral conditions. In general it is possible to identify two data clouds: one more scattered during the night, and one less scattered and with lower values of $\bar{U}/u_*$ during daytime. To understand something more I plotted the half hour average of these values. In Figure 5.20(b) it is shown the result, where the bar indicates the mean uncertainty for the half hour period. In this figure it is more clear the behaviour, during daytime hours the values are *lower* than the expected value, meanwhile during nighttime they are *greater*.

From these first scaling results I could state that for Arbeser, a mountain top site in complex terrain, the MOST seems to be incomplete.

In Figure 5.21(a) there are shown all the unstable periods for thermally driven days. The first remarkable aspect is the scarcity of points, in fact as it is possible to see from Tab. 5.8, only the 12.89% of half hour periods are unstable. But, as expected, the data cloud is more dense in daytime hours, between 8:15 UTC and 16:15 UTC. This is normal because instability is expected when the sun heats the ground and the convection starts. For unstable cases there is not a particular

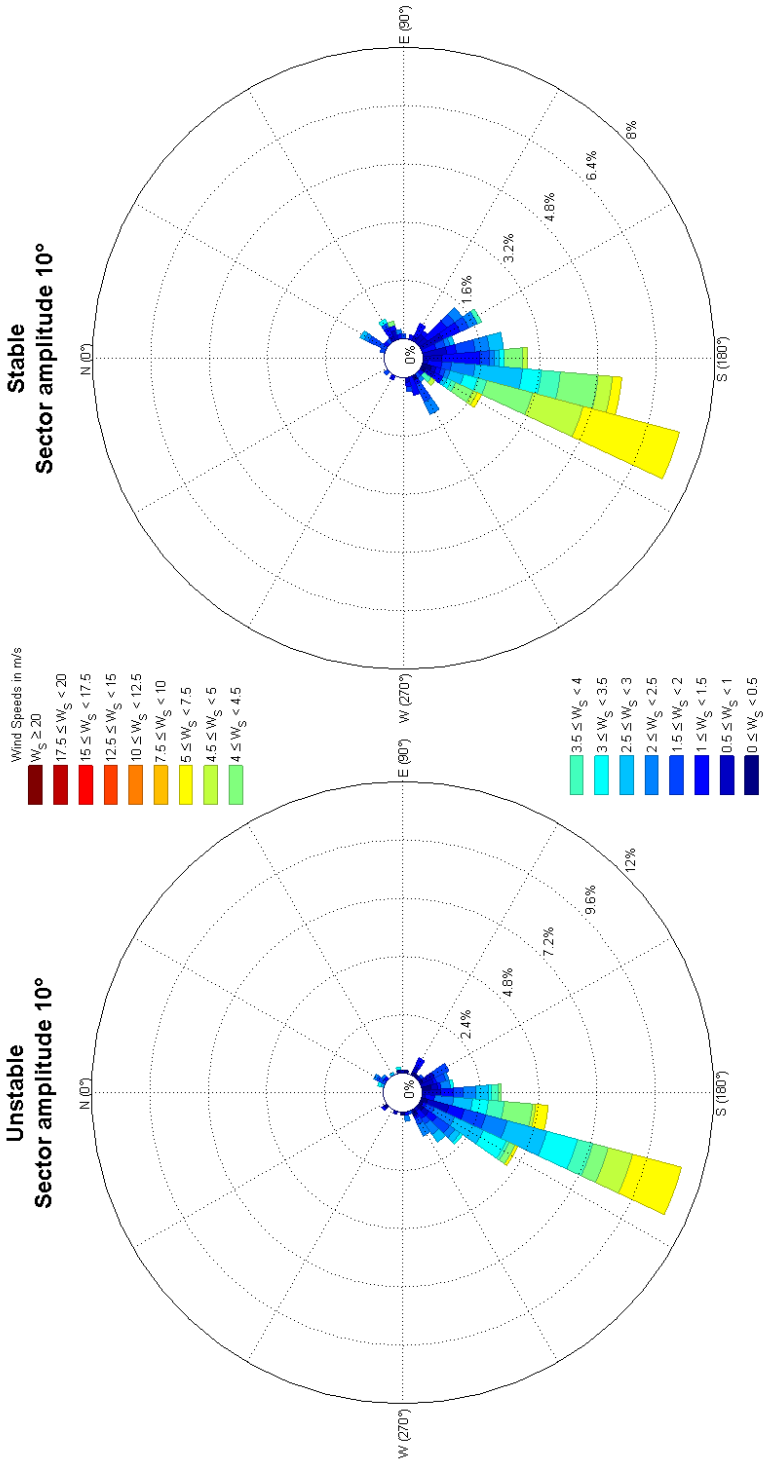

Figure 5.19: Wind rose of thermally driven days separated on the base of stability parameter.

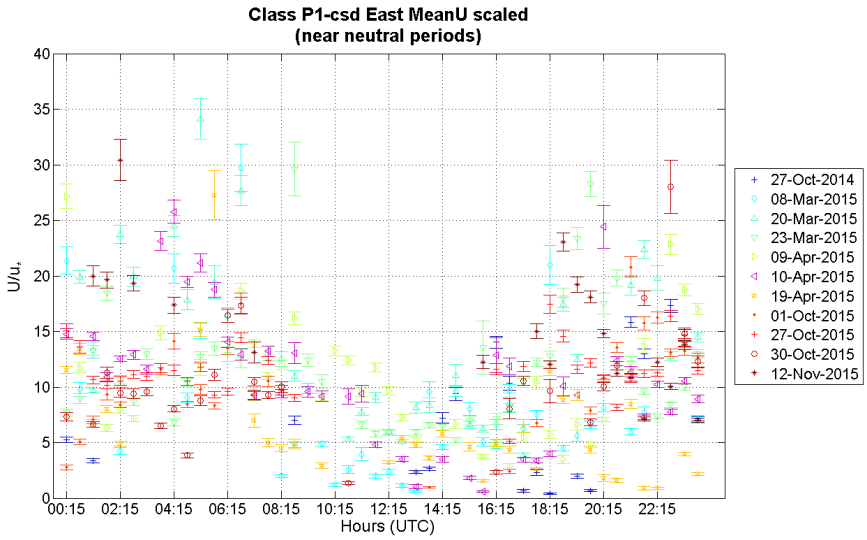

(a) The mean flow speed scaled with the friction velocity, each color and marker represent one daily cycle from the selected thermally driven days.

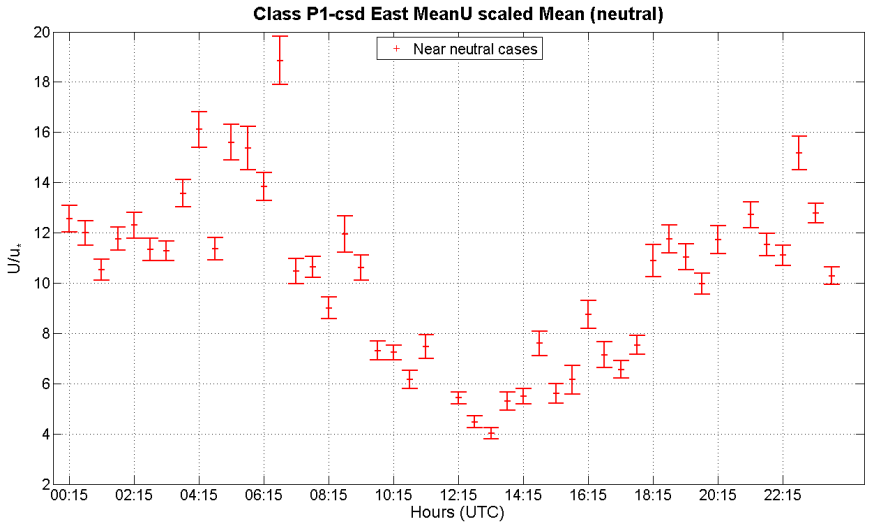

(b) The averaged mean flow speed scaled, this is the mean of data shown with the previous plot 5.20(a).

Figure 5.20: The flow velocity scaled by u_* after the double rotation for thermally driven days, for near neutral cases.

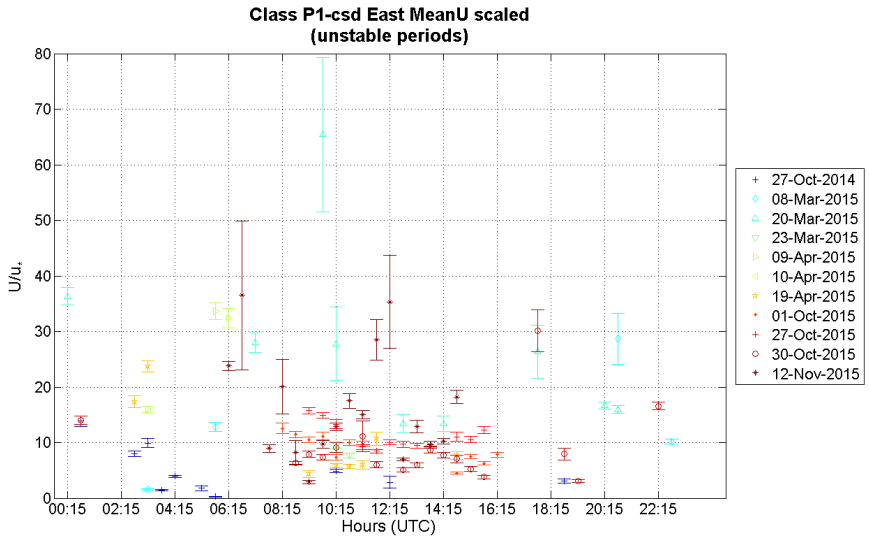

(a) The mean flow speed scaled with the friction velocity, each color and marker represent one daily cycle from the selected thermally driven days.

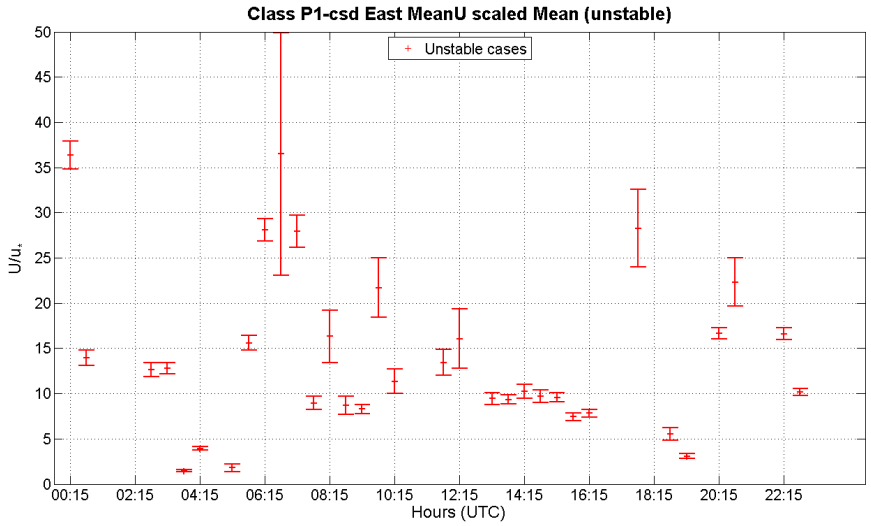

(b) The averaged mean flow speed scaled, this is the mean of data shown with the previous plot 5.21(a).

Figure 5.21: The flow velocity scaled by u_* after the double rotation for thermally driven days, in unstable cases.

expectation from the logarithmic profile, because it is verified only for neutral cases. Looking at the mean plot in Figure 5.21(b), that is the average of points presented in Fig. 5.21(a), it is possible to see that a well define behaviour is not present.

Turbulent Kinetic Energy

The TKE is a parameter that assess the kinetic energy of the turbulence. In the the first chapter is stated that usually during a clear day, and thermally driven days are clear, the turbulent motion starts to develop in the morning and it reaches the maximum after noon. Thus the expectation is the maximum of TKE in the first afternoon, and during the night a minimum.

On TKE (Figure 5.22(a)) the uncertainties are quite small, because, as you can see from Equation (5.18), they are related to Wyngaard relative error on u, v, w that are usually small, and they are related to the variances that are also formerly controlled by the "harsh" flagging. After the calculation of the weighted average it is clearly possible to see the daily cycle expected for the TKE (Figure 5.22(b)). Here there are small uncertainties, evaluated as the maximum error, that is the sum of each uncertainty that enter in the mean divided by the square root of the number of entries (see Eq. (5.29)). These are higher than that calculated with the standard error propagation method.

Turning to TKE scaled with friction velocity (TKE/u_*^2 or $\overline{e}/u_*^2$), the new target is a constant $\overline{e}/u_*^2$ during the day for a stable surface layer (Stull, 1988 [45])[7]. The threshold used for stability is $\zeta > 0.05$, as stated previously. It is possible to appreciate the plots in Figure 5.23, and in the first one where I plotted each daily cycle it is obvious that there are days with very high and uncertain $\overline{e}/u_*^2$, but the overall trend is under 6 even though with an oscillation in the middle of the day. In Figure 5.23(b) it is possible to appreciate that even if there are some data points with huge uncertainties, it is possible to fit them with an horizontal line, and affirm that, considering the uncertainties, the mean trend is constant, as expected by the surface layer scaling in stable conditions. In any case this group of data is very small (only 58 points, see Tab. 5.8), and more data are required for a reliable result.

[7]For more accuracy, the $\overline{e}/u_*^2$ tends to a constant value with higher stability of the surface layer. In near neutral condition and with small values of ζ the scaling function that describe the TKE is not constant, it is possible to see that in the Figure 1.7 of Kaimal and Finnigan, 1994 [22].

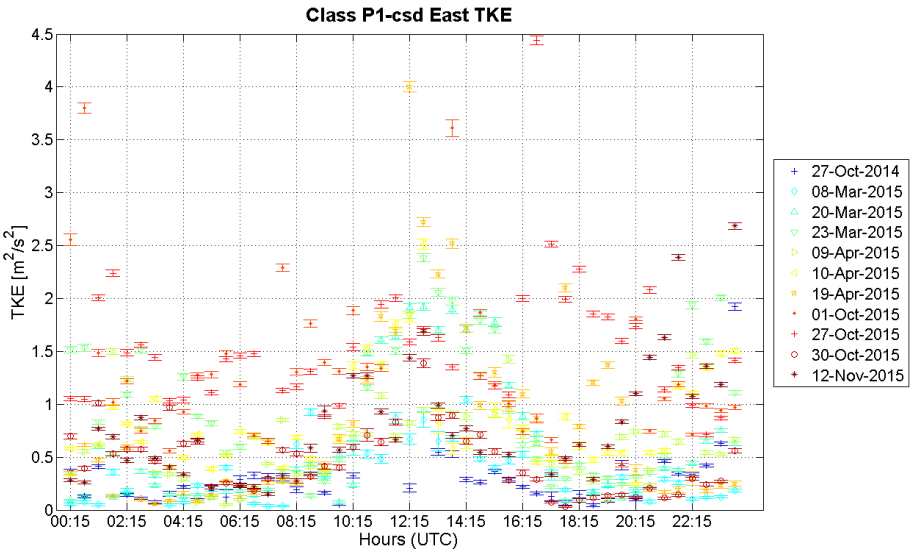

(a) TKE for thermally driven days.

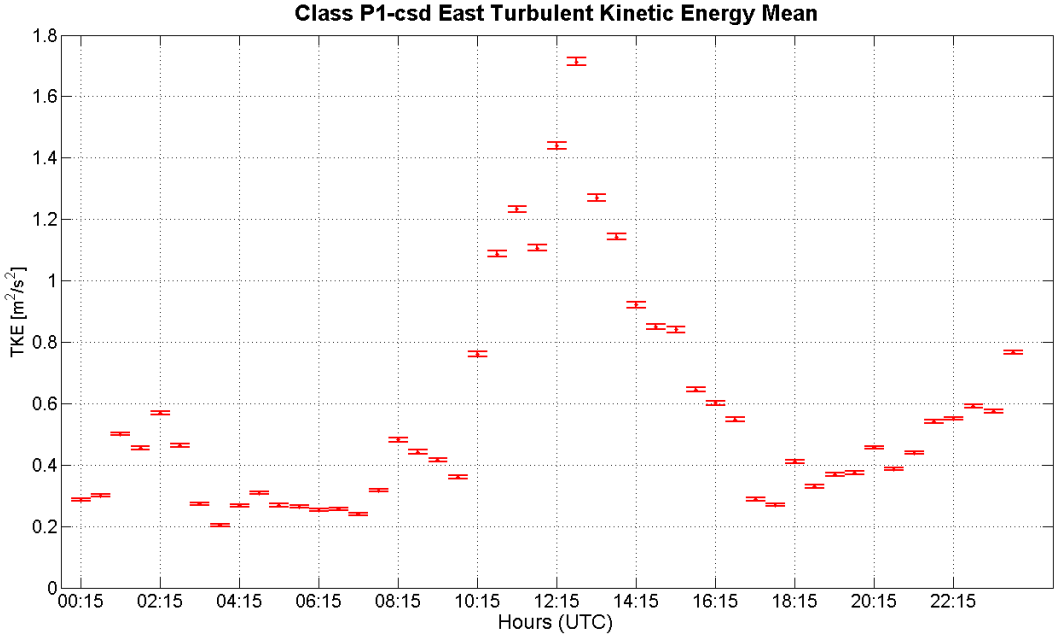

(b) The averaged TKE, the error bars denote the maximum error according to Eq (5.29).

Figure 5.22: Daily cycle of turbulent Kinetic Energy for thermally driven days.

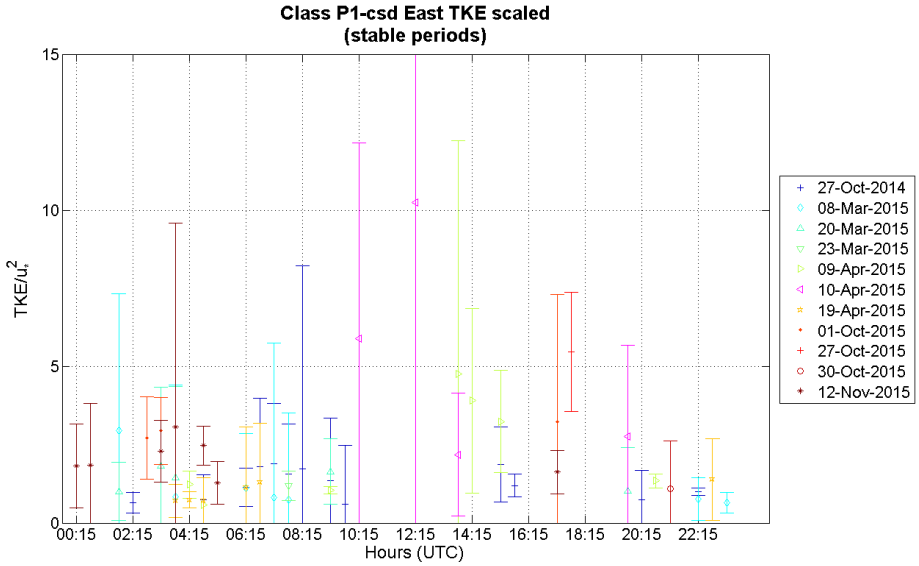

(a) TKE scaled for themally driven days.

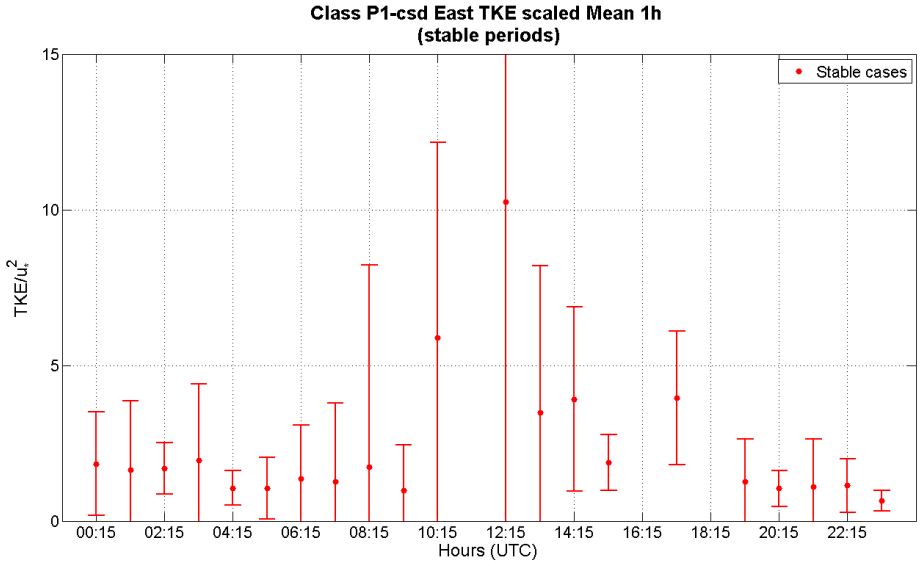

(b) The averaged and scaled TKE over one hour intervals. Here is possible to see that the scaled TKE is quite constant during the day.

Figure 5.23: Turbulent Kinetic Energy scaled with friction velocity for thermally driven days, for stable half hour periods. The mean cycle is with one hour average intervals.

Sensible Heat Flux

The sensible heat flux (SH) is related to the covariance between sonic temperature fluctuations T_s' and vertical wind fluctuations w'; for all the analyses I use the corrected value of SH (see Eq. (3.15)). The definition of SH is (1.24), that I rewrite here for clearness

$$SH = -\rho c_p \overline{w'\theta'}, \tag{5.32}$$

where θ' represents the fluctuation of potential temperature, that are the same as sonic temperature fluctuations T_s'.

The typical behaviour of SH for clear days (Stull 1988, [45]) is quite flat and slightly negative during the night (the air heats the ground, and the flux is directed downward, see Fig. 1.6) and positive with values around some hundreds of Watt per square metre, but in theory less than the maximum incoming energy (net radiation), during the day (clear).

In Fig. 5.24, the daily cycles of the sensible heat flux on the 11 thermally driven days are presented, in Fig. 5.24(b) the mean daily cycle is presented and it shows approximately zero values during nighttime and positive values during daytime. In this case a normal mean, following Eq. (5.30), is evaluated. Instead the individual days in Fig. 5.24(a) show that SH ranges from values around zero during the night to a very wide range during the day, from tens of W/m^2 to values greater than 800W/m^2. On October, 27th 2015 the SH reaches values between 700 to 850 W/m^2, but i.e. during April, 10th 2015 it does not raise more than 20 W/m^2 but also with negative values during a sunny day, that was classified as a *thermally driven day*.

It is possible to scale the sensible heat flux daily cycle using the relative maximum of each day. In this way if a similarity between different days is present it could be illustrated. In Figure 5.25 are depicted the daily cycles of SH normalised with the maximum of each day. As you can see only some day present a common behaviour, but many points are strewn on the plot grid.

These values appear quite uncommon for SH during a clear day with also a relatively calm wind (always lower than 8 m/s). Thus I tried to understand better this behaviour, selecting three days with different SH daily cycles. I chose them using as a criterion the incoming short wave radiation ($SW\downarrow$). Usually a value of SH higher than the $SW\downarrow$ it might be wrong, especially considering the energy exchange restricted to a small area near the station.

The three days selected are summarised in Table 5.9, where I chose opposite cases: one with a SH higher than the theoretically maximum available energy; one that seems normal; one with a practically flat SH.

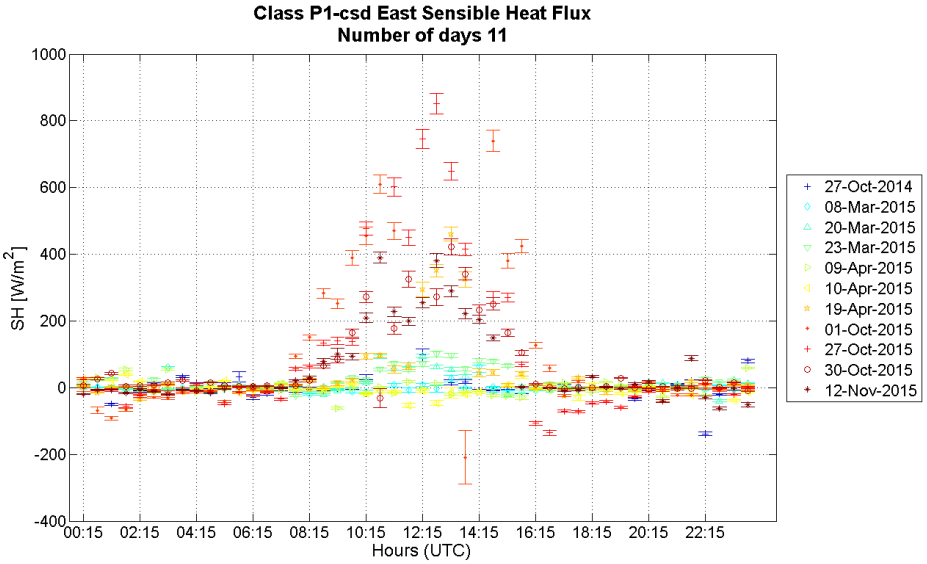

(a) All thermally driven days SH.

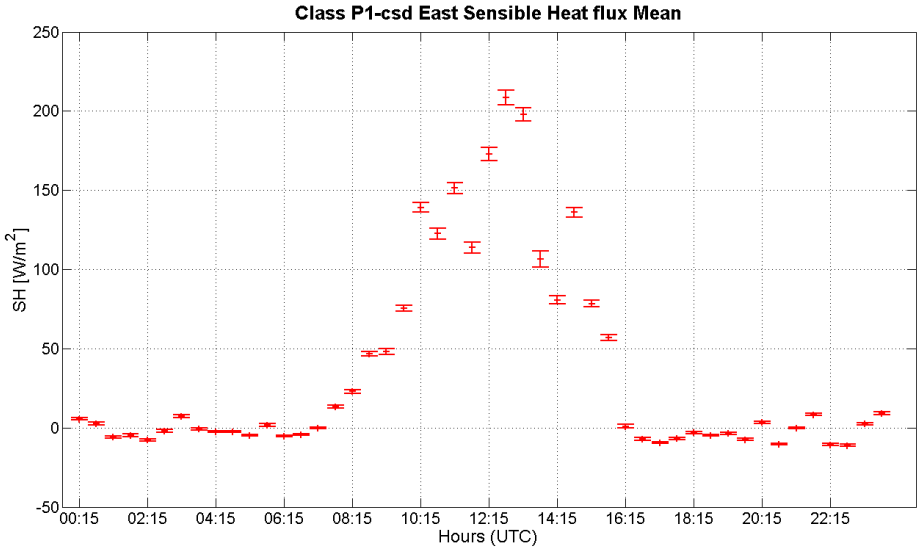

(b) The averaged SH.

Figure 5.24: Sensible Heat flux for thermally driven days. In the second panel (b) there is the normal average (Eq. 5.30) with associated the maximum error (Eq. 5.31).

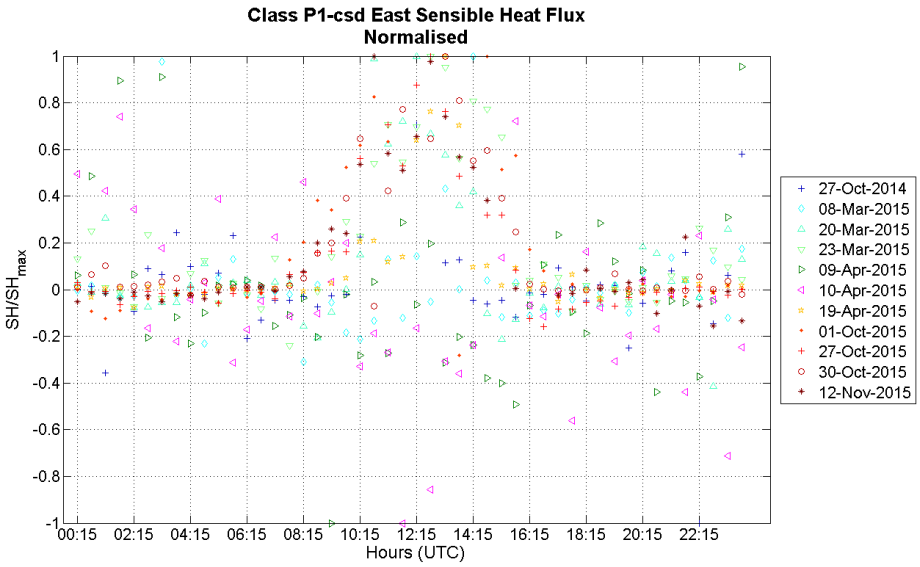

Figure 5.25: The SH daily cycles for thermally driven days, normalised with the SH maximum of each day. This simple scaling approach does not reveal so much, in fact many points are still scattered.

In Fig. 5.26 is shown the comparison between the short wave incoming radiation and the sensible heat flux for the three selected days in Table 5.9. Here it is possible to appreciate the meaning of adjectives "flat", "higher" and "medium".

The available energy is not the incoming short wave radiation, but rather the net radiation subtracted of the ground heat flux (and theoretically the latent heat flux, that I neglect because I do not have reliable measurements of it for those days), as stated by Equations (1.18) and (1.19) in Chapter 1. In Figure 5.27 I compare the SH for these three days to the net radiation plus the ground heat flux (HG is negative during the day, meanwhile the net radiation is considered positive). I obtain that the SH is greater of the available energy also in the "medium" day.

Different hypotheses could be formulated to explain these opposite behaviours in theoretically thermally driven days. In fact I remind that these eleven selected days, were selected using the Clear Days Algorithm (see 4.3.4), and theoretically could be characterised by a thermally driven flow.

The first hypothesis is a wrong covariance between sonic temperature and vertical wind speed, in particular I mean that it might be possible that the variables assume an opposite fluctuation a number of time so frequent that can reduce

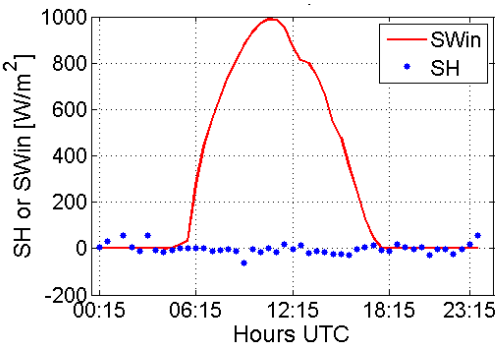

(a) 9th April 2015

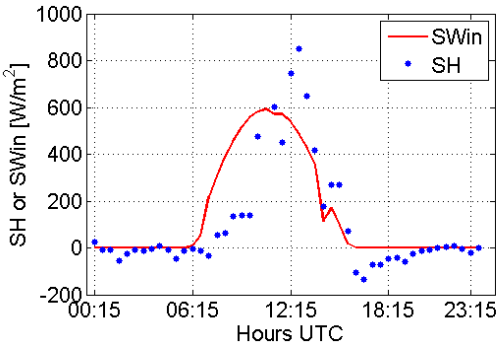

(b) 27th October 2015

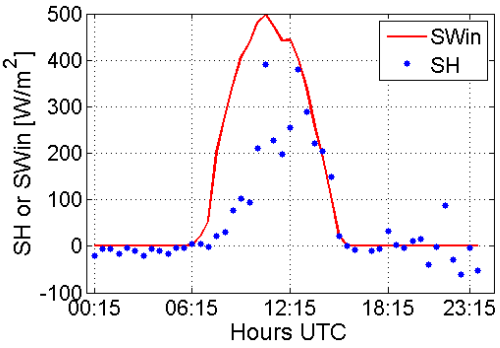

(c) 12th November 2015

Figure 5.26: Comparison between SW incoming radiation, the theoretically maximum available energy, and the sensible heat flux (SH) for three selected thermally driven days: one "flat" (top), one "higher" (middle) and one "medium" (bottom). The relation between $SW\downarrow$ and SH is the criterion used to choose these significant days.

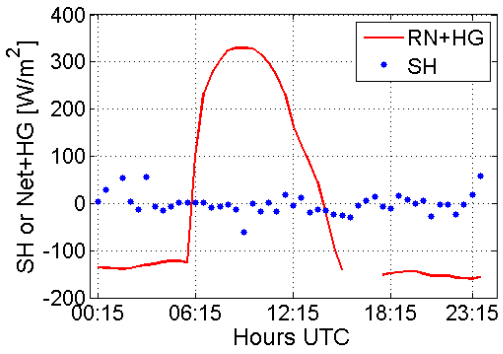

(a) 9th April 2015

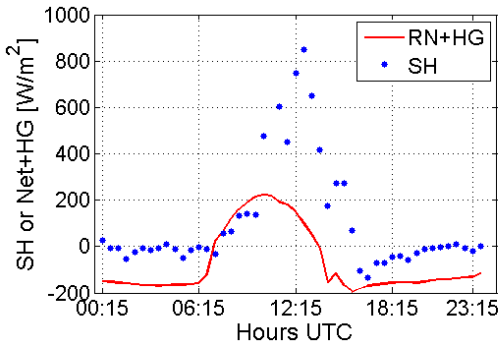

(b) 27th October 2015

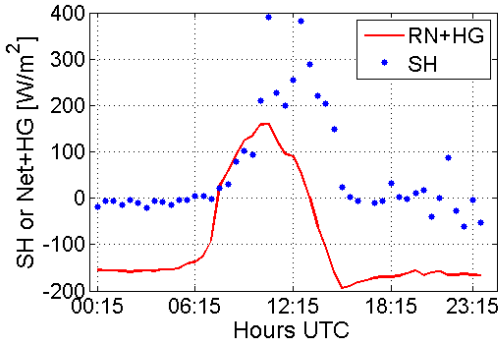

(c) 12th November 2015

Figure 5.27: Comparison between net radiation minus ground heat flux (theoretical available energy), and the sensible heat flux (SH) for three selected thermally driven days: one "flat" (a), one "higher" (b) and one "medium" (c). In Fig. 5.26 only the "higher" day exceeds the maximum energy, here only the "flat" day stays beyond the total available energy, a possible explanation is contribution of energy from the advection.

Date	SH type	Period analysed	Similar SH days
09-Apr-2015	Flat	11:15 UTC	5 of 11
27-Oct-2015	Higher	13:15 UTC	1 of 11
12-Nov-2015	Medium	11:15 UTC	5 of 11

Table 5.9: Selected days for further analysis on sensible heat flux behaviours. The last column reports how many days are present, in the 11 thermally driven days selected, with the same behaviour of those subselection. The judgement was done comparing SH with incoming short radiation.

the covariance. At the opposite can happen that more positive and according fluctuations raise the covariance to much higher values.

In plots in Fig. 5.28 it is possible to see three half hour periods extracted from the sample days of Table 5.9. On the left panels there is the sonic temperature, instead on the right panels there is the vertical speed. It is not simple to understand the reasons of the opposite behaviour observed in clear days. First of all it is possible to see that no spikes are present in these data, it means that the instrument works well in those selected periods, and as a consequence the evaluated covariances are not invalidated. In the second and third day selected (Figure 5.28(b) and 5.28(c)) the departure from the running mean of T_s are around 2 to 3 °C, instead in the "flat" day in Fig. 5.28(a) the oscillations of T_s are less than 0.5 °C. On the other side the departure form the running mean for w (that is w') is around 0.5 m/s for the first case, and it is around 1 m/s in "medium" and 1.5 m/s in "higher" cases. From this qualitative inspection I can state that for the April 9th the "flat" behaviour is due to a small temperature fluctuations and a generally smaller w'. In the other two cases the sonic temperature is much varying during the thirty minutes of observation, and combined with a bigger fluctuations of vertical speed gives a positive value to the covariance.

Furthermore it is possible to analyse the standard deviations of temperature and vertical speed for these three selected days. In Figure 5.29 are depicted the standard deviations for these three days.

In this case the "flat" day (9th April) the standard deviations are small, less than 0.7 m/s or °C, instead in the "medium" and "higher" days they are bigger. In particular the sonic temperature standard deviation depicts a peak in the middle of the day, this peak is bigger (around 1.5°C) for the "higher" day (27th October). These behaviours explain the sensible heat flux.

This is from the data point of view, but physically what happens? Why does

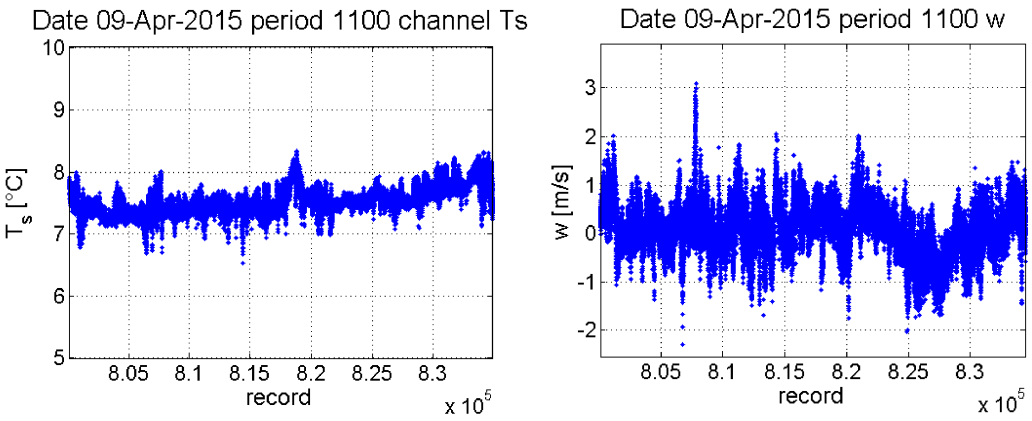

(a) 9th April 2015, from 11:00 to 11:30 UTC.

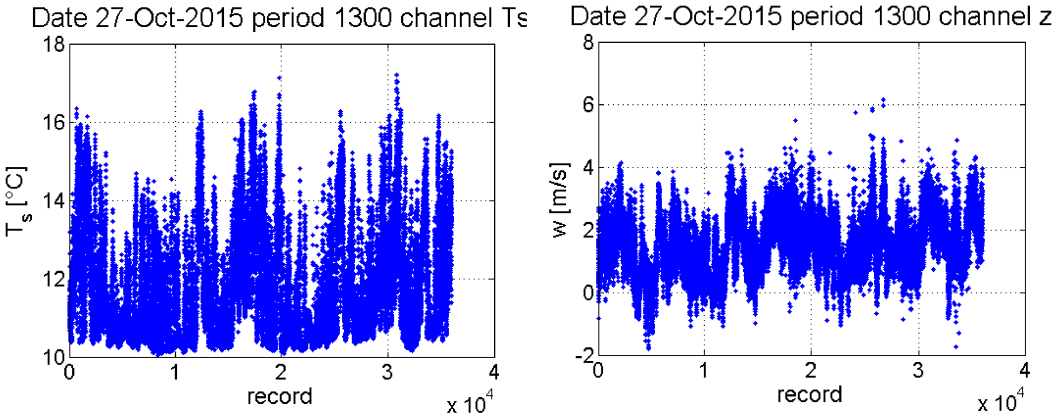

(b) 27th October 2015, from 13:00 to 13:30 UTC.

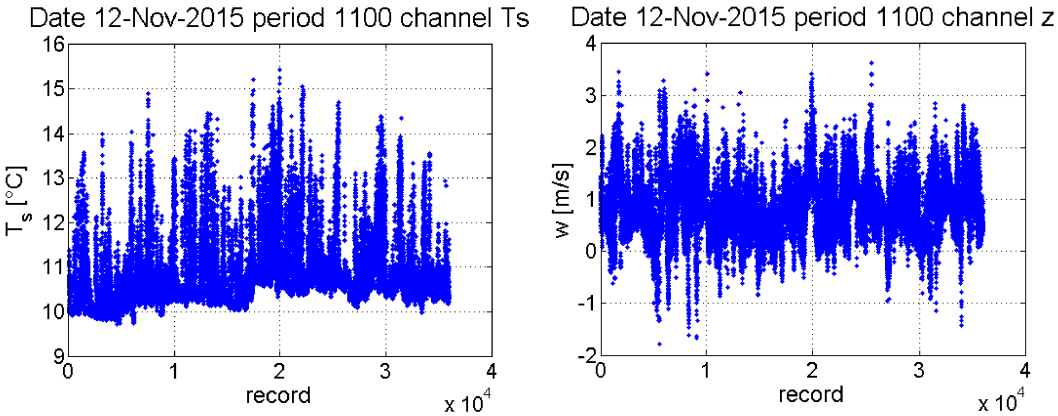

(c) 12th November 2015, from 11:00 to 11:30 UTC.

Figure 5.28: Raw data for w and T_s of the three selected days in Tab. 5.9. The sample frequency is 20 Hz.

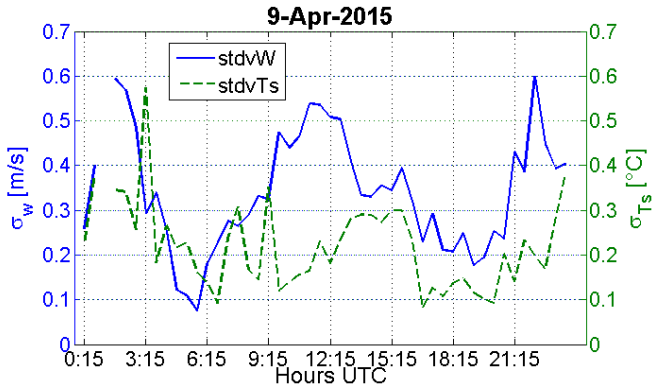

(a) 9th April 2015, daily cycle.

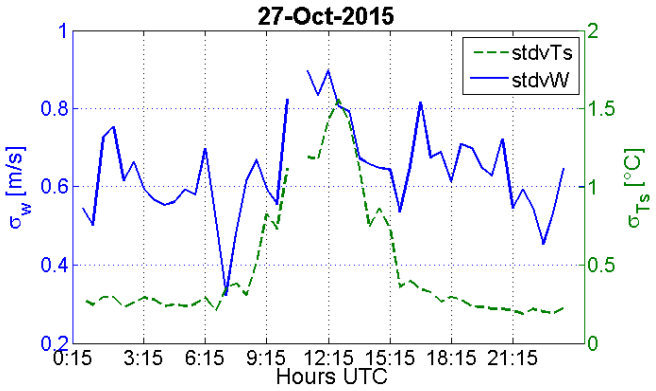

(b) 27th October 2015, daily cycle.

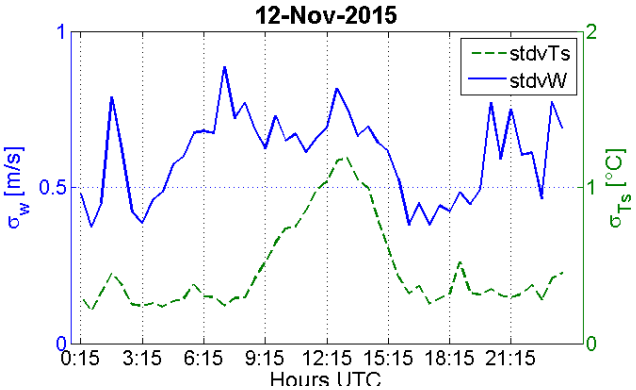

(c) 12th November 2015, daily cycle

Figure 5.29: Daily cycles of standard deviations of sonic temperature and vertical wind speed for the three selected days in Tab. 5.9. In (a) the "flat" day, in (b) the "higher" day and in (c) the "medium" day.

the atmosphere has such a different behaviour in days with quite similar radiative condition, especially in the sonic temperature? And the main question remains: where does the energy come from, or go to?

This is the issue, how to explain it?

The first aspect that I considered is the mean flow wind speed. Looking back to Figure 5.18 it is immediately clear that in the middle of the day of April 9th the wind was practically calm, meanwhile in the other two days it was around $4 \div 6$ m/s. Thus the advection plays an important role, because it takes air parcel from the side of the mountain that are outside of the SL, and has different thermodynamics properties from the measurements site. Another aspects of not calm wind is that it raises the fluctuation of sonic temperature, as basically happen, and consequently the covariance $\overline{w'T'_s}$ changes.

Thus generally the advection can play a significant role in the evaluation of SH and also of other turbulent quantities. This is relevant especially if the comparison between turbulence data, for example, and radiation data or ground heat flux data is wished. The footprint of these data can be terribly different.

In order to understand more about the advection I deeply analyse the second rotation angle, β, that indicates the rotation of XZ-plane around y-axis (see Figure 4.3 and Section 4.4.2). Combining this angle with the wind speed (Fig. 5.31) and direction (Fig. 5.30(b)) it is possible to understand the origin of the air parcel.

For the first part of these three days the wind direction is practically the same: 200°. Only the 9th of April has a rotation in the wind direction toward north between 16:15 and 19:15 UTC. The wind speed is more fluctuating between 2 and 8 m/s, in general the 27th of October has a constant wind speed with a mean value of 6 m/s, while the 9th of April shows in the second part of the day (corresponding to the north wind pattern of the afternoon, Fig. 5.30(b)) lower speeds, around 2 m/s. Thus for low wind speed the advected air parcel comes from relatively near places, instead for higher wind speeds it comes from more far away.

The β angle indicates the inclination, referred to the sonic reference system (that at Arbeser it is with the z-axis normal to the gravity, and normal to the small flat plain near the mast), of the air flow approaching the sonic anemometer (see Figure 5.32). Thus for positive angles the air parcel comes from a place at lower altitude with respect the sonic, while if it is negative the air parcel comes from a place at higher altitude with respect to the sonic.

From Figure 5.30(a), it is possible to understand that for the days 27th of October and 12th of November the angles are always greater than zero, therefore the air flow approaches the ridge approximately parallel to the south slope. The direction is confirmed from Fig. 5.30(b) and the velocity says that for these two

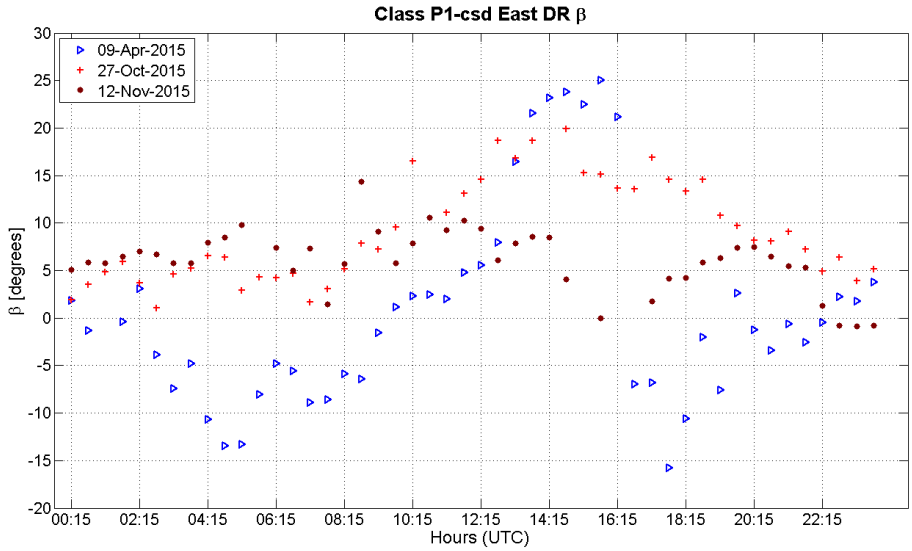

(a) Second rotation angle β for selected day as Tab. 5.9. This angle is sketched in Fig. 4.3 of Section 4.4.2.

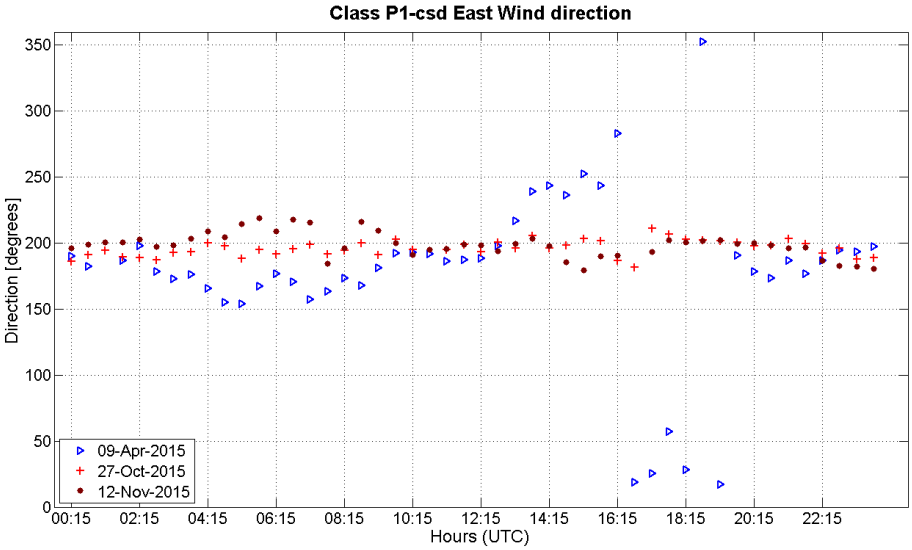

(b) Streamline wind direction for the selected thermally driven days.

Figure 5.30: Study of advection. The three days of Tab. 5.9 are depicted.

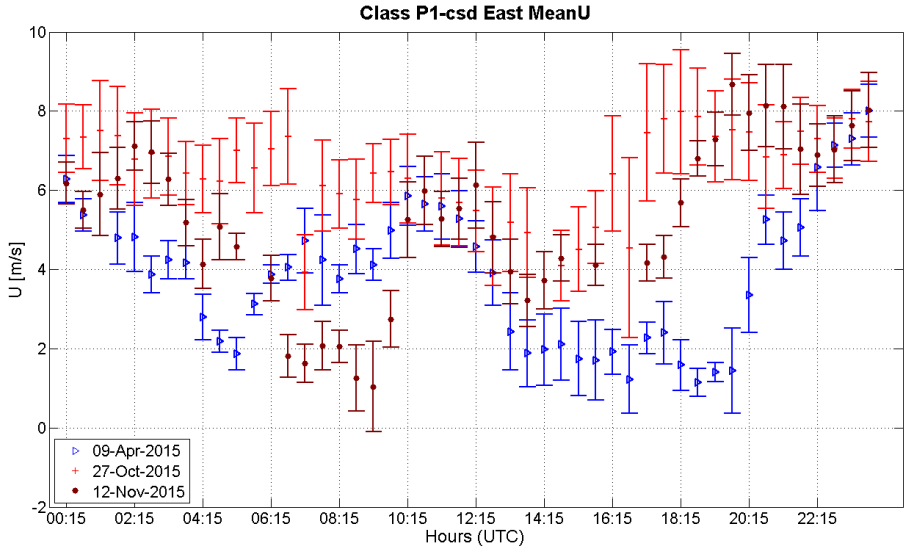

Figure 5.31: Streamline wind speed for the selected thermally driven days, as Tab. 5.9. The wind speed could help in the study of advection.

days the air parcels come from relatively far away. In Figure 5.33 I try to depict this situation, with a 200° wind direction approximately parallel to the south slope. The red arrow lays on the same direction of the red arrow in Fig. 5.32, and in fact, the β angle is positive as you can see from Fig. 5.30(a).

The 9th of April instead is different, in the morning β was lower than zero, the air parcel comes from an higher altitude, while during the afternoon $\beta > 0$, thus the air parcel is approaching parallel to and from the ridge slope first and later form a higher altitude from north direction. The wind speed is low, so the air comes from places relatively close to the mast.

Summarising:

- For 12th November 2015 and 27th October 2015, surely the fluxes are influenced by horizontal and vertical advection. In fact, the β angle, the wind direction and the wind speed seem to justify this hypothesis.
- For the 9th of April 2015, the advection could be less important, or of different nature, in fact the advected air parcel comes from north or west (ridge slope) directions. However the wind speed is relatively low, thus the advected air come from places nearby the mast.

Another possible explanation for these uncommon behaviours is the ground

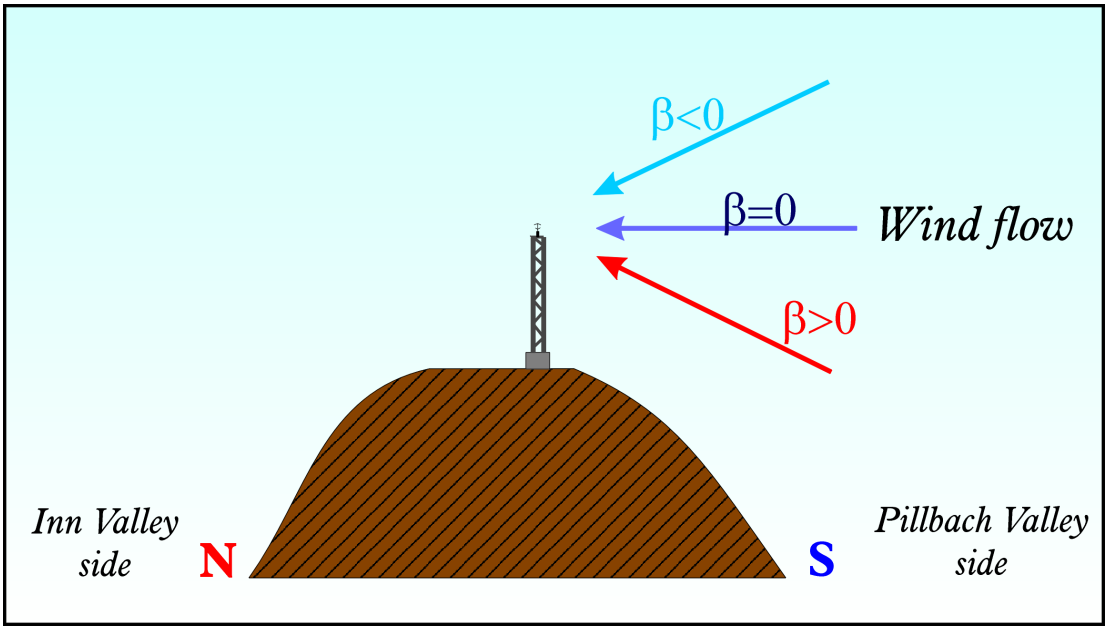

Figure 5.32: The north-south cross section of the Arbeser Kogel ridge is drawn at the location of the station. On the left there are the Inn Valley and the north slope, and on the right there are the Pillbach Valley and the south slope. The mast is depicted and three possible wind flow are approaching from the south site (arrows), if the flow arrives parallel to the slope the β angle is *negative*, instead if the flow arrives horizontal the β angle is *zero*, else it is *positive*.

conditions. In particular the presence or not of the snow. From Tab. 5.5 is clear that most of analysed days are with ground covered by the snow. This assumption is done on the base of albedo calculations, because the snow sensor does not work properly. A surprising correlation between "flat" SH cases and snow was found: whenever the ground is covered by the snow the SH presents a "flat" behaviour. This is valid for the 11 thermally driven days analysed, surely a wider data sample would clarify this, but if it is a real correlation, and not only a coincidence, it is necessary to understand why and how the snow affects the SH.

In the literature I found a experimental campaign in Kärkevagge Valley in Swedish Lapland (Arck and Scherer, 2002 [1]) that explored the evaluation of turbulent fluxes over snow. In this case they have used three different methods to evaluate turbulent fluxes and they have compared them. They used the flux-profile method, two bulk methods and the eddy covariance method (as is done

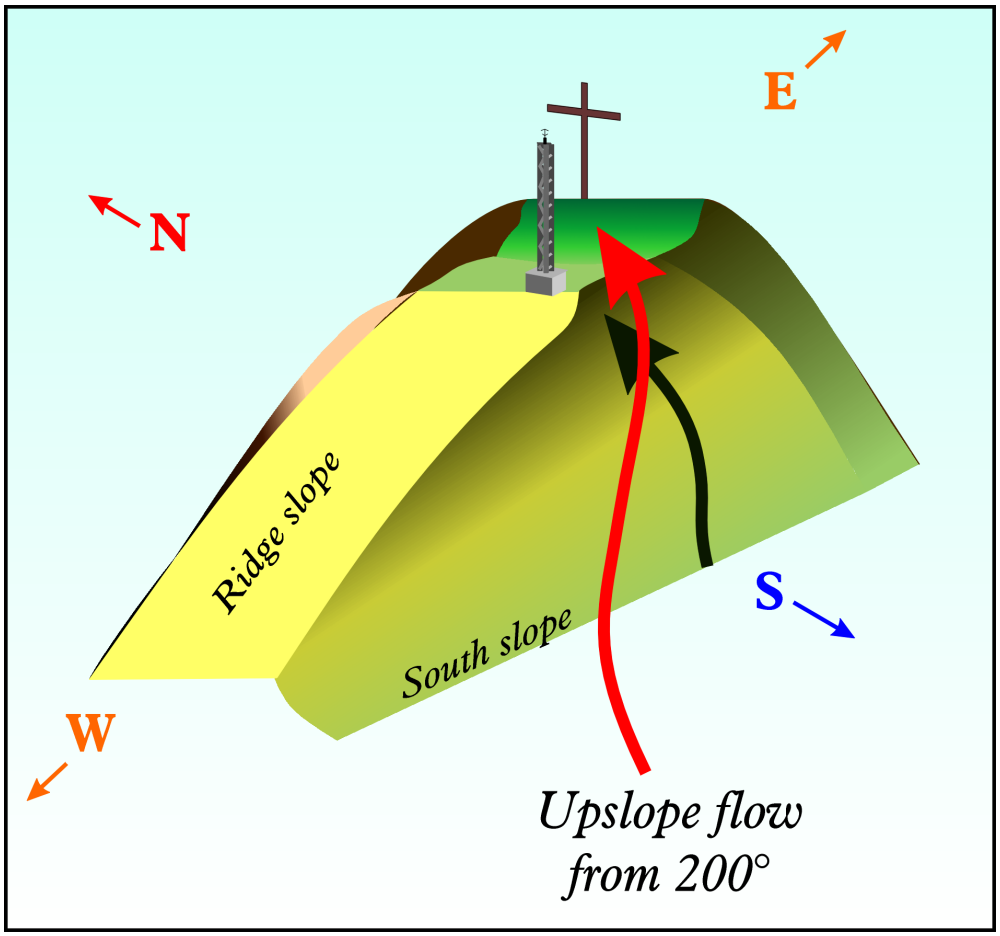

Figure 5.33: A 3D view from the SW side of Arbeser Kogel is presented in this picture. The ridge slope, in light yellow, and the south slope, in light green, are affected by a south upslope flow (red arrow, with the shadow on the slope in black). In this case is represented the situation of 27th of October 2015 and 12th November 2015, where the wind direction was $\approx 200°$ and the $\beta > 0$.

at Arbeser). The results depicts that the most stable and reliable are bulk and eddy covariance method, but the most important prerequisite of both is that the measurements are done *inside* the surface layer.

Arck and Scherer pointed out a particular case in their dataset. In one case they measured an unstable profile near ground (warm layer above the ground) with a colder and stable layer standing above it during the day. Due to the unstable layer they expect a positive SH, but the values are approximately zero.

In Arbeser data this situation is verified only on 20th March 2015 when a layer of warm air is present in the lower level (unstable) and the upper level results stable. In this case the SH was not completely flat, but shows small positive values around noon. Other very flat daily cycles, such as 8th March, 9th April and 10th April 2015 are mainly characterised by a stable potential temperature profile, thus this seems to be the principal reason: an absence of local convection.

With this explanation it is possible to clarify the "flat" daily cycle of 9th April, in fact, it is possible that the ground was not heated by the solar radiation ad thus the SH was flat. Probably, but data is not available, the latent heat flux was positive and compensated for the lack of SH. It is probable that the energy coming from the sun melt the snow, and this heat was spent as latent heat. Unfortunately it is not possible to verify that because there is no data from the krypton hygrometer, and also the Bowen ratio method has failed.

Summarising the results for sensible heat flux are:

- The "higher" values could be explained using the advection, and this was investigated using the second rotation angle, the wind direction and speed.
- The "flat" daily cycle of SH (the only one analysed in depth, 9th April 2015) could be due to the presence of the snow on the ground that gives to the layer a stable profile, and no local convection is present despite of the *thermally driven day*.

Dimensionless Standard Deviations of Wind Velocity Components

The study on dimensionless standard deviations of wind velocity components and also on sonic temperature (following section), is done following the article of Nadeau *et al.* (2013) [31] and de Franceschi *et al.* (2009) [14].

Using the subdivision in stable, unstable and near neutral just done with ζ, it is possible to plot the dimensionless standard deviations of velocity components. This is a typical local similarity scaling procedure aimed to organise the data on a specific curve, of which it is possible to define a function, and thus to study the physical properties of such complex flows.

Here discourse moves to *local similarity* from the previous MOST, because probably, but I cannot control that because at Arbeser there is only one turbulence measurements, the heat fluxes are not constant with the height.

The scaling function that I would like to find and test is

$$\Phi_i = a_i(1 + b_i|\zeta|)^{1/3}. \tag{5.33}$$

The coefficients reported by Nadeau *et al.* [31] are shown in Table 5.10, and they are relative to a 1.5m high sonic anemometer settled on a steep slope (40°).

Variable	ζ	a	b	R^2
$\frac{\sigma_u}{u_*}$	< 0	2.84	−3.61	0.44
	> 0	2.85	10.55	0.66
$\frac{\sigma_v}{u_*}$	< 0	2.15	−3.99	0.47
	> 0	2.33	5.46	0.58
$\frac{\sigma_w}{u_*}$	< 0	1.01	−5.02	0.84
	> 0	0.95	11.23	0.91

Table 5.10: Nadeau fit parameters.

I tried to plot these scaling functions on my data and the results are summarised in Figures 5.34(a), 5.35(a) and 5.36(a). From these figures Arbeser data shows a scattering with respect to the fit line, and they do not seem to scale well. Nadeau *et al.*'s functions on Arbeser data are quite far from the best fit, especially for σ_u and σ_v. For σ_w Nadeau's function passes in the middle of data cloud, but on the other side Nadeau's data and plots scale better. In fact the R^2 associated with the best fit on Arbeser data is always less than 0.2, instead Nadeau's R^2 is at least 0.4, but sometimes greater than 0.8.

There are two main reasons to explain that: the first regards the data pre-processing, Nadeau *et al.* have excluded all points with a small sensible heat flux $|SH| < 10$ W/m^2, and has not applied some correction that I have applied; the second reason regards the experimental set up and location, the experiment was settled on a steep slope, that has different flow patterns compared to a mountain top. I know that in theory if the scaling is consistent then the site, the time and the instrumentation must not influence the similarity relation.

The big scatter of my plot is due to the medium quality data at first. In fact the stationarity conditions are for sure not fulfilled, instead the level of uncertainty is quite well respected.

The next attempt done is to find the best fit with the same function of (5.33). In Figures 5.34(b), 5.35(b) and 5.36(b) I show Arbeser data with my best fit. From Table 5.11 it is possible to appreciate these fit function that are far from being perfect.

	ζ	a (conf. level)	b (conf. level)	RMSE	R^2
$\frac{\sigma_u}{u_*}$	< 0	$1.31(1.24 \div 1.38)$	$-10.64(-16.06 \div -5.23)$	3.07	0.14
	> 0	$1.42(1.33 \div 1.51)$	$14.17(5.38 \div 22.97)$	3.31	0.09
$\frac{\sigma_v}{u_*}$	< 0	$1.76(1.72 \div 1.81)$	$-3.05(-4.44 \div -1.65)$	1.87	0.12
	> 0	$1.84(1.78 \div 1.90)$	$5.40(2.64 \div 8.16)$	1.94	0.10
$\frac{\sigma_w}{u_*}$	< 0	$0.81(0.77 \div 0.84)$	$-10.20(-13.98 \div -6.42)$	1.71	0.24
	> 0	$0.90(0.87 \div 0.93)$	$2.21(0.13 \div 4.55)$	1.61	0.02

Table 5.11: Best fit parameters for thermally driven days data, with the expressed 95% confidence bounds.

Both RMSE and R^2, two statistical parameters for the estimation of fit function goodness, are very low; in particular the hit test for the R^2 is 1 thus in my case the really best fit is not reached. Otherwise the RMSE has the hit test to 0, thus a perfect model can produce a curve that pass exactly across each point. The main reason is the wide scattering of data and the relatively high uncertainties.

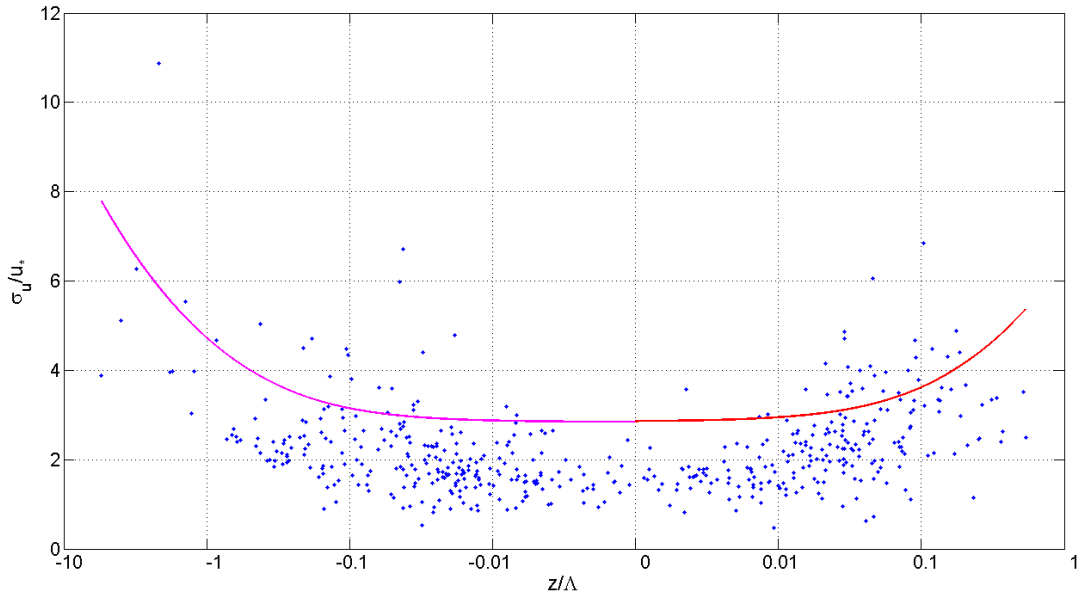

(a) Surface scaling for σ_u.

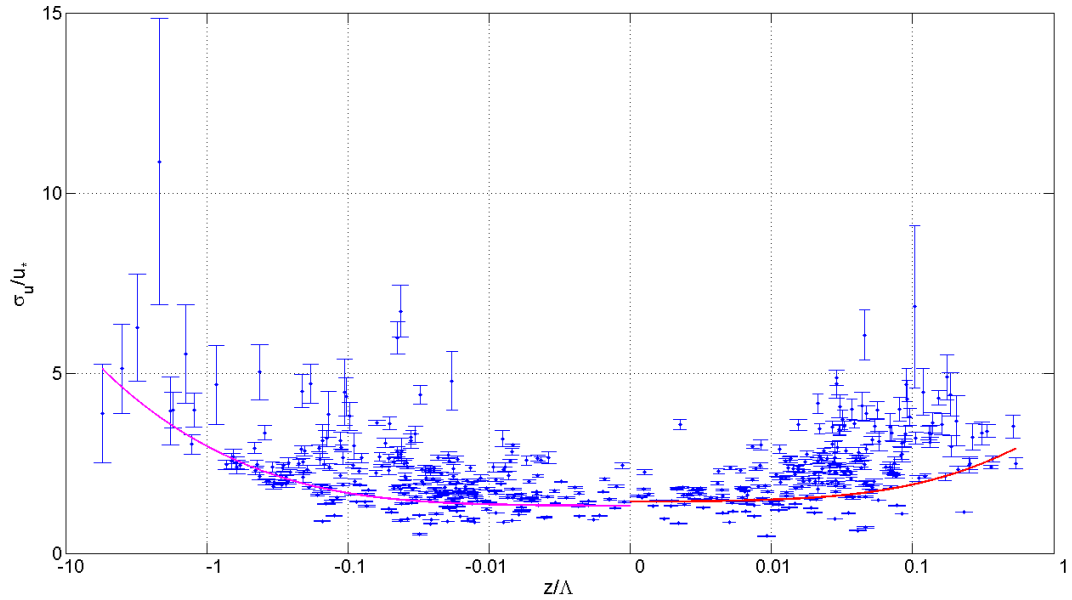

(b) Best fit on surface scaling for σ_u.

Figure 5.34: Surface layer scaling of σ_u with Nadeau *et al.*'s scaling function (coefficients in Tab. 5.10) and Best fit fuction (coefficients in Tab. 5.11) superimposed to Arbeser thermally driven data.

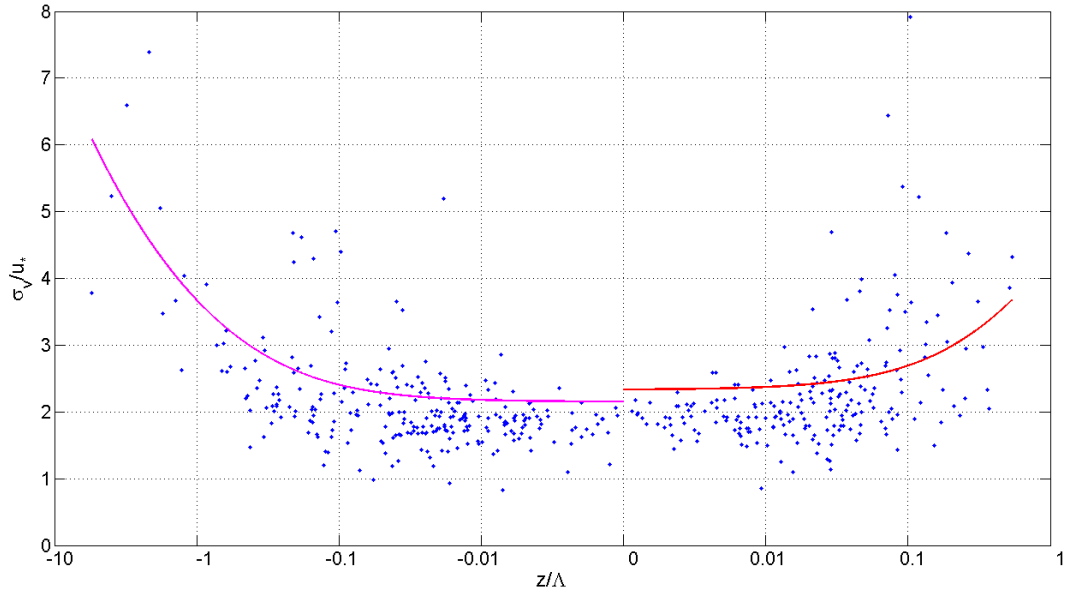

(a) Surface scaling for σ_v.

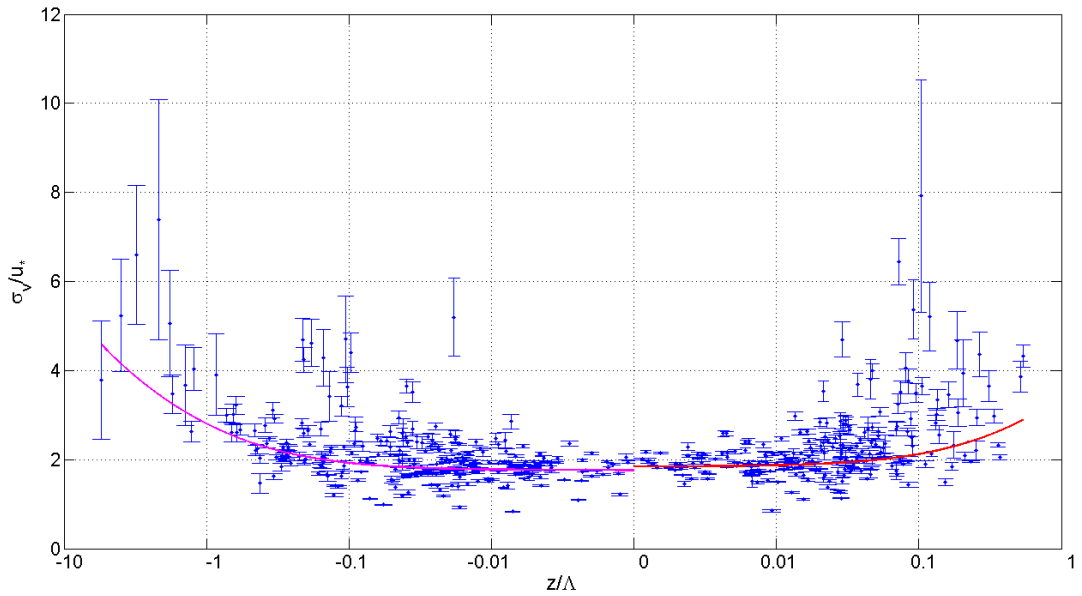

(b) Best fit on surface scaling for σ_v.

Figure 5.35: Local layer scaling of σ_v with Nadeau *et al.*'s scaling function (coefficients in Tab. 5.10) and Best fit fuction (coefficients in Tab. 5.11) superimposed to Arbeser thermally driven data.

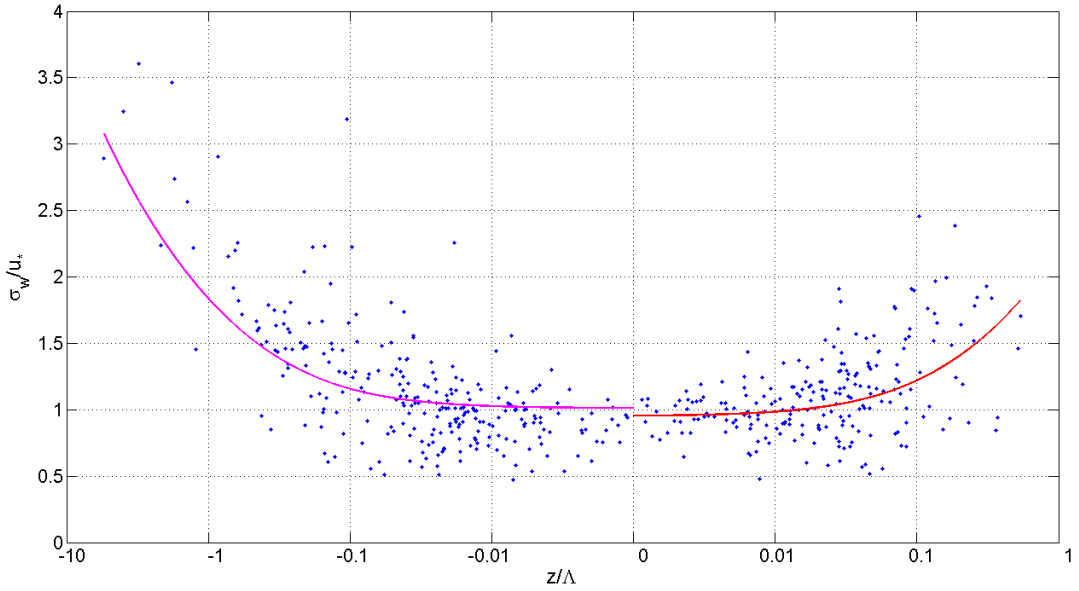

(a) Surface scaling for σ_w.

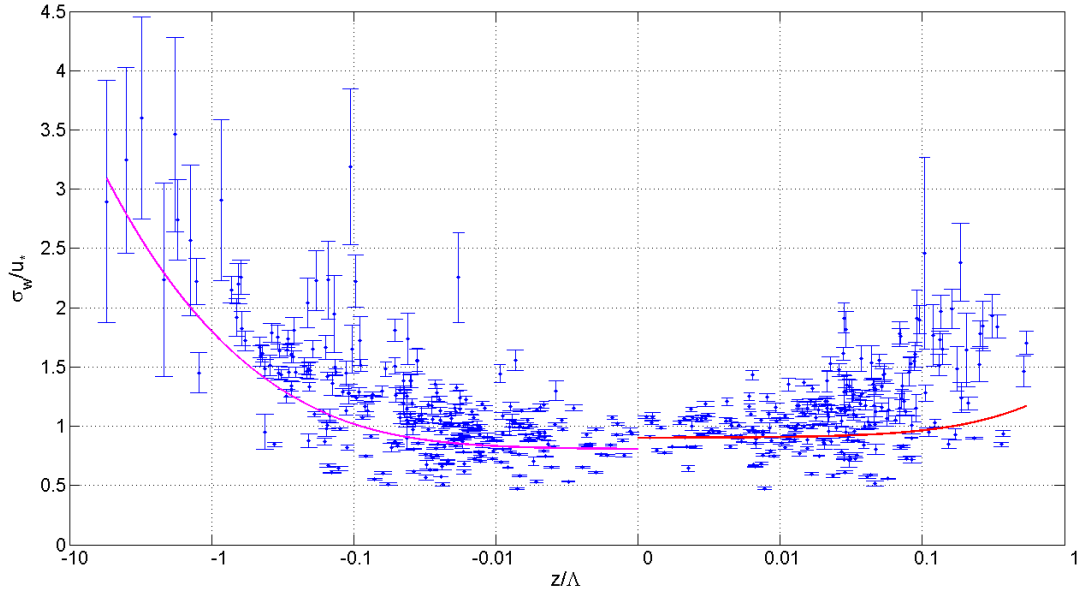

(b) Best fit on surface scaling for σ_w.

Figure 5.36: Local layer scaling of σ_w with Nadeau *et al.*'s scaling function (coefficients in Tab. 5.10) and Best fit fuction (coefficients in Tab. 5.11) superimposed to Arbeser thermally driven data.

Dimensionless Standard Deviation of Temperature

The dimensionless standard deviation of sonic temperature has as expected scaling function the Equations 5.34, as reported by Nadeau *et al.* [31].

$$\frac{\sigma_\theta}{|\Theta_*|} = \begin{cases} 2.67(1-16.29\zeta)^{-1/3} & \text{for } \zeta < -0.05, \\ 3.22(1+0.83\zeta)^{-1} & \text{for } \zeta > 0.05. \end{cases} \tag{5.34}$$

I applied Eq. (5.34) to my data, and what I founded is depicted in Figure 5.37.

In my case I have not removed the near neutral data. They have a bigger uncertainty and do not follow the MOST forecast of values between 2 and 3. In Figure 5.38(a) it is possible to see the data with their error bar, and as I mentioned the bar are huge in the near neutral range.

The two Nadeau's fitting curves (red and magenta) stop at $\zeta = \pm 0.05$ and, especially for the unstable part, they fit quite well the data. Looking at Figure 5.38(b) it is possible to see that the best data, with smaller uncertainties, are under the fit line of Nadeau. From other stations of i-Box project the data are mostly *greater* than the fit line. In the next plot (Figure 5.39) I use a logarithmic scale also for y-axis, and here is more clear the trend. There are many points greater than the magenta line, but those with the smaller uncertainties are *under* this line. Thus I have an opposite scaling behaviour when compared to other i-Box stations (see for example Eggen in Fig. 5.40). Different hypotheses can be made on this topic, the first difference between Arbeser data analysis and other i-Box stations analysis is the averaging mode. As specified in Section 4.4 I used a block average instead of low pass filter averaging mode. However I do not expect significantly different results on this hand, probably the main reason for this difference has to be sought into the advection contribution to the energy balance. In fact if the advection contributes as a source of heat a larger heat fluxes are got, thus the value of $\sigma_\theta/|\Theta_*|$ gets smaller than expected by the energy balance.

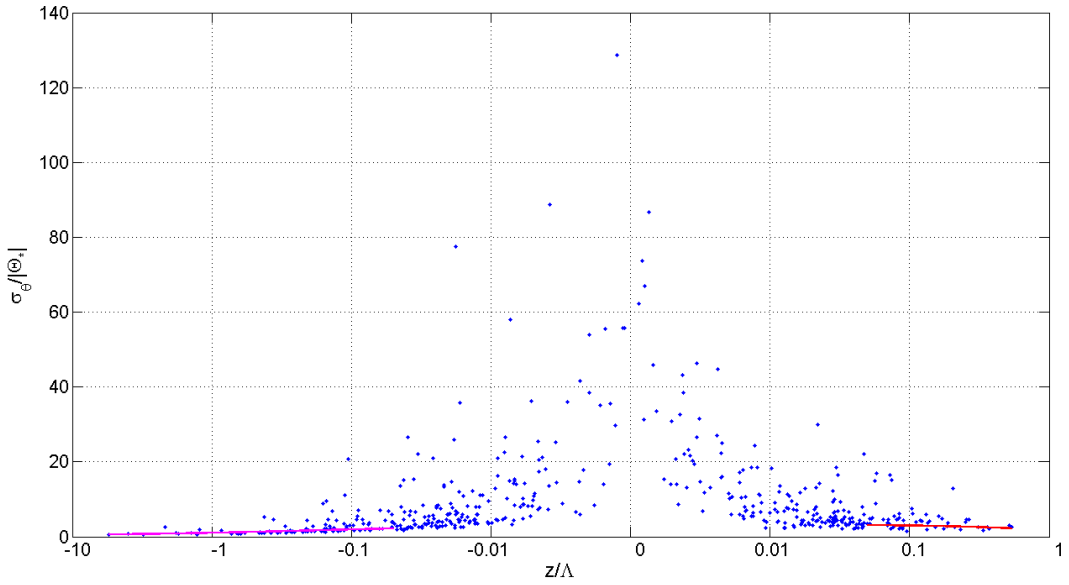

(a) All data without error bars.

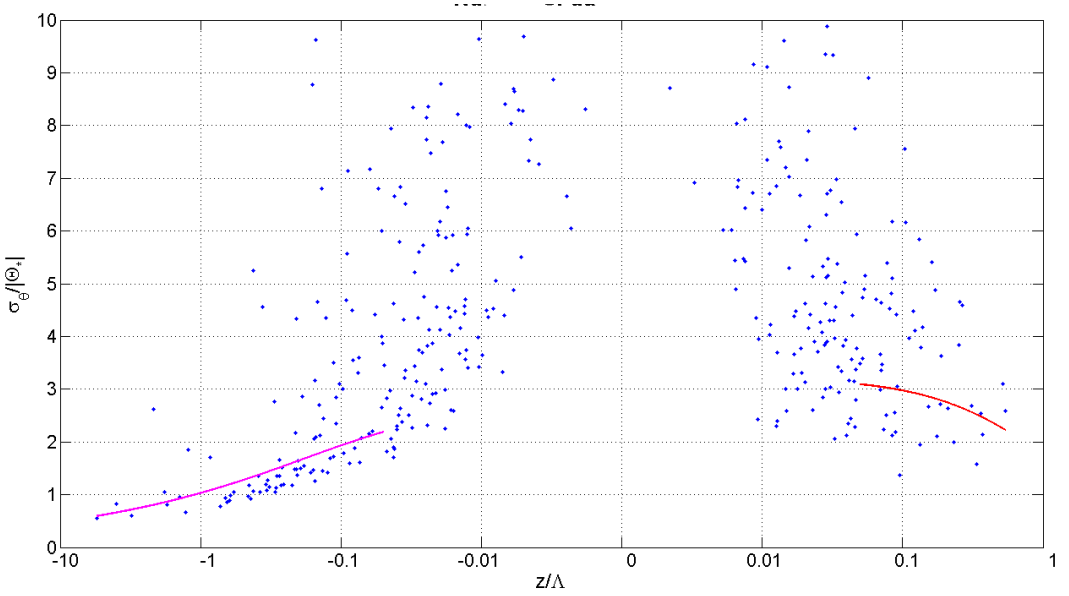

(b) A zoom on the lower part.

Figure 5.37: Dimensionless temperature standard deviation with Nadeau's fit function (Eq. (5.34)) superimposed on Arbeser data. In panel (a) the near neutral points, with very high values, flatten the stable and unstable tails. In panel (b) a zoomed view permit to appreciate the fit curves. In the unstable part the data cloud is significantly under the fit line.

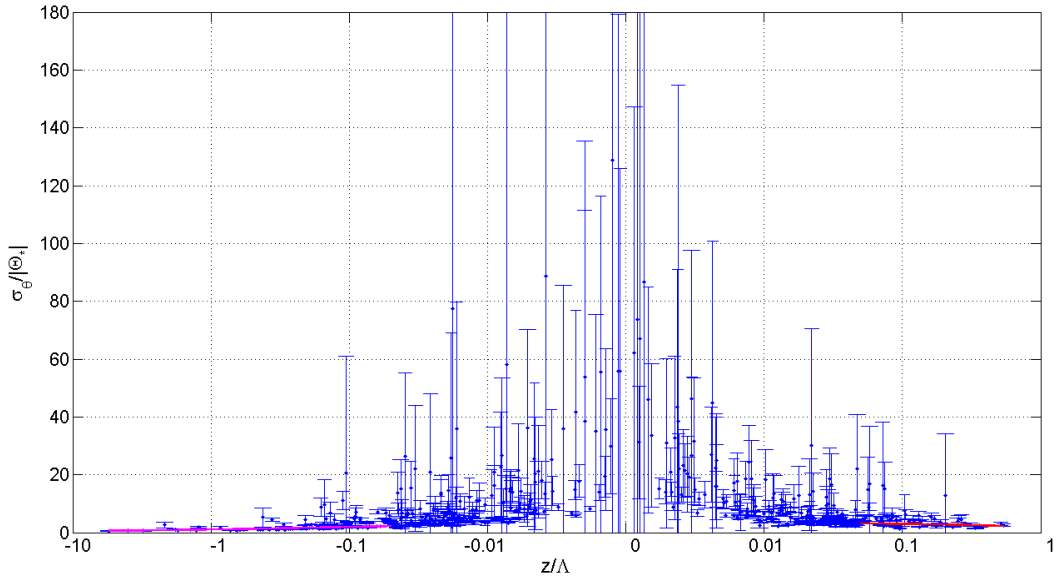

(a) All data with error bars.

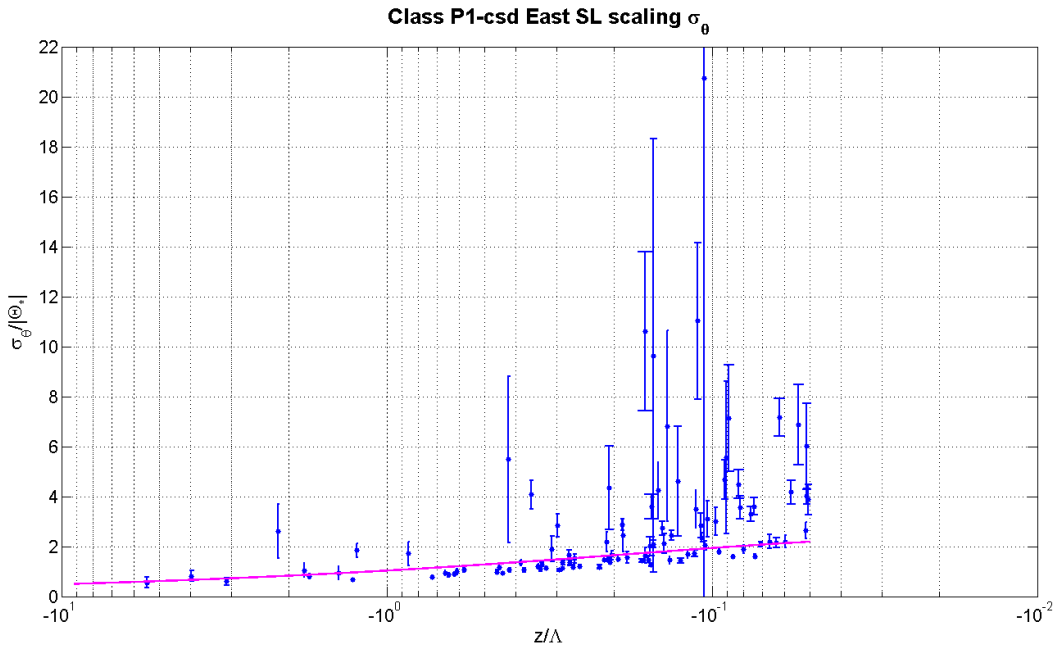

(b) The unstable part of the data, with fit function of Nadeau.

Figure 5.38: Dimensionless temperature standard deviation with Nadeau's fit function.

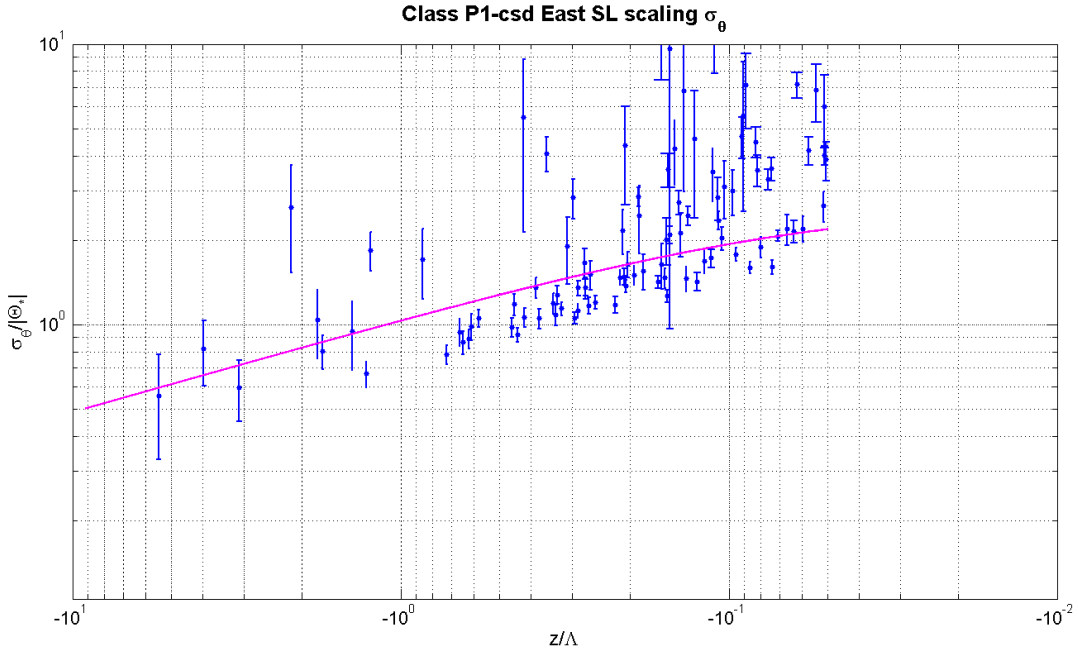

Figure 5.39: Bi-logarithmic plot of the unstable part for the dimensionless standard deviation of sonic temperature.

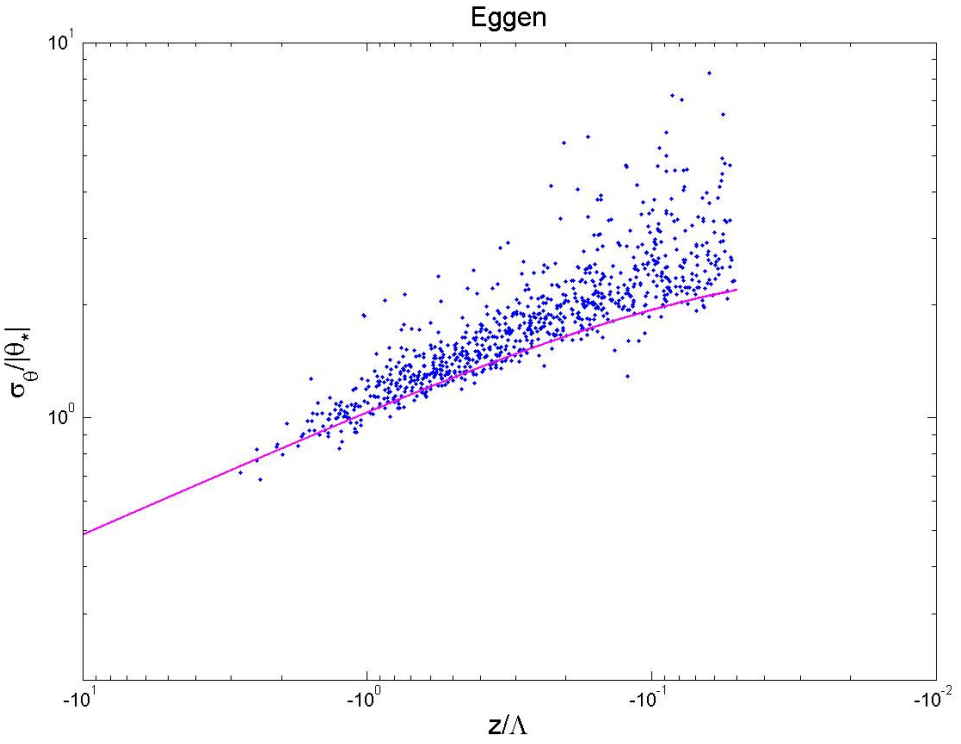

Figure 5.40: Bi-logarithmic plot of the unstable part for the dimensionless standard deviation of sonic temperature measured at Eggen station. In this plot it is possible to see that the data cloud is higher than the Nadeau's fitting line. The data base is the HiQ from 2013.08.01 to 2014.12.29. Plot credits Eleni Sfyri.

5.3.3 Energy Surface Balance Closure Overview

I have also dedicated some time to the energy surface balance. The equation of the surface balance is (from Eq. (1.19))

$$R_N = SH + LE + H_G + \Delta H_S \tag{5.35}$$

and as previously stated in Section 1.4.2, the closure of this balance is not zero. The problems are formerly analysed, what I would like to show here is the surface balance at Arbeser for some days.

As previously stated the latent heat flux is hardly ever available, in thermally driven days only one day is complete (the 27th of October 2014), all the others did not have the LE measured with the fast response hygrometer. Therefore, as seen at the beginning of Section 5.3, I can use the Bowen ratio method to integrate when possible the data. In energy balance plots I will distinguish between the LE from Bowen ratio method and from eddy covariance method (using the measurements from the krypton lamp), and if both are available I plot LE from krypton and from Bowen ratio.

Previously I showed you the problem with the sensible heat flux that has a behaviour not so clear. If I add also the latent heat flux our problem grows in complexity.

In the first plot (Fig. 5.41) I show the only complete clear day with all the components of the energy balance: October 27th, 2014. The SH of this day is a "flat" case, because it is under the red thick curve of the net radiation. The LE on the other side has a strange behaviour with very high peaks and small values very close one to the other. From the incoming radiation ($SW\downarrow$ $+LW\downarrow$) it is possible to see that this day was completely free from clouds, the small hollow in the middle is due to the tie rod shadow previously described. The ground heat flux has a delay of one hour because it is buried in the soil of some centimetres.

I have tried to apply the equation (1.28) and for this day the residual obtained is in Table 5.12. For the net radiation R_N the signs convention is positive for incoming energy and negative for outgoing energy, for the heat fluxes is negative downward and positive upward. Thus for sensible heat and latent heat that are measured in air upon the "balance surface" the fluxes are positive upward and negative downward that comes from the definition of latent and sensible heat flux as the covariances between the vertical wind speed fluctuations and the potential temperature or the specific humidity, meanwhile for ground heat flux is the same, where during the daytime the flux is negative (downward) and represent the storage of heat in the soil (thus not available heat for the atmospheric motions),

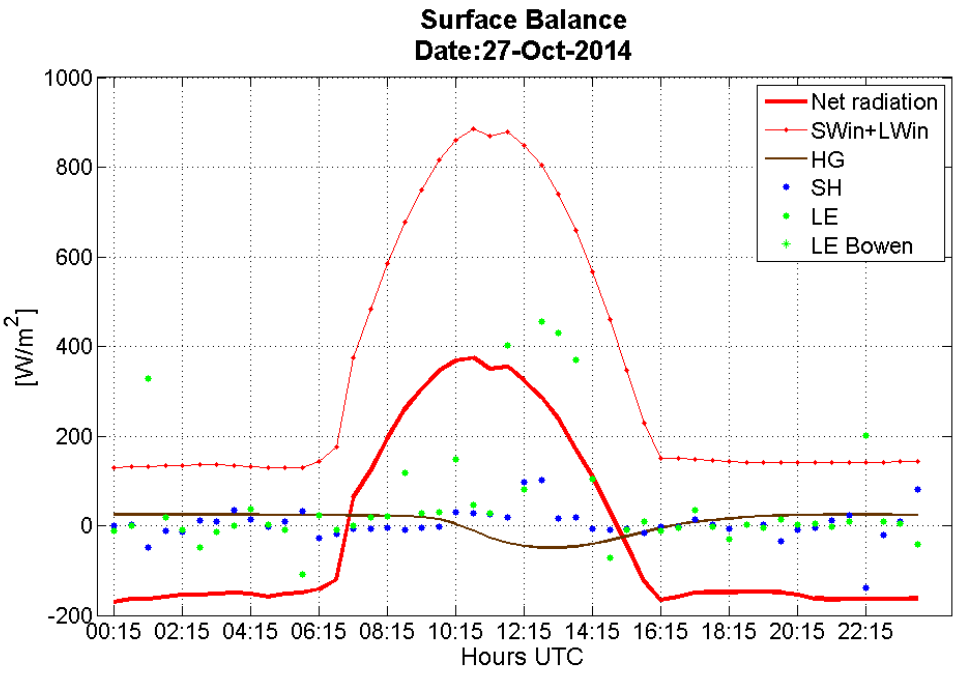

Figure 5.41: All the components of the surface balance are drawn for the 27th of October 2014 the most complete day of thermally driven days. I have also added the incoming radiation (long wave and short wave summed) to have a reference on the incoming energy.

during the night instead it is positive (upward), and in this case the ground loss heat in favour of the atmosphere.

In general during the night there is an energy loss (negative residual) and during the day an energy surplus (positive residual). This is only one case, but it is clearly far from the balance closure. In my opinion at Arbeser more experience on the behaviour of the sonic is needed, and certainly a working Krypton lamp. The sonic data in fact are too trembling and not completely reliable on fluxes, on the other side this data seems quite correct (look back to the SH uncertainties) then something else might occur. In previous sections I cited the advection (both vertical or horizontal) that may justify the large amount of non closure for the energy balance.

This is the only complete energy balance for a clear day. Looking at other clear days sometimes it is possible to partially integrate with the Bowen ratio method, but not always because this method has many controls on temperature and specific humidity profiles. In general the frame is the same, but sometimes

Var	00:15	00:45	1:15	1:45	2:15	2:45	3:15	3:45	4:15	4:45	5:15	5:45
HF	-35	-22	254	-19	-47	-61	-30	8	27	-25	-24	-101
R_N	-171	-163	-163	-159	-155	-154	-152	-150	-152	-159	-152	-150
Res	-136	-141	-417	-140	-108	-93	-122	-158	-179	-134	-128	-49
Var	6:15	6:45	7:15	7:45	8:15	8:45	9:15	9:45	10:15	10:45	11:15	11:45
HF	-29	-50	-30	-11	-6	87	5	11	174	87	81	460
R_N	-142	-121	61	122	194	260	305	345	368	375	350	356
Res	-113	-71	91	132	200	172	300	334	194	288	269	-104
Var	12:15	12:45	13:15	13:45	14:15	14:45	15:15	15:45	16:15	16:45	17:15	17:45
HF	225	606	495	435	139	-47	7	7	-9	-9	39	-13
R_N	324	286	237	172	108	32	-45	-123	-166	-159	-149	-148
Res	99	-320	-258	-263	-31	79	-52	-130	-157	-150	-188	-135
Var	18:15	18:45	19:15	19:45	20:15	20:45	21:15	21:45	22:15	22:45	23:15	23:45
HF	-54	-14	-23	-42	-30	-24	-15	6	38	-35	-12	14
R_N	-148	-148	-147	-148	-155	-162	-165	-164	-163	-163	-163	-163
Res	-94	-134	-124	-106	-125	-138	-150	-170	-201	-128	-151	-177

Table 5.12: Surface balance of October 27th, 2014. HF = sum of heat fluxes (SH, LE and H_G); R_N is the net radiation ($(SW + LW)\downarrow - (SW + LW)\uparrow$; *Res* is the residual, thus the difference between net radiation and heat fluxes. Values in W/m^2.

there is an energy loss during the day due to a very high SH, or a huge surplus due to a flat SH.

The ground heat flux is practically always of the same order of magnitude. Only during winter the snow cover reduces the ground heat flux to very small or zero values.

Integrating the missing data of LE with the Bowen ratio method, it is possible to look at more days with mostly complete surface energy balance. In Figure 5.42 the surface balance of 1st October 2015 is presented. In this case some points of LE from Bowen ratio are present, the net radiation is smaller than the sum of SH, LE and HG, and in the afternoon the incoming radiation (SW and LW summed) is even smaller than heat fluxes.

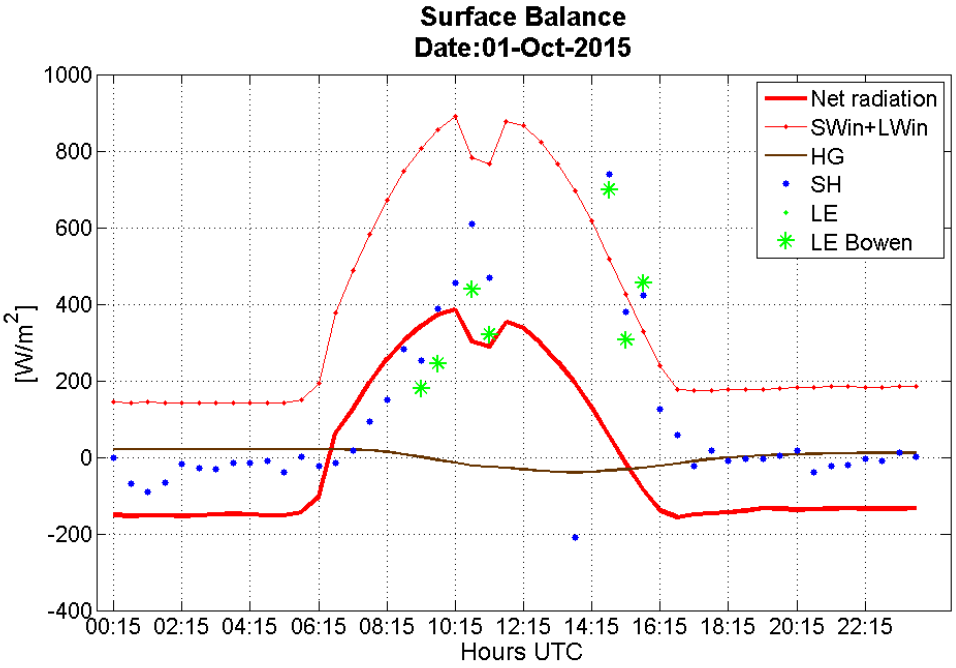

Figure 5.42: Surface energy balance for the 1st October 2015. In this case some points of LE are integrated using the Bowen ration method. In the central hours of the day is clearly out-of-balance, in fact the heat fluxes sum is bigger than the net radiation.

In Figure 5.43 the surface energy balance for 27th October 2015 is depicted, this is the previously seen "higher" case, adding the LE it remains an higher case, or even the available energy is four time smaller than heat fluxes.

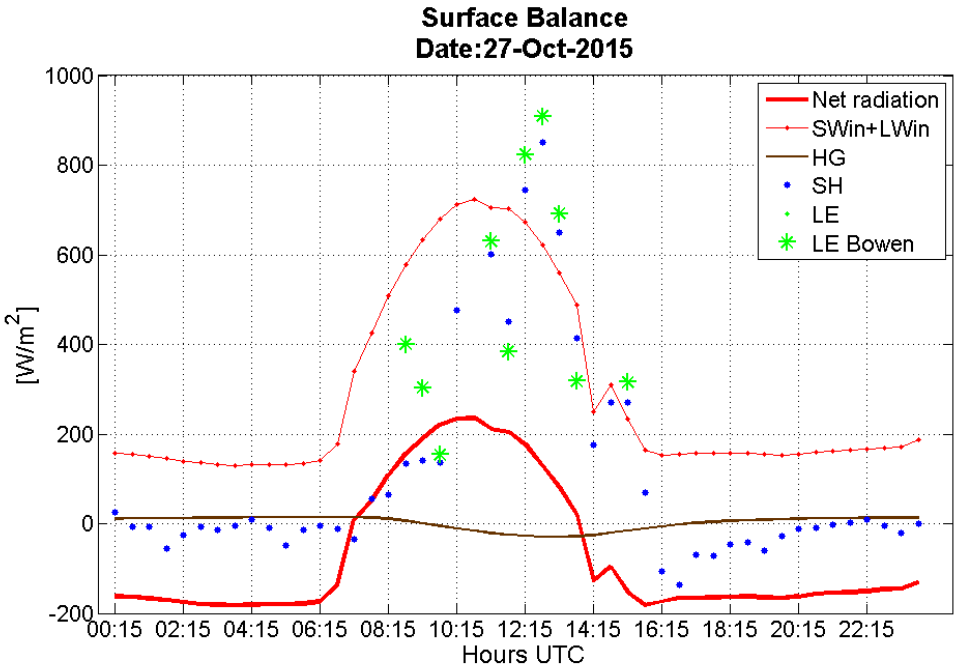

Figure 5.43: Surface energy balance for the "higher" day 27th October 2015. In this case, as previously seen, the heat and sensible fluxes even overpass the incoming radiation ($SW + LW$). In this case the LE is evaluated with the Bowen ratio method.

In Figure 5.44 the surface energy balance for 30th October 2015 is depicted, in this case the heat fluxes lay down the dotted curve of incoming radiation, but remain bigger than the net radiation curve.

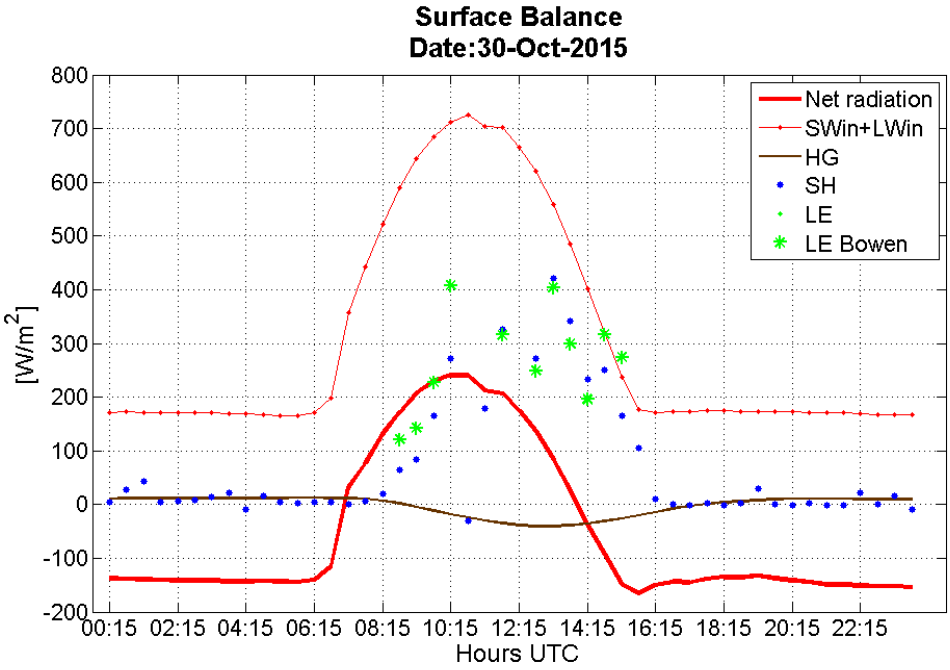

Figure 5.44: Surface energy balance for 30th October 2015. This can be classified as a "medium" day, even if the total fluxes overpass the net radiation.

The last plot of thermally driven days with some LE point available is the 12th November 2015 (Fig. 5.45). This may be called a "medium" case using the same former conditions, but the fluxes also in this case doubled the net radiation. After all these plots and comments is clear that the advection play a fundamental role in the Arbeser site. I cannot distinguish with my analyses between horizontal advection and vertical advection, but for sure more studies has to be conducted on this line.

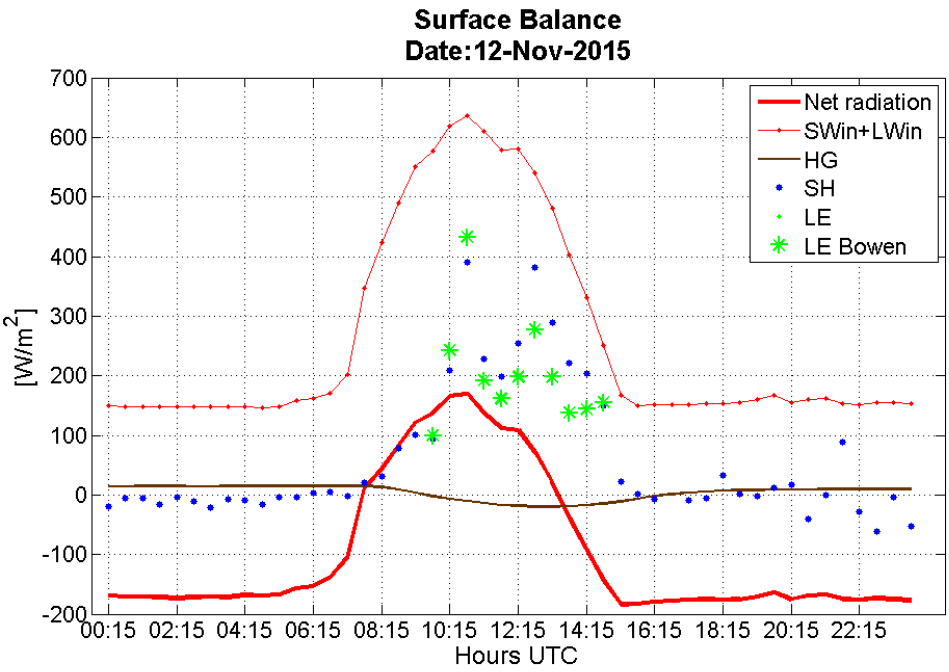

Figure 5.45: Surface energy balance for 12th November 2015. In the previous example of Tab. 5.9, this is the "medium" day. In fact SH and LE stay beyond the incoming radiation curve. Although these fluxes widely pass the net radiation.

5.3.4 Overview on the Entire Dataset

In this brief section I present some plot of the High Quality dataset, even if from Arbeser I do not have any complete day. The main reason, as stated before and as wrote in Section 4.4.3, is the stationarity requirement not being fulfilled.

In the following figures it is possible to see the same variables analysed through this chapter, in this section I show also the plot of LE, that theoretically has only the best data of the entire dataset.

The first is the plot of streamline velocity immediately followed by the scaled one with the friction velocity (Fig. 5.46). In Fig.5.46(a) the mean velocity is around 8m/s with higher values during the nighttime. In Fig.5.46(b) there are a lot of points that respect the MOST, but also some other that are completely out. I recall that in this case no distinction between stable and unstable situations was done, thus the MOST cannot be applied at all.

In Figure 5.47(a) I plot the turbulent kinetic energy for the high quality

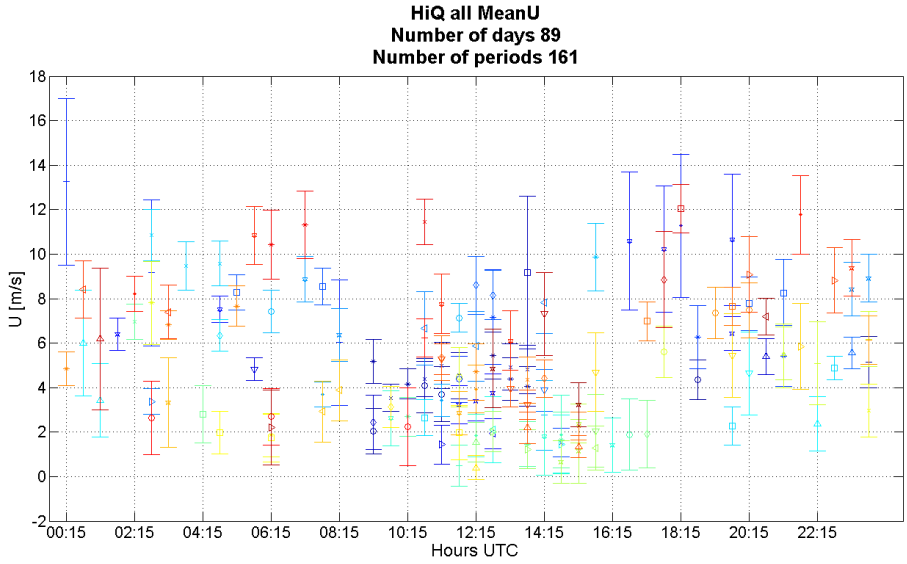

(a) Half hour mean streamline velocity.

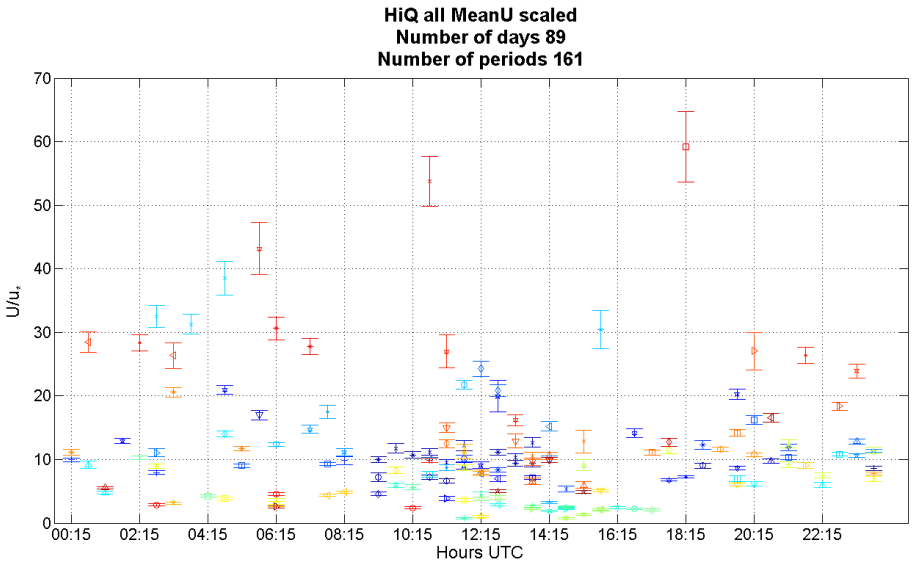

(b) Half hour mean streamline velocity scaled with friction velocity.

Figure 5.46: Streamline velocities (half hour averages) for the HiQ dataset, all data points that fulfill the HiQ requirements are shown, irrespective of the day when they were measured.

dataset, here it is not simple to see the daily cycle, but in this case different days are shown, and they come from completely different weather situations (or I do not know each weather situation). Instead in Fig. 5.47(b) a set of comparable results are shown, and in this the surface layer requirement for a stable layer cannot be verified for the scarcity of data.

Now I move to the sensible heat flux, in this case it is simple to see the expected daily cycle, even if it is not very well defined. In the Fig. 5.49(b) I plot only those half hour periods when the Krypton hygrometer was working. In the next plot in Figure 5.48 there is the latent heat flux for those very high quality data. As you can see it is very difficult to make any hypothesis or reliable analysis on those.

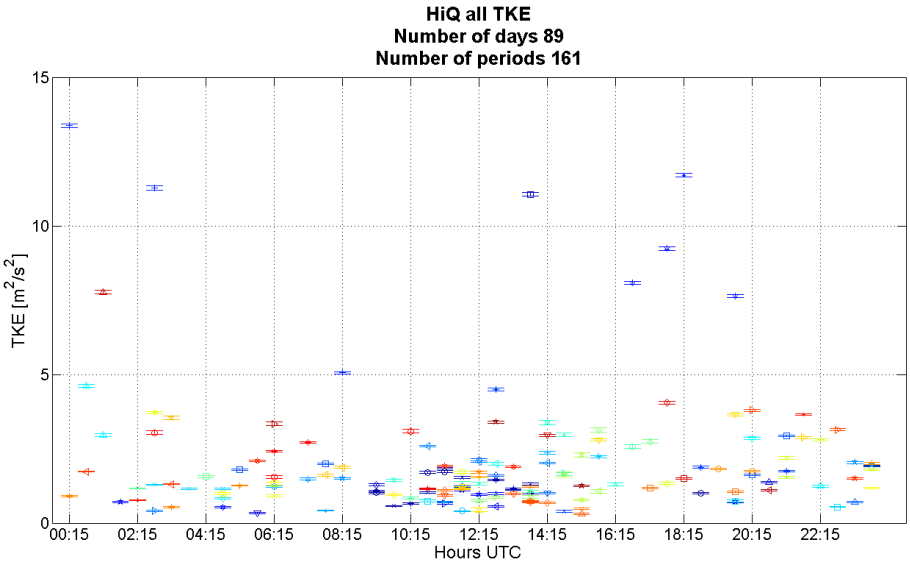

(a) Turbulent Kinetic Energy.

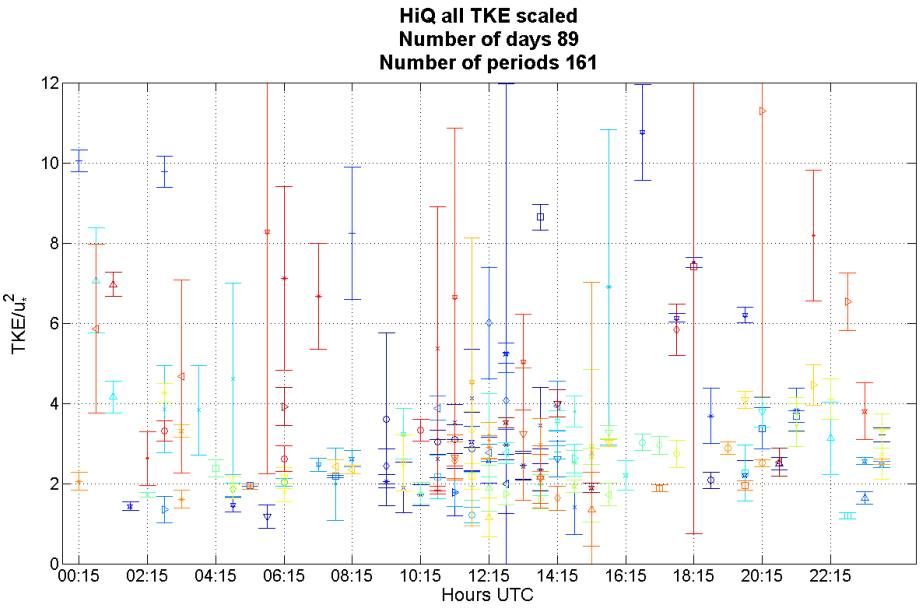

(b) TKE scaled with friction velocity.

Figure 5.47: The TKE for the HiQ dataset, that contains only 161 half hour periods.

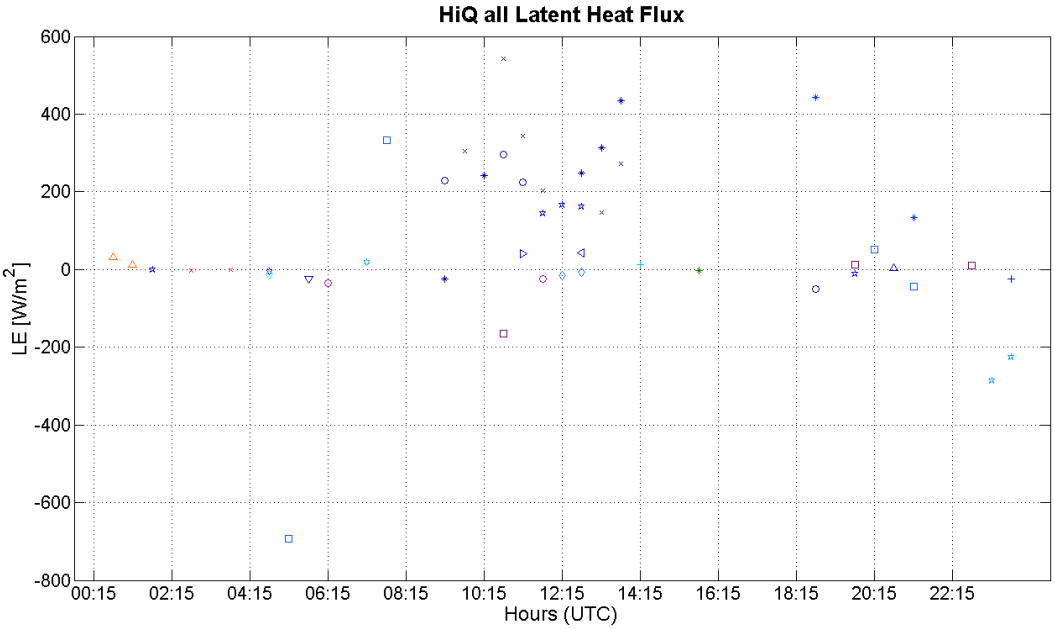

Figure 5.48: Latent heat flux from HiQ dataset. These are all the periods when the krypton hygrometer worked, and the data measured had passed all the quality controls.

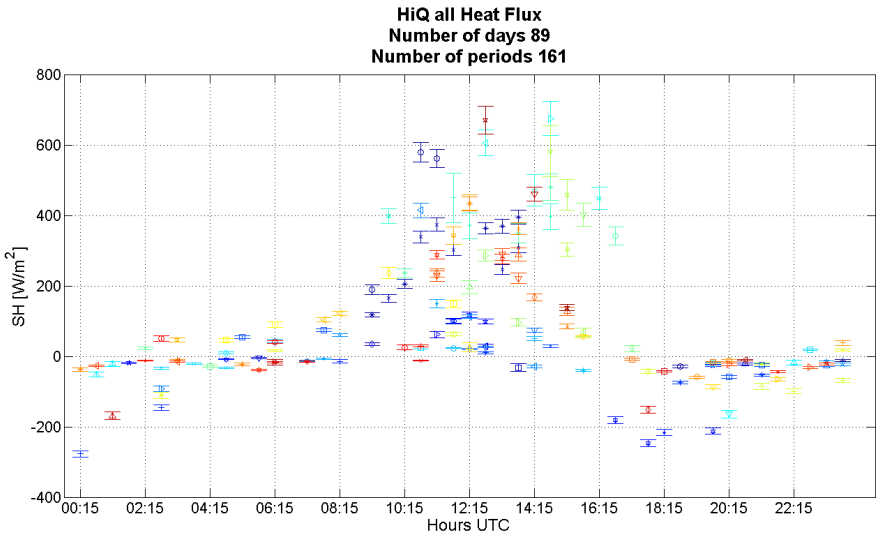

(a) Sensible heat flux. Each point represents an half hour period that had passed all the quality controls required by the HiQ dataset.

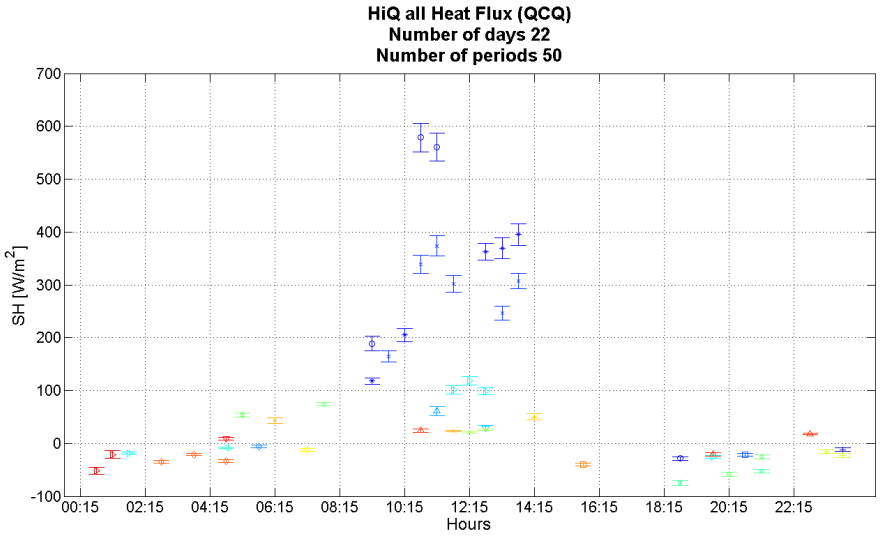

(b) Sensible heat flux only of periods when the krypton hygrometer was working.

Figure 5.49: Sensible heat flux for HiQ data set (a), and for the very HiQ data set (b), when the KH20 was working. On the sesible heat flux are done some corrections for the humidity content of the air, thus the very HiQ sensible heat flux is only when the specific humidity measurements are available. Otherwise, as previously stated in Section 4.4, these corrections are effect less, and the sensible heat flux data are as well meaningful.

Chapter 6

Conclusions

6.1 Standard Meteorological Data

The standard meteorological data, or low frequency data, were used essentially to find some interesting days that could be easily analysed on the turbulence side. But also they worked as a solid bedrock for the understanding of the mean meteorology at Arbeser.

On these data I built a Clear Days Algorithm that had selected the *thermally driven days*, which are deeply studied in the part of my work regarding the turbulence.

The classification results were remarkable, in fact the algorithm had worked well, and had demonstrated its reliability. Thus on this side I can recommend its use also for future analysis.

The weather conditions at Arbeser showed the scarcity of complete clear days, especially during summer season. And on a period spanning from the 1st October 2014 to the 26th January 2016[1] 33 clear days with a low pressure gradients had been found, of those only 17 *thermally driven days* with a normal valley wind regime had been found (class P1 CSD - East).

The analysis on high frequency data was conducted on those classes, especially on *thermally driven days* class.

A special attention was done regarding the wind patterns at Arbeser compared to the theory of valley winds. Two cases were presented, and the overall conclusion is that Arbeser is generally out of the valley boundary layer, thus it is not influenced by the valley circulation. Although in these two cases, with

[1]The pressure data, used for pressure gradient classification, end on this date, and I have not updated them in the following to concentrate my attention on high frequency data analysis.

a particularly clear weather and a proved mountain-plain circulation inside the Inn Valley, I saw that during the mid afternoon somehow the wind at Arbeser changed direction from SW to NE. This probably states that the upvalley wind can sometimes reach Arbeser station. However the main wind direction is from the third quarter with the most frequent angle 200°. This corresponds to a middle way between the south slope and the ridge slope. The daytime convection on the south slope might play a relevant role, but this behaviour is observed also during the night, and a clear explanation was not found.

6.2 Turbulence Data

The turbulence data analysis had given only an overview on Arbeser dataset.

As previously said, I focused my attention only on those days selected using the low frequency data. Thus the entire analysis presented deals only with the 11 *thermally driven days* effectively available inside the high frequency dataset.

I did an accurate error analysis on turbulence data, because the turbulence dataset used for the analysis was the medium quality one. Thus it was necessary to assess the uncertainty of each variable to create some reliable results.

First the data completeness was assessed, and I had realised that the high frequency measurements of specific humidity are very poor, thus the latent heat flux (LE) is rarely available. I tried to complement the LE measurements using the low frequency data through the Bowen ratio method; this part was partially successful and had permitted to integrate the energy surface balance. In particular I evaluated the Bowen ratio using the gradient method on the low frequency measurements, and for each half hour period I evaluated the B_0^* for all the combinations of available temperature/humidity measurements levels. The best combination resulted was the first-third levels gradient.

Some controls on temperature inversions and flat gradients were implemented, and these cases were rejected. B_0^* was compared with the Bowen ratio (B_0) evaluated with sensible (SH) and latent fluxes, when both were present. The comparison had revealed a small overestimation of B_0^* with respect to B_0. From B_0^* I evaluated the LE using the high frequency measurements of SH and I obtained, as expected, a slightly overestimated values of LE respect to LE from high frequency data. This discrepancy was not too big then I used this method to integrate the LE measurements.

The first part of the analysis regards daily cycles, this is a preliminary to the second part where I analysed the standard deviation surface layer scaling.

The variables analysed are:

- The mean flow velocity;
- The turbulent kinetic energy;
- The sensible heat flux;
- The local stability parameter;
- The dimensionless standard deviations of wind velocity components and
- The dimensionless standard deviation of sonic temperature.

I tried to assess whether there exists a relationship between wind direction and flow stability, but unstable and stable cases shows a very similar wind rose. Only the few NE cases, which probably represent a upvalley wind interaction with Arbeser have a mostly stable behaviour.

The stability parameter, z/L, has a mean normal behaviour. In fact, it is positive during nighttime (stable configuration) and negative during day time (unstable configuration). However the daily cycles of single days do not show the same behaviour, but sometimes a slightly stable profile during the day. To verify the correctness of this data I analysed the potential temperature profiles measured with low frequency instruments. The overall analysis showed a preponderance of stable or near neutral periods and only sometimes a clearly unstable profile during daytime.

Removing the near neutral cases (defined as $|z/L| < 0.05$) the daytime situation is more clear: it is practically always unstable. Instead, the nighttime situation has some unstable periods. These periods are not understandable neither with the potential temperature nor with the SH. Excluding the inaccuracy of measurements I cannot state the origin of these values.

A thorough analysis was done on sensible heat flux, and its behaviour was various: from very high (even more than measured available energy) to practically null. I explored the possibility of advection contribution and possible mistakes in SH measurements. It was clear that during three sample days the measurements were correct and reliable, and observing the wind velocity (on streamline coordinates), wind direction and the second rotation angle β I concluded that the advection was present, both vertical and horizontal, at least in the three special cases analysed. I was not able to assess the magnitude of this advection, but

probably it constitutes the excess or lack of energy in the surface energy balance (furthermore analysed). Using the albedo values I determined whenever the ground was covered by the snow, and I found a correspondence between snow coverage and SH. When the ground was covered by the snow (mean daily albedo around 0.6) the SH was always nearly "flat", or rather with small fluctuations around zero. Thus I suppose a correlation between snow, that covers the ground, and SH measurements.

The next part of the analysis was done on dimensionless standard deviations σ/u_*, and I compared them with Nadeau *et al.* (2013) results. First I fitted Arbeser data with Nadeau *et al.*'s functions, and I obtained that generally the data cloud is under the fitting function, both for stable and unstable sides. The most evident case is for σ_u/u_*. Surely the different experimental set-up may influence the results and also the differences in terrain complexity. In fact, Nadeau *et al.* experiment was set on a steep slope, instead Arbeser is a mountain-top site. But in this case the aim is the surface layer scaling thus if these functions effectively works for truly complex mountainous terrain they have to represent both sites. In fact the general behaviour, apart from the coefficients, of these functions seems to well depict the data distribution.

The dimensionless standard deviation of temperature was fitted only outside the near neutral zone (for $|z/\Lambda| > 0.05$), and in this case for the unstable side, where more data were available, the Nadeau *et al.* function passes inside the data-cloud, but it is generally greater than the data with smaller uncertainties. This result is opposite to the most of other i-Box stations, where the data-cloud was above this function. The explanation might be in the same reason of smaller SH, thus smaller variation of temperature and consequently smaller standard deviations.

The last part of the work concerned an overview on surface energy balance. As previously described the LE for the balance was rarely available, then I used the Bowen ratio method to integrate this data. The only complete day (with all the components for the surface balance) was the 27th October 2014. This day has shown a quite normal behaviour, but the balance was not closed, a huge residual energy was present. The same happened for other days, even if the LE data were less complete. Some extreme cases were found (e.g. the 27th October 2015) where the overall fluxes were even bigger than incoming energy. In those cases the advection contribution was clear, but now I am not able to explain how the advection interact at Arbeser. Certainly the advection was present in both horizontal and vertical components.

From this preliminary study on sensible heat flux, surface energy balance and turbulence scaling, I can suggest that the Monin-Obukhov theory for such a complex site is incomplete. In fact, large scattering, and fluctuations in scaled plot were found. This could be due to a key-variable not included in the variable set of MOST, in particular this variable could be a representation of the advection, that, from this study, seems to play a relevant role. Probably adding a variable that describe the advection might permit a better scaling of aforementioned variables.

6.3 Final Remarks

This work MSc thesis work has pointed out some peculiarities of such a complex site as Arbeser is. I got some scientific results that partly confirm literature knowledge, but also some new or particular behaviour that should be investigated in deeply.

I am satisfied with all the work done, and I wish that it might be useful for future studies, as a first stone to build a house.

Part III

Appendices

Appendix A

Metek Ultrasonic Anemometer Calculations

Metek ultrasonic anemometer USA-1 and uSonic3 have the same building configuration, that consists on three sonic paths with an attack angle of 45° that it is possible to call P1, P2 and P3 (see Fig.3.9). The propagation times for the sonic pulses are measured with a resolution of 40MHz (about $2.5 \cdot 10^{-8} s$). The pulses travel in both direction as explain in previous chapters, and in order to get the travelling times for the 6 pulses the 6 counter values $p_{p,dir}$ in combination with the 6 offset values Oi are used (the offset values Oi are determined during the calibration procedure with the wind tunnel, calibration made by Metek). In this way we have six time:

$$\begin{aligned} t_{1,up} &= \frac{p_{1,up} - O1}{40MHz} \\ t_{1,down} &= \frac{p_{1,down} - O2}{40MHz} \\ t_{2,up} &= \frac{p_{2,up} - O3}{40MHz} \\ t_{2,down} &= \frac{p_{2,down} - O4}{40MHz} \\ t_{3,up} &= \frac{p_{3,up} - O5}{40MHz} \\ t_{3,down} &= \frac{p_{3,down} - O6}{40MHz} \end{aligned} \tag{A.1}$$

from these travel times we can obtain the radial sound velocities

$$c_{p,dir} = \frac{d_p}{t_{p,dir}} \tag{A.2}$$

where d_p is the path length stored in P1, P2 and P3 variables with a precision of 0.1 mm.

These six sound velocities are affected by radial wind component and temperature; for eliminate the radial component of wind we need to averaging these six velocities. For each pair the influence of radial wind component is once positive and once negative (assuming there is no change of radial wind while measuring $c_{p,up}$ and $c_{p,down}$), so adding these values will omit their influence, and the average sound speed in motionless air is:

$$c_0 = \frac{1}{6}\sum_{p=1}^{3}(c_{p,up} + c_{p,down}) \tag{A.3}$$

The derived *sound temperature* (or "acoustic temperature") is given by the following equation

$$T_s = \left[\frac{c_0}{20.05m/s}\right]^2 \cdot 1K - 273.15K \tag{A.4}$$

where $20.05m/s$ comes from $\gamma_d R_d = 1.4 * 287.04 = 401.856m^2/s^2$ with γ_d is the dry adiabatic lapse rate and R_d is the gas constant for dry air. The square root of $\gamma_d R_d$ is approximately $20.05m/s$.

The radial wind components are calculated as half of the differences of the radial sound components $c_{p,up}$ and $c_{p,down}$. Calculation of the differences eliminates the influence of temperature which is assumed to be constant for each single shot (6 sonic pulses). Thus the radial wind components for each path p are then defined by:

$$v_p = \frac{1}{2}(c_{p,up} + c_{p,down}) \tag{A.5}$$

where upward velocities are represented with positive values.

A.1 Coordinate transformation

The coordinate transformation is different for USA-1 and uSonic3, because the first one uses left-hand Cartesian coordinate system instead the second one uses a right-hand Cartesian coordinate system.

USA-1 coordinate transformation:

$$\begin{aligned} x &= k\sqrt{\frac{2}{3}}(v_2 - v_3) \\ y &= k\frac{\sqrt{2}}{3}(2v_1 - v_2 - v_3) \\ z &= k\frac{\sqrt{2}}{3}(v_1 + v_2 + v_3) \end{aligned} \tag{A.6}$$

uSonic3 coordinate transformation:

$$\begin{aligned} x &= k\frac{\sqrt{2}}{3}(2v_1 - v_2 - v_3) \\ y &= k\sqrt{\frac{2}{3}}(v_2 - v_3) \\ z &= k\frac{\sqrt{2}}{3}(v_1 + v_2 + v_3) \end{aligned} \tag{A.7}$$

We see that the difference is between x and y calculation. The correction constant is $k = 1.153$, that is an increasing common factor between USA-1 and uSonic3.

Acknowledgements

I wish to thanksgiving Metek personal, in particular Olaf Brökmann and Gerhard Peters for the materials[1], support and patience. I also would like to thank Dr. Roberto Gavioso of INRiM (National Institue for Metrological Research) of Turin for the support and the help in comprehension of sound speed in air.

[1]For USA-1 Internal Report of 01.01.2001, for uSonic3 an Internal Memo of 30.04.2014.

Appendix B

Analysis Source Code

Here all the scripts of the programs used for the Arbeser data's analysis are collected.

The Low Frequency (LF) data was analyse with Matlab®, meanwhile the High Frequency binary files are treated firstly with EdiRe.

B.1 EdiRe Processing List

The following script is the EdiRe processing list for the uSonic3 ultrasonic anemometer. As previously seen in Chapter 3 the first sonic anemometer was an USA-1. The processing list is practically the same, the only difference is the presence of a instrument flag (called CQT), and consequently of some instructions in this processing list that are not in the USA-1. A relevant difference between USA-1 and uSonic3 Edire's processing lists, as previously seen, is the coordinate system of these sonic anemometers. In fact, the USA-1 has a left-hand reference system, meanwhile the uSonic3 has a right-hand reference system. Thus in the "Wind direction" item (row 376) for the uSonic3 there is the options "Wind Direction Components = **U+W V+S**", however for the USA-1 there is "Wind Direction Components = **U+S V+W**".

```
1 Comments
2   Comment = Station Arbeser Kogl 106
3   Comment = 1 level
4   Comment =  Upper level Metek uSonic3, KH20, 3 rotronic temperature/humidity, 3
      wind speed
5 Comments
6   Comment =   computes raw fluxes
7   Comment = 2d rotation, block averaging
8   Comment = despiking, spikes replace with NaN
```

```
  Comment = sonicT corrected by cross wind, HF corrected also for humidity
  Comment =   frequency response correction with 1/3 physical distance
Comments
  Comment = Author Alessio Golzio (after Ivana Stiperski)
  Comment = Date: 2016.04.08
  Comment = Proc list for daily files
Location Output Files
  Output File Calculations =  D:\alessio\UniTo\tesi\magistrale\Dati\hf_data\
    halfhourAvg\106_complete6.csv
  Output File Spectral =
  Output File Wavelet =
  Output File Cross Correlation =
  Output File Distribution =
  Output File Quadrant =
  Output File Reference =
Preprocessed Files
  File <0> =  D:\alessio\UniTo\tesi\magistrale\Dati\lf_data\106_arbeser_meteo.csv
  File <1> =
  File <2> =
  File <3> =
  File <4> =
  File <5> =
  File <6> =
  File <7> =
  File <8> =
  File <9> =
  File <9> =
Set Values
  From Time =
  To Time =
  Number of Variables = 3
  Storage Label = P
  Assignment value = <0> pressure
  Storage Label =  Tair
  Assignment value = <0> Tair_3
  Storage Label = RHair
  Assignment value = <0> Rhair_3
Set Values
  From Time =
  To Time =
  Number of Variables = 2
  Storage Label =  HT
  Assignment value = <0> Zref2
  Storage Label =  Zepldi
  Assignment value = 0
Set Values
  From Time =
  To Time =
  Number of Variables = 1
  Storage Label = theta
  Assignment value =  <0> Sonic_angle
Extract
  From Time =
  To Time =
  Channel = 4
  Label for Signal = U
Extract
  From Time =
  To Time =
```

```
  Channel = 5
  Label for Signal =  V
Extract
  From Time =
  To Time =
  Channel = 6
  Label for Signal = W
Extract
  From Time =
  To Time =
  Channel = 7
  Label for Signal = T
Extract
  From Time =
  To Time =
  Channel = 7
  Label for Signal = T_nc
Extract
  From Time =
  To Time =
  Channel = 9
  Label for Signal = Q
Extract
  From Time =
  To Time =
  Channel = 8
  Label for Signal =  CQT
Despike
  From Time =
  To Time =
  Signal = U
  Standard Deviations = 10
  Spike width = 4
  Spike % consistency = 30
  Replace spikes =    NaN
  Storage Label spike count = Spike_U
  Outlier Standard Deviations =
Despike
  From Time =
  To Time =
  Signal = V
  Standard Deviations = 10
  Spike width = 4
  Spike % consistency = 30
  Replace spikes = NaN
  Storage Label spike count = Spike_V
  Outlier Standard Deviations =
Despike
  From Time =
  To Time =
  Signal = W
  Standard Deviations = 10
  Spike width = 4
  Spike % consistency = 30
  Replace spikes = NaN
  Storage Label spike count = Spike_W
  Outlier Standard Deviations =
Despike
  From Time =
```

```
  To Time =
  Signal = T
  Standard Deviations = 10
  Spike width = 4
  Spike % consistency = 30
  Replace spikes = NaN
  Storage Label spike count = Spike_T
  Outlier Standard Deviations =
Despike
  From Time =
  To Time =
  Signal = T_nc
  Standard Deviations = 10
  Spike width = 4
  Spike % consistency = 30
  Replace spikes = NaN
  Storage Label spike count =
  Outlier Standard Deviations =
Despike
  From Time =
  To Time =
  Signal = Q
  Standard Deviations = 10
  Spike width = 4
  Spike % consistency = 30
  Replace spikes = NaN
  Storage Label spike count = Spike_Q
  Outlier Standard Deviations =
Despike
  From Time =
  To Time =
  Signal = CQT
  Standard Deviations = 50
  Spike width = 1
  Spike % consistency = 30
  Replace spikes = NaN
  Storage Label spike count = Spike_CQT
  Outlier Standard Deviations =
Statistical QC
  From Time =
  To Time =
  Signal = U
  Signal =
  Storage Label % good = statQC_U
  Storage Label % acceptable = statQC_Uacc
  Good upper limit max = 45
  Good lower limit min = -45
  Good upper limit mean =
  Good lower limit mean =
  Good upper limit std dev =
  Good lower limit std dev =
  Good upper limit skewness = 1.0
  Good lower limit skewness = -1.0
  Good upper limit kurtosis = 2.0
  Good lower limit kurtosis = -1.0
  Acceptable upper limit max = 45
  Acceptable lower limit min = -45
  Acceptable upper limit mean =
  Acceptable lower limit mean =
```

```
  Acceptable upper limit std dev =
  Acceptable lower limit std dev =
  Acceptable upper limit skewness = 2.0
  Acceptable lower limit skewness = -2.0
  Acceptable upper limit kurtosis = 8.0
  Acceptable lower limit kurtosis = -2.0
Statistical QC
  From Time =
  To Time =
  Signal = V
  Signal =
  Storage Label % good = statQC_V
  Storage Label % acceptable = statQC_Vacc
  Good upper limit max = 45
  Good lower limit min = -45
  Good upper limit mean =
  Good lower limit mean =
  Good upper limit std dev =
  Good lower limit std dev =
  Good upper limit skewness = 1.0
  Good lower limit skewness = -1.0
  Good upper limit kurtosis = 2.0
  Good lower limit kurtosis = -1.0
  Acceptable upper limit max = 45
  Acceptable lower limit min = -45
  Acceptable upper limit mean =
  Acceptable lower limit mean =
  Acceptable upper limit std dev =
  Acceptable lower limit std dev =
  Acceptable upper limit skewness = 2.0
  Acceptable lower limit skewness = -2.0
  Acceptable upper limit kurtosis = 8.0
  Acceptable lower limit kurtosis = -2.0
Statistical QC
  From Time =
  To Time =
  Signal = W
  Signal =
  Storage Label % good = statQC_W
  Storage Label % acceptable = statQC_Wacc
  Good upper limit max = 45
  Good lower limit min = -45
  Good upper limit mean =
  Good lower limit mean =
  Good upper limit std dev =
  Good lower limit std dev =
  Good upper limit skewness = 1.0
  Good lower limit skewness = -1.0
  Good upper limit kurtosis = 2.0
  Good lower limit kurtosis = -1.0
  Acceptable upper limit max = 45
  Acceptable lower limit min = -45
  Acceptable upper limit mean =
  Acceptable lower limit mean =
  Acceptable upper limit std dev =
  Acceptable lower limit std dev =
  Acceptable upper limit skewness = 2.0
  Acceptable lower limit skewness = -2.0
  Acceptable upper limit kurtosis = 8.0
```

```
  Acceptable lower limit kurtosis = -2.0
Statistical QC
  From Time =
  To Time =
  Signal = T
  Signal =
  Storage Label % good = statQC_T
  Storage Label % acceptable = statQC_Tacc
  Good upper limit max = 60
  Good lower limit min = -40
  Good upper limit mean =
  Good lower limit mean =
  Good upper limit std dev =
  Good lower limit std dev =
  Good upper limit skewness = 1.0
  Good lower limit skewness = -1.0
  Good upper limit kurtosis = 2.0
  Good lower limit kurtosis = -1.0
  Acceptable upper limit max = 60
  Acceptable lower limit min = -40
  Acceptable upper limit mean =
  Acceptable lower limit mean =
  Acceptable upper limit std dev =
  Acceptable lower limit std dev =
  Acceptable upper limit skewness =  2.0
  Acceptable lower limit skewness = -2.0
  Acceptable upper limit kurtosis = 8.0
  Acceptable lower limit kurtosis = -2.0
1 chn statistics
  From Time =
  To Time =
  Signal = CQT
  Storage Label Mean = MeanCQT
  Storage Label Std Dev = StdvCQT
  Storage Label Skewness =
  Storage Label Kurtosis =
  Storage Label Maximum =
  Storage Label Minimum =
  Storage Label Variance =
  Storage Label Turbulent Intensity =
  Alt Turbulent Intensity Denominator =
Comments
  Comment = Correct sonic temperature for crosswind components
  Comment = From Liu et al. 2001 and Metek 2014
  Comment =
User defined fast
  From Time =
  To Time =
  Equation = ((T+273.15)+3*(U^2+V^2)/(4*403))-273.15
  Number of signals = 3
  Signal = T
  Signal = U
  Signal = V
  Variable =
  Variable =
Gas conversion
  From Time =
  To Time =
  Storage Label = e
```

```
303   Apply to =
304   Apply by =
305   Measured variable = RHair
306   Convert from = Relative humidity
307   Convert to = Partial Pressure kPa
308   Temperature (C) = Tair
309   Pressure (kPa) = P
310   Water vapour =
311   Water vapour units =
312   Molecular weight (g/mole) =
313 Sensible heat flux coefficient
314   From Time =
315   To Time =
316   Storage Label = rhoCp
317   Apply to =
318   Apply by =
319   Vapour pressure (KPa) = e
320   Min or QC =
321   Max or QC =
322   Temperature (C) = Tair
323   Min or QC =
324   Max or QC =
325   Pressure (KPa) = P
326   Min or QC =
327   Max or QC =
328   Alternate rhoCp =
329 Latent heat of evaporation
330   From Time =
331   To Time =
332   Storage Label = LH
333   Apply to =
334   Apply by =
335   Temperature (C) = Tair
336   Min or QC =
337   Max or QC =
338   Pressure (KPa) = P
339   Min or QC =
340   Max or QC =
341   LE flux coef, L =
342 1 chn statistics
343   From Time =
344   To Time =
345   Signal = Q
346   Storage Label Mean =
347   Storage Label Std Dev =
348   Storage Label Skewness =
349   Storage Label Kurtosis =
350   Storage Label Maximum =
351   Storage Label Minimum = MinQ_mV
352   Storage Label Variance =
353   Storage Label Turbulent Intensity =
354   Alt Turbulent Intensity Denominator =
355 User defined
356   From Time =
357   To Time =
358   Storage Label = QCQ
359   Apply to =
360   Apply by =
361   Equation = IIF(MinQ_mV<5,9999,0)
```

```
  Variable = MinQ_mV
  Variable =
Comments
  Comment = The KH20 serial number is 1735
  Comment = Full vapour scaled window
  Comment = XKw = -0.189 Intercept 3946mV
User defined fast
  From Time =
  To Time =
  Equation = (LN(Q+QCQ)-LN(3946))/(-0.189)
  Number of signals = 1
  Signal =  Q
  Variable = QCQ
  Variable =
Wind direction
  From Time =
  To Time =
  Signal (u) = U
  Signal (v) = V
  Orientation = theta
  Wind Direction Components = U+W_V+S
  Wind Direction Output =  N_0_deg-E_90_deg
  Storage Label Wind Direction = Wind_Dir
  Storage Label Wind Dir Std Dev = Wind_Dir_stdV
1 chn statistics
  From Time =
  To Time =
  Signal = U
  Storage Label Mean = MeanU_unrot
  Storage Label Std Dev = StdvU_unrot
  Storage Label Skewness =
  Storage Label Kurtosis =
  Storage Label Maximum =
  Storage Label Minimum =
  Storage Label Variance =
  Storage Label Turbulent Intensity =
  Alt Turbulent Intensity Denominator =
1 chn statistics
  From Time =
  To Time =
  Signal = V
  Storage Label Mean = MeanV_unrot
  Storage Label Std Dev = StdvV_unrot
  Storage Label Skewness =
  Storage Label Kurtosis =
  Storage Label Maximum =
  Storage Label Minimum =
  Storage Label Variance =
  Storage Label Turbulent Intensity =
  Alt Turbulent Intensity Denominator =
1 chn statistics
  From Time =
  To Time =
  Signal = W
  Storage Label Mean = MeanW_unrot
  Storage Label Std Dev = StdvW_unrot
  Storage Label Skewness =
  Storage Label Kurtosis =
  Storage Label Maximum =
```

```
421   Storage Label Minimum =
422   Storage Label Variance =
423   Storage Label Turbulent Intensity =
424   Alt Turbulent Intensity Denominator =
425 Rotation coefficients
426   From Time =
427   To Time =
428   Signal (u) = U
429   Signal (v) = V
430   Signal (w) = W
431   Storage Label Alpha = alpha
432   Storage Label Beta  = beta
433   Storage Label Gamma = gamma
434   Optional mean u =
435   Optional mean v =
436   Optional mean w =
437 Rotation
438   From Time =
439   To Time =
440   Signal (u) = U
441   Signal (v) = V
442   Signal (w) = W
443   Alpha = alpha
444   Beta = beta
445   Gamma = gamma
446   Do 1st Rot = x
447   Do 2nd Rot = x
448   Do 3rd Rot =
449 1 chn statistics
450   From Time =
451   To Time =
452   Signal = U
453   Storage Label Mean = MeanU
454   Storage Label Std Dev = StdvU
455   Storage Label Skewness = SkewU
456   Storage Label Kurtosis = KurtU
457   Storage Label Maximum =
458   Storage Label Minimum =
459   Storage Label Variance =
460   Storage Label Turbulent Intensity =
461   Alt Turbulent Intensity Denominator =
462 1 chn statistics
463   From Time =
464   To Time =
465   Signal = V
466   Storage Label Mean = MeanV
467   Storage Label Std Dev = StdvV
468   Storage Label Skewness = SkewV
469   Storage Label Kurtosis = KurtV
470   Storage Label Maximum =
471   Storage Label Minimum =
472   Storage Label Variance =
473   Storage Label Turbulent Intensity =
474   Alt Turbulent Intensity Denominator =
475 1 chn statistics
476   From Time =
477   To Time =
478   Signal = W
479   Storage Label Mean = MeanW
```

```
  Storage Label Std Dev = StdvW
  Storage Label Skewness = SkewW
  Storage Label Kurtosis = KurtW
  Storage Label Maximum =
  Storage Label Minimum =
  Storage Label Variance =
  Storage Label Turbulent Intensity =
  Alt Turbulent Intensity Denominator =
1 chn statistics
  From Time =
  To Time =
  Signal = T_nc
  Storage Label Mean = MeanTV_nc
  Storage Label Std Dev = StdvTV_nc
  Storage Label Skewness =
  Storage Label Kurtosis =
  Storage Label Maximum =
  Storage Label Minimum =
  Storage Label Variance =
  Storage Label Turbulent Intensity =
  Alt Turbulent Intensity Denominator =
1 chn statistics
  From Time =
  To Time =
  Signal = T
  Storage Label Mean = MeanTV
  Storage Label Std Dev = StdvTV
  Storage Label Skewness = SkewTV
  Storage Label Kurtosis = KurtTV
  Storage Label Maximum =
  Storage Label Minimum =
  Storage Label Variance =
  Storage Label Turbulent Intensity =
  Alt Turbulent Intensity Denominator =
1 chn statistics
  From Time =
  To Time =
  Signal = Q
  Storage Label Mean = MeanQ
  Storage Label Std Dev = StdvQ
  Storage Label Skewness = SkewQ
  Storage Label Kurtosis = KurtQ
  Storage Label Maximum =
  Storage Label Minimum =
  Storage Label Variance = QQ
  Storage Label Turbulent Intensity =
  Alt Turbulent Intensity Denominator =
2 chn statistics
  From Time =
  To Time =
  Signal = W
  Signal = U
  Storage Label Covariance = UW
  Storage Label Correlation =
  Storage Label Flux =
  Flux coefficient =
2 chn statistics
  From Time =
  To Time =
```

```
  Signal = W
  Signal = V
  Storage Label Covariance = VW
  Storage Label Correlation =
  Storage Label Flux =
  Flux coefficient =
2 chn statistics
  From Time =
  To Time =
  Signal = U
  Signal = T
  Storage Label Covariance = UT
  Storage Label Correlation =
  Storage Label Flux =
  Flux coefficient =
2 chn statistics
  From Time =
  To Time =
  Signal = V
  Signal = T
  Storage Label Covariance = VT
  Storage Label Correlation =
  Storage Label Flux =
  Flux coefficient =
2 chn statistics
  From Time =
  To Time =
  Signal = W
  Signal = T
  Storage Label Covariance = WT
  Storage Label Correlation =
  Storage Label Flux = H
  Flux coefficient = rhoCp
2 chn statistics
  From Time =
  To Time =
  Signal = W
  Signal = T_nc
  Storage Label Covariance = WT_nc
  Storage Label Correlation =
  Storage Label Flux = H_nc
  Flux coefficient = rhoCp
2 chn statistics
  From Time =
  To Time =
  Signal = Q
  Signal = T
  Storage Label Covariance = QT
  Storage Label Correlation =
  Storage Label Flux =
  Flux coefficient =
2 chn statistics
  From Time =
  To Time =
  Signal = W
  Signal = Q
  Storage Label Covariance = WQ
  Storage Label Correlation =
  Storage Label Flux = LE
```

```
598   Flux coefficient = LH
599 Comments
600   Comment = Correction on sonic temperature standard deviation
601   Comment = From Liu et al 2001, BLM100: 459-468
602   Comment =
603 User defined
604   From Time =
605   To Time =
606   Storage Label = rho_m
607   Apply to =
608   Apply by =
609   Equation = (P-0.38*e)*1000/(0.28704*(Tair+273.15))
610   Variable = Tair
611   Variable = P
612   Variable = e
613 User defined
614   From Time =
615   To Time =
616   Storage Label = StdvTV_corr
617   Apply to =
618   Apply by =
619   Equation =  SQRT(ABS(StdvTV^2-1.02*(Tair+273.15)*QT/rho_m-0.51^2*QQ*(Tair
        +273.15)^2/rho_m^2))
620   Variable = QQ
621   Variable = QT
622   Variable = MeanTV
623   Variable = Tair
624   Variable = StdvTV
625   Variable = rho_m
626 Friction Velocity
627   From Time =
628   To Time =
629   Signal (u) = U
630   Signal (v) = V
631   Signal (w) = W
632   Storage Label U* (uw) =
633   Storage Label U* (uw vw) = Ustr
634 Stability - Monin Obhukov
635   From Time =
636   To Time =
637   Storage Label = ZoL
638   Apply to =
639   Apply by =
640   Measurement height (m) = HT
641   Zero plane displacement (m) = Zepldi
642   Virtual Temperature (C) = MeanTV
643   Min or QC =
644   Max or QC =
645   H flux (W/m2) = H
646   Min or QC =
647   Max or QC =
648   H flux coef, RhoCp = rhoCp
649   Min or QC =
650   Max or QC =
651   Scaling velocity (m/s) = Ustr
652   Min or QC =
653   Max or QC =
654 Stability - Monin Obhukov
655   From Time =
```

```
656   To Time =
657   Storage Label = ZoL_nc
658   Apply to =
659   Apply by =
660   Measurement height (m) = HT
661   Zero plane displacement (m) = Zepldi
662   Virtual Temperature (C) = MeanTV
663   Min or QC =
664   Max or QC =
665   H flux (W/m2) = H_nc
666   Min or QC =
667   Max or QC =
668   H flux coef, RhoCp = rhoCp
669   Min or QC =
670   Max or QC =
671   Scaling velocity (m/s) = Ustr
672   Min or QC =
673   Max or QC =
674 Frequency response
675   From Time =
676   To Time =
677   Storage Label = UWFresp
678   Apply to =
679   Apply by =
680   Correction type = UW
681   Measurement height (m) = HT
682   Zero plane displacement (m) = Zepldi
683   Boundary layer height (m) = 1000
684   Stability Z/L = ZoL
685   Wind speed (m/s) = MeanU
686   Sensor 1 Flow velocity (m/s) = MeanU
687   Sensor 1 Sampling frequency (Hz) = 20
688   Sensor 1 Low pass filter type =
689   Sensor 1 Low pass filter time constant =
690   Sensor 1 High pass filter type =
691   Sensor 1 High pass filter time constant =
692   Sensor 1 Path length (m) = 0.175
693   Sensor 1 Time constant (s) =
694   Sensor 1 Tube attenuation coef =
695   Sensor 2 Flow velocity (m/s) = MeanU
696   Sensor 2 Sampling frequency (Hz) = 20
697   Sensor 2 Low pass filter type =
698   Sensor 2 Low pass filter time constant =
699   Sensor 2 High pass filter type =
700   Sensor 2 High pass filter time constant =
701   Sensor 2 Path length (m) = 0.175
702   Sensor 2 Time constant (s) =
703   Sensor 2 Tube attenuation coef =
704   Path separation (m) = 0
705   Get spectral data type = Model
706   Get response function from = model
707   Reference Tag =
708   Reference response condition =
709   Sensor 1 subsampled =
710   Sensor 2 subsampled =
711   Apply velocity distribution adjustment =
712   Use calculated distribution =
713   Velocity distribution std dev=
714   Stability distribution std dev=
```

```
Frequency response
  From Time =
  To Time =
  Storage Label = HFresp
  Apply to =
  Apply by =
  Correction type = WX
  Measurement height (m) = HT
  Zero plane displacement (m) = Zepldi
  Boundary layer height (m) = 1000
  Stability Z/L = ZoL
  Wind speed (m/s) = MeanU
  Sensor 1 Flow velocity (m/s) = MeanU
  Sensor 1 Sampling frequency (Hz) = 20
  Sensor 1 Low pass filter type =
  Sensor 1 Low pass filter time constant =
  Sensor 1 High pass filter type =
  Sensor 1 High pass filter time constant =
  Sensor 1 Path length (m) = 0.175
  Sensor 1 Time constant (s) =
  Sensor 1 Tube attenuation coef =
  Sensor 2 Flow velocity (m/s) = MeanU
  Sensor 2 Sampling frequency (Hz) = 20
  Sensor 2 Low pass filter type =
  Sensor 2 Low pass filter time constant =
  Sensor 2 High pass filter type =
  Sensor 2 High pass filter time constant =
  Sensor 2 Path length (m) = 0.175
  Sensor 2 Time constant (s) =
  Sensor 2 Tube attenuation coef =
  Path separation (m) = 0
  Get spectral data type = Model
  Get response function from = model
  Reference Tag =
  Reference response condition =
  Sensor 1 subsampled =
  Sensor 2 subsampled =
  Apply velocity distribution adjustment =
  Use calculated distribution =
  Velocity distribution std dev=
  Stability distribution std dev=
Frequency response
  From Time =
  To Time =
  Storage Label = LEFresp
  Apply to =
  Apply by =
  Correction type = WX
  Measurement height (m) = HT
  Zero plane displacement (m) = Zepldi
  Boundary layer height (m) = 1000
  Stability Z/L = ZoL
  Wind speed (m/s) = MeanU
  Sensor 1 Flow velocity (m/s) = MeanU
  Sensor 1 Sampling frequency (Hz) = 20
  Sensor 1 Low pass filter type =
  Sensor 1 Low pass filter time constant =
  Sensor 1 High pass filter type =
  Sensor 1 High pass filter time constant =
```

```
  Sensor 1 Path length (m) = 0.175
  Sensor 1 Time constant (s) =
  Sensor 1 Tube attenuation coef =
  Sensor 2 Flow velocity (m/s) = MeanU
  Sensor 2 Sampling frequency (Hz) = 20
  Sensor 2 Low pass filter type =
  Sensor 2 Low pass filter time constant =
  Sensor 2 High pass filter type =
  Sensor 2 High pass filter time constant =
  Sensor 2 Path length (m) = 0.01254
  Sensor 2 Time constant (s) =
  Sensor 2 Tube attenuation coef =
  Path separation (m) = 0.3551
  Get spectral data type = Model
  Get response function from = model
  Reference Tag =
  Reference response condition =
  Sensor 1 subsampled =
  Sensor 2 subsampled =
  Apply velocity distribution adjustment =
  Use calculated distribution =
  Velocity distribution std dev=
  Stability distribution std dev=
Mathematical operation
  From Time =
  To Time =
  Storage Label = UWc
  Apply to =
  Apply by =
  Measured variable A = UW
  Operation  = *
  Measured variable B = UWFresp
Mathematical operation
  From Time =
  To Time =
  Storage Label = VWc
  Apply to =
  Apply by =
  Measured variable A = VW
  Operation  = *
  Measured variable B = UWFresp
Mathematical operation
  From Time =
  To Time =
  Storage Label = Hc
  Apply to =
  Apply by =
  Measured variable A = H
  Operation  = *
  Measured variable B = HFresp
Mathematical operation
  From Time =
  To Time =
  Storage Label = H_cw
  Apply to =
  Apply by =
  Measured variable A = H
  Operation  = *
  Measured variable B = HFresp
```

```
Mathematical operation
  From Time =
  To Time =
  Storage Label = LEc
  Apply to =
  Apply by =
  Measured variable A = LE
  Operation  = *
  Measured variable B = LEFresp
Comments
  Comment = After first set of frequency response correction
  Comment = Correction of Sensible HF with humidity, and corrected momentum
    fluxes
  Comment = Using Liu et al. 2001, Kaimal and Gaynor 1991
User defined
  From Time =
  To Time =
  Storage Label = WTc
  Apply to =
  Apply by =
  Equation =  Hc/rhoCp-0.32*(LEc/LH)*(Tair+273.15)*((8.314472*Tair)/(P
    *1000*18.01))+(3*(Tair+273.15)*UWc*MeanU)/(2*(MeanTV+273.15)*403)
  Variable = LEc
  Variable = Hc
  Variable = UWc
  Variable = LH
  Variable = rhoCp
  Variable = MeanU
  Variable = Tair
  Variable = MeanTV
  Variable = P
Mathematical operation
  From Time =
  To Time =
  Storage Label = Hcc
  Apply to =
  Apply by =
  Measured variable A = WTc
  Operation  = *
  Measured variable B = rhoCp
User defined
  From Time =
  To Time =
  Storage Label = WTc_cw
  Apply to =
  Apply by =
  Equation = Hc/rhoCp+(3*(Tair+273.15)*UWc*MeanU)/(2*(MeanTV+273.15)*403)
  Variable = Hc
  Variable = UWc
  Variable = rhoCp
  Variable = Tair
  Variable = MeanU
  Variable = MeanTV
Mathematical operation
  From Time =
  To Time =
  Storage Label = Hcc_cw
  Apply to =
  Apply by =
```

```
890   Measured variable A = WTc_cw
891   Operation  = *
892   Measured variable B = rhoCp
893 User defined
894   From Time =
895   To Time =
896   Storage Label = oc_LE
897   Apply to =
898   Apply by =
899   Equation =   LH*0.0045*0.2095*32*P/(-0.151*0.008314*(Tair+273.15)^2)*(Hcc/rhoCp
        )
900   Variable = LH
901   Variable = P
902   Variable = Tair
903   Variable = Hcc
904   Variable = rhoCp
905 Mathematical operation
906   From Time =
907   To Time =
908   Storage Label = LEco
909   Apply to =
910   Apply by =
911   Measured variable A = LEc
912   Operation  = -
913   Measured variable B = oc_LE
914 Webb correction
915   From Time =
916   To Time =
917   Storage Label = Webb_LE
918   Apply to =
919   Apply by =
920   Scalar value type = Density (g/m3)
921   Scalar value = MeanQ
922   Min or QC =
923   Max or QC =
924   Water vapour value type = Partial Pressure (kPa)
925   Water vapour value = e
926   Min or QC =
927   Max or QC =
928   Temperature (C) = Tair
929   Min or QC =
930   Max or QC =
931   Pressure (KPa) = P
932   Min or QC =
933   Max or QC =
934   H flux (W/m2) = Hcc
935   Min or QC =
936   Max or QC =
937   LE flux (W/m2) = LEco
938   Min or QC =
939   Max or QC =
940   H flux coef, RhoCp = rhoCp
941   Min or QC =
942   Max or QC =
943   LE flux coef, L = LH
944   Min or QC =
945   Max or QC =
946   Scalar molecular wt. = 18.01
947   Scalar flux type = LE (W/m2)
```

```
  Scalar flux coefficient =
  Min or QC =
  Max or QC =
  Alternate water vapour pressure (kPa) =
  Alternate temperature (C) =
  Alternate pressure (kPa) =
Mathematical operation
  From Time =
  To Time =
  Storage Label = LEcw
  Apply to =
  Apply by =
  Measured variable A = LEco
  Operation  = +
  Measured variable B = Webb_LE
User defined
  From Time =
  To Time =
  Storage Label = Ustr
  Apply to =
  Apply by =
  Equation = ((UWc)^2+(VWc)^2)^(1/4)
  Variable = UWc
  Variable = VWc
Stability - Monin Obhukov
  From Time =
  To Time =
  Storage Label = ZoL
  Apply to =
  Apply by =
  Measurement height (m) = HT
  Zero plane displacement (m) = Zepldi
  Virtual Temperature (C) = MeanTV
  Min or QC =
  Max or QC =
  H flux (W/m2) = Hcc
  Min or QC =
  Max or QC =
  H flux coef, RhoCp = rhoCp
  Min or QC =
  Max or QC =
  Scaling velocity (m/s) = Ustr
  Min or QC =
  Max or QC =
Stability - Monin Obhukov
  From Time =
  To Time =
  Storage Label = ZoL_cw
  Apply to =
  Apply by =
  Measurement height (m) = HT
  Zero plane displacement (m) = Zepldi
  Virtual Temperature (C) = MeanTV
  Min or QC =
  Max or QC =
  H flux (W/m2) = Hcc_cw
  Min or QC =
  Max or QC =
  H flux coef, RhoCp = rhoCp
```

```
  Min or QC =
  Max or QC =
  Scaling velocity (m/s) = Ustr
  Min or QC =
  Max or QC =
Frequency response
  From Time =
  To Time =
  Storage Label = UWFresp
  Apply to =
  Apply by =
  Correction type = UW
  Measurement height (m) = HT
  Zero plane displacement (m) = Zepldi
  Boundary layer height (m) = 1000
  Stability Z/L = ZoL
  Wind speed (m/s) = MeanU
  Sensor 1 Flow velocity (m/s) = MeanU
  Sensor 1 Sampling frequency (Hz) = 20
  Sensor 1 Low pass filter type =
  Sensor 1 Low pass filter time constant =
  Sensor 1 High pass filter type =
  Sensor 1 High pass filter time constant =
  Sensor 1 Path length (m) = 0.175
  Sensor 1 Time constant (s) =
  Sensor 1 Tube attenuation coef =
  Sensor 2 Flow velocity (m/s) = MeanU
  Sensor 2 Sampling frequency (Hz) = 20
  Sensor 2 Low pass filter type =
  Sensor 2 Low pass filter time constant =
  Sensor 2 High pass filter type =
  Sensor 2 High pass filter time constant =
  Sensor 2 Path length (m) = 0.175
  Sensor 2 Time constant (s) =
  Sensor 2 Tube attenuation coef =
  Path separation (m) = 0
  Get spectral data type = Model
  Get response function from = model
  Reference Tag =
  Reference response condition =
  Sensor 1 subsampled =
  Sensor 2 subsampled =
  Apply velocity distribution adjustment =
  Use calculated distribution =
  Velocity distribution std dev=
  Stability distribution std dev=
Frequency response
  From Time =
  To Time =
  Storage Label = UWFresp_cw
  Apply to =
  Apply by =
  Correction type = UW
  Measurement height (m) = HT
  Zero plane displacement (m) = Zepldi
  Boundary layer height (m) = 1000
  Stability Z/L = ZoL_cw
  Wind speed (m/s) = MeanU
  Sensor 1 Flow velocity (m/s) = MeanU
```

```
  Sensor 1 Sampling frequency (Hz) = 20
  Sensor 1 Low pass filter type =
  Sensor 1 Low pass filter time constant =
  Sensor 1 High pass filter type =
  Sensor 1 High pass filter time constant =
  Sensor 1 Path length (m) = 0.175
  Sensor 1 Time constant (s) =
  Sensor 1 Tube attenuation coef =
  Sensor 2 Flow velocity (m/s) = MeanU
  Sensor 2 Sampling frequency (Hz) = 20
  Sensor 2 Low pass filter type =
  Sensor 2 Low pass filter time constant =
  Sensor 2 High pass filter type =
  Sensor 2 High pass filter time constant =
  Sensor 2 Path length (m) = 0.175
  Sensor 2 Time constant (s) =
  Sensor 2 Tube attenuation coef =
  Path separation (m) = 0
  Get spectral data type = Model
  Get response function from = model
  Reference Tag =
  Reference response condition =
  Sensor 1 subsampled =
  Sensor 2 subsampled =
  Apply velocity distribution adjustment =
  Use calculated distribution =
  Velocity distribution std dev=
  Stability distribution std dev=
Frequency response
  From Time =
  To Time =
  Storage Label = HFresp
  Apply to =
  Apply by =
  Correction type = WX
  Measurement height (m) = HT
  Zero plane displacement (m) = Zepldi
  Boundary layer height (m) = 1000
  Stability Z/L = ZoL
  Wind speed (m/s) = MeanU
  Sensor 1 Flow velocity (m/s) = MeanU
  Sensor 1 Sampling frequency (Hz) = 20
  Sensor 1 Low pass filter type =
  Sensor 1 Low pass filter time constant =
  Sensor 1 High pass filter type =
  Sensor 1 High pass filter time constant =
  Sensor 1 Path length (m) = 0.175
  Sensor 1 Time constant (s) =
  Sensor 1 Tube attenuation coef =
  Sensor 2 Flow velocity (m/s) = MeanU
  Sensor 2 Sampling frequency (Hz) = 20
  Sensor 2 Low pass filter type =
  Sensor 2 Low pass filter time constant =
  Sensor 2 High pass filter type =
  Sensor 2 High pass filter time constant =
  Sensor 2 Path length (m) = 0.175
  Sensor 2 Time constant (s) =
  Sensor 2 Tube attenuation coef =
  Path separation (m) = 0
```

```
  Get spectral data type = Model
  Get response function from = model
  Reference Tag =
  Reference response condition =
  Sensor 1 subsampled =
  Sensor 2 subsampled =
  Apply velocity distribution adjustment =
  Use calculated distribution =
  Velocity distribution std dev=
  Stability distribution std dev=
Frequency response
  From Time =
  To Time =
  Storage Label = HFresp_cw
  Apply to =
  Apply by =
  Correction type = WX
  Measurement height (m) = HT
  Zero plane displacement (m) = Zepldi
  Boundary layer height (m) = 1000
  Stability Z/L = ZoL_cw
  Wind speed (m/s) = MeanU
  Sensor 1 Flow velocity (m/s) = MeanU
  Sensor 1 Sampling frequency (Hz) = 20
  Sensor 1 Low pass filter type =
  Sensor 1 Low pass filter time constant =
  Sensor 1 High pass filter type =
  Sensor 1 High pass filter time constant =
  Sensor 1 Path length (m) = 0.175
  Sensor 1 Time constant (s) =
  Sensor 1 Tube attenuation coef =
  Sensor 2 Flow velocity (m/s) = MeanU
  Sensor 2 Sampling frequency (Hz) = 20
  Sensor 2 Low pass filter type =
  Sensor 2 Low pass filter time constant =
  Sensor 2 High pass filter type =
  Sensor 2 High pass filter time constant =
  Sensor 2 Path length (m) = 0.175
  Sensor 2 Time constant (s) =
  Sensor 2 Tube attenuation coef =
  Path separation (m) = 0
  Get spectral data type = Model
  Get response function from = model
  Reference Tag =
  Reference response condition =
  Sensor 1 subsampled =
  Sensor 2 subsampled =
  Apply velocity distribution adjustment =
  Use calculated distribution =
  Velocity distribution std dev=
  Stability distribution std dev=
Frequency response
  From Time =
  To Time =
  Storage Label = LEFresp
  Apply to =
  Apply by =
  Correction type = WX
  Measurement height (m) = HT
```

```
  Zero plane displacement (m) = Zepldi
  Boundary layer height (m) = 1000
  Stability Z/L = ZoL
  Wind speed (m/s) = MeanU
  Sensor 1 Flow velocity (m/s) = MeanU
  Sensor 1 Sampling frequency (Hz) = 20
  Sensor 1 Low pass filter type =
  Sensor 1 Low pass filter time constant =
  Sensor 1 High pass filter type =
  Sensor 1 High pass filter time constant =
  Sensor 1 Path length (m) = 0.175
  Sensor 1 Time constant (s) =
  Sensor 1 Tube attenuation coef =
  Sensor 2 Flow velocity (m/s) = MeanU
  Sensor 2 Sampling frequency (Hz) = 20
  Sensor 2 Low pass filter type =
  Sensor 2 Low pass filter time constant =
  Sensor 2 High pass filter type =
  Sensor 2 High pass filter time constant =
  Sensor 2 Path length (m) = 0.01254
  Sensor 2 Time constant (s) =
  Sensor 2 Tube attenuation coef =
  Path separation (m) = 0.3551
  Get spectral data type = Model
  Get response function from = model
  Reference Tag =
  Reference response condition =
  Sensor 1 subsampled =
  Sensor 2 subsampled =
  Apply velocity distribution adjustment =
  Use calculated distribution =
  Velocity distribution std dev=
  Stability distribution std dev=
Frequency response
  From Time =
  To Time =
  Storage Label = LEFresp_cw
  Apply to =
  Apply by =
  Correction type = WX
  Measurement height (m) = HT
  Zero plane displacement (m) = Zepldi
  Boundary layer height (m) = 1000
  Stability Z/L = ZoL_cw
  Wind speed (m/s) = MeanU
  Sensor 1 Flow velocity (m/s) = MeanU
  Sensor 1 Sampling frequency (Hz) = 20
  Sensor 1 Low pass filter type =
  Sensor 1 Low pass filter time constant =
  Sensor 1 High pass filter type =
  Sensor 1 High pass filter time constant =
  Sensor 1 Path length (m) = 0.175
  Sensor 1 Time constant (s) =
  Sensor 1 Tube attenuation coef =
  Sensor 2 Flow velocity (m/s) = MeanU
  Sensor 2 Sampling frequency (Hz) = 20
  Sensor 2 Low pass filter type =
  Sensor 2 Low pass filter time constant =
  Sensor 2 High pass filter type =
```

```
  Sensor 2 High pass filter time constant =
  Sensor 2 Path length (m) = 0.01254
  Sensor 2 Time constant (s) =
  Sensor 2 Tube attenuation coef =
  Path separation (m) = 0.3551
  Get spectral data type = Model
  Get response function from = model
  Reference Tag =
  Reference response condition =
  Sensor 1 subsampled =
  Sensor 2 subsampled =
  Apply velocity distribution adjustment =
  Use calculated distribution =
  Velocity distribution std dev=
  Stability distribution std dev=
Mathematical operation
  From Time =
  To Time =
  Storage Label = UWc
  Apply to =
  Apply by =
  Measured variable A = UW
  Operation  = *
  Measured variable B = UWFresp
Mathematical operation
  From Time =
  To Time =
  Storage Label = UWc_cw
  Apply to =
  Apply by =
  Measured variable A = UW
  Operation  = *
  Measured variable B = UWFresp_cw
Mathematical operation
  From Time =
  To Time =
  Storage Label = VWc
  Apply to =
  Apply by =
  Measured variable A = VW
  Operation  = *
  Measured variable B = UWFresp
Mathematical operation
  From Time =
  To Time =
  Storage Label = VWc_cw
  Apply to =
  Apply by =
  Measured variable A = VW
  Operation  = *
  Measured variable B = UWFresp_cw
Mathematical operation
  From Time =
  To Time =
  Storage Label = Hc
  Apply to =
  Apply by =
  Measured variable A = H
  Operation  = *
```

```
  Measured variable B = HFresp
Mathematical operation
  From Time =
  To Time =
  Storage Label = Hc_cw
  Apply to =
  Apply by =
  Measured variable A =  H
  Operation  = *
  Measured variable B = HFresp_cw
Mathematical operation
  From Time =
  To Time =
  Storage Label = LEc
  Apply to =
  Apply by =
  Measured variable A = LE
  Operation  = *
  Measured variable B = LEFresp
Mathematical operation
  From Time =
  To Time =
  Storage Label = LEc_cw
  Apply to =
  Apply by =
  Measured variable A = LE
  Operation  = *
  Measured variable B = LEFresp_cw
User defined
  From Time =
  To Time =
  Storage Label = WTc
  Apply to =
  Apply by =
  Equation = Hc/rhoCp-0.32*(LEc/LH)*(Tair+273.15)*((8.314472*Tair)/(P*1000*18.01)
    )+(3*(Tair+273.15)*UWc*MeanU)/(2*(MeanTV+273.15)*403)
  Variable = LEc
  Variable = Hc
  Variable = UWc
  Variable = LH
  Variable = rhoCp
  Variable = MeanU
  Variable = Tair
  Variable = MeanTV
  Variable = P
Mathematical operation
  From Time =
  To Time =
  Storage Label = Hcc
  Apply to =
  Apply by =
  Measured variable A = WTc
  Operation  = *
  Measured variable B = rhoCp
User defined
  From Time =
  To Time =
  Storage Label = WTc_cw
  Apply to =
```

```
  Apply by =
  Equation = Hc_cw/rhoCp+(3*(Tair+273.15)*UWc*MeanU)/(2*(MeanTV+273.15)*403)
  Variable = Hc_cw
  Variable = UWc
  Variable = rhoCp
  Variable = Tair
  Variable = MeanU
  Variable = MeanTV
Mathematical operation
  From Time =
  To Time =
  Storage Label = Hcc_cw
  Apply to =
  Apply by =
  Measured variable A = WTc_cw
  Operation  = *
  Measured variable B = rhoCp
User defined
  From Time =
  To Time =
  Storage Label = oc_LE
  Apply to =
  Apply by =
  Equation =  LH*0.0045*0.2095*32*P/(-0.157*0.008314*(Tair+273.15)^2)*(Hcc/rhoCp)
  Variable = LH
  Variable = P
  Variable = Tair
  Variable = Hcc
  Variable = rhoCp
Mathematical operation
  From Time =
  To Time =
  Storage Label = LEco
  Apply to =
  Apply by =
  Measured variable A = LEc
  Operation  = -
  Measured variable B = oc_LE
Webb correction
  From Time =
  To Time =
  Storage Label = Webb_LE
  Apply to =
  Apply by =
  Scalar value type = Density (g/m3)
  Scalar value = MeanQ
  Min or QC =
  Max or QC =
  Water vapour value type = Partial Pressure (kPa)
  Water vapour value = e
  Min or QC =
  Max or QC =
  Temperature (C) = Tair
  Min or QC =
  Max or QC =
  Pressure (KPa) = P
  Min or QC =
  Max or QC =
  H flux (W/m2) = Hcc
```

```
  Min or QC =
  Max or QC =
  LE flux (W/m2) = LEco
  Min or QC =
  Max or QC =
  H flux coef, RhoCp = rhoCp
  Min or QC =
  Max or QC =
  LE flux coef, L = LH
  Min or QC =
  Max or QC =
  Scalar molecular wt. = 18.01
  Scalar flux type = LE (W/m2)
  Scalar flux coefficient =
  Min or QC =
  Max or QC =
  Alternate water vapour pressure (kPa) =
  Alternate temperature (C) =
  Alternate pressure (kPa) =
Mathematical operation
  From Time =
  To Time =
  Storage Label = LEcw
  Apply to =
  Apply by =
  Measured variable A = LEco
  Operation  = +
  Measured variable B = Webb_LE
Stationarity
  From Time =
  To Time =
  Signal (A) = U
  Signal (B) = W
  Storage Label A StdDev Stationarity = Stat_U
  Storage Label B StdDev Stationarity =
  Storage Label AB Covariance Stationarity = Stat_UW
  Segment length, minutes = 5
  Linear detrend segments =
  Linear detrend run =
  Storage Label AB StdDev Stationarity =
Stationarity
  From Time =
  To Time =
  Signal (A) = V
  Signal (B) = W
  Storage Label A StdDev Stationarity = Stat_V
  Storage Label B StdDev Stationarity =
  Storage Label AB Covariance Stationarity = Stat_VW
  Segment length, minutes = 5
  Linear detrend segments =
  Linear detrend run =
  Storage Label AB StdDev Stationarity =
Stationarity
  From Time =
  To Time =
  Signal (A) = U
  Signal (B) = T
  Storage Label A StdDev Stationarity =
  Storage Label B StdDev Stationarity =
```

```
  Storage Label AB Covariance Stationarity = Stat_UT
  Segment length, minutes = 5
  Linear detrend segments =
  Linear detrend run =
  Storage Label AB StdDev Stationarity =
Stationarity
  From Time =
  To Time =
  Signal (A) = V
  Signal (B) = T
  Storage Label A StdDev Stationarity =
  Storage Label B StdDev Stationarity =
  Storage Label AB Covariance Stationarity = Stat_VT
  Segment length, minutes = 5
  Linear detrend segments =
  Linear detrend run =
  Storage Label AB StdDev Stationarity =
Stationarity
  From Time =
  To Time =
  Signal (A) = W
  Signal (B) = T
  Storage Label A StdDev Stationarity = Stat_W
  Storage Label B StdDev Stationarity = Stat_T
  Storage Label AB Covariance Stationarity = Stat_H
  Segment length, minutes = 5
  Linear detrend segments =
  Linear detrend run =
Stationarity
  From Time =
  To Time =
  Signal (A) = W
  Signal (B) = Q
  Storage Label A StdDev Stationarity =
  Storage Label B StdDev Stationarity = Stat_Q
  Storage Label AB Covariance Stationarity = Stat_LE
  Segment length, minutes = 5
  Linear detrend segments =
  Linear detrend run =
User defined fast
  From Time =
  To Time =
  Equation = ((U-MeanU)*(W-MeanW))^2
  Number of signals = 2
  Signal = U
  Signal = W
  Variable = MeanU
  Variable = MeanW
1 chn statistics
  From Time =
  To Time =
  Signal = U
  Storage Label Mean = MeanUWWyn
  Storage Label Std Dev =
  Storage Label Skewness =
  Storage Label Kurtosis =
  Storage Label Maximum =
  Storage Label Minimum =
  Storage Label Variance =
```

```
  Storage Label Turbulent Intensity =
  Alt Turbulent Intensity Denominator =
User defined fast
  From Time =
  To Time =
  Equation = ((V-MeanV)*(W-MeanW))^2
  Number of signals = 2
  Signal = V
  Signal = W
  Variable = MeanV
  Variable = MeanW
1 chn statistics
  From Time =
  To Time =
  Signal = V
  Storage Label Mean = MeanVWWyn
  Storage Label Std Dev =
  Storage Label Skewness =
  Storage Label Kurtosis =
  Storage Label Maximum =
  Storage Label Minimum =
  Storage Label Variance =
  Storage Label Turbulent Intensity =
  Alt Turbulent Intensity Denominator =
User defined fast
  From Time =
  To Time =
  Equation = ((T-MeanTV)*(W-MeanW))^2
  Number of signals = 2
  Signal = T
  Signal = W
  Variable = MeanTV
  Variable = MeanW
1 chn statistics
  From Time =
  To Time =
  Signal = T
  Storage Label Mean = MeanTWWyn
  Storage Label Std Dev =
  Storage Label Skewness =
  Storage Label Kurtosis =
  Storage Label Maximum =
  Storage Label Minimum =
  Storage Label Variance =
  Storage Label Turbulent Intensity =
  Alt Turbulent Intensity Denominator =
User defined
  From Time =
  To Time =
  Storage Label = WynU
  Apply to =
  Apply by =
  Equation = SQRT((HT-Zepldi)/(1800*MeanU)*ABS((KurtU+3)-1))
  Variable = KurtU
  Variable = HT
  Variable = Zepldi
  Variable = MeanU
User defined
  From Time =
```

```
  To Time =
  Storage Label = WynV
  Apply to =
  Apply by =
  Equation = SQRT((HT-Zepldi)/(1800*MeanU)*ABS((KurtV+3)-1))
  Variable = KurtV
  Variable = HT
  Variable = Zepldi
  Variable = MeanU
User defined
  From Time =
  To Time =
  Storage Label = WynW
  Apply to =
  Apply by =
  Equation = SQRT((HT-Zepldi)/(1800*MeanU)*ABS((KurtW+3)-1))
  Variable = KurtW
  Variable = HT
  Variable = Zepldi
  Variable = MeanU
User defined
  From Time =
  To Time =
  Storage Label = WynT
  Apply to =
  Apply by =
  Equation = SQRT((HT-Zepldi)/(1800*MeanU)*ABS((KurtTV+3)-1))
  Variable = KurtTV
  Variable = HT
  Variable = Zepldi
  Variable = MeanU
User defined
  From Time =
  To Time =
  Storage Label = WynUW
  Apply to =
  Apply by =
  Equation =  SQRT((HT-Zepldi)/(1800*MeanU)*ABS(MeanUWWyn/Ustr^4-1))
  Variable = MeanUWWyn
  Variable = Ustr
  Variable = HT
  Variable = Zepldi
  Variable = MeanU
User defined
  From Time =
  To Time =
  Storage Label = WynVW
  Apply to =
  Apply by =
  Equation = SQRT((HT-Zepldi)/(1800*MeanU)*ABS(MeanUWWyn/Ustr^4-1))
  Variable = MeanVWWyn
  Variable = Ustr
  Variable = HT
  Variable = Zepldi
  Variable = MeanU
User defined
  From Time =
  To Time =
  Storage Label = WynTW
```

```
  Apply to =
  Apply by =
  Equation =  SQRT((HT-Zepldi)/(1800*MeanU)*ABS(MeanTWWyn/((Hcc/rhoCp)^2)-1))
  Variable = MeanTWWyn
  Variable = rhoCp
  Variable = Hcc
  Variable = HT
  Variable = Zepldi
  Variable = MeanU
User defined
  From Time =
  To Time =
  Storage Label = QC_Q
  Apply to =
  Apply by =
  Equation = IIF(MinQ_mV<5,1,0)
  Variable = MinQ_mV
  Variable =
```

B.2 Read a TOA5 file

The following function is useful to read a TOA5 file, these files usually store low frequency variables as output of Campbell's data logger.

```
function [ data1 ] = read_toa5( file )
%READ_TOA5 reading text files formatted in TOA5
%   Description (EN):
%   This function bring the input file and first control if it is a TOA5
%   formatted file, then starts reading the header. There are 4 header row,
%   the first one contains the name of the station and other informations
%   about the datalogger program; the second row contains the column's name
%   the third the units, and the fourth the value's type.
%   From the previous version of read_toa5 I've add the control of NAN
%   string in fields that contains numbers. This script search '"NAN"'
%   strings and replace them with the correct Matlab nan format, that is
%   'NaN'.
%   Finally I have add a control on data repetition, this control is
%   performed on the TIMESTAMP field, if this field is not present in your
%   file the quality control is skipped. This quality control remove all
%   data duplicates, and write down a new matrix.
%   input:
%       file: full file path;
%   output:
%       data1: structure array with data retrieved from the file, the
%       structure is data.var_name.
%           value: all data
%           name: the variable name, the same of the var_name
%           units: unit of measure of the variable
%
%
%================================
%   Author: Alessio Golzio
%   Date: 2015.10.27 10.00
%   Last modified: 2015.11.09 11.00
%================================
```

```
32
33      n_header=4;
34
35      if exist(file,'file')==2
36          fid=fopen(file,'r');
37
38          %check file format
39          fileform=fscanf(fid,'%s',1); %first row
40          if ~strcmp(fileform(2:5),'TOA5')
41              error('The file %s is not in format TOA5!',file);
42          end
43
44          %saving header
45          header2=fscanf(fid,'%s',1);
46          header3=fscanf(fid,'%s',1);
47          header4=fscanf(fid,'%s',1);
48
49          %remove brackets from cols name (useful for creating the scructured
50          %array with this name
51          header2(strfind(header2,'('))='';
52          header2(strfind(header2,')'))='';
53
54          commas2=find(header2==char(44));
55          commas3=find(header3==char(44));
56          commas4=find(header4==char(44));
57
58          %How many fields are there?
59          Nfields=size(commas2,2)+1;
60
61          begfields2 = [1 commas2+1];
62          endfields2 = [commas2-1 size(header2,2)-1];
63          begfields3 = [1 commas3+1];
64          endfields3 = [commas3-1 size(header3,2)-1];
65          begfields4 = [1 commas4+1];
66          endfields4 = [commas4-1 size(header4,2)-1];
67
68          %store col header: variables name, units and type
69          col_name=cell(1,Nfields);
70          col_units=cell(1,Nfields);
71          col_type=cell(1,Nfields);
72
73          for i=1:Nfields
74              % don't read the quotes at beginning and end of each field
75              col_name{i} = header2(begfields2(i)+1:endfields2(i)-1);
76              col_units{i} = header3(begfields3(i)+1:endfields3(i)-1);
77              col_type{i} = header4(begfields4(i)+1:endfields4(i)-1);
78          end
79          fclose(fid);
80
81          % determining the format of data
82          data1 = textread(file,'%s',1,'delimiter','','headerlines',4); %skip 4
    lines
83          data1 = strread(char(data1),'%s','delimiter',',');
84
85          format = [];
86
87          for i = 1:length(data1)
88              tmp = char(data1{i});
89              if strcmp(tmp,'"NAN"') % if there is a NAN in the first line consider
```

```
    the field as double
90              format = [format '%f '];
91          elseif isempty(str2num(tmp)) || ~isempty(strfind(tmp,':'))
92              format = [format '%q '];
93          else
94              format = [format '%f '];
95          end
96      end
97
98      % preparing reading data
99      fid = fopen(file,'r');
100     fscanf(fid,'%s',n_header); %skip first 4 rows of the header
101
102     % removing "NAN" and replace with NaN, than the floating point
103     % format will work well.
104     scan=fscanf(fid,'%c',inf);
105     nan_loc=strfind(scan,'"NAN"');
106     fprintf('\n NAN present in data: %d',size(nan_loc,2));
107
108     % replace "NAN"->NaN
109     for i=1:size(nan_loc,2)
110         scan(nan_loc(i):nan_loc(i)+4)='NaN  ';
111     end
112
113     dquote=strfind(scan,'"');
114     for i=1:size(dquote,2)
115         scan(dquote(i))=' ';
116     end
117
118     % second control of NAN after cleaning...
119     nan_loc=strfind(scan,'"NAN"');
120     fprintf('\n NAN present in data after cleaning: %d',size(nan_loc,2));
121
122     % now save the data in data array.
123     data = textscan(scan,format,'delimiter',',');
124     fclose(fid);
125
126     clear scan nan_loc;
127
128     % Quality control of data, search duplicate lines and removing
129     % them. For control I use TIMESTAMP, record number isn't always
130     % unique. If TIMESTAMP is not present the QC is skipped.
131     %% DA FARE!
132     % Controllare anche sul record nei casi di date uguali, se ci sono
133     % anche i record uguali si eliminano le righe in pi  se sono
134     % diversi? Booo?
135
136
137
138     if mean(strcmp(col_name,'TIMESTAMP'))>0
139         for i=1:Nfields
140             if strcmp(col_name(i),'TIMESTAMP')
141                 pos_ts=i;
142                 continue
143             end
144             if strcmp(col_name(i),'RECORD')
145                 pos_rec=i;
146                 continue
147             end
```

```
148             end
149             [~,id_data]=unique(data{pos_ts},'R2012a'); %fin qui controllo solo su
     timestamp: funziona
150
151
152             % control if these timestamp are repeted but data is unique, if
153             % data is unique in the two "repeted" lines then leave them and
154             % prepare a error message with indexes of wrong timestamps.
155             %id_new = zeros(size(data{1},1),1);
156             %skip = 0;
157             %for i=1:length(id_data)-1
158             %    if (id_data(i+1)-id_data(i)) > 1 %there is a gap
159             %        gap = id_data(i+1)-id_data(i);
160             %        fprintf('\ngap trovato: id inizio %d, id fine %d',id_data(i)
    ,id_data(i+1))
161             %        [~,id_ctrl] = unique(data{pos_rec}(id_data(i-gap):id_data(i
    +1)),'R2012a');
162             %        if length(id_ctrl) > gap
163             %            for a=1:length(id_ctrl)
164             %                id_new(i+skip) = id_ctrl(a)+id_data(i-gap)-1;
165             %                skip = skip+1;
166             %            end
167             %        else
168             %            id_new(i+skip)=id_data(i);
169             %        end
170             %    else
171             %        id_new(i+skip)=id_data(i);
172             %    end
173             %end
174
175             %[id_def] = unique(id_new,'R2012a');
176
177             % allocating new array
178             data1=cell(1,Nfields);
179             for var=1:Nfields
180                 for i=1:length(id_data)
181                     data1{var}(i)=data{var}(id_data(i));
182                 end
183             end
184         else
185             fprintf('\nTIMESTAMP field is not available, quality control of data
    is not performed');
186             data1=data;
187         end
188         clear data;
189
190         % store data in structure array: create the structure array
191         tmp = [];
192         for i = 1:Nfields
193             tmp = setfield(tmp,col_name{i},'value',data1{i});
194             tmp = setfield(tmp,col_name{i},'name',col_name{i});
195             tmp = setfield(tmp,col_name{i},'units',col_units{i});
196         end
197         data1 = tmp;
198
199         % create additional date/time parameters:
200         if isfield(data1,'TIMESTAMP')
201             % create Matlab serial data:
202             tmp = char(data1.TIMESTAMP.value);
```

```
203             data1=setfield(data1,'sdate','value',datenum(tmp,'yyyy-mm-ddHH:MM:SS'
    )); %(tmp),'yyyy-mm-ddHH:MM:SS'
204             data1=setfield(data1,'sdate','name','Matlab_date');
205             data1=setfield(data1,'sdate','units',' ');
206             % order fields in structure (sdate at the 1st place):
207             Nfileds = size(fieldnames(data1),1);
208             data1 = orderfields(data1,[Nfileds 1:Nfileds-1]);
209         else
210             error('Array TIMESTAMP not available in input file!')
211         end
212         clear tmp;
213 
214     else
215         error('File %s does not exist!',file);
216     end
217 
218 return
```

B.3 Read EdiRe "csv" file

The following function is created by Ivana Stiperski and developed by the Author and it is useful to read a *.csv* file created as output by EdiRe.

```
1  function [ data1 ] = read_edire( file )
2  %READ_EDIRE This function read the Edire output csv file and store the data
3  %in a struct variable.
4  %   Description (EN)
5  %   This script brings a input file name and read it storing all the
6  %   variables in a struct variable. The input file is a CSV generated by
7  %   EdiRe Eddy Coviariance software.
8  %   History:
9  %   2016.02.19   Modified if condition for create line reading format, I
10 %                have moved the condition "isempty(str2num(tmp))" to the
11 %                first statement instead of the second one. (now line 49)
12 %   2016.02.24   Correction to the format detection, now if the last field
13 %                is empty (nodata) the program recognise it anyway. Because
14 %                edire after the last field doesn't write a comma then if
15 %                there isn't a value the program reduce the dimension of
16 %                one column. Now this problem is fixed.
17 %=========================================
18 %   Authors: Ivana Stiperski, Alessio Golzio
19 %   Date: 2016.02.04 10.00
20 %   Last modified: 2016.02.19 13:29
21 %=========================================
22 
23     n_header = 1;
24     clear Nfields;
25     if exist(file,'file')==2
26         header=textread(file,'%s',1,'delimiter','');
27         %remove brace
28         header = char(header{1});
29         header(strfind(header,'('))='';
30         header(strfind(header,')'))='';
```

```
31          header(strfind(header,'/'))='';
32          header(strfind(header,' '))='';
33          commas=find(header==char(44));
34          %How many fields are there?
35          Nfields=size(commas,2)+1;
36
37          begfields = [1 commas+1];
38          endfields = [commas-1 size(header,2)];
39          col_name=cell(1,Nfields);
40          for i=1:Nfields
41              % don't read the quotes at beginning and end of each field
42              col_name{i} = header(begfields(i):endfields(i));
43          end
44
45          data1 = textread(file,'%s',1,'delimiter','','headerlines',n_header);
46          data1 = strread(char(data1),'%q','delimiter',',');
47          format = [];
48          if length(data1) == length(commas) %the program missed the last field
    because is empty
49              data1(end+1) = {''}; %add the last field.
50          end
51          for i = 1:length(data1)
52              tmp = char(data1{i});
53              if strcmp(tmp,'Error') || isempty(str2num(tmp)) % set here the type
    of Not a Number for EdiRe files
54                  format = [format '%f '];
55              elseif ~isempty(strfind(tmp,':')) || ~isempty(strfind(tmp,'/'))
56                  format = [format '%q '];
57              else
58                  format = [format '%f '];
59              end
60          end
61          % preparing reading data
62          fid = fopen(file,'r');
63          data = textscan(fid,format,'delimiter',',','headerlines',n_header);
64          fclose(fid);
65
66          if mean(strcmp(col_name,'DateTime'))>0
67              for i=1:Nfields
68                  if strcmp(col_name(i),'DateTime')
69                      pos_ts=i;
70                      continue
71                  end
72              end
73              [~,id_data]=unique(data{pos_ts},'R2012a');
74              % allocating new array
75              data1=cell(1,Nfields);
76              for var=1:Nfields
77                  for i=1:length(id_data)
78                      data1{var}(i)=data{var}(id_data(i));
79                  end
80              end
81          else
82              fprintf('\nDateTime field is not available, quality control of data
    is not performed');
83              data1=data;
84          end
85          clear data;
86
```

```
87          tmp = [];
88          for i = 1:Nfields
89              tmp = setfield(tmp,col_name{i},'value',data1{i});
90          end
91          data1 = tmp;
92
93          % create additional date/time parameters:
94          if isfield(data1,'DateTime')
95              % create Matlab serial data:
96              tmp = char(data1.DateTime.value);
97              data1=setfield(data1,'sdate','value',datenum(tmp,'dd/mm/yyyy HH:MM'))
    ; %(tmp),'yyyy-mm-ddHH:MM:SS'
98              data1=setfield(data1,'sdate','name','Matlab_date');
99              data1=setfield(data1,'sdate','units',' ');
100             % order fields in structure (sdate at the 1st place):
101             Nfileds = size(fieldnames(data1),1);
102             data1 = orderfields(data1,[Nfileds 1:Nfileds-1]);
103         else
104             error('Array DateTime not available in input file!')
105         end
106     else
107         error('File %s does not exist!',file);
108     end
109 end
```

B.4 Particular functions

A selection of functions that processes some action deeply describe in previous chapters, and that are fundamental for the rest part of the analysis. I list them starting from the low frequency data analysis part.

sole This function, using the equations introduced in Section 1.4.1, evaluates the TOA irradiance over Arbeser, and with the transmissivity it calculates the maximum irradiance at Arbeser altitude. The outputs of this function are the mean daily irradiance at TOA over Arbeser, the reduced total theoretical irradiance (with a clear sky) at Arbeser, and the daily mean short wave incoming radiation measured at Arbeser.

csi analysis This function computes the Clear-Sky Index following Marty and Philipona (2000)[27]. The outputs of this function are the Clear-Sky Index for Arbeser station, and the related Clear-Sky Index for Innsbruck uploaded (in the main script "`lf_analyzer.m`") from the ARAD database (that is a .dat file).

bowen ratio The Bowen ration function works with low frequency data. It has not to be confused with another function with practically the same name,

`bowen_hf.m`, but working with high frequency data. This function calculates the Bowen ration using the gradients approximated method, and applying it to all combinations of measurements levels. The principle is explained in Section 5.3.

B.4.1 Radiation function

```
function [ QTOA_day, Q_Arb, Q_real, err_QTOA, err_QArb, err_real] = sole( sw_in,
    sw_std, dn )
%SOLE This function computes the Total TOA Solar radiation and TOTAL
%Theoretical Solar radiation at the latitute of Arbeser Station.
%   Description (EN)
%
%   References:
%   Hartmann Dennis L., Global Physical Climatology, 1994
%   Oerlemens Johannes, Glaciers and Climate Change, 2001
%   Wikipedia EN Solar Irradiance
%
%================================
%Station: Arbeser Kogel
%Author: Alessio Golzio
%Date: 2016.01.28 11:03
%Last modified: 2016.01.29 15:29
%================================

    %constants
    S0 = 1367;        % solar costant at mean distance from sun [W/m^2]
    err_S0 = 3;
    lat = 47.32065;  % north latitute of Arbeser [deg]
    err_lat = 0.00005;
    alt = 2015;       % altitude of the Arbeser station.
    omega = 283.152; % Longitude of Pherihelion (avg 2014-2016) [deg]
    ecc = 0.016698;  % Eccentricity of Earth's orbit (avg 2014-2016)
    obl = 23.4378;   % Obliquity of Earth's orbit (avg 2014-2016) [deg]

    % latitude in radians
    lat = (lat*pi)/180;

    % day angle: express the year as a 2pi angle, 20-Mar is 0
    theta_d = (2*pi*(dn-81))/365; % radians (no error)

    % sun scaled distance
    d_sun = (1+ecc*cos(theta_d-((omega*pi)/180)))^2;

    %sun declination [rad]
    decl = asin(sind(obl)*sin(theta_d-((omega*pi)/180)));

    % sunrise (negative) and sunset(positive) angles [rad]
    h0 = acos(-tan(lat)*tan(decl));
    err_h0 = (tan(decl)*err_lat)/((cos(lat))^2*sqrt(1+tan(lat)*tan(decl)));

    % Solar radiation for a clear-sky day over Arbeser station depends from
    % the transmissivity of clear-sky on Arbeser; the transmissivity
    % depends itself on the hour of the day, than from the Solar Zenith
    % Angle. Here I compute the QTOA: Integral of Solar radiantion at the
```

```
    % Top Of Atmosphere, and the theoretical Solar radiation at Arbeser,
    % then when the sky is completely clear.

    i = 1;
    t_atm = zeros(24,1);
    QTOA_day = (1/pi)*S0*d_sun*(h0*sin(lat)*sin(decl)+cos(lat)*cos(decl)*sin(h0))
    ;
    err_QTOA = sqrt(((1/pi)*d_sun*(h0*sin(lat)*sin(decl)+cos(lat)*cos(decl)*sin(
    h0)))^2*err_S0^2+...
        ((1/pi)*d_sun*(sin(lat)*sin(decl)+cos(lat)*cos(decl)+cos(h0)))^2*err_h0
    ^2+...
        ((1/pi)*d_sun*(h0*cos(lat)*sin(decl)-sin(lat)*cos(decl)*sin(h0)))^2*
    err_lat^2);
    for h=-h0:(2*h0/24):h0
        czen = (sin(lat)*sin(decl)+cos(lat)*cos(decl)*cos(h));
        t_atm(i) = (0.79+2.4*10^-5*alt)*(1-0.08*(acos(czen)/(pi*0.5)));
        i = i+1;
    end
    t_atm_day = nanmean(t_atm);

    % evaluation of daily mean SW solar radiation for the same day measure in
    % Arbeser.
    Q_real = nanmean(sw_in);
    err_real = nanmean(sw_std)/sqrt(length(sw_in));
    Q_Arb = t_atm_day*QTOA_day;
    err_QArb = t_atm_day*err_QTOA;
end
```

B.4.2 CSI function

```
function [ csi ] = csi_analysis( date, temp, rh, lw_in, csi )
%CSI Clear-Sky Index.
%   This function compute a Clear-Sky Index following Marty and Philipona
%   2000: The Clear Sky-Index to separate Clear-Sky from Cloudy-Sky
%   Situation in Climate Reaserch, Geo. Res. Let vol27, n 17, pp 2649-2652.
%   It use only incoming long wave radiation, temperature and humidity.
%
%==============================
%Station: Arbeser Kogl
%Author: Alessio Golzio
%Date: 2016.01.26 8:35
%Last modified: 2016.01.28 9:00
%==============================

%   variables initialization
    e_sat = zeros(length(temp),1);
    e_vap = zeros(length(temp),1);
    e1 = zeros(length(temp),1);
    epsi_a = zeros(length(temp),1);  % apparent emittance
    epsi_ac = zeros(length(temp),1); % apparent emittance of a clear sky
    sbcost = 5.670373*10^(-8);       % Stefan-Boltzmann Constant(W/m^2*K^4)
    k = 0.433; % da calcolare!!
    epsi_ad = 0.218; %praticamente corretto (da fit exp dei dati dell'articolo)
    value_csi = zeros(length(temp),1);

%   calculation of water vapor pressure
```

```
    for i = 1:length(temp)
        if temp(i) >= 0
            e_sat(i) = 6.1078*exp((17.269388*temp(i))/(temp(i)+237.29));
        else
            e_sat(i) = 6.1078*exp((21.8745584*temp(i))/(temp(i)+265.49));
        end
        e_vap(i) = rh(i)*0.01*e_sat(i)*100; % in Pascal
        epsi_a(i) = lw_in(i)/(sbcost*(temp(i)+273.16)^4);
        e1(i) = e_vap(i)/(temp(i)+273.16);

        epsi_ac(i) = epsi_ad + k*(e_vap(i)/(temp(i)+273.16))^(1/8);
        value_csi(i) = epsi_a(i)/epsi_ac(i);
    end

    %append to the struct variable "csi", the value calculated for Arbeser
    csi = setfield(csi,'csi_arb','value',value_csi);

    %find days with a clear-sky index lower than 1.
    low_csi_ibk = find(csi.csi_ibk.value <= 1);
    low_csi_arb = find(csi.csi_arb.value <= 1);

    %save in csi struct
    csi = setfield(csi,'clear_sky','ibk',low_csi_ibk);
    csi = setfield(csi,'clear_sky','arb',low_csi_arb);

    %plots
    figure('Name','CSI')
    hold on
    plot(date,csi.csi_ibk.value,'.r');
    plot(date,csi.csi_arb.value,'.b');
        datetick('x',0,'keepticks','keeplimits');
    hold off
end
```

B.4.3 Bowen ratio

```
function [ bowenratio, sigB, q, qc, e_sat, e_vap ] = bowen_ratio( rh, temp, theta
    , press, sigtheta, levels)
%BOWEN_RATIO This function calculates the bowen ration considering constant
%the flux coefficients before the temperature and humidity gradients.
%   Description (EN)
%   This script bring temperature (air temperature in  C), the potential
%   temperature (K) and relative humidity and evaluate the Bowen Ratio as
%   DeltaTheta/DeltaQ, where the delta is temperature differences between
%   two different levels. First with temperature evaluate the vapour
%   pressure and then with potetial temperature it calculates the Bowen
%   ratio.
%   In "levels" variable it is requested the number of levels available,
%   then the program give as output all the possible combination of levels.
%
%   QC and limits:
%   From the theory on energy balance the Bowen ratio is generally
%   positive, but if the SH and LE are of opposite sign is possible that
%   the Bw is negative. The qc is performed on its absolute value, and the
%   threshold is set to 25.
%
```

```
%    INPUT VARIABLES
%    rh, temp ( C), theta (K): matrix(i,j) row i= time; columns j= levels
%    levels : integer number indicating the number of levels
%    press : pressure array (i row) in kPa.
%
%    History
%    2016.06.14 Bug fixed in calculation of q.
%    2016.06.15 Added controls on Deltaq and DeltaTheta to prevent wrong
%               Bowen ratio calculations.
%================================
%Station: Arbeser Kogel
%Author: Alessio Golzio
%Date: 2016.04.29 7:50
%Last modified: 2016.06.15 14:30
%================================


    if (size(temp,2)~=levels || size(rh,2)~=levels || size(theta,2)~=levels)
        warning(1502,'BW: Declaration of levels different from size of temp, rh
    or theta matrixes.');
        levels = size(temp,2);
    end
    if (size(temp,2)~=size(rh,2) || size(temp,2)~=size(theta,2) || size(theta,2)
    ~=size(rh,2))
        warning(1503,'BW: Different number of levels between matrixes.');
        levels = min([size(temp,2) size(rh,2) size(theta,2)]);
    end
    if (size(temp,1)~=size(rh,1) || size(temp,1)~=size(theta,1) || size(theta,1)
    ~=size(rh,1) || size(press,1)~=size(temp,1))
        warning(1504,'BW: Different lenght of matrixes.');
        lung = min([size(temp,1) size(rh,1) size(theta,1) size(press,1)]);
        fprintf('\nBW: Set lenght to %d',lung);
    else
        lung = size(temp,1);
    end

    % variables
    e_sat = zeros(lung,levels); % saturation vapour pressure
    e_vap = zeros(lung,levels); % vapour pressure
    q = zeros(lung,levels);     % specific humidity
    psic_cost = 0.00041;        % g_water/(g_air*Kelvin)

    % estimate of relative error on q [%]
    relq = 0.6;

    % combination of levels
    cc = combnk(1:levels,2);
    % storage for results
    bowenratio = NaN(lung,size(cc,1));
    sigB = NaN(lung,size(cc,1));
    qc = NaN(lung,size(cc,1)); % quality control

    % Conversion from relative humidity to vapour pressure
    for i = 1:lung      % row(time)
        for j = 1:levels  % columns(level)
            if temp(i,j) >= 0
                e_sat(i,j) = 6.1078*exp((17.269388*temp(i,j))/(temp(i,j)+237.29))
    ; % in hPa
            else
```

```
75                  e_sat(i,j) = 6.1078*exp((21.8745584*temp(i,j))/(temp(i,j)+265.49)
    ); % in hPa
76              end
77              e_vap(i,j) = rh(i,j)*e_sat(i,j); % in Pa
78              q(i,j) = 0.622*e_vap(i,j)/(press(i)*1000-(1-0.622)*e_vap(i,j)); %
    specific humidity g_water/g_air
79          end
80          e_sat = e_sat*100; % in Pa
81          for c = 1:size(cc,1)
82              if isnan(temp(i,cc(c,:))) | isnan(theta(i,cc(c,:))) | isnan(press(i))
     | isnan(rh(i,cc(c,:)))
83                  bowenratio(i,c) = NaN;
84                  qc(i,c) = 0.;
85              else
86                  % control on theta profile: inversion not allowed and flat
87                  % profile not allowed (for theta I control that the
88                  % DeltaTheta is greater than the standard deviation and for
89                  % q I control that the Delta q is greater than 0.0005 g/g
90                  if ((theta(i,2) > theta(i,1) && theta(i,2) > theta(i,3)) || (
    theta(i,2) < theta(i,1) && theta(i,2) < theta(i,3))) || ...
91                      (theta(i,cc(c,1))-theta(i,cc(c,2))) < sigtheta(i,cc(c,1)) ||
    (q(i,cc(c,1))-q(i,cc(c,2))) < 0.0005
92                      bowenratio(i,c) = NaN;
93                      qc(i,c) = 0.;
94                  else
95                      bowenratio(i,c) = psic_cost*(theta(i,cc(c,1))-theta(i,cc(c,2)
    ))/(q(i,cc(c,1))-q(i,cc(c,2)));
96                      % estimation of uncertainty
97                      sigB(i,c) = psic_cost*sqrt((1/(q(i,cc(c,1))-q(i,cc(c,2))))
    ^2*(sigtheta(i,cc(c,1))+sigtheta(i,cc(c,2)))^2+...
98                          ((theta(i,cc(c,1))-theta(i,cc(c,2)))/(q(i,cc(c,1))-q(i,cc
    (c,2)))^2)^2*(q(i,cc(c,1))*relq+q(i,cc(c,2))*relq)^2);
99                      if abs(bowenratio(i,c)) >=25 % too high values for Bowen
    ratio
100                         qc(i,c) = 0.;
101                     else
102                         qc(i,c) = 1;
103                     end
104                 end
105             end
106         end
107     end
108 end
```

B.5 Program's Flow Charts

The following two figures depict the flow charts for the low frequency data analysis (Fig. B.1) and for high frequency data analysis (Fig. B.2).

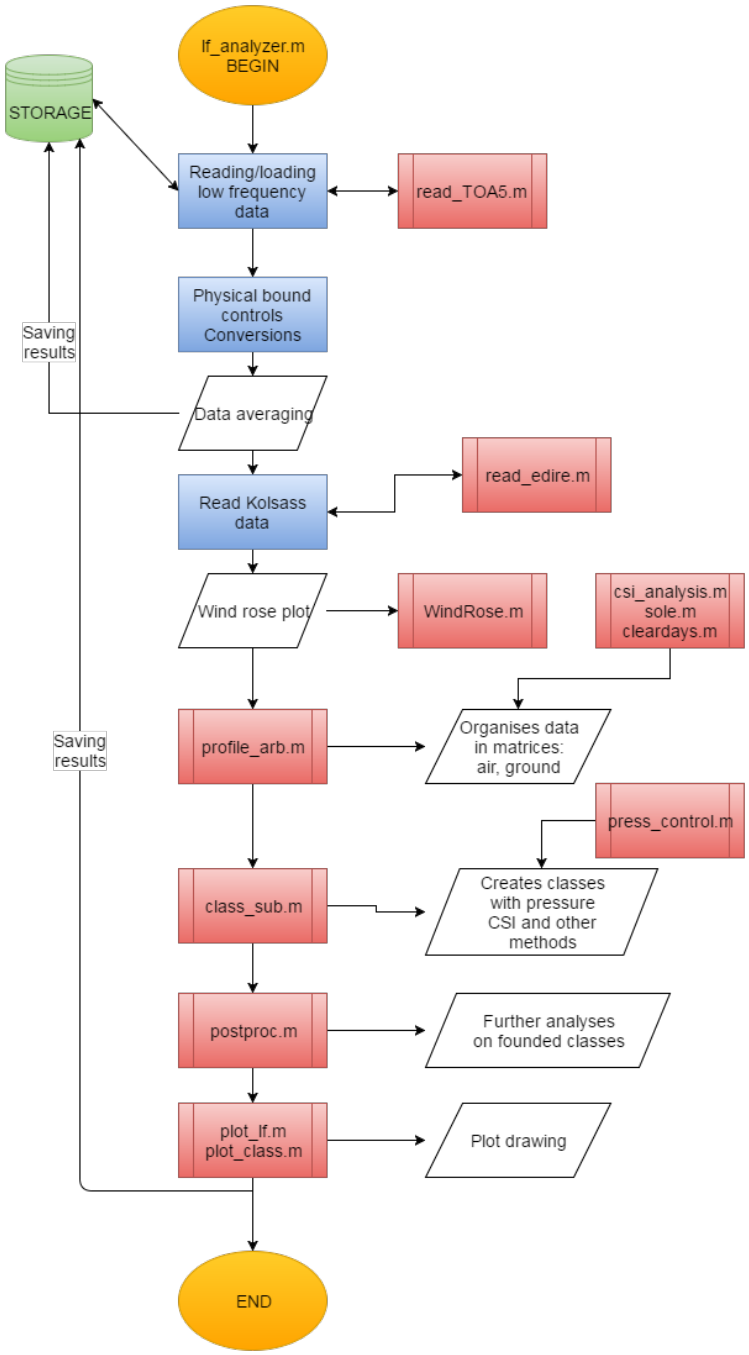

Figure B.1: The low frequency analysis script's flow chart. Here it is summarise the entire structure with the name of functions involved into this analysis.

Figure B.2: The high frequency analysis script's flow chart. Here it is summarise the entire structure with the name of functions involved into this analysis.

Appendix C

Abbreviations

ABL Atmospheric Boundary Layer. 3.

BL Boundary Layer

DNS Direct Numerical Simulation, is a simulation in computational fluid dynamics in which the NavierStokes equations are numerically solved without any turbulence model. This means that the whole range of spatial and temporal scales of the turbulence must be resolved. All the spatial scales of the turbulence must be resolved in the computational mesh, from the smallest dissipative scales (Kolmogorov microscales), up to the integral scale L, associated with the motions containing most of the kinetic energy.

DR Double Rotation. Coordinate rotation around z-axis and y-axis to put the x-axis of the reference system in the streamline direction, thus $\overline{u} \neq 0$, $\overline{v} = \overline{w} = 0$. 99.

i-Box Innsbruck Box project.

LE Latent heat flux.

LES Large Eddy Simulation, is a mathematical model for turbulence used in computational fluid dynamics. It was initially proposed in 1963 by Joseph Smagorinsky to simulate atmospheric air currents, and first explored by Deardorff (1970). LES is currently applied in a wide variety of engineering applications, including combustion, acoustics, and simulations of the atmospheric boundary layer. The simulation of turbulent flows by numerically solving the NavierStokes equations requires to resolve an ample range of

time- and length-scales. Such a resolution can be achieved with Direct numerical simulation (DNS) but is computationally expensive and currently prohibitive for practical problems. The main idea behind LES is to reduce this computational cost by reducing the range of time- and length-scales that are being solved for via a low-pass filtering of the NavierStokes equations. Such a low-pass filtering, which can be viewed as a time- and spatial-averaging, effectively removes small-scale information from the numerical solution. This information is not irrelevant and needs further modeling, a task which is an active area of research for problems in which small-scales can play an important role, problems such as near-wall flows, reacting flows, and multiphase flows.

MOS Model Output Statistics is a multiple linear regression technique in which predicands, often near-surface quantities, such as 2-meter air temperature, horizontal visibility, and wind direction, speed and gusts, are related statistically to one or more predictors. The predictors are typically forecasts from a numerical weather prediction (NWP) model, climatic data, and, if applicable, recent surface observations. Thus, output from NWP models can be transformed by the MOS technique into sensible weather parameters that are familiar to the "person on the street".

MOST Monin-Obukhov Similarity Theory (see section 1.7.1)

NSE Navier-Stokes Equation of motion, these equation are at the basis of the atmosphere dynamics, and the deal about conservation of momentum. 22.

NWP Numerical Weather Prediction (model) uses mathematical models of the atmosphere and oceans to predict the weather based on current weather conditions.

PBL Planetary Boundary Layer (see ABL)

SH Sensible heat flux.

SL Surface Layer, the lowest part of the boundary layer.

TCMT Truly Complex Mountainous Terrain, used by Rotach *et al.* to indicate the highly complex terrain of, e.g., an Alpine valley.

TKE Turbulent Kinetic Energy.

TOA Top Of the Atmosphere, is the ideally place where the absorption and emission of short wave (principally) of atmospheric molecules can be neglected. Then in this place the short wave coming from the sun is completely due to sun's irradiance.

VHR Very High Resolution numerical modelling. These are models with a resolution equal or less than one kilometre.

WMO World Meteorological Organisation

Bibliography

[1] M. Arck and D. Scherer. "Problems in the determination of sensible heat flux over snow". *Geografiska Annaler* 84A.3-4 (2002), pp. 157–169 (cit. on p. 168).

[2] S. P. Arya. *Introduction to Micrometeorology*. Ed. by R. Dmowska, J. R. Holton, and H. T. Rossby. Academic Press, 2001 (cit. on pp. 16, 18).

[3] M. Aubinet, T. Vesala, and D. Papale. *Eddy Covariance: a practical guide to measurement and data analysis*. Springer Atmospheric Sciences, 2012. DOI: 10.1007/978-94-007-2351-1 (cit. on pp. 45, 46, 104).

[4] I. S. Bowen. "The ratio of heat losses by conduction and by evaporation from any water surface". *Physical Review* 27 (1926), pp. 779–787 (cit. on p. 133).

[5] W. Brutsaert. "On a derivable formula for long-wave radiation from clear skies". *Water Resources Research* 11.5 (1975), pp. 742–744. DOI: 10.1029/WR011i005p00742 (cit. on p. 93).

[6] G. S. Campbell and B. D. Tanner. "A krypton hygrometer for measurement of atmospheric water vapour concentration". *Moisture and Humidity* 85 (1985), pp. 609–612 (cit. on p. 78).

[7] C. Cassardo, D. Sacchetti, M. G. Morselli, D. Anfossi, G. Brusasca, and A. Longetto. "A study of the assessment of air temperature, and sensible and latent-heat fluxes from sonic-anemometer observations." *Il nuovo cimento* 18C.4 (1995), pp. 419–440 (cit. on pp. 99, 100).

[8] R. J. Clement and J. Moncreif. *EdiRe Software*. Tech. rep. University of Edinburgh, 2007. URL: http://www.geos.ed.ac.uk/homes/rclement/micromet/EdiRe/ (cit. on p. 95).

[9] R. J. Clement. "Mass and energy exchange of a plantation forest in Scotland using micrometeorological methods". PhD thesis. University of Edinburgh, 2004 (cit. on pp. 98, 101).

[10] T. Foken and H. Falke. "Technical note: Calibration instrument for the Krypton Hygrometer KH20". *Atmospheric Measurement Techniques Discussion* 5 (2012), pp. 1861–1867 (cit. on p. 78).

[11] T. Foken and B. Wichura. "Tolls for quality assessment of surface-based flux measurements". *Agricultural and Forest Meteorology* 78 (1996), pp. 83–105 (cit. on p. 104).

[12] T. Foken. *Micrometeorology*. Ed. by C. J. Nappo. Springer, 2008 (cit. on pp. 8, 20).

[13] T. Foken. "The energy balance closure problem: an overview". *Ecological Applications* 18.6 (2008), pp. 1351–1367 (cit. on pp. 19, 21).

[14] M. de Franceschi, D. Zardi, M. Tagliazucca, and F. Tampieri. "Analysis of second-order moments in surface layer turbulence in an Alpine valley". *Quarterly Journal of the Royal Meteorological Society* 135 (2009), pp. 1750–1765 (cit. on p. 171).

[15] A. Hammerle et al. "Eddy covariance measurements of carbon dioxide, latent and sensible energy fluxes above a meadow on a mountain slope." *Boundary-Layer Meteorology* 122 (2007), pp. 397–416. DOI: 10.1007/s10546-006-9109-x (cit. on p. 46).

[16] D. L. Hartmann. *Global Physical Climatology*. Academic Press, 1994 (cit. on pp. 15, 20).

[17] P. Hignett. "Correction to temperature measurements with a sonic anemometer". *Boundary-Layer Meteorology* 61 (1992), pp. 175–187 (cit. on p. 75).

[18] J. R. Holton. *An Introduction to Dynamic Meteorology*. Ed. by G. J. Hakim. 5th edition. Academic Press, 2013 (cit. on p. 34).

[19] T. W. Horst, S. R. Semmer, and G. Maclean. "Correction of a non-orthogonal, three-component sonic anemometer for flow distortion by transducer shadowing". *Boundary-Layer Meteorology* 155.3 (2015), pp. 371–395. DOI: 10.1007/s10546-015-0010-3 (cit. on p. 72).

[20] J. V. Iribarne and W. L. Godson. *Atmospheric Thermodynamics*. D. Reidel, 1973 (cit. on p. 118).

[21] J. C. Kaimal and J. A. Businger. "A continuous wave sonic anemometer-thermometer". *Journal of Applied Meteorology* 2 (1963), pp. 156–164 (cit. on p. 71).

[22] J. C. Kaimal and J. J. Finnigan. *Atmospheric Boundary Layer Flows: Their Structure and Measurements*. Oxford University Press, 1994 (cit. on pp. 73, 99, 154).

[23] J. C. Kaimal and J. E. Gaynor. "Another look at sonic thermometry". *Boundary-Layer Meteorology* 56 (1991), pp. 401–410 (cit. on pp. 75, 101).

[24] H. Liu, G. Peters, and T. Foken. "New equations for sonic temperature variance and buoyancy heat flux with an omnidirectional sonic anemometer". *Boundary-Layer Meteorology* 100 (2001), pp. 459–468 (cit. on pp. 75, 76, 98, 101).

[25] P. Markowski and Y. Richardson. *Mesoscale Meteorology in Midlatitudes*. Wiley-Blackwell, 2010 (cit. on pp. 40, 43, 91).

[26] C. Marty, R. Philipona, C. Froehlich, and A. Ohmura. "Altitude dependence of surface radiation fluxes and cloud forcing in the Alps: results from the alpine surface radiation budget network." *Theoretical and Applied Climatology* 72 (2002), pp. 137–155 (cit. on p. 92).

[27] C. Marty and R. Philipona. "The Clear-Sky Index to separate Clear-Sky from Cloudy-Sky situations in climate research." *Geophysical Research Letters* 27.17 (Sept. 2000), pp. 2649–2652 (cit. on pp. 15, 92, 240).

[28] G. Massaro, I. Stiperski, B. Pospichal, and M. W. Rotach. "Accurancy of retrieving temperature and humidity profiles by gound-based microwave radiometry in truly complex terrain." *Atmospheric Measurement Techniques Discussion* 8 (2015), pp. 2263–2298. DOI: 10.5194/amtd-8-2263-2015 (cit. on p. 55).

[29] A. Monin and A. Obukhov. "Basic laws of turbulent mixing in the surface layer of the atmosphere". *Tr. Akad. Nauk USSR Geophiz. Inst.* 24.151 (1954), pp. 163–187 (cit. on pp. 32, 41).

[30] R. B. Montgomery. "Vertical eddy flux of heat in the atmosphere". *Journal of Meteorology* (1948) (cit. on p. 44).

[31] D. F. Nadeau, E. R. Pardyjak, C. W. Higgins, and M. B. Parlange. "Similarity scaling over a steep Alpine slope". *Boundary-Layer Meteorology* 147 (2013), pp. 401–419. DOI: 10.1007/s10546-012-9787-5 (cit. on pp. 140, 171, 176).

[32] J. Oerlemans. "Glaciers and Climate Change". Balkema, 2001. Chap. 3, pp. 15–40 (cit. on p. 15).

[33] M. Olefs et al. "The Austrian radiation monitoring network ARAD - best practice and added value". *Atmospheric Measurement Techniques* 9 (2016), pp. 1513–1531. DOI: 10.5194/amt-9-1513-2016 (cit. on p. 94).

[34] M. W. Rotach et al. "MAP D-phase, Real-time demonstration of weather forecast quality in the Alpine region". *Bullettin of American Meteorological Society* (2009). DOI: 10.1175/2009BAMS2776.1 (cit. on p. 44).

[35] M. W. Rotach. "Notes for Atmospheric Physics Lecture, Chapter 4: Similarity Theory". 2015 (cit. on p. 29).

[36] M. W. Rotach and D. Zardi. "On the boundary-layer structure over highly complex terrain: key findings from MAP". *Quarterly Journal of the Royal Meteorological Society* 133 (2007), pp. 937–948. DOI: 10.1002/qj.71 (cit. on p. 44).

[37] M. W. Rotach et al. "Investigating exchange processes over complex topography: the Innsbruck-Box (i-Box)" (cit. on pp. 49, 53).

[38] P. Schotanus, F. T. M. Nieuwstadt, and H. A. R. De Bruin. "Temperature measurement with a sonic anemometer and its application to heat and moisture fluxes". *Boundary-Layer Meteorology* 26 (1983), pp. 81–93 (cit. on pp. 73, 74).

[39] R. M. Schotland. "The measurement of wind velocity by sonic means". *Journal of Meteorology* 12 (1955), pp. 386–391 (cit. on p. 71).

[40] H. Siebert et al. "High-resolution measurement of cloud microphysics and turbulence at moiuntaintop station". *Atmospheric Measurement Techniques* 8 (2015), pp. 3219–3228. DOI: 10.5194/amt-8-3219-2015 (cit. on p. 59).

[41] R. Solanki, N. Singh, K. N. V. P. Kumar, K. Rajeev, and S. K. Dhaka. "Time variability of surface-layer characteristics over a mountain ridge in the central Himalayas during the spring season". *Boundary-Layer Meteorology* 158 (2016), pp. 453–471. DOI: 10.1007/s10546-015-0098-5 (cit. on p. 59).

[42] R. Steinacker. "Area-height distribution of a valley and its relation to the valley wind". *Contr. Atmos.Phys.* 57.1 (1984), pp. 64–71 (cit. on p. 39).

[43] I. Stiperski and M. W. Rotach. "On the measurement of turbulence over complex Mountainous terrain." *Boundary-Layer Meteorology* 159 (2016), pp. 97–121. DOI: 10.1007/s10546-015-0103-z (cit. on pp. 53, 96, 105, 141).

[44] I. Stiperski, M. W. Rotach, and A. Gohm. "Boundary Layer Measurements in Complex Terrain: Innsbruck-Box". *Geophysical Research Abstracts* 14.EGU2012-8863 (2012) (cit. on p. 47).

[45] R. B. Stull. *An Introduction to Boundary Layer Meteorology*. Springer, 1988 (cit. on pp. 4, 7, 27, 75, 135, 154, 157).

[46] J. R. Taylor. *An introduction to error analysis*. University Science Book, 1997 (cit. on p. 144).

[47] J. Tillman. "Humidity and Moisture, I: Principles and methods of measuring humidity in gases". Ed. by A. Wexler and R. E. Ruskin. Reinhold Publishing Corporation, 1965. Chap. Water vapor density measurements utilizing the absorbition of vacuum ultraviolet and infrared radiation, pp. 428–443 (cit. on p. 79).

[48] I. Vergeiner. "An elementary valley wind model". *Meteorology and Atmospheric Physics* 36 (1987), pp. 255–263 (cit. on p. 123).

[49] I. Vergeiner and E. Dreiseitl. "Valley wind and slope wind - observations and elementary thoughts". *Meteorology and Atmospheric Physics* 36 (1987), pp. 264–286 (cit. on pp. 39, 123).

[50] D. Vickers and L. Mahrt. "Quality control and flux sampling problems for tower and aircraft data". *Journal of Atmospheric and Oceanic Technology* 14 (1997) (cit. on p. 108).

[51] E. K. Webb, G. I. Pearman, and R. Leuning. "Correction of flux measurements for density effects due to heat and water vapour transfer". *Quarterly Journal of Royal Meteorological Society* 106 (1980), pp. 85–100 (cit. on pp. 102, 103).

[52] C. D. Whiteman. *Mountain Meteorology*. Oxford University Press, 2000 (cit. on pp. 36, 42, 44).

[53] C. D. Whiteman. "Observations of Thermally Developed Wind Systems in Mountainous Terrain". Ed. by W. Blumen. American Meteorological Society, 1990. Chap. 2 in Atmospheric Process Over Complex Terrain (cit. on p. 40).

[54] J. M. Wilczak, S. P. Oncley, and S. A. Stage. "Sonic anemometer tilt correction algorithms". *Boundary-Layer Meteorology* 99 (2001), pp. 127–150 (cit. on p. 99).

[55] J. C. Wyngaard. “On surface-layer turbulence”. Ed. by D. A. Haugen. Amer, 1973. Chap. 3 in Workshop on micrometeorology, pp. 101–149 (cit. on pp. 104, 142).

Index

Acknowledgements

Writing this thesis has taught me many things, about physics, about atmosphere but also about living abroad and to grow. Many people have met my path, thus the time to thank them has come.

First, I would like to thank my thesis supervisor Prof. Dr. Mathias Rotach of the Institute for Atmospheric and Cryospheric Sciences at University of Innsbruck that had friendly and kindly hosted and welcomed me in his working group. Mathias was very patient, he encouraged and motivated me during the MSc Thesis research, suggesting and teaching me in the new field of atmospheric turbulence. He consistently allowed this paper to be my own work, but steered me in the right direction whenever he thought I needed it.

I would like to thank my thesis supervisor at University of Turin: Dr. Silvia Ferrarese. She considerably helped me, especially during the thesis writing. With patience, she had corrected all my formal mistakes, and warned me from being too much high-flown in the writing. She guided me through all troubles encountered during my foreign sojourn.

I would also like to thank all the Dynamic Meteorology staff that helped me during this Austrian period. Lets start with the researchers: Dr. Friedrich Obleitner (Friedl), his door was always open whenever I ran into a trouble; Dr. Ivana Stipersky (Iva), who has shared her office with me, and also that has guided me at the very beginning with completely new software analysis, MSc. Eleni Syfri, who had collaborated with me in the last part of my work. How can I forget Philipp Vettori (Phil) and our trips around the Inn Valley for the i-Box stations maintenance: thanks for these days spent out of office!

I would also like to acknowledge Dr. Silvia Trini Castelli of the ISAC-CNR, as the second reader of this thesis, and I am gratefully indebted to her because she had contacted Mathias for the first time, and permitted me to come here in Innsbruck.

Finally the most important people, not directly involved in this work, but that have been supporting me during this long living abroad and throughout my

years of study: mum and dad, and also my grandparents and the whole family. A paragraph uniquely dedicated to Francesca, my future spouse, who have been supporting and encouraging me during and before this far adventure away from home; but also I would like to thank her for reading my long thesis and because she went through this long period of separation, doing wedding planning, and still loving me also with 600 km of distance.

I thank the Lord for all the good things he gave to me, for guiding me in this long and arduous path.

I also would like to thank all my friends, a very beautiful group that had changed my life and my Faith, and even though everyone walks along their own way, we still remain together.

A new climb starts tomorrow, and with the experience done here and during my studies, I hope to reach all my aspirations.